A Novel Liquid Argon Time Projection Chamber Detector: The ArgonCube Concept

Inauguraldissertation
der Philosophisch-naturwissenschaftlichen Fakultät
der Universität Bern

vorgelegt von

Damian Goeldi

von Sennwald SG

Leiter der Arbeit
Prof. Dr. A. Ereditato

Albert Einstein Center for Fundamental Physics
Laboratory for High Energy Physics
Physics Institute

A Novel Liquid Argon Time Projection Chamber Detector: The ArgonCube Concept

Inauguraldissertation

der Philosophisch-naturwissenschaftlichen Fakultät

der Universität Bern

vorgelegt von

Damian Goeldi

von Sennwald SG

Leiter der Arbeit

Prof. Dr. A. Ereditato

Albert Einstein Center for Fundamental Physics

Laboratory for High Energy Physics

Physics Institute

Von der Philosophisch-naturwissenschaftlichen Fakultät angenommen.

Bern, 20.04.2018 Der Dekan:

Prof. Dr. G. Colangelo

To Bäschu, it was always inspiring and great fun conducting research with you.

Abstract

The Standard Model (SM) of particle physics has proven to be remarkably consistent in its explanation of experimental observations. An exception is the intriguing nature of neutrinos. Particularly, neutrino flavour eigenstates do not coincide with their mass eigenstates. The flavour eigenstates are a mixture of the mass eigenstates, resulting in oscillations for non-zero neutrino masses. Neutrino mixing and oscillations have been extensively studied during the last few decades probing the parameters of the three flavour model. Nevertheless, unanswered questions remain: the possible existence of a Charge conjugation Parity symmetry (CP) violating phase in the mixing matrix and the ordering of the neutrino mass eigenstates. The Deep Underground Neutrino Experiment (DUNE) is being built to answer these questions via a detailed study of long-baseline neutrino oscillations. Like any beam experiment, DUNE requires two detectors: one near the source to characterise the unoscillated beam, and one far away to measure the oscillations. Achieving sensitivity to CP violation and mass ordering will require a data sample of unprecedented size and precision. A high-intensity beam (2 MW) and massive detectors (40 kt at the far site) are required. The detectors need to provide excellent tracking and calorimetry. Liquid Argon Time Projection Chambers (LArTPCs) were chosen as Far Detectors (FDs) because they fulfil these requirements. A LArTPC component is also necessary in the Near Detector (ND) complex to bring systematic uncertainties down to the required level of a few percent. A drawback of LArTPCs is their comparatively low speed due to the finite charge drift velocity ($\sim 1\,\mathrm{mm\,\mu s^{-1}}$). Coupled with the high beam intensity this results in event rates of 0.2 piled-up events per tonne in the ND. Such a rate poses significant challenges to traditional LArTPCs: Their 3D tracking capabilities are limited by wire charge readouts providing only 2D projections. To address this problem a pixelated charge readout was developed and successfully tested as part of this thesis.

This is the first time pixels were deployed in a single-phase LArTPC, representing the single largest advancement in the sensitivity of LArTPCs—enabling true 3D tracking. A software framework was established to reconstruct cosmic muon tracks recorded with the pixels. Another problem with traditional LArTPCs is the large volume required by their monolithic design resulting in long drift distances. Consequentially, high drift voltages are required. Current LArTPCs are operating at the limit beyond which electric breakdowns readily occur. This prompted world-leading studies of breakdowns in LAr including high-speed footage, current-voltage characteristics, and optical spectrometry. A breakdown-mitigation method was developed which allows LArTPCs to operate at electric fields an order of magnitude higher than previously achieved. It was found however that a safe and prolonged operation can be achieved more effectively by keeping fields below $40\,\mathrm{kV\,cm^{-1}}$ at all points in the detector. Therefore, high inactive clearance volumes are required for traditional monolithic LArTPCs. Avoiding dead LAr volume intrinsically motivates a segmented TPC design with lower cathode voltages. The comprehensive conclusion of the HV and charge readout studies is the development of a novel fully modular and pixelated LArTPC concept—ArgonCube. Splitting the detector volume into independent self-contained TPCs sharing a common LAr bath reduces the required drift voltages to a manageable level and minimises inactive material. ArgonCube is incompatible with traditional PMT-based light readouts occupying large volumes. A novel cold SiPM-based light collection system utilised in the pixel demonstrator TPC enabled the development of the compact ArgonCube Light readout system (ArCLight). ArgonCube's pixelated charge readout will exploit true 3D tracking, thereby reducing event pile-up and improving background rejection. Results of the pixel demonstration were used in simulations of the impact of pile-up for ArgonCube in the DUNE ND. The influence piled-up π^0-induced EM showers have on neutrino energy reconstruction was investigated. Misidentified neutrino energy in ArgonCube is conservatively below $0.1\,\%$

for more than 50 % of the neutrino events, well within the DUNE error budget. The work described in this thesis has made ArgonCube the top candidate for the LAr component in the DUNE ND complex.

Preface

This thesis studies most of the relevant challenges for LArTPC neutrino detectors in future high-multiplicity environments alongside potential solutions, namely the dielectric strength of LAr, new charge and light readout methods, as well as the required next-generation charge readout electronics. Chapter 1 sets the stage and motivates my work, it is a combination of various sources.

The theoretical background of neutrino detection and oscillation is elucidated in Chapter 2. It is started with a short historical introduction loosely based on Giunti and Kim [1] who also provide a very detailed overview of neutrino physics. Details on the detectors used in the historical experiments are taken from Grupen and Schwartz [2], as is the section on final state detection. The theory of neutrino oscillations is inspired by Schmitz' book on neutrino physics [3].

Chapter 3 introduces the LArTPC detector with all its subsystems and peculiarities. It is based on the book on "Noble Gas Detectors" by E. Aprile et al. [4] and the LHEP Master thesis of M. Schenk [5].

Various studies of the technologies required by ArgonCube are presented in Chapter 4. Most of this is my work. I made crucial contributions to the setup of the electric breakdown measurements and played a leading role in data analysis and writing of the paper presenting the results [6], of which I am corresponding author. These studies resulted in a second paper [7] on a method to mitigate breakdowns, which I co-authored. With the HV issues addressed I started investigating new charge readout technologies.

Two technologies are presented: a replacement for wires using copper traces on a thin Kapton layer and a pixelated readout. Both ideas are not new but they have never been used in LAr before. I built, commissioned and operated the test setup including a small TPC for the copper on Kapton readout. The section on the pixelated readout introduces the theory of the applied analogue multiplexing scheme based on [8]. Also described is a composite effort I lead to reduce the noise present in the setup used to test the pixelated readout. Crucial input on the electronics modifications was kindly provided by D. Shooltz from the LArIAT collaboration. Details on the test setup and results are presented in Chapter 5. At BNL, NY, USA I tested new cold charge readout electronics. Based on the knowledge gained from these tests, I advised the neutrino group at LBNL, CA, USA on the testing of their new bespoke pixel electronics, LArPix. Also presented in this chapter are cold SiPM tests performed with the pixel demonstrator described in Chapter 5. They enabled the development of ArCLight [9] by the LHEP LAr group, which I helped testing and characterising.

Chapter 5 presents the novel ArgonCube LArTPC concept developed at LHEP. I designed and constructed a bigger TPC, the pixel demonstrator, to test the pixelated charge readout. I lead its commissioning and operation. For the analysis of the recorded cosmic muon tracks I wrote a reconstruction framework from scratch. Y.-T. Tsai and T. Usher from SLAC, CA, USA provided valuable input on the employed reconstruction algorithms. Based on these findings, a scaled-up version of the pixelated readout was placed in LArIAT with my relevant contributions to the pixel plane design and detector operation. I have presented the pixel demonstration at several conferences (e.g. [10]) and am corresponding author of a resulting paper [11]. All the aforementioned work went into the design of ArgonCube described in the last section of this chapter. The design is the work of the ArgonCube collaboration and will be written up in an appropriate document in the near future.

The detailed implementation of ArgonCube in the DUNE ND is described in Chapter 6. Again, this is the work of the ArgonCube collaboration based on the findings I present in this thesis. To support our proposal of ArgonCube for the DUNE ND we needed to prove its ability to cope with the high rates expected. I provide this proof in the last section of Chapter 6 using a reconstruction simulation I wrote based on my previous findings on the performance of pixelated LArTPCs. C. Marshall from LBNL, CA, USA kindly provided guidance and the raw simulated neutrino events.

The thesis is wrapped up in Chapter 7. This is my work.

Contents

List of Figures

List of Tables

Acronyms

1D 1-Dimensional. 2, 59

2D 2-Dimensional. v, 2, 28, 33, 35, 58, 122–128, 131, 160–173

3D 3-Dimensional. v, vi, 1, 2, 9, 33, 35, 58, 60, 82, 89, 93–95, 101, 114, 128, 130–133

AC Alternating Current. 72

ADC Analogue-to-Digital Converter. 69–72, 74

AGS Alternating Gradient Synchrotron. 4, 5

ARAPUCA Argon R&D Advanced Program at UniCamp. 77, 81, 97

ArCLight ArgonCube Light readout system. vi, vii, 3, 77–81, 96, 97, 102, 106, 110, 132, 133

ArgonNeuT Argon Neutrino Test. 88, 95

ASIC Application-Specific Integrated Circuit. 63, 70, 71

BNL Brookhaven National Laboratory. vii, 4, 63, 69–73, 134

CC Charged Current. 17–20

CCD Charge-Coupled Device. 8

CMOS Complimentary Metal-Oxide-Semiconductor. 71

COH Coherent. 17, 18, 112

CP Charge conjugation Parity symmetry. v, 1, 9, 14, 16, 131

CRT Cosmic Ray Tagger. 76, 85

CSA Charge-Sensitive Amplifier. 73

DAC Digital-to-Analogue Converter. 73–75

DAQ Data Acquisition. 33, 57–59, 64, 76

DIS Deep Inelastic Scattering. 17, 18

DONUT Direct Observation of the Nu Tau. 8, 9

DUNE Deep Underground Neutrino Experiment. v, vi, viii, 1–3, 9, 13, 14, 16, 17, 19, 20, 35, 69–72, 75, 100, 103, 106–112, 118, 130–133

EM ElectroMagnetic. vi, 3, 14, 26–29, 62, 98, 110, 112–130, 132, 148–185

FD Far Detector. v, 2, 13, 16, 69, 70, 72, 75, 108, 130, 131, 133

FEB Front-End Board. 76

FEM Finite Element Method. 36

FIFO First In First Out. 73, 74

FNAL Fermi National Accelerator Laboratory. 8, 13, 19, 45, 80, 81, 95, 103, 106, 108, 132, 133

FPGA Field-Programmable Gate Array. 74

FR4 Flame Retardant 4. 55

GENFIT Generic track-Fitting toolkit. 93, 132

GPU Graphics Processing Unit. 8

HF High Frequency. 33, 72

HV High Voltage. v, vii, 2, 5, 33, 35–37, 39, 40, 53, 55, 84, 87, 98, 100, 103, 131, 133

IC Integrated Circuit. 34

ICARUS Imaging Cosmic And Rare Underground Signals. 88

ID Identifier. 74

IMB Irvine-Michigan-Brookhaven. 6

KamiokaNDE Kamioka Nucleon Decay Experiment. 6, 7, 9

KamLAND Kamioka Liquid scintillation AntiNeutrino Detector. 8, 9

LAr Liquid Argon. v–vii, 2, 3, 9, 17, 28–31, 34–36, 40, 44, 46–49, 53–55, 61, 69, 71, 75–78, 81, 85, 87, 93, 95, 98, 100, 101, 103, 108–110, 112–114, 117, 118, 131–133

LArIAT Liquid Argon In A Testbeam. vii, viii, 64, 95–97, 134

LArPix Liquid Argon Pixel readout ASIC. vii, 69, 71–75, 95, 101, 106, 108, 110, 114, 130, 132–134

LArTPC Liquid Argon Time Projection Chamber. v, vii, viii, 1–3, 13, 16, 21, 28–31, 33–36, 53, 55, 58, 60, 69, 71, 75, 81, 82, 89, 95, 97, 98, 100, 103, 107, 110, 112, 114, 120, 131–133

LBNL Lawrence Berkeley National Laboratory. vii, viii, 69, 71, 75, 95, 108, 113, 132, 134

LHEP Laboratory for High Energy Physics at the University of Bern. vii, 2, 3, 29, 31, 33, 36, 42, 45, 59, 63, 76, 77, 85, 87, 88, 95, 97–101, 103–106, 110, 131–135

LoRCA Low Redshift survey at Calar Alto. 134

MCS Multiple Coulomb Scattering. 24, 93, 95, 114, 125

MEC Meson Exchange Current. 19, 20

MG Motor Generator set. 64

MicroBooNE Micro Booster Neutrino Experiment. 63, 71, 76, 85, 108, 114

MicroMeGaS Micro-Mesh Gaseous Structure. 59, 60

MINERνA Main Injector Experiment for ν-A. 19

MIP Minimum Ionising Particle. 22, 23, 34, 60, 73, 88–92

MSW Mikheyev-Smirnov-Wolfenstein. 13–15, 18

MWPC Multi-Wire Proportional Chamber. 28

NC Neutral Current. 17–20

ND Near Detector. v, vi, viii, 2, 3, 9, 13, 14, 16, 17, 19, 35, 69–72, 75, 100, 101, 103, 106–110, 112–114, 118, 120, 127, 130–134

NIM Nuclear Instrumentation Module. 61, 63, 64

NOνA NuMI Off-axis ν_{e} Appearance. 19

OPERA Oscillation Project with Emulsion-tRacking Apparatus. 9

PAI PolyAmide-Imide. 85

PCA Principal Component Analysis. 93–95, 132

PCB Printed Circuit Board. 55, 60, 64, 69, 77, 78, 82–84, 97, 98, 100, 102, 132

PDE Photon Detection Efficiency. 78, 79, 81

PEEK PolyEther Ether Ketone. 85

PET-C Crystalline PolyEthylene Terephthalate. 37, 87

PMNS Pontecorvo-Maki-Nakagawa-Sakata. 9

PMT PhotoMultiplier Tube. vi, 3–7, 33, 34, 57, 75, 78, 81, 101, 102, 132

POT Protons On Target. 14, 17, 117

PSU Power Supply Unit. 36, 39, 40, 52

QE Quasi-Elastic. 17–20

RC Resistor Capacitor. 87

RES Resonant. 17–20, 112

RGB Red Green Blue. 40

RMS Root Mean Square. 24

ROI Region Of Interest. 58–60, 65–69, 82, 84, 88–93, 97

SAR Successive Approximation Register. 73

SBND Short Baseline Neutrino Detector. 76, 85

SiPM Silicon PhotoMultiplier. vi, vii, 3, 36, 75–78, 81, 85, 87, 89, 102, 106, 132

SM Standard Model. v, 1

SNO Sudbury Neutrino Observatory. 5, 8, 9

SNR Signal-To-Noise Ratio. 28, 57, 60, 63, 87–89, 97, 132

SPI Serial Peripheral Interface bus. 63, 74, 75

SSM Standard Solar Model. 5, 8

SURF Sanford Underground Research Facility. 13

T2K Tokai To Kamioka. 8, 9

TPB TetraPhenyl Butadiene. 34, 75–78, 85, 87

TPC Time Projection Chamber. v–vii, 2, 3, 28, 29, 31, 36, 55–57, 59, 60, 70, 72, 73, 75, 76, 85–87, 95–98, 100, 101, 103–106, 108, 110, 111, 114, 131–133

TTL Transistor-Transistor Logic. 40

UART Universal Asynchronous Receiver-Transmitter. 74

USB Universal Serial Bus. 64

UV UltraViolet. 6

VME VERSAmodule Eurocard. 64

VUV Vacuum UltraViolet. 34, 78

WLS WaveLength Shifter. 34, 75–78, 85, 87

1. Introduction

The Standard Model (SM) of particle physics has proven to be remarkably consistent in its explanation of experimental observations over the last decades. An exception is the intriguing nature of neutrinos. Not only are their mass eigenstates a mixture of their flavour eigenstates, but also their masses are smaller than charged lepton masses by several orders of magnitude. Measuring these effects is not simplified by the fact that the interaction rates (cross-section) of neutrinos are extremely small, raising the need for high-intensity sources along with extremely massive detectors. This is the reason why it took almost 25 years from their proposal [12] to the first measurement [13] of neutrinos. As of today, neutrino mixing is well established and their masses have been proven to be non-zero. The basis for this was the discovery of neutrino oscillations [14–16], a consequence of neutrino flavour mixing [17, 18] paired with non-zero masses. However, there are still several unknowns in today's neutrino mixing and oscillation model. In particular, a theory exists with three Charge conjugation Parity symmetry (CP) violation phases that have yet to be measured [17–19]. The consequences of measuring CP violation in neutrino oscillation could be far-reaching. Via cosmological models [20], it could explain the asymmetry between matter and antimatter in the universe. Besides, while it is certain that at least two out of the three neutrinos have non-zero masses, their ordering is still unknown. Its determination will help to integrate massive neutrinos into the SM, where they are currently massless.

Measuring the unknown parameters of the neutrino mixing and oscillation model will require a neutrino interaction sample of unprecedented size. Much of today's knowledge was gained from neutrinos produced in the Sun [16, 21, 22] and the Earth's atmosphere [14, 15]. However, these and other natural sources have become neither intense or precise enough to probe oscillation physics. The same is true for nuclear reactor neutrinos [13, 23]. Therefore, artificially produced neutrino beams and massive detectors [24] are being deployed. Not only are neutrino interactions with matter very rare, they are also very manifold, giving raise to the need for detectors capable of recording complex event topologies and precisely reconstructing the kinematic variables of the events. Liquid Argon Time Projection Chambers (LArTPCs) are prime candidates for the aforementioned requirements. They combine a high-density target material with high-precision 3-Dimensional (3D) tracking and calorimetry.

The Deep Underground Neutrino Experiment (DUNE) [25–28] is a next generation long-baseline beam neutrino oscillation experiment, placing LArTPCs in an accelerator-produced muon (anti)neutrino beam. Several implications result from the required number of neutrino interactions to be sensitive to CP violation and neutrino mass ordering. As mentioned above, a very intense neutrino beam and a large target mass are necessary [27, 28]. However, this is not enough; at the same time, uncertainties have to be kept under control. Statistical uncertainties can be lowered by acquiring more neutrino interactions, but this is not true for systematic uncertainties, which will therefore become the limiting factor. To largely cancel systematic uncertainties a *Near Detector (ND)* complex containing a LArTPC will be placed close to the neutrino source (574 m) in addition to the *Far Detector (FD)* complex at the end of the baseline, at 1300 km distance.

Up until now LArTPC charge readouts have been realised by means of multiple 1-Dimensional (1D) wire planes due to technological limitations. Combined with the time of the drifting charge this results in one 2-Dimensional (2D) image of the event topology per wire plane, effectively reducing the 3D capabilities of the Time Projection Chamber (TPC) to multiple 2D projections. In this thesis I will show how to implement a true 3D LArTPC and demonstrate its performance by reconstructing cosmic muon tracks by exploiting a method based on the use of a Kalman filter.

LArTPCs are comparatively slow detectors. The maximum drift velocity of charge in Liquid Argon (LAr) (and thus the readout time) is limited to $\sim 1\,\mathrm{mm\,\mu s^{-1}}$ by constraints on the maximum cathode voltage. Both the above have not prevented the success of LArTPCs up to now. Due to the low interaction cross-section event rates in current-generation LArTPCs have been low enough to cope with. While this still applies to the DUNE FD, it is certainly not true for the ND. The high-intensity neutrino beam will result in event rates in the ND significantly higher than what contemporary LArTPCs have seen. Furthermore, the beam is delivered in very short pulses (spills) of very high intensity. These spills are from one to two orders of magnitude shorter than a typical LArTPC readout cycle. Therefore, the detector registers several neutrino interactions simultaneously, so-called event pile-up. Combined with the 2D projection readout this leads to significant difficulties in event reconstruction: disentangling the 3D interaction topologies from the recorded 2D projections. An obvious solution to this challenge is to regain true 3D information from the TPC by replacing the projective 1D wire planes with a true 2D pixelated charge readout. I will show how the related technological challenges can be addressed. In particular, new charge readout electronics with a stringent power management are necessary to keep heat dissipation to a minimum and prevent the LAr from boiling.

In addition to these readout issues, future large LArTPCs face several other challenges. In particular for the High Voltage (HV) and light readout systems. Earlier studies by the Laboratory for High Energy Physics at the University of Bern (LHEP) [29] showed that the dielectric strength of LAr is much lower than predicted by studies performed in the 1950s [30, 31]. Current LArTPCs are already operating at the limit beyond which electric breakdowns readily occur [32]. Electronegative impurities present in the LAr result in a finite charge lifetime. This results in a lower limit on the required drift field and therefore cathode voltage. Due to the finite dielectric strength of LAr the required clearance volume outside the TPC scales with detector size unless accounted for by a modified HV system. I will also present a detailed study of the dielectric strength of LAr alongside a method to increase the cathode voltage without additional clearance.

In order to get proper timing for the third coordinate in a LArTPC the collected scintillation light needs to be matched to the corresponding detected charge. This becomes problematic in large monolithic LArTPCs with many simultaneous particle interactions. Furthermore, traditional light readout systems based on PhotoMultiplier Tubes (PMTs) occupy large volumes. I will introduce the ArgonCube Light readout system (ArCLight), a novel compact light readout system based on Silicon PhotoMultipliers (SiPMs).

ArgonCube is a new LArTPC concept developed at LHEP and addressing all aforementioned issues by means of a modular TPC design combined with a pixelated charge readout. It remains to be shown that such a detector is actually able to cope with the event rates expected in the DUNE ND. At DUNE energies ElectroMagnetic (EM) showers produced by decaying π^0 result in a plethora of apparently unconnected charge clusters. Associating all those separate charge clusters to the correct neutrino interaction is one of the most difficult reconstruction tasks, even for a LArTPC. Energy misidentifications significantly impair the overall energy resolution of the experiment. I will show a simulation of such interactions in ArgonCube to investigate its behaviour under high event rates, as expected in the DUNE ND.

The goal of this work is to establish the key technologies enabling the successful deployment of an ArgonCube LArTPC component in the DUNE ND complex. An introduction to the history and theory of neutrino detection as well as an overview of

DUNE are given in Chapter 2. The standard LArTPC design is explained in Chapter 3, including a description of its limitations. Chapter 4 contains several studies addressing the challenges met by future LArTPCs. These include a thorough investigation of dielectric breakdowns in LAr, the development of new charge and light readout methods, as well as the evaluation of electronics for pixelated charge readouts. My main contribution to ArgonCube is the demonstration of a pixelated LArTPC readout in Chapter 5. A general description of the ArgonCube concept is also given in this chapter. Chapter 6 introduces the proposed ArgonCube detector for the DUNE ND complex together with a feasibility study of a LArTPC in such an environment. The thesis is summarised in Chapter 7.

2. Neutrinos and their Detection

Neutrino physics has seen an outstanding progress from first detection 60 years ago to planned huge experiments in the near future. This chapter will give an overview of the history of neutrino detectors, describe the current state of the field, and then introduce the most relevant physics.

2.1. History

In 1914 Chadwick proved that the energy spectrum of the β-decay was continuous [33]. To explain this Wolfgang Pauli proposed the *neutron*, a neutral weakly interacting fermion, to the *Radioactive Ladies and Gentlemen* of the Tübingen conference on radioactivity in 1930 [12]. However, the same Chadwick discovered the particle we today call neutron in 1932 [34]. Upon this Fermi proposed the name *neutrino* and a little later came up with a new theory for β-decay [35].

It took almost another quarter of a century until the neutrino was experimentally detected for the first time by Reines and Cowan in 1956 [13]. They built a detector for the reaction

$$\overline{\nu}_{\mathrm{e}}\mathrm{p} \rightarrow \mathrm{e}^{+}\mathrm{n} \tag{2.1}$$

and placed it next to a nuclear reactor on the Savannah River Site in South Carolina, USA. It consisted of two water tanks sandwiched in between three liquid scintillator tanks with PMTs on the sidewalls. The water was the target to induce the above reaction while the scintillator tanks had the task of detecting the resulting positron and neutron. A free positron slows down in matter and eventually gets captured by a shell electron, producing two back-to-back photons with an energy of 511 keV each. These produce scintillation light in the two adjacent tanks and thus can be detected by forming a coincidence between PMTs of the two tanks. Neutron detection is achieved by doping the water target with cadmium which captures the free neutrons. This produces multiple photons that can again be detected using the coincidence of the two adjacent scintillator tanks. Neutron capture is much slower than positron capture. Therefore, the process in Equation (2.1) produces a very distinct signal in the detector: a low-amplitude pulse from the positron capture followed by a high-amplitude pulse from the neutron capture a few µs later. Backgrounds can be efficiently rejected employing this technique. The drawback is that detection is limited to the $\overline{\nu}_{\mathrm{e}}$ interaction in Equation (2.1).

In 1962 Lederman et al. proved the existence of the ν_μ at the Alternating Gradient Synchrotron (AGS) at Brookhaven National Laboratory (BNL) in New York, USA [36]. For the first time, they produced ν_μ using an accelerator. The protons from the AGS were guided onto a beryllium target producing pions which in turn decay according to

$$\pi^+ \to \mu^+\nu_\mu \quad \text{and} \quad \pi^- \to \mu^-\overline{\nu}_\mu \tag{2.2}$$

producing a beam of muon (anti)neutrinos. *Spark chambers* were used to detect the neutrinos. They were placed behind a 13.5 m wall of iron shielding used to stop the muons and remaining hadrons from the beam.

A spark chamber consists of several parallel conducting plates immersed in a counting gas, typically a mixture of helium and neon. Every other plate is connected to a pulsed HV power supply while the rest are grounded. Triggering detectors (usually scintillators coupled to PMTs) are placed at either end of the stack. Whenever two coinciding signals from these are received, an HV pulse is applied to the plates. If this happens fast enough ($\sim 10\,\mu\text{s}$), a spark forms along the electric field lines where the counting gas has been ionised by the incident particle(s). Amplitude and duration of the HV pulse need to be carefully tuned in order to reach the threshold of spark formation but prevent random sparks on sharp edges and spacers etc. A gas amplification of 10^8 to 10^9 is required to achieve this. Furthermore, the rising edge of the HV pulse needs to be extremely short ($\sim 1\,\text{ns}$). If it is too long, it drifts the ionised track towards the electrodes before the field is high enough to initiate a discharge. Switching HV at this speed is not easy. Additionally, spark chambers require quite high dead times of $\sim 100\,\text{ms}$ to clear the ionisation charge. A *clearing field* or an electronegative quenching gas additive can be used to speed up this process.

In the 1960s, after Davis had failed to measure the lepton-number-violating reaction

$$\overline{\nu}_{\mathrm{e}}\,{}^{37}\mathrm{Cl} \to \mathrm{e}^{-}\,{}^{37}\mathrm{Ar}, \tag{2.3}$$

he decided to replace reactor $\overline{\nu}_{\mathrm{e}}$ with solar ν_{e} and measure

$$\nu_{\mathrm{e}}\,{}^{37}\mathrm{Cl} \to \mathrm{e}^{-}\,{}^{37}\mathrm{Ar} \tag{2.4}$$

instead [21, 22]. Surprisingly, they measured a flux approximately one third lower than predicted by the Standard Solar Model (SSM). This result became famous as the solar neutrino problem, only to be resolved more than 30 years later by the Sudbury Neutrino Observatory (SNO). Davis' experiment was located 1478 m (4200 m water equivalent) underground in the Homestake Gold Mine in South Dakota, USA. The detector consisted of a tank filled with 615 t of tetrachloroethylene, C_2Cl_4. As opposed to the two experiments above, this was a *radiochemical* detector which can only detect neutrino interactions offline. According to Equation (2.4), an incident neutrino converts one of the chlorine atoms in the detector into an unstable argon isotope. After exposure, the tank is purged by pumping helium gas through the liquid to extract the argon isotopes. In order for this to work a certain amount of ^{36}Ar is introduced into the tank as a carrier. Through a sophisticated system the argon is purified, and finally its ^{37}Ar content is measured in a *proportional counter*. By counting the number of decaying argon isotopes and extrapolating using its half-life of 35 days it is possible to calculate the number of neutrino interactions during the exposure.

A proportional counter is a container with two electrodes (usually a cylinder with a wire in its centre) filled with a counting medium (usually gaseous). Incident charged particles ionise the counting medium—neutral particles can be detected if they first produce charged particles via interaction with matter in or surrounding the detector. If an electric field is applied to the electrodes, the produced electron-ion pairs are separated and drift towards the corresponding electrode. By reading out the current on the electrodes one can measure the amount of ionisation produced inside the detector. Usually, the anode is read out because the drift velocity of electrons in an electric field is much higher than the one of ions. If the ionisation charge is simply drifted towards the electrodes, the detector is in fact an ionisation counter rather than a proportional counter. The problem is that the charge produced by the ionisation is very low and the current detector needs to be very sensitive. Sensitivity can be improved by increasing the voltage across the electrodes. If the field inside the counter is above a certain threshold, the drifting ionisation electrons become energetic enough to ionise the counting medium themselves and thus start an avalanche that produces more charge. In the appropriate voltage range the produced charge is still proportional to the primary ionisation charge, hence the name proportional counter. The voltage can be raised further to enter the Geiger regime where the avalanches produce UltraViolet (UV) photons in addition to the ionisation.

These UV photons travel independently of the electric field and can start new avalanches via the photoelectric effect. The process can only be stopped by quenching the discharge either electrically (temporary voltage reduction) or chemically (quenching additive).

While the Homestake experiment provided a clean way of counting ν_e interactions, it provided no information on timing, direction, and kinematics. Only a lower energy threshold is given by the reaction in Equation (2.4). Due to this, it was not possible to tell which reaction chain in the sun the detected neutrinos originated from. Furthermore, care needs to be taken for a very good understanding of all background processes that can produce ^{37}Ar or its signature in the counting tube. Finally, this experiment was only capable of detecting ν_e, a limitation that proved to be crucial in the solution of the solar neutrino problem: oscillation.

In 1988, the Kamioka Nucleon Decay Experiment (KamiokaNDE), in the Kamioka mine in Japan, and the Irvine-Michigan-Brookhaven (IMB) detector [37], in a Morton Salt mine in Ohio, USA, found a similar deficiency in atmospheric neutrinos. These were actually a background for the original experiments looking for proton decays. Atmospheric neutrinos are produced in a similar fashion to Lederman et al. in their muon neutrino beam experiment. Cosmic rays strike the Earth's atmosphere and produce secondary particles many of which are pions subsequently decaying according to Equation (2.2). Thus, atmospheric neutrinos are mainly $\nu_\mu/\overline{\nu}_\mu$. KamiokaNDE measured a muon neutrino flux of only $(59 \pm 7)\,\%$ of the value predicted by simulations [38]. After an upgrade (KamiokaNDE-II), the collaboration furthermore confirmed the solar neutrino problem discovered by the Homestake experiment [39]. The detector was a 3000 t water tank equipped with 1000 PMTs to detect *Cherenkov* radiation produced by incoming charged particles.

Upon passage of a charge particle the atoms of the medium become electric dipoles by means of polarisation. If the velocity of the incident particle v is greater than the speed of light inside the medium $\frac{c}{n}$, defined by the refractive index n, this polarisation is not symmetric anymore, resulting in a non-vanishing dipole moment. A characterisitic cone-shaped radiation in the direction of the particle is the result. The half opening angle of the cone is given by

$$\cos(\theta_\mathrm{c}) = \frac{c}{n(\lambda)v}, \tag{2.5}$$

and the radiation spectrum is

$$\frac{\mathrm{d}N}{\mathrm{d}x} = 2\pi\alpha z^2 \int_{\lambda_1}^{\lambda_2} \left(\frac{\sin(\theta_\mathrm{c}(\lambda))}{\lambda}\right)^2 \mathrm{d}\lambda\,, \tag{2.6}$$

with the number of Cherenkov photons N, path length x, fine-structure constant α, and electric charge of the particle z. By recording the ring produced by this cone with light detectors it is possible to determine timing, direction, momentum, and type of the incident charged particle within certain restrictions. Often employed detection media include water and oil while the photodetectors are usually PMTs.

The charged particles detectable by a Cherenkov detector can be produced by neutrinos in multiple ways. Only the two most important processes are introduced here, a more detailed description will be given in Section 2.4. Analogously to Equation (2.1), neutrinos of all three flavours can interact with nucleons according to

$$\nu_\ell \mathrm{n} \rightarrow \ell^- \mathrm{p} \quad \text{and} \tag{2.7}$$

$$\bar{\nu}_\ell \mathrm{p} \rightarrow \ell^+ \mathrm{n}, \tag{2.8}$$

with $\ell = \mathrm{e}, \mu, \tau$. It should be noted however that τ leptons are usually too short-lived and heavy to produce enough Cherenkov radiation to be detected. A second interaction path of neutrinos with matter is scattering off shell electrons according to

$$\nu_\ell \mathrm{e}^- \to \nu_\ell \mathrm{e}^- \quad \text{and} \tag{2.9}$$

$$\bar{\nu}_\ell \mathrm{e}^- \to \bar{\nu}_\ell \mathrm{e}^- . \tag{2.10}$$

If the neutrino momentum is high enough, the electron recoil can be detected by a Cherenkov detector for all three flavours.

Registering timing and directionality in addition to being able to detect and distinguish ν_e and ν_μ was a huge improvement over the radiochemical Homestake experiment. Still, Cherenkov detectors suffer from some deficiencies in particle identification. One of them is that they can only detect charged particles with sufficient momentum to produce Cherenkov radiation rather than detecting the whole event topology. The detector cannot distinguish between processes producing the same ring signature. An important example is a π^0 produced by a ν_μ, inducing a signal in a Cherenkov detector very similar to the one of a ν_e. This is a crucial background for neutrino oscillation experiments.

Super-KamiokaNDE, the 50 kt successor of KamiokaNDE, solved the atmospheric neutrino problem in 1998 [14, 15]. It measured the flavour ratio of the atmospheric neutrino flux as a function of zenith angle. The number ratio of upward to downward muon-like events was found to be $\approx 50\,\%$ while from Monte Carlo simulations it was expected to be $\approx 100\,\%$. This result suggested a disappearance of ν_μ via neutrino oscillations for atmospheric neutrinos that travelled along the much longer baseline through the Earth.

The solar neutrino problem was solved in 2002 by SNO, in the INCO Ltd. Creighton Mine in Ontario, Canada [16]. SNO was a 1 kt heavy water Cherenkov detector located 2039 m below the Earth surface (≈ 6000 m water equivalent). Its use of heavy water

(D_2O) allowed it to detect neutrinos flavour-independently via

$$\nu_\ell \mathrm{d} \to \nu_\ell \mathrm{pn} \quad \text{and} \tag{2.11}$$

$$\bar{\nu}_\ell \mathrm{d} \to \bar{\nu}_\ell \mathrm{pn} \tag{2.12}$$

in addition to the interaction channels detectable by light water Cherenkov detectors given by Equations (2.7), (2.8), (2.9), and (2.10). For this to work, the emerging neutron needs to be detected which was achieved using ^{3}He-filled proportional counters inside the heavy water tank. The additional neutrino detection channel allowed SNO to prove that only the solar ν_e flux is below the predictions by the SSM while the combined flux of all three flavours is consistent with the model. This was a direct evidence for neutrino oscillation.

The ν_τ was first detected by the Direct Observation of the Nu Tau (DONUT) experiment at Fermi National Accelerator Laboratory (FNAL) in Illinois, USA in 2001 [40]. Similarly to the ν_μ discovery, a neutrino beam was produced by shooting 800 GeV protons from the Tevatron onto a tungsten beam dump. The ν_τ were detected via the interactions described by Equations (2.7) and (2.8) for $\ell = \tau$. Therefore, it was required to detect very short-lived τ, requiring a detector with a very good spatial resolution.

Nuclear emulsions were chosen as the core component of the detector. They consist of fine-grained ($\sim 0.1\,\mu\mathrm{m}$) silver-halide crystals (AgBr and/or AgCl) embedded in a gelatine substrate. Ionisation by passing charged particles causes some of the silver-halide molecules to be reduced to metallic silver. A subsequent development process reduces the silver-halide crystals, preferentially affecting those microcrystals already disturbed and partly reduced by the ionisation. Finally, the remaining crystals are dissolved in the fixation process, leaving a stable image of elemental silver particles along the ionisation tracks. These charge images can be digitised using Charge-Coupled Device (CCD) cameras attached to computer-controlled microscopes. Pattern recognition accelerated by Graphics Processing Units (GPUs) can be employed for event reconstruction.

The spatial resolution of emulsions is limited by crystal size. On the other hand, the crystals need to have a certain size in order for ionising particles to be able to reduce enough silver-halide molecules to create a track inside the emulsion. A compromise needs to be found based on the experimental requirements. Typically, the spatial resolution is $\approx 2\,\mu\mathrm{m}$. The price for the high resolution is that emulsions are an offline detector that cannot be triggered or vetoed. An external tracking detector (scintillating fibres in the case of DONUT) is required to record event timing. Its data needs to be matched to the emulsion data before the actual analysis.

Nowadays, the concept of neutrino oscillation is well-established and characterised by the Daya Bay [23], Tokai To Kamioka (T2K) [24], Kamioka Liquid scintillation AntiNeutrino Detector (KamLAND) [41], SNO, Super-KamiokaNDE, Oscillation Project with Emulsion-tRacking Apparatus (OPERA) [42], and many other experiments. Daya Bay and KamLAND employ the same technique as Reines and Cowan to look for disappearance of nuclear reactor $\overline{\nu}_{\mathrm{e}}$. The only difference being that they use one big scintillator tank shielded and vetoed by water and/or mineral oil Cherenkov detectors instead of multiple tanks in coincidence. T2K directs a ν_μ beam similar to the one of Lederman et al. towards Super-KamiokaNDE to look for ν_μ disappearance and ν_{e} appearance over a long baseline. In particular, Daya Bay and T2K measured a non-zero θ_{13} mixing angle, enabling a potential discovery of CP violation in the lepton sector via neutrino oscillation in matter (see Section 2.2). OPERA used an emulsion detector similar to the one of DONUT to observe ν_τ appearance in a ν_μ beam.

2.2. Neutrino Oscillation

ArgonCube has been proposed as the LAr component of the ND for the DUNE long-baseline neutrino oscillation experiment. Therefore, this section will give a basic introduction to neutrino oscillation.

The root cause of neutrino oscillation is that the flavour eigenstates (ν_α with $\alpha = \mathrm{e}, \mu, \tau$) of the three neutrinos are not equal to their three mass eigenstates (ν_i with $i = 1, 2, 3$). The mass composition of the flavour eigenstates can be written as

$$\begin{pmatrix} \nu_\mathrm{e} \\ \nu_\mu \\ \nu_\tau \end{pmatrix} = U_\mathrm{PMNS} \begin{pmatrix} \nu_1 \\ \nu_2 \\ \nu_3 \end{pmatrix}, \tag{2.13}$$

where

$$\begin{aligned} & U_\mathrm{PMNS} \\ & = \\ U_\mathrm{sol} \times U_\mathrm{rea} & \times U_\mathrm{atm} \times U_\mathrm{maj} \\ & = \\ \begin{bmatrix} 1 & 0 & 0 \\ 0 & C_{23} & S_{23} \\ 0 & -S_{23} & C_{23} \end{bmatrix} \times \begin{bmatrix} C_{13} & 0 & S_{13}e^{-i\delta_\mathrm{CP}} \\ 0 & 1 & 0 \\ -S_{13}e^{-i\delta_\mathrm{CP}} & 0 & C_{13} \end{bmatrix} & \times \begin{bmatrix} C_{12} & S_{12} & 0 \\ -S_{12} & C_{12} & 0 \\ 0 & 0 & 1 \end{bmatrix} \times \begin{bmatrix} e^{i\frac{\alpha_1}{2}} & 0 & 0 \\ 0 & e^{i\frac{\alpha_2}{2}} & 0 \\ 0 & 0 & 1 \end{bmatrix} \end{aligned} \tag{2.14}$$

is the Pontecorvo-Maki-Nakagawa-Sakata (PMNS) matrix [17, 18]. It can be written as the product of three rotation matrices corresponding to the three Euler angles in 3D space, the mixing angles θ_{12}, θ_{13} and θ_{23}. In Equation (2.14) they are represented by $S_{ij} = \sin\theta_{ij}$ and $C_{ij} = \cos\theta_{ij}$. Due to their first measurement with solar, reactor, and atmospheric neutrinos, respectively the matrices and angles are often named accordingly. In addition to the mixing angles there is a Dirac, δ_CP, and two Majorana [19] CP-violating phases, α_1 and α_2. An important feature of the Dirac phase is that it is suppressed for $\theta_{13} = 0$, as can be seen from U_rea in Equation (2.14). The Majorana phases can only be measured by experiments sensitive to a Majorana nature of the neutrinos, such as neutrinoless double beta decay experiments. In neutrino oscillation experiments they cancel out. Therefore, they are ignored for the rest of this work. An illustration of the relation between the mass and flavour neutrino eigenstates is shown in Figure 2.1.

The mass eigenstates ν_i from Equation (2.13) evolve in time as

$$|\nu_\mathrm{i}(t)\rangle = e^{-iE_it}\,|\nu_\mathrm{i}\rangle \tag{2.15}$$

where E_i is the energy of the mass eigenstate ν_i. Furthermore, Equation (2.13) can be solved for ν_i:

$$\begin{pmatrix} \nu_1 \\ \nu_2 \\ \nu_3 \end{pmatrix} = U^\dagger_\mathrm{PMNS} \begin{pmatrix} \nu_\mathrm{e} \\ \nu_\mu \\ \nu_\tau \end{pmatrix}, \tag{2.16}$$

where $U^\dagger_\mathrm{PMNS}$ is the adjoint matrix of U_PMNS. This leads to

$$\begin{pmatrix} \nu_\mathrm{e} \\ \nu_\mu \\ \nu_\tau \end{pmatrix} = U_\mathrm{PMNS} D U^\dagger_\mathrm{PMNS} \begin{pmatrix} \nu_\mathrm{e} \\ \nu_\mu \\ \nu_\tau \end{pmatrix} \tag{2.17}$$

with the diagonal matrix

$$D_{ij} = \delta_{ij} e^{-iE_it}, \tag{2.18}$$

where δ_{ij} is the Kronecker delta. The energy can be replaced by a second-order Taylor approximation,

$$E_i = \sqrt{p^2 + m_i^2} \approx p + \frac{m_i^2}{2p}, \tag{2.19}$$

Table 2.1.: Oscillation parameters obtained from a recent global fit for the normal mass ordering case. The uncertainties are given for 1σ. [43]

Parameter	Value	Unit
θ_{12}	33.2(12)	$\circ$
θ_{13}	8.45(15)	$\circ$
θ_{23}	41.4(16)	$\circ$
δ_{CP}	$-100(50)$	$\circ$
Δm^2_{21}	$7.45(25) \times 10^{-5}$	eV^2
$\left\|\Delta m^2_{31}\right\|$	$2.55(5) \times 10^{-3}$	eV^2

assuming the same momentum p for all mass eigenstates. After some further conversions one obtains

$$
\begin{aligned}
P\Big(\nu_\alpha \to \nu_\beta\Big) &= \left|\sum_i U_{\alpha i} U^*_{\beta i} e^{-iE_i t}\right|^2 \\
&= \sum_i \left|U_{\alpha i} U^*_{\beta i}\right| + 2\,\mathrm{Re}\left\{\sum_{i>j} U_{\alpha i} U^*_{\alpha j} U^*_{\beta i} U_{\beta j} e^{-i\Delta_{ij}}\right\}
\end{aligned}
\tag{2.20}
$$

for the transition probability from ν_α into ν_β. The phase difference

$$
\begin{aligned}
\Delta_{ij} &= \Big(E_i - E_j\Big)t \\
&= \frac{\Delta m^2_{ij}}{2} \frac{t}{p} \\
&\approx \frac{\Delta m^2_{ij}}{2} \frac{L}{E}
\end{aligned}
\tag{2.21}
$$

depends on the mass splitting $\Delta m^2_{ij} = m^2_i - m^2_j$. In the relativistic case $p \gg m_i$ momentum can be approximated by energy ($p \approx E$) and time by baseline ($t = ct \approx L$). To improve readability, U_{PMNS} was abbreviated by U.

The second term of Equation (2.20) is of oscillatory nature. This implies that the frequency of the oscillation is determined by the mass splitting, and the amplitude by the matrix elements of U_{PMNS}, i.e. the mixing angles θ_{12}, θ_{13} and θ_{23}. A particular consequence of this is that the observation of neutrino oscillations between all three flavours proves a finite mass of at least two of the three neutrinos.

It is worth noting two important facts at this point. First, the same result can be obtained by replacing time propagation e^{-iE_it} with spatial propagation $e^{i\vec{\mathbf{p}}_\mathbf{i}\vec{\mathbf{x}}}$ and assuming equal energy instead of momentum for all mass eigenstates. Second, both assumptions are wrong from a physics point of view. Furthermore, a plane wave function is assumed in both derivations, which is also wrong. A wave packet approach is required to correctly describe neutrino oscillations. However, it can be shown that the plane wave approximation in conjunction with either an equal momentum or equal energy assumption leads to the correct result. Both points have been illustrated by Akhmedov and Smirnov [44].

Despite predicting neutrino mixing and oscillation, the model does not predict the values of the oscillation parameters. They need to be determined experimentally. The three-neutrino paradigm described above is well-established and has withstood tests by many experiments in the last few decades. Table 2.1 shows the results of a recent global fit [43]. In particular, it can be seen that the uncertainties on δ_{CP} are huge and the sign of Δm^2_{31} is not yet known. The latter gives rise to two different orderings of the neutrino masses as depicted in Figure 2.1. Much higher statistics than were achieved in neutrino experiments so far are needed to determine these parameters.

Various effects can be exploited to enhance the oscillation probability from Equation (2.20), such as $\frac{L}{E}$ tuning and matter effects. Tuning of $\frac{L}{E}$ is trivial to understand from theory but not so easy to achieve in practice. Originally, neutrino oscillations were discovered and characterised using solar and atmospheric neutrinos. While neutrinos produced in the Earth's atmosphere allow for some $\frac{L}{E}$ tuning by means of a zenith angle selection, and similarly via time of year for solar neutrinos, the gain is limited. Much more fine-grained control is possible by directing an artificially produced neutrino beam with a well-defined energy spectrum towards an underground detector at an optimised

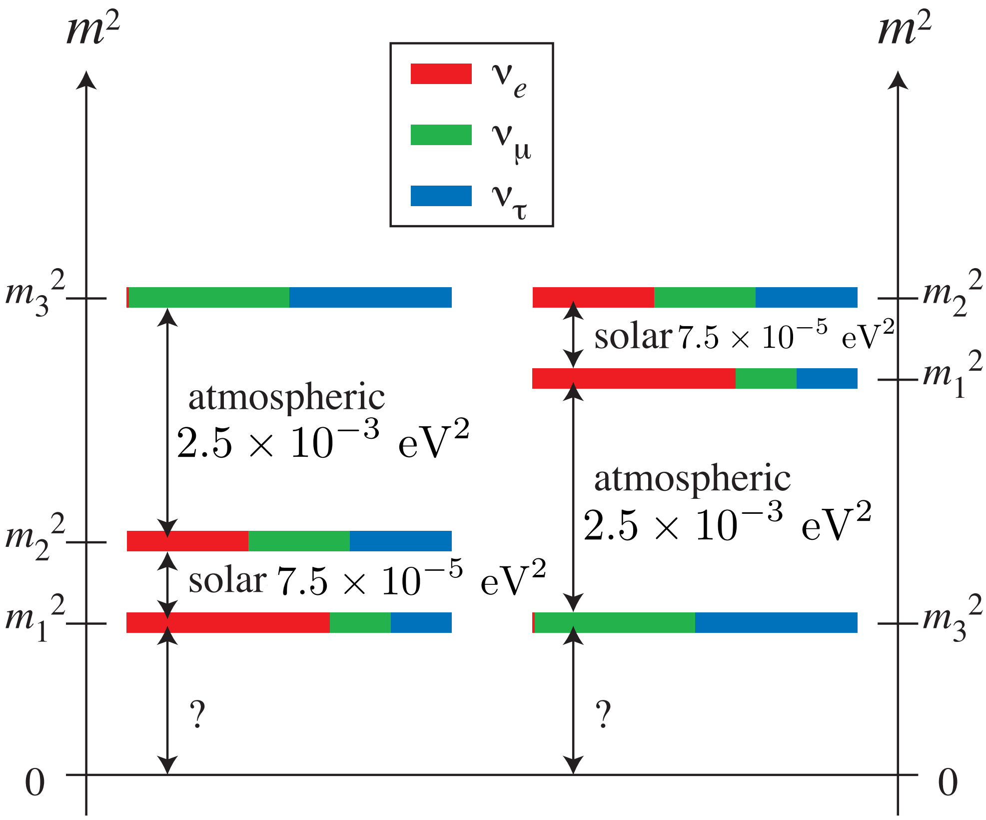

Figure 2.1.: The two possible neutrino mass orderings arising from the unknown sign of Δm^2_{31}: normal ordering (NO) on the left and inverted ordering (IO) on the right. Neutrino oscillation experiments can only determine $\Delta m^2_{ij} = m^2_i - m^2_j$, not the absolute mass scale. Also shown is the flavour content (colour bars) of the three mass eigenstates. [43]

distance L.

Neutrino oscillation is different in matter than in vacuum. The neutrinos are coherently scattered off the shell electrons, similar to the propagation of light through matter. As will be shown in Section 2.4, the interactions of ν_e and $\overline{\nu}_\mathrm{e}$ differ from the other flavours, they are possible through an additional channel. Thus, the interaction probability of electron neutrinos is higher. From Figure 2.1 it can be seen that ν_e are primarily present in ν_1 and ν_2. Therefore, the propagation of these two is altered while ν_3 is almost unaffected. Named after its discoverers, the Mikheyev-Smirnov-Wolfenstein (MSW) effect [45, 46] can be exploited to determine the mass ordering with a properly tuned $\frac{L}{E}$.

2.3. DUNE

The Deep Underground Neutrino Experiment (DUNE) [25–28] is a long-baseline neutrino oscillation experiment measuring $P\left(\nu_\mu \to \nu_\mathrm{e}\right)$ and $P\left(\overline{\nu}_\mu \to \overline{\nu}_\mathrm{e}\right)$ planned to start data taking after 2025. It consists of a neutrino beamline at FNAL in Illinois, USA and LArTPC Far Detectors (FDs) at a baseline of 1300 km in the Sanford Underground Research Facility (SURF) in South Dakota, USA. An artistic view of DUNE is shown in Figure 2.2.

The beamline at FNAL produces pions by shooting a pulsed proton beam onto a graphite target. A variable proton energy of 60 GeV to 120 GeV allows for the production of different neutrino fluxes. One pulse is called a spill and has a duration of 10 µs at a period of 0.7 s to 1.2 s, depending on the proton energy. During phase one of the experiment, each spill will contain 7.5×10^{13} protons, resulting in an beam power of 1.03 MW to 1.20 MW. In the later phase two the number of protons per spill will be doubled, doubling the power as well as the average number of events per spill in the detectors. A summary of the various proton beam configurations is given in Table 2.2. In accordance with [26] most calculations in this work assume the 2 MW 80 GeV beam,

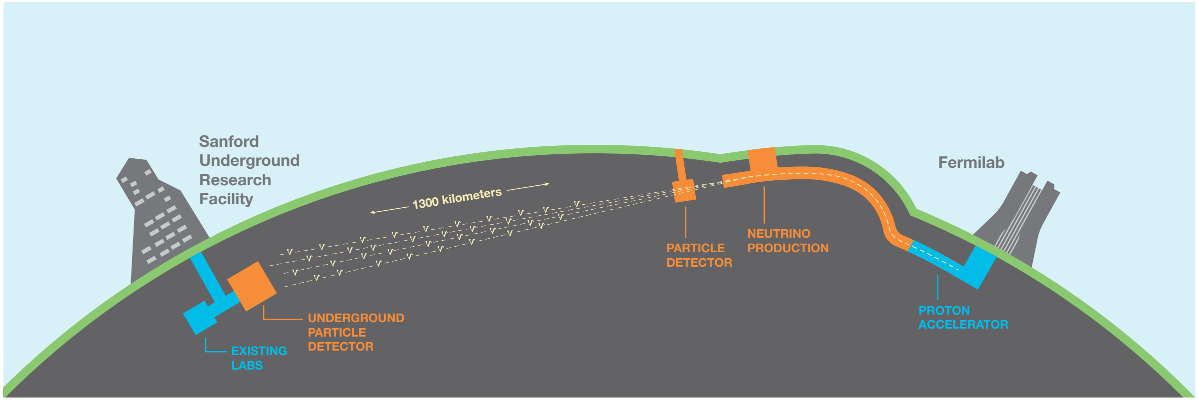

Figure 2.2.: DUNE, a next-generation long-baseline neutrino oscillation experiment consisting of a neutrino beamline and ND complex at FNAL, and LArTPC FDs at SURF. [25]

i.e. 0.2 events per tonne of argon and beam spill. The produced pions pass through several EM focusing horns to enter a decay pipe where they decay to μ^+ (μ^-) and ν_μ ($\overline{\nu}_\mu$) according to Equation (2.2). By altering the polarity of the current in the focusing horns either π^+ or π^- can be selected primarily, enhancing the ν_μ or $\overline{\nu}_\mu$ content of the beam, respectively. Alongside the pions a small amount of kaons is produced as well. These in turn can decay to ν_e and $\overline{\nu}_\mathrm{e}$ with a branching ratio of $\approx 5\,\%$ [20], producing a significant ν_e ($\overline{\nu}_\mathrm{e}$) beam contamination. The neutrino beam flux is depicted in Figure 2.7. Delivered neutrino flux integrated over time is usually given in Protons On Target (POT) because the effective neutrino flux depends on several factors and can only be precisely assessed by Near Detector (ND) measurements. More information on the beamline can be found in [26].

The baseline and energy spectrum of DUNE are optimised to measure δ_CP and determine the mass ordering. Figure 2.3 shows the (anti)neutrino oscillation probability as a function of neutrino energy at the DUNE baseline for normal and inverted mass ordering. In very simple terms, δ_CP can be derived from the difference in oscillation probability between neutrino and antineutrino mode. The MSW effect enhances either neutrino or antineutrino oscillation depending on the mass ordering, allowing for a determination of

Table 2.2.: Summary of the DUNE proton beam parameters for various configurations. Initially, the beamline will operate with the phase one parameters. Later, it will be upgraded to support the phase two parameters. The spill duration is 10 µs for all configurations. The last column gives the expected total number of neutrino interactions per tonne of argon and beam spill in the ND. It is calculated by multiplying the expected neutrino flux with the cross-section on argon from the GENIE[a] neutrino event generator. Note that these values are slightly different from the ones in Table 2.2 because the latter are outdated. In accordance with [26] most calculations in this work assume the 2 MW 80 GeV beam, i.e. 0.2 events per tonne of argon and beam spill. Taken from [27, 47].

Phase	E_p [GeV]	POT per spill	Spill period [s]	Power [MW]	ND rate [evt/$\mathrm{t_{Ar}}$]
I	60	7.5×10^{13}	0.7	1.03	0.078
II	60	1.5×10^{14}	0.7	2.06	0.16
I	80	7.5×10^{13}	0.9	1.07	0.11
II	80	1.5×10^{14}	0.9	2.14	0.21
I	120	7.5×10^{13}	1.2	1.20	0.17
II	120	1.5×10^{14}	1.2	2.40	0.33

[a] `https://genie.hepforge.org`

the latter. For more thorough sensitivity treatments, see [43, 48, 49].

Figure 2.4 shows the sensitivities of DUNE to determination of the mass ordering and discovery of CP violation. An exposure of 1320 ktMW years is required to reach a 3σ sensitivity for a 75 % coverage of the δ_CP parameter space. Assuming the reference design of a 40 kt FD complex and a 1 MW beam results in a data-taking time of 33 years. Therefore, a beam > 1 MW is required to reach the sensitivity goal earlier.

Another important feature of Figure 2.4 are the indicated signal normalisation uncertainties. The aforementioned exposure assumes an uncertainty of $5\,\% \oplus 2\,\%$. In particular the second number has a significant influence on sensitivity. A detailed explanation of this is out of the scope of this work and can be found in [26]. Precise constraints of neutrino flux rate and shape by means of a ND (in addition to hadron measurements with replica targets) are needed to reach the quoted uncertainties. The ND complex is placed at a distance of 574 m downstream of the proton beam target.

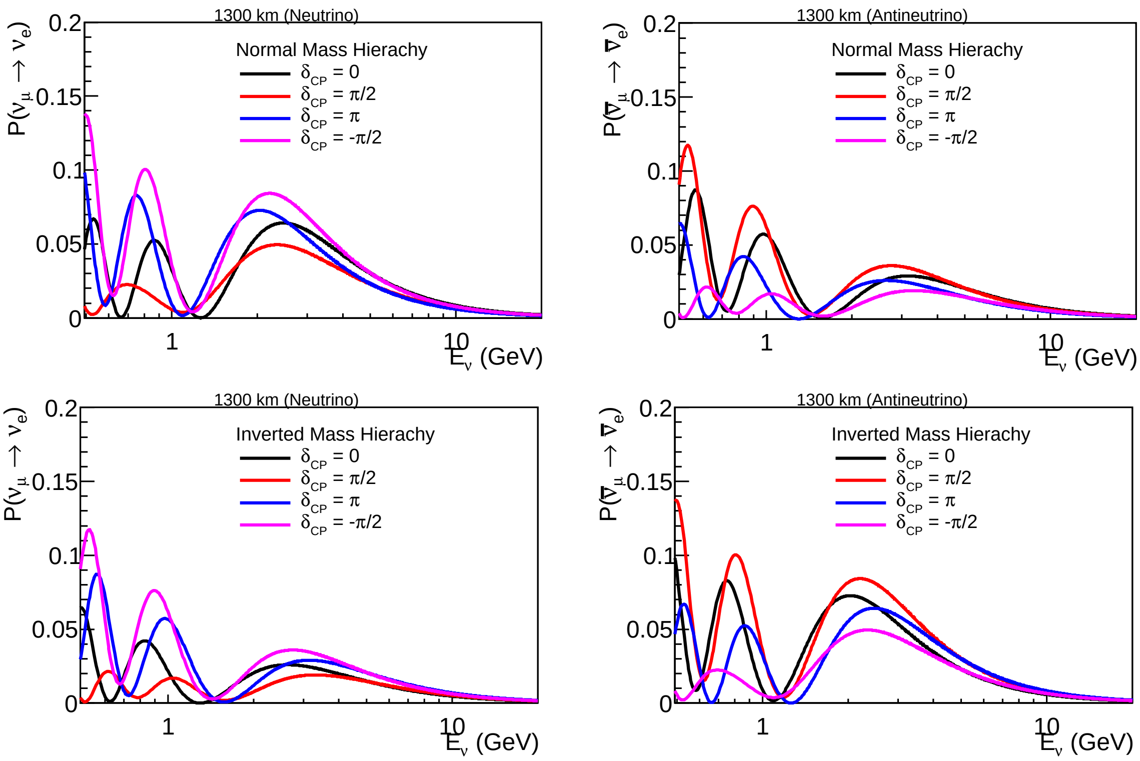

Figure 2.3.: Muon to electron neutrino (left) and antineutrino (right) oscillation probability for normal (top) and inverted (bottom) mass ordering (hierarchy in the figure). The oscillation probabilities are calculated from equation (2.20). δ_{CP} can be obtained from the difference between neutrino and antineutrino mode. The MSW effect enhances the probability in either neutrino or antineutrino mode depending on the mass ordering, allowing for a determination or the latter. [49]

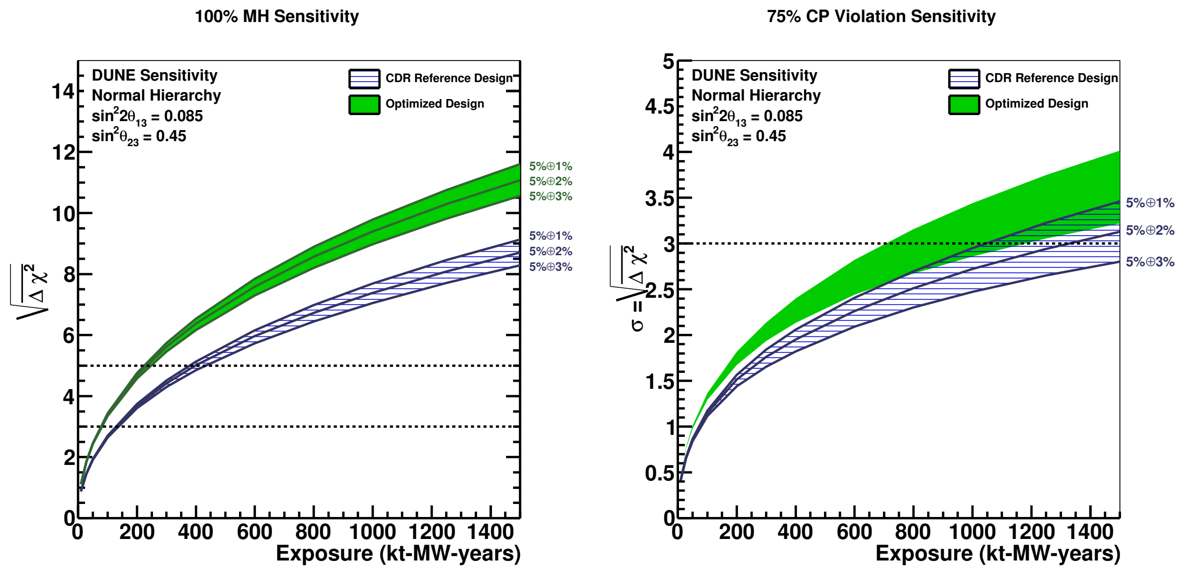

Figure 2.4.: Expected sensitivity of DUNE to determination of the neutrino mass ordering (hierarchy, left) and discovery of CP violation, i.e. $\delta_{\mathrm{CP}} \neq 0$ or π, (right) as a function of exposure in ktMW years, assuming equal running in neutrino and antineutrino mode, for a range of values for the ν_e and $\overline{\nu}_e$ signal normalisation uncertainties from $5\,\% \oplus 3\,\%$ to $5\,\% \oplus 1\,\%$. The sensitivities quoted are the minimum sensitivity for $100\,\%$ of δ_{CP} values in the case of mass ordering and $75\,\%$ of δ_{CP} values in the case of CP violation. The two bands on each plot represent a range of potential beam designs described in [26]: the blue hashed band is for the reference design and the solid green band is for the optimised design. For CP violation sensitivities true mass ordering is assumed to be normal but unknown. Taken from [26].

It is important to have a ND component employing the same target material and detector technology as the FD, i.e. a LArTPC, to eliminate the introduction of further extrapolation uncertainties.

LArTPCs are slow detectors, as will be explained in Chapter 3. This is problematic in the high-multiplicity ND environment of DUNE. Event rates of 0.2 events per tonne of argon lead to significant pile-up (see Table 2.2). It is for this reason that [26] does not mention a ND LAr component.

2.4. Neutrino Interaction with Matter

Neutrinos cannot be directly detected, they need to pass on some of their energy and momentum to secondary particles that can be detected, i.e. they need to interact with a detection medium. This section will give a brief overview of the different types of these interactions. In general, neutrino interactions are divided into Charged Current (CC) and Neutral Current (NC) mediated by charged ($\mathrm{W}^{\pm}$) or neutral (Z^0) gauge bosons, respectively. In a CC interaction the neutrino is transformed into its corresponding charged lepton while it survives an NC interaction. Furthermore, they can be subdivided according to the type of interaction into Quasi-Elastic (QE), Resonant (RES), Deep Inelastic Scattering (DIS), and Coherent (COH).

QE is characterised by the reactions

$$\nu_\ell \mathrm{n} \rightarrow \ell^- \mathrm{p} \quad \text{and} \quad \bar{\nu}_\ell \mathrm{p} \rightarrow \ell^+ \mathrm{n}, \tag{2.22}$$

and the kinematics are similar to those of an elastic collision, hence QE. Apparent from the equation above, this can only happen as a CC interaction.

The NC equivalent is an actual elastic interaction of a neutrino with a target nucleon

Table 2.3.: Estimated number of interactions per tonne of argon in the DUNE ND for approximately one month (1×10^{20} POT) exposure to an (anti)neutrino beam produced from a primary proton beam of 120 GeV and 1.2 MW. Note that these rates are slightly different from the ones in Table 2.2. The reason for this is that the values below are outdated. However, their order of magnitude is correct and no such detailed breakdown is available for the more recent values. Therefore, they are presented as a rough estimate for the expected rates for the different interaction channels. Taken from [26].

Production mode	Reaction	ν_μ beam	$\overline{\nu}_\mu$ beam
CC QE	$\nu_\mu \mathrm{n} \to \mu^- \mathrm{p}$	30 000	13 000
NC elastic	$\nu_\mu N \to \nu_\mu N$	11 000	6700
CC RES	$\nu_\mu \mathrm{p} \to \mu^- \mathrm{p} \pi^+$	21 000	0
CC RES	$\nu_\mu \mathrm{n} \to \mu^- \mathrm{n} \pi^+ \, (\mathrm{p}\pi^0)$	23 000	0
CC RES	$\overline{\nu}_\mu \mathrm{p} \to \mu^+ \mathrm{p} \pi^- \, (\mathrm{n}\pi^0)$	0	8300
CC RES	$\overline{\nu}_\mu \mathrm{n} \to \mu^+ \mathrm{n} \pi^-$	0	12 000
NC RES	$\nu_\mu \mathrm{p} \to \nu_\mu \mathrm{p} \pi^0 \, (\mathrm{n}\pi^+)$	7000	0
NC RES	$\nu_\mu \mathrm{n} \to \nu_\mu \mathrm{n} \pi^+ \, (\mathrm{p}\pi^0)$	9000	0
NC RES	$\overline{\nu}_\mu \mathrm{p} \to \overline{\nu}_\mu \mathrm{p} \pi^- \, (\mathrm{n}\pi^0)$	0	3900
NC RES	$\overline{\nu}_\mu \mathrm{n} \to \overline{\nu}_\mu \mathrm{n} \pi^-$	0	4700
CC DIS	$\nu_\mu N \to \mu^- X$ or $\overline{\nu}_\mu N \to \mu^+ X$	95 000	24 000
NC DIS	$\nu_\mu N \to \nu_\mu X$ or $\overline{\nu}_\mu N \to \overline{\nu}_\mu X$	31 000	10 000
CC COH π^+	$\nu_\mu A \to \mu^- A \pi^+$	930	0
CC COH π^-	$\overline{\nu}_\mu A \to \mu^+ A \pi^-$	0	800
NC COH π^0	$\nu_\mu A \to \nu_\mu A \pi^0$ or $\overline{\nu}_\mu A \to \overline{\nu}_\mu A \pi^0$	520	450
NC elastic electron	$\nu_\mu \mathrm{e}^- \to \nu_\mu \mathrm{e}^-$ or $\overline{\nu}_\mu \mathrm{e}^- \to \overline{\nu}_\mu \mathrm{e}^-$	16	11
Inverse muon decay	$\nu_\mu \mathrm{e}^- \to \mu^- \nu_\mathrm{e}$	9.5	0
Total CC		170 000	59 000
Total CC+NC		230 000	84 000

according to

$$\nu_\ell N \to \nu_\ell N. \tag{2.23}$$

RES involves the excitation of the involved nucleon to a resonant state, e.g.

$$\nu_\mu \mathrm{p} \to \mu^- \Delta^{++} \to \mu^- \mathrm{p} \pi^+, \tag{2.24}$$

where the Δ^{++} resonance is too short-lived to be seen by the detectors. There are a lot of different RES interactions which all work in a similar manner.

In DIS the momentum transfer is high enough to destroy the nucleon. The neutrino detaches a quark which in turn starts to hadronise and form jets. The reactions are

$$\nu_\ell N \to \ell X \quad \text{or} \quad \nu_\ell N \to \nu_\ell X, \tag{2.25}$$

where N is the target nucleon and X a group of hadrons. They happen in a very similar manner to deep inelastic electron scattering off nucleons.

In a COH reaction the opposite happens. The neutrino interacts with a target nucleus A as a whole but the latter is left intact as a spectator. Instead, an additional particle is produced. An example reaction is

$$\nu_\mu A \to \nu_\mu A \pi^0, \tag{2.26}$$

where a pion is produced from a muon neutrino interacting with a target nucleus.

Inverse muon decay,

$$\nu_\mu \mathrm{e}^- \to \mu^- \nu_\mathrm{e}, \tag{2.27}$$

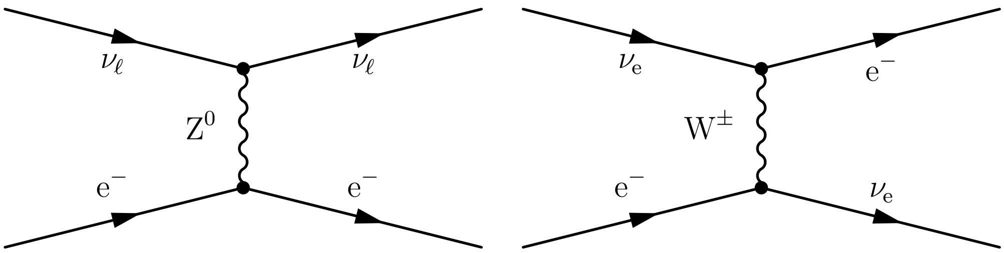

Figure 2.5.: NC (left) and CC (right) neutrino electron scattering.

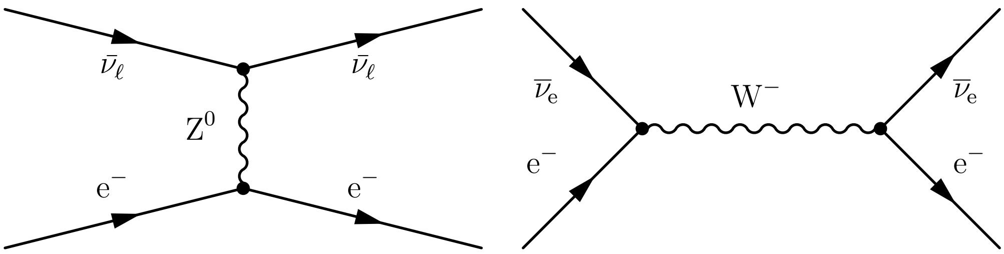

Figure 2.6.: NC (left) and CC (right) antineutrino electron scattering.

requires neutrino energies above 11 GeV [26], hence the low rate in Table 2.3.

Of particular importance is elastic scattering off shell electrons,

$$\nu_\ell e^- \rightarrow \nu_\ell e^- \quad \text{or} \quad \bar{\nu}_\ell e^- \rightarrow \bar{\nu}_\ell e^-, \tag{2.28}$$

which is possible for all (anti)neutrino flavours. For $\nu_e/\overline{\nu}_e$, the interaction is also possible in the CC channel via the exchange of a $W^\pm$ boson as depicted in Figures 2.5 and 2.6. This gives rise to a flavour-dependent term in the oscillation probability in matter, the MSW effect (see Section 2.2).

A summary of the expected rates of the different interactions in the DUNE ND is given in Table 2.3. Figure 2.7 depicts the cross-section (explained below) of neutrino interactions as a function of neutrino energy. For comparison, the flux shapes of several experiments[1] are shown (in arbitrary units). The cross-section is split into contributions from CC and NC interactions. For CC, the individual contributions from RES and

[1] The Main Injector Experiment for ν-A (MINERνA) [50] is a neutrino scattering experiment at FNAL measuring neutrino interaction cross-sections on various target materials. NuMI Off-axis ν_e Appearance (NOνA) [51] is a neutrino oscillation experiment at FNAL.

1p1h+2p2h are shown, where xpyh refers to x particles and y holes; i.e. the target nucleus is missing y nucleons after the interactions. 1p1h corresponds to a CC QE interaction whereas in 2p2h interactions a virtual meson is exchanged inside the target nucleus, also called Meson Exchange Current (MEC). Interactions involving MECs are important because they can mimic the detector response of CC QE events.

A brief explanation of the cross-section concept is given here to better understand the meaning of Figure 2.7. For a beam consisting of particles A incident on a target made of particles B the rate of the interaction $AB \to X$ is given by

$$R_X = \phi_A N_B \sigma_{ABX}, \tag{2.29}$$

where ϕ_A is the flux of beam particles, N_B is the number of target particles, and σ_{ABX} is the cross-section. Therefore, the cross-section

$$\sigma_{ABX} = \frac{R_X}{\phi_A N_B} \tag{2.30}$$

is a measure for the interaction rate R_X normalised by the number of both beam and target particles. As flux is given in units of inverse time and area, and interaction rate in units of inverse time, the cross-section needs to have the dimension of an area.

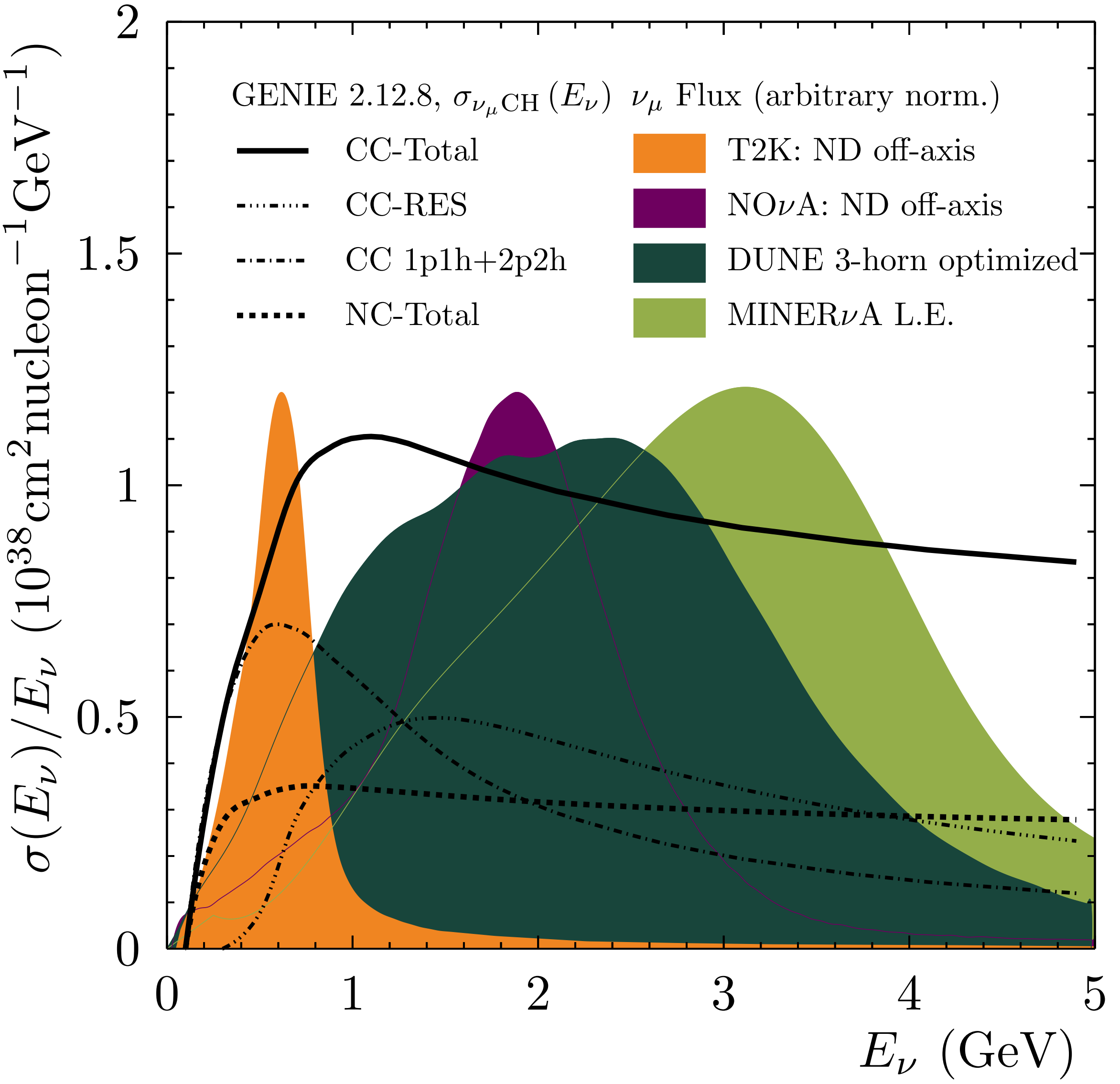

Figure 2.7.: Neutrino interaction cross-section per nucleon as a function of neutrino energy, from the GENIE[a] neutrino event generator. The cross-section is split into contributions from CC and NC interactions. For CC the individual contribution from RES interactions is shown, as well as from the sum of 1p1h and 2p2h. The latter two correspond to the QE channel and interactions involving MECs, respectively. Overlaid are the flux shapes of various beam experiments in arbitrary units. The DUNE neutrino flux is drawn for the optimised beam design with an 80 GeV proton beam. Kindly provided by L. Pickering and C. Wilkinson [52] with DUNE flux information from L. Fields [47].

[a] `https://genie.hepforge.org`

2.5. Final State Detection

Particles need to interact with a detection medium to be detected. This section describes the most important interaction of charged particles as well as neutral particles with matter. It is focused on charged interactions as these are the most important ones for LArTPCs. The energy loss per distance or stopping power $\frac{\mathrm{d}E}{\mathrm{d}x}$ is used as a measure of interaction strength.

The main interaction of charged particles with matter happens on atomic electrons. That is why for most of these interactions one needs to treat the interaction of electrons separately. For all other charged particles the stopping power is described by the *Bethe-Bloch* formula

$$-\frac{1}{\rho}\frac{\mathrm{d}E}{\mathrm{d}x} = 4\pi N_{\mathrm{A}} r_{\mathrm{e}}^2 m_{\mathrm{e}} c^2 z^2 \frac{Z}{A}\frac{1}{\beta^2}\left[\ln\left(\frac{2m_{\mathrm{e}}c^2\gamma^2\beta^2}{I}\right) - \beta^2 - \frac{\delta}{2}\right], \tag{2.31}$$

where

$\boldsymbol{\rho}$ is the density of the absorber material,

$\boldsymbol{N_{\mathrm{A}}}$ is Avogadro's number,

$\boldsymbol{r_{\mathrm{e}} = \frac{1}{4\pi\varepsilon_0}\frac{e^2}{m_{\mathrm{e}}c^2}}$ is the classical electron radius using the permittivity of free space ε_0,

$\boldsymbol{m_{\mathrm{e}}}$ is the electron mass,

$\boldsymbol{z}$ is the charge of the incident particle,

$\boldsymbol{Z}$ is the atomic number of the absorber,

$\boldsymbol{A}$ is the atomic weight of the absorber,

$\boldsymbol{\beta = \frac{v}{c}}$ with v the velocity of the incident particle,

$\boldsymbol{\gamma = \frac{E}{m_0c^2}}$ with E the energy and m_0 the rest mass of the incident particle,

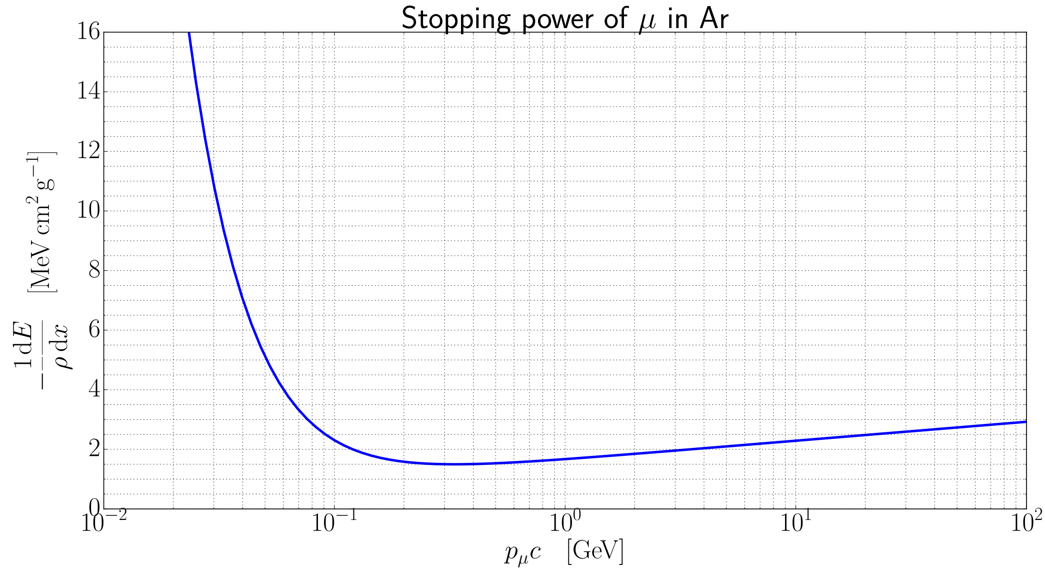

Figure 2.8.: Bethe-Bloch mass stopping power of μ in Ar.

I is the mean excitation energy of the absorber material, which can be approximated by

$$I = 16Z^{0.9}\text{eV} \quad \text{for} \quad Z > 1, \text{ and} \tag{2.32}$$

δ is a parameter describing the screening of the extended transverse electric field of relativistic incident particles by the charge density of the atomic electrons of the absorber.

Equation (2.31) describes the stopping power of particles with $m_0 \gg m_\mathrm{e}$ by ionisation and excitation of the atoms in the absorber material. As the stopping power is proportional to the electron density and thus the mass density of the absorber material, it is often divided by the latter. Therefore, Equation (2.31) more precisely gives the mass stopping power. The only remaining dependence on the absorber material is $\frac{Z}{A}$ which is ≈ 0.5 for most light materials, and the mean excitation energy which only contributes logarithmically.

Figure 2.8 shows the mass stopping power of muons in argon, neglecting the $\frac{\delta}{2}$ term for simplicity. As can be seen, there is a broad minimum, which is characteristic of the

Bethe-Bloch formula. Particles in this momentum range are called Minimum Ionising Particles (MIPs). They are important for detectors because this energy loss is a measure for the required energy resolution of a detector. As mentioned, the mass stopping power only loosely depends on the absorber material and therefore its minimum is

$$-\frac{1}{\rho}\frac{\mathrm{d}E}{\mathrm{d}x}\bigg|_{\mathrm{min}} \approx 2\,\mathrm{MeV\,cm^2\,g^{-1}} \tag{2.33}$$

for singly charged incident particles on most (light) absorbers. To the left of the minimum the stopping power rises with a strong $\frac{1}{\beta^2}$ dependence. A consequence of this is a pronounced peak in the energy loss as a function of the travelled distance of a particle near its stopping point. This *Bragg peak* is especially important for radiation therapy with heavy charged particles (e.g. protons). After the minimum the stopping power rises again with a logarithmic dependence on β and the mean excitation energy of the absorber I. The reason for this *logarithmic rise* is the extension of the transverse electric field of the incident particle in the relativistic regime. Due to increasing shielding of the transverse electric field by the shell electrons of the absorber materials, taken into account by the $\frac{\delta}{2}$ term, the rise is only asymptotic. For electrons and positrons Equation (2.31) does not hold because their mass is equal to the mass of the atomic electrons of the absorber. The stopping power changes further for electrons because the incident particle cannot be distinguished from its collision partner. On the other hand, a positron will be annihilated by an electron upon stopping, which needs to be taken into account as well. The equivalent of Equation (2.31) for $\mathrm{e}^{\pm}$ can be found in [2].

At high velocities further effects come into play. *Bremsstrahlung* describes the radiation energy loss of a fast charged particle in the Coulomb field of the absorber nuclei. It can be described by

$$-\frac{1}{\rho}\frac{\mathrm{d}E}{\mathrm{d}x} = \frac{E}{X_0}, \tag{2.34}$$

where

$$X_0 = \frac{A}{4\alpha N_A Z(Z+1)\left(\frac{1}{4\pi\varepsilon_0}\frac{e^2}{mc^2}\right)^2 \ln\left(183Z^{-\frac{1}{3}}\right)} \tag{2.35}$$

1 is the *radiation length* of the absorber material using

2 $\boldsymbol{\alpha \approx \frac{1}{137}}$, the fine-structure constant, and

3 $\boldsymbol{m}$, the mass of the incident particle.

Again, the energy loss is proportional to the density of the absorber and for convenience divided by the latter. Bremsstrahlung is emitted in interactions of the incident particle with the absorber nuclei ($\propto Z^2$) as well as with the atomic electrons of the absorber ($\propto Z$). By neglecting the latter one obtains the important relation

$$X_0^{-1} \propto Z^2 \tag{2.36}$$

as opposed to the $\propto Z$ dependence of the Bethe-Bloch formula. Equation (2.34) also holds for electrons as long as $E \gg \frac{m_{\mathrm{e}}c^2}{\alpha Z^{\frac{1}{3}}}$. Looking at the dependence on the mass of the incident particle, one finds

$$X_0 \propto m^2 \tag{2.37}$$

using Equation (2.35). Therefore, the radiation length of an absorber material is usually given for electrons, and the relation

$$X_0 = X_0^{\mathrm{e}}\frac{m^2}{m_{\mathrm{e}}^2} \tag{2.38}$$

can be used to get the radiation length for any charged particle of mass m. Radiation losses play a significant role only at energies much higher than the energy of MIPs. Using

Equations (2.31) and (2.34), one can define a *critical energy* E_c by

$$\left.\frac{\mathrm{d}E}{\mathrm{d}x}_{\mathrm{ion}}\right|_{E_\mathrm{c}} = \left.\frac{\mathrm{d}E}{\mathrm{d}x}_{\mathrm{brems}}\right|_{E_\mathrm{c}} \tag{2.39}$$

at which radiation losses take over from ionisation losses. Similar to the radiation length the critical energy is proportional to m^2. Thus, it is most important for electrons while for other particles it becomes significant only at very high energies. If we take an iron absorber for instance, we get $E_c^\mathrm{e} = 20.7\,\mathrm{MeV}$ and $E_c^\mu = 890\,\mathrm{GeV}$.

At high energies there are additional types of radiation loss taking place, for example direct electron-pair production and photonuclear interactions. They are not described here, but their $\propto E$ relation similar to bremsstrahlung losses is pointed out. A description of those effects can be found in [2].

In addition to the processes described above charged particles traversing matter also undergo scattering in the Coulomb field of the nuclei of the traversed medium. Accordingly, this process is called *Multiple Coulomb Scattering (MCS)*. The Root Mean Square (RMS) of the *scattering-angle distribution*

$$\Theta_{\mathrm{RMS}} = \frac{13.6\,\mathrm{MeV}}{\beta c p} z \sqrt{\frac{2x}{X_0}} \left[1 + 0.038 \ln\left(\frac{x}{X_0}\right)\right] \tag{2.40}$$

is defined by the momentum p, velocity βc and charge z of the scattered particle, and the thickness of the scattering medium $\frac{x}{X_0}$ in radiation lengths. The distinct momentum dependence of this *Highland formula* can be used to reconstruct the momentum of the incident particle, provided the angular resolution of the detector is fine enough.

While charge produced in interactions (i.e. ionisation) can be detected directly, light (i.e. excitation photons and photon radiation) first needs to be converted to charge to be detected. The three most important interactions converting photons to charge are the *photoelectric effect*, *Compton Scattering*, and *pair production*. All of them have in common that they attenuate photon beams exponentially according to

$$I = I_0 e^{-\mu x}, \tag{2.41}$$

where I_0 and I denote the intensity before and after passing the absorber, respectively. The thickness of the absorber is given by x and

$$\mu = \frac{N_A}{A} \sum_i \sigma_i \tag{2.42}$$

is the *mass attenuation coefficient*, defined by the sum of the cross-sections σ_i of the different interaction processes.

At low energies (ionisation energy $\leq E_\gamma \leq 100\,\mathrm{keV}$) photons primarily undergo conversion to charge by the photoelectric effect. The photon is absorbed by an atom of the absorber, which in turn is ionised and ejects one of its shell electrons. The cross-section is given by

$$\sigma_{\mathrm{photo}} = \left(\frac{32}{\epsilon^7}\right)^{\frac{1}{2}} \alpha^4 Z^5 \sigma^{\mathrm{e}}_{\mathrm{Th}}, \tag{2.43}$$

where

$\boldsymbol{\epsilon = \frac{E_\gamma}{m_{\mathrm{e}} c^2}}$ is the reduced photon energy, and

$\boldsymbol{\sigma^{\mathrm{e}}_{\mathrm{Th}} = \frac{8}{3}\pi r_{\mathrm{e}}^2} = 6.65 \times 10^{-25}\,\mathrm{cm}^2$ is the *Thomson cross-section* for elastic scattering of photons on electrons.

For energies $\approx 1\,\mathrm{MeV}$, Compton scattering dominates the interaction of photons with matter. Thereby, the photon is not absorbed by the atom but simply scatters off one of its shell electrons with the cross-section

$$\sigma_{\mathrm{c}} = 2\pi r_{\mathrm{e}}^2 Z \left\{ \left[\frac{1+\epsilon}{\epsilon^2}\right] \left[\frac{2(1+\epsilon)}{1+2\epsilon} - \frac{1}{\epsilon}\ln(1+2\epsilon)\right] \right. \tag{2.44}$$

$$\left. + \frac{1}{2\epsilon}\ln(1+2\epsilon) - \frac{1+3\epsilon}{(1+2\epsilon)^2} \right\}, \tag{2.45}$$

obtained from the *Klein-Nishina* formula. As only part of the photon's energy is absorbed while the rest is scattered, it makes sense to divide this cross-section into a scattering cross-section

$$\sigma_{\mathrm{cs}} = \frac{E'_\gamma}{E_\gamma} \tag{2.46}$$

and an absorption cross-section

$$\sigma_{\mathrm{ca}} = \sigma_{\mathrm{c}} - \sigma_{\mathrm{cs}}, \tag{2.47}$$

where E_γ and E'_γ is the energy of the photon before and after scattering, respectively.

At $E_\gamma \geq 2m_{\mathrm{e}}c^2$, photons are capable of producing pairs of e^+ and e^-. Due to momentum conservation this process can only happen in the Coulomb field of a so-called spectator particle. The spectator is usually a nucleus of the absorber material because pair-production in the field of an electron is strongly suppressed. Therefore, the cross-section of pair-production depends on the shielding of the Coulomb field by the shell electrons and thus on the proximity to the nucleus. Eventually, this results in an energy dependence. The cross-section is given by

$$\sigma_{\mathrm{pair}} = 4\alpha r_{\mathrm{e}}^2 Z^2 \left(\frac{7}{9}\ln 2\epsilon - \frac{109}{54}\right) \tag{2.48}$$

for $1 \ll \epsilon < \frac{1}{\alpha Z^{\frac{1}{3}}}$, and

$$\sigma_{\text{pair}} = 4\alpha r_{\text{e}}^2 Z^2 \left[\frac{7}{9} \ln\left(\frac{183}{Z^{\frac{1}{3}}}\right) - \frac{1}{54}\right] \tag{2.49}$$

for $\epsilon \gg \frac{1}{\alpha Z^{\frac{1}{3}}}$.

As mentioned above, for Compton scattering two different cross-sections are defined: σ_{cs} for the scattered energy and σ_{ca} for the absorbed energy. Consequentially, there are also different definitions of the coefficient μ in Equation (2.42). Replacing the total Compton cross-section σ_{c} by σ_{ca} from Equation (2.47), one gets the *mass absorption coefficient* μ_{a}, only taking into account photon absorption processes. While μ is more precisely called the *total mass attenuation coefficient*.

An interesting effect takes place for $\text{e}^{\pm}$ traversing material at energies higher than the critical energy E_{c} defined by Equation (2.39). In this regime, the energy loss is dominated by bremsstrahlung for $\text{e}^{\pm}$ and by pair production for photons. This leads to an *EM cascade* or *shower* where $\text{e}^{\pm}$ and γ produce each other alternately in a self-sustaining process. The mean free path of a photon before pair production

$$\lambda_{\text{prod}} = \frac{9}{7} X_0 \tag{2.50}$$

is very close to the mean free path of an $\text{e}^{\pm}$ before bremsstrahlung, the radiation length X_0. Therefore, the number of particles participating in the shower doubles roughly every radiation length resulting in an exponential growth. This allows EM showers to be approximated by the following rather simple model. When the average energy per particle drops below the critical energy, ionisation losses begin to dominate over radiative losses for $\text{e}^{\pm}$, and Compton scattering and photoelectric effect over pair production for photons. At this point the shower reaches its maximum and

$$t_{\mathrm{max}}^{\mathrm{EM}} = \frac{\ln\left(\frac{E}{E_{\mathrm{c}}}\right)}{\ln(2)} \tag{2.51}$$

is its longitudinal extent in radiation lengths. The *Molière radius*

$$R_{\mathrm{M}}^{\mathrm{EM}} = \frac{21\,\mathrm{MeV}}{E_{\mathrm{c}}} X_0 \tag{2.52}$$

is the transversal extent of the shower. Both $t_{\mathrm{max}}^{\mathrm{EM}}$ and $R_{\mathrm{M}}^{\mathrm{EM}}$ are important benchmarks for the dimensioning of EM calorimeters. Naturally, a photon in the energy range where pair production dominates will produce a shower as well. On the other hand, $\mu^{\pm}$ can also start EM cascades if their energy is high enough to produce bremsstrahlung.

Similarly, hadrons interacting with matter via the strong force can produce cascades as well. As opposed to the EM showers governed only by $\mathrm{e}^{\pm}$ and γ, the hadronic process is much more complex because many different secondary particle can be involved. Hadrons start to shower because they mainly interact inelastically with matter, producing secondary strongly interacting particles. That is why the hadronic cross-section

$$\sigma_{\mathrm{total}} = \sigma_{\mathrm{elastic}} + \sigma_{\mathrm{inel}} \tag{2.53}$$

is usually split. From σ_{inel} one can derive the *interaction length*

$$\lambda_{\mathrm{int}} = \frac{A}{N_{\mathrm{A}} \rho \sigma_{\mathrm{inel}}} \tag{2.54}$$

which describes the absorption of hadrons in matter according to

$$N = N_0 e^{-\frac{x}{\lambda_{\mathrm{int}}}} \tag{2.55}$$

with the initial number of hadrons N_0 and number of hadrons N after a distance x of absorber material. For absorbers with $Z \geq 6$ the interaction length is much larger than the radiation length X_0 meaning that hadronic calorimeters usually need to be much larger than their EM counterparts. Experimental data shows that hadronic showers from a few GeV to a few 100 GeV can be approximated by similar parameters as EM showers. The shower maximum is reached at

$$t_{\mathrm{max}}^{\mathrm{had}} = 0.2 \ln\left(\frac{E}{\mathrm{GeV}}\right) + 0.7 \tag{2.56}$$

interaction lengths. From this the longitudinal extent containing 95 % is given by

$$L_{0.95}^{\mathrm{had}} = t_{\mathrm{max}}^{\mathrm{had}} + 2.5\left(\frac{E}{\mathrm{GeV}}\right)^{0.13}, \tag{2.57}$$

in interaction lengths again. Transversally, 95 % of the shower are contained within a cylinder of radius

$$R_{0.95}^{\mathrm{had}} \leq \lambda_{\mathrm{int}}, \tag{2.58}$$

1 which is independent of energy and smaller for high-Z materials [53].

3. The Liquid Argon Time Projection Chamber

The Time Projection Chamber (TPC) is a derivative of Charpak's Multi-Wire Proportional Chamber (MWPC) [54], developed by Nygren in the late 1970s [55]. Crossing charged particles ionise the detection medium, which was gaseous in the original design. An electric field is applied to prevent the recombination of the ions and electrons. In this field the electrons drift towards a 2D readout plane (an MWPC in the original design). The charge readout is triggered by a scintillation light readout, also providing accurate timing of an event. This allows to measure the time for the ionisation electrons to reach the readout plane. As the drift speed of charged particles in the detection medium is constant and provided it is known, the coordinate in drift direction can be calculated from the drift time.

While gaseous TPCs already provide very accurate tracking, they have the disadvantage that the target mass and thus the cross-section of the detection medium is quite low, resulting in a low interaction rate. In 1977 Rubbia proposed the usage of Liquid Argon (LAr) as a detection medium to solve this problem [56]. This requires a cryogenic detector while gaseous detectors can be operated at room temperature. The type of LArTPC investigated in this work is fully emerged in LAr and is called single-phase. A slightly altered scheme uses avalanche charge amplification to improve the Signal-To-Noise Ratio (SNR). As of today, avalanche amplification is only possible with the charge readout

Table 3.1.: Properties of LAr, taken from [4] where not specified otherwise.

Property	Symbol	Value	Unit
Molar mass	μ	3.9948×10^{1}	$\mathrm{g\,mol^{-1}}$
Boiling point at $1.013\,25 \times 10^{5}\,\mathrm{Pa}$	T_S	8.726×10^{1}	K
Density at T_S	ρ_S	1.399×10^{3}	$\mathrm{kg\,m^{-3}}$
Dielectric constant [57]	ε_r	1.504	
Required energy per electron-ion pair	W_i	2.36×10^{1}	eV
Required energy per photon	W_sc	1.95×10^{1}	eV
Fano factor	F	1.07×10^{-1}	
EM radiation length	X_0	1.4×10^{-1}	m
Hadronic interaction length	λ_int	8.37×10^{-1}	m
Peak scintillation wavelength	λ_scint	1.28×10^{-7}	m
Scintillation attenuation length	λ_att	6.6×10^{-1}	m
Concentration in air by volume		9.34×10^{-1}	%

situated in a gas phase above the LAr. The details of such a dual-phase design are out of the scope of this work, they have been described by Aprile et al. [4] for instance.

3.1. Liquid Argon as a Detection Medium

For an efficient particle detection by a TPC several properties of the sensitive medium are of interest, such as ionisation and light yield, electron-ion pair recombination, dielectric strength, length scales of EM and hadronic interactions, density, transparency to its own scintillation light, and the boiling point. LAr is quite unique as it has all the necessary properties while at the same time it is comparably cheap because it is readily available in the Earth's atmosphere. A summary of its properties can be found in Table 3.1. Xenon, for instance, slightly surpasses argon in many aspects but is prohibitively expensive to build large detectors. A boiling point of $\approx 87\,\mathrm{K}$ raises the need for strong thermal insulation and a potent cooling system for LAr, though the requirements are far less stringent then for liquid helium. This section outlines the most important LAr properties.

Two processes are crucial to the registration of ionisation tracks of charged particles in a TPC: charge production and transport. The charge production needs to be high enough to be detectable by the available electronics. This is given by the energy required to produce an electron-ion pair W_i. The W_i value of 23.6 eV for LAr is challenging but manageable with contemporary electronics, as will be shown in Section 3.5. Naturally, this imposes a lower limit on detectable $\frac{\mathrm{d}E}{\mathrm{d}x}$.

Free electron transport is mainly influenced by three processes: *recombination*, *diffusion*, and *lifetime*. The ultimate goal is to collect as much of the produced charge as possible. Recombination is the main process opposing this. While it can be partially mitigated by increasing the electric field, it cannot be eliminated completely. Even if that was possible, it would not be beneficial because the scintillation light needed for the drift time measurement is partly produced by recombining electron-ion pairs. The relation between drift field strength and charge yield can be described by the *box model* [58]. It assumes that the ion-electron pairs are isolated and initially uniformly populate a box of a given size. Furthermore, the diffusion of electrons and ions as well as the ion drift velocity (1×10^5 times smaller than for electrons) are assumed to be negligible. For a produced charge Q_0 and a collected charge Q the collection ratio is given by

$$\frac{Q}{Q_0} = \frac{1}{\xi} \ln(1 + \xi) \tag{3.1}$$

with a parameter ξ depending on the drift field, electron mobility, initial number of electron-ion pairs, chosen size of the box and recombination coefficient. Figure 3.1 shows a measurement by LHEP of the collected charge in an 8 mm-drift LArTPC for various drift field intensities and concentrations of nitrogen mixed into the LAr.

Ionisation charge clouds will start to diffuse over time due to thermal motion. The process is characterised by the diffusion coefficient D. In the presence of a drift field longitudinal (D_L) and transversal (D_T) components need to be treated separately. The

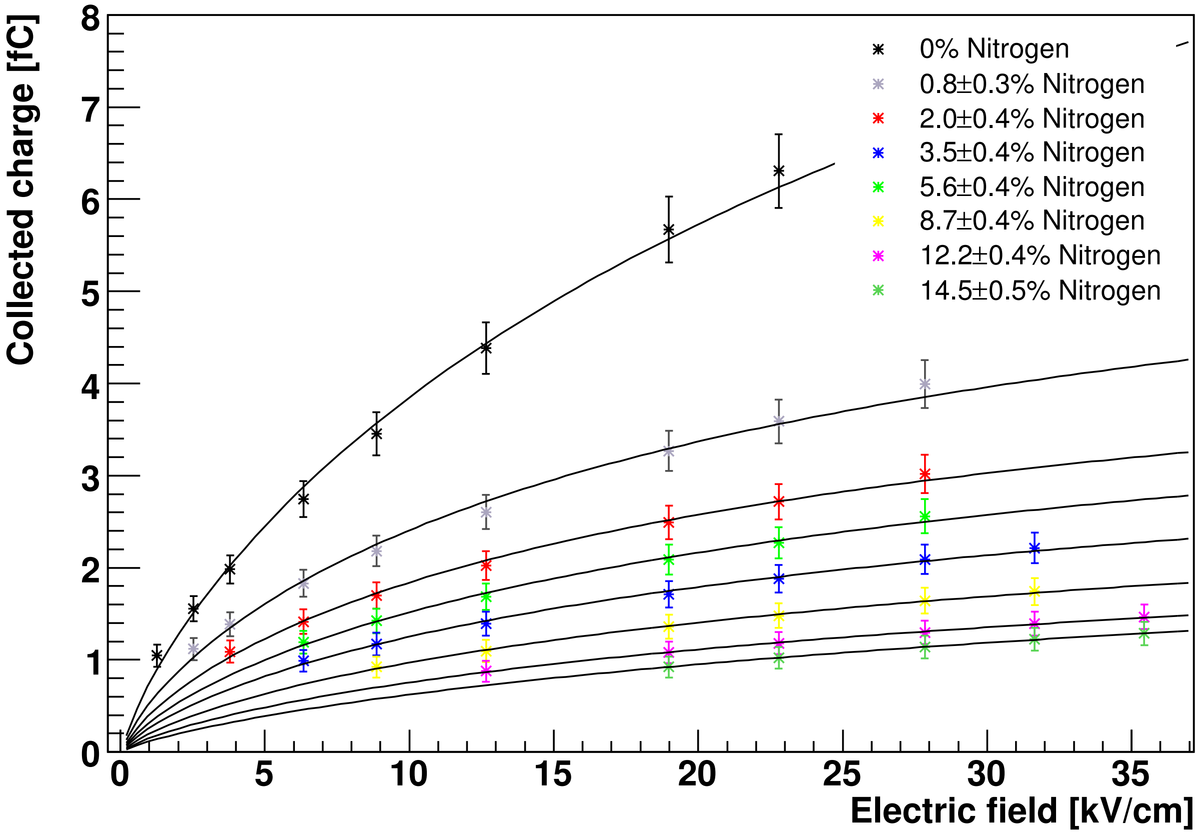

Figure 3.1.: Collected charge in an 8 mm-drift LArTPC as a function of electric field, for various concentrations of nitrogen mixed into the LAr. The lines represent box model fits. [59]

resulting smearing of the ionisation charge cloud after a drift time t is given by

$$\sigma_{\mathrm{L/T}} = \sqrt{2D_{\mathrm{L/T}}t} \tag{3.2}$$

for longitudinal and transversal diffusion, respectively. Therefore, D has the dimension of area per time. [60]

A third process affecting charge transport is electron trapping by impurities, the probability of an electron becoming attached to an atom in the medium. For the argon itself this is highly unlikely because its outer electron shell is fully populated. This is one of the reasons why (liquefied) noble gases are a prime choice for TPCs. Nevertheless, drifting electrons can be captured by impurities in the argon. Oxygen is particularly bad due to its high electronegativity. Impurities are therefore often measured in oxygen-equivalent concentration. Finite purity gives rise to a finite lifetime of free electrons in the medium.

$$N_{\mathrm{e}}(t) = N_{\mathrm{e}}(0)e^{-\frac{t}{\tau}} \tag{3.3}$$

is the charge left after a time t for an electron lifetime τ.

The velocity of the charge drifting in an electric field is related to the mobility μ by

$$\vec{\mathbf{v}} = \mu\left(\vec{\mathbf{E}}\right)\vec{\mathbf{E}}, \tag{3.4}$$

where μ in general depends on the electric field and is different for electrons and ions. This means that the higher the field is, the higher is the charge velocity and thus the lower the drift time. Drift times need to be kept low for multiple reasons. One of them are the aforementioned impurities. A low lifetime caused by a high impurity concentration can be partially compensated by a higher field. Increasing the drift time in an experiment exposed to high rates of cosmic radiation will increase pile-up, i.e. the number of events simultaneously present in the detector. Pile-up in turn complicates event reconstruction. On the other hand, the readout electronics need to be fast enough to guarantee the required spatial resolution in the drift coordinate, defining an upper limit for the drift velocity. A reasonable value from a purity point of view is a drift time of $\sim 1\,\mathrm{ms}$. For a detector size of $\sim 1\,\mathrm{m}$ the required drift speed is $\sim 1\,\mathrm{mm\,\mu s^{-1}}$, requiring a field of $\sim 1\,\mathrm{kV\,cm^{-1}}$.

A drift field of $1\,\mathrm{kV\,cm^{-1}}$ becomes challenging in detectors much larger than 1 m due to the high required cathode voltage. Soon after entering LArTPC R&D, the LHEP group realised that the reported dielectric strength of LAr is much lower [29] than measured by Swan et al. in 1960 [30, 31]. It turned out, opposing the assumption of Swan et al., that the dielectric strength is not independent of the absolute dimensions of the electrodes. This led to a very detailed study of breakdowns in LAr in the course of this thesis, which will be presented in Section 4.1.

3.2. Electric Field Generation

For charge separation and drift an electric field of $\sim 1\,\mathrm{kV\,cm^{-1}}$ is needed inside the fiducial volume of a LArTPC. An easy way to achieve this is by means of field-shaping rings fed by a resistive divider between cathode and anode. The drawback is the need for a feedthrough capable of withstanding the full cathode voltage. An alternative is to generate the HV inside the cryostat, for instance using a Greinacher voltage multiplier circuit as the one used for the ARGONTUBE experiment at LHEP [62]. A Greinacher multiplier works by pumping up a cascade of capacitors and diodes using a High Frequency (HF) source. While the voltage generation worked well, this approach proved to be impractical because the HF charging voltage interfered with the charge readout and therefore had to be turned off during data-taking. Charging a Greinacher circuit is an asymptotic process, as can be seen in Figure 3.2. It depicts voltage and resulting electric field as a

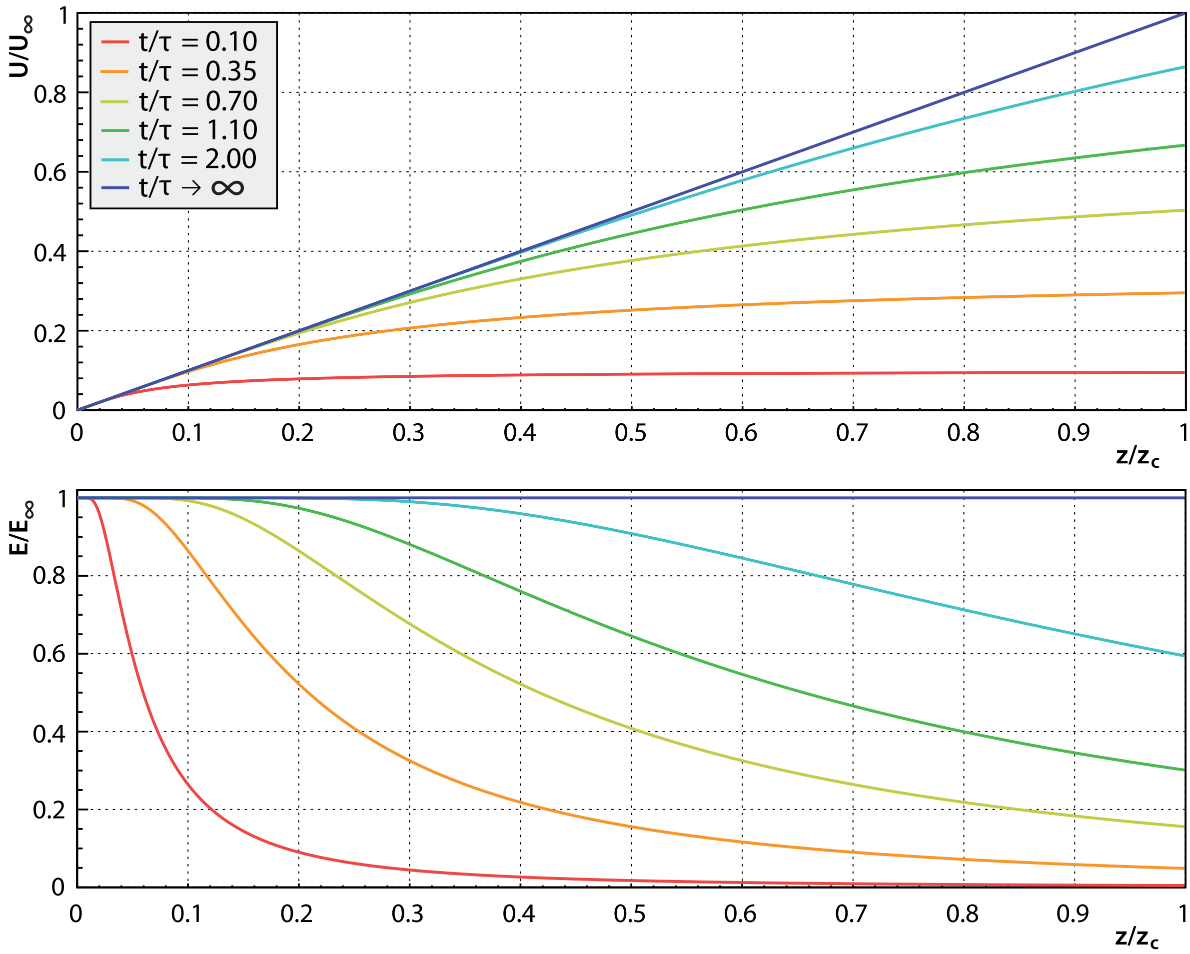

Figure 3.2.: Relative voltage (U/U_∞, top) and longitudinal electric field (E/E_∞, bottom) obtained with a Greinacher multiplier as a function of relative drift coordinate z/z_c, for different charging states t/τ. The dark blue curves correspond to a fully charged Greinacher circuit. [61]

function of drift distance for various charging states. The characteristic charging time τ of ARGONTUBE was $\sim 10\,\mathrm{min}$. Due to leakage currents and protection resistors the circuit needed frequent recharging: approximately 1 min every 15 min. This caused a lot of detector down time, making a Greinacher circuit impractical for physics experiments. More information on the ARGONTUBE Greinacher multiplier can be found in [5, 61, 63].

3.3. Charge Readout

Classically, the charge readout of a LArTPC is done using wires with a diameter of $\sim 0.1\,\mathrm{mm}$. One wire plane delivers a 2D projection of the ionisation tracks in the detection medium. This has two consequences:

1. At least two parallel wire planes are needed to be able to reconstruct the 3D event topology.

2. In theory, the more complex the event topology, the more planes are required to fully reconstruct it.

Multiple wire planes can be realised by operating only the last one (in drift direction) in charge collection mode. All the preceding wire planes are biased in such a way that they are transparent to the incoming charge but pick up an induction signal during the passage of the latter. A typical number of wire planes for currently operational detectors is three, tilted at 60° w.r.t. each other.

3.4. Light Readout

Drift time needs to be measured to calculate the distance the charge has drifted along the electric field (i.e. the space coordinate perpendicular to the readout plane). The Data

Acquisition (DAQ) can record the time of the arrival of the charge at the readout plane. What is missing is the time of charge production. It can be acquired by registering the scintillation light produced alongside the ionisation of the detection medium. Contemporary detector designs employ PMTs for this purpose. PMTs are a well-established technology with a high quantum efficiency and fast response, but they require a lot of space.

A photon impinging on a PMT is converted to an electron by a photocathode covering the sensitive surface of the PMT. These photo cathodes have a limited absorption spectrum. In particular, the scintillation light of LAr does not fall inside the spectra of most photocathodes. That is why the Vacuum UltraViolet (VUV) scintillation light needs to be converted to the visible range, where it can be efficiently detected by a PMT. TetraPhenyl Butadiene (TPB) is a widespread WaveLength Shifter (WLS) capable of achieving this. A common setup consists of coating either the PMT [64] or a surface in front of it [32] with TPB.

3.5. Charge Readout Electronics

This section gives an overview of charge readout electronics from the physics perspective. A more detailed review will be given in Section 4.7. Using W_i, the energy required to produce one electron-ion pair, from Section 3.1 and assuming a MIP in LAr (see Section 2.5) one gets

$$\frac{\mathrm{d}Q}{\mathrm{d}x} = \frac{\left.\frac{\mathrm{d}E}{\mathrm{d}x}\right|_{\mathrm{MIP}}}{W_\mathrm{i}} e = \frac{210\,\mathrm{keV\,mm^{-1}}}{23.6\,\mathrm{eV}} e \approx 8900\,e\,\mathrm{mm^{-1}} \approx 1.4\,\mathrm{fC\,mm^{-1}}$$

as a rough estimation for the charge yield. This calculation does not incorporate recombination, diffusion, and charge lifetime, meaning that in a real experiment the value will be even lower. The result is that the readout electronics need to be capable of detecting $\sim 1\,\mathrm{fC}$ charges.

That is why the charge signal needs to be amplified before digitisation. This is achieved by means of an integrating amplifier, converting the charge to a voltage. Early LArTPC designs used preamplifiers outside the cryostat at room temperature. From a noise point of view though it is beneficial to put the amplifiers inside the cryostat submerged in LAr for two reasons. First, the closer to the source the amplifier is located, the shorter the low-signal lines will be, resulting in less pick-up noise. Second, the temperature-dependent Johnson-Nyquist noise of the amplifiers will be reduced at cryogenic temperatures (see Section 4.7).

For the same reasons it makes sense to operate the entire analogue signal chain at cryogenic temperatures. This would also help to eliminate ground loops, which can pick up noise inductively or provoke self-oscillation of the analogue signal circuitry. However, it is not easy to operate electronics at cryogenic temperatures. Usually, a complete redesign of the circuit is necessary due to most components operating outside their guaranteed temperature range. For some complex active components like the amplifiers and digitisers even a redesign of the Integrated Circuit (IC) might be necessary. On the other hand, placing the digitisers too close to the readout might result in elevated noise levels due to the digital clocks coupling into the analogue signal path.

The requirements on the electronics are given by the required sensitivity of the detector. The necessary bit depth of the digitisers is given by the required dynamic range, i.e. the minimum and maximum amount of charge the readout needs to be able to register. While the spatial resolution in the two coordinates parallel to the readout plane is given by the pitch of the electrodes, the accuracy of the third coordinate is given by the timing accuracy. This in turn depends on three properties: the timing accuracy of the light readout, the sampling time of the digitisers, and the peaking time of the preamplifiers.

Peaking time is the time needed until the output of the preamplifier reaches its maximum (peak) for a delta pulse input.

3.6. Challenges of Future Detectors

To accomplish the physics goals of future neutrino detectors, outlined in Chapter 2, much higher statistics than with today's experiments are necessary. There are two obvious ways to do this: Increase beam flux and/or detector size. Scaling up a LArTPC brings several challenges, in particular for the drift HV and wire readout planes.

For a constant drift field cathode voltage scales with the size of the detector in drift direction. This in turn increases the required clearance distance between the cathode and grounded components. Where the cathode is close to the LAr vessel this inevitably leads to more dead volume that cannot be used for particle detection. The situation is worsened by the fact that an increased drift distance also results in an increased drift time for the same field. This can either be compensated by increasing the charge lifetime and thus the LAr purity accordingly, or by increasing the drift speed and thus the drift field. In summary, for a constant LAr purity the cathode voltage scales more than linearly with detector size in drift direction.

Further problems are associated with the classic wire readouts employed in LArTPCs, such as mechanical construction and event pile-up. One of the mechanical requirements on a wire readout is that it should be as planar as possible. Sagging wires caused by insufficient mechanic tension lead to distortions in spatial reconstruction. For large detectors, possessing thousands of wires on a single frame, this becomes quite challenging. Every wire that has a slight deviation in tension from its neighbours will start to sag. This is worsened by the fact that the construction needs to withstand extreme temperature gradients during detector cool-down and warm-up.

The second problem of wires, event pile-up, is a consequence of the increased flux required for future experiments. It is rooted in the way event reconstruction works for wires. As mentioned above, wire planes do not produce real 3D event topologies but rather multiple 2D projections. In order to achieve true 3D events they need to be disentangled from the 2D projections. If an event is complex enough, this cannot be done unambiguously with a limited number of 2D projections. The problem is especially serious in case of a ND. The envisioned DUNE ND, for instance, is expected to see 0.2 neutrino events per tonne of argon and beam spill (see Table 2.2).

On top of the event reconstruction problems event pile-up also poses a challenge for trigger accuracy. In a monolithic detector the scintillation light produced alongside the ionisation charge scatters across a large volume, triggering a big portion of the light readout system. Thus, matching a scintillation flash to the corresponding charge to get the correct timing of the event is a non-trivial task.

4. Experimental Studies on High Voltage, Charge and Light Readout

Chapter 3 gave an overview of the traditional LArTPC design and concluded with the challenges such a design will face in future experiments. This chapter comprises several studies of these challenges and potential solutions. First, an in-depth study of the dielectric strength of LAr and the implications on the drift High Voltage (HV) systems and LArTPC design in general are presented. Then, the theory of a pixelated charge readout and the resulting requirements for new charge readout electronics are discussed. Finally, a new light collection system based on cold SiPMs coupled with a light trap is introduced.

4.1. Study of Electric Breakdowns in Liquid Argon

During the commissioning and operation of the ARGONTUBE detector demonstrator [62] at LHEP it was found that the dielectric strength of LAr was much lower [29] than predicted by earlier studies [30, 31]. Subsequently, I conducted a detailed study of dielectric breakdowns in LAr, including high-speed footage, current-voltage characteristics, and optical spectrometry. The results are presented in this section, they have been published in a paper [6], of which I am corresponding author.

The setup used in this study is very similar to the one described in [29] and is shown

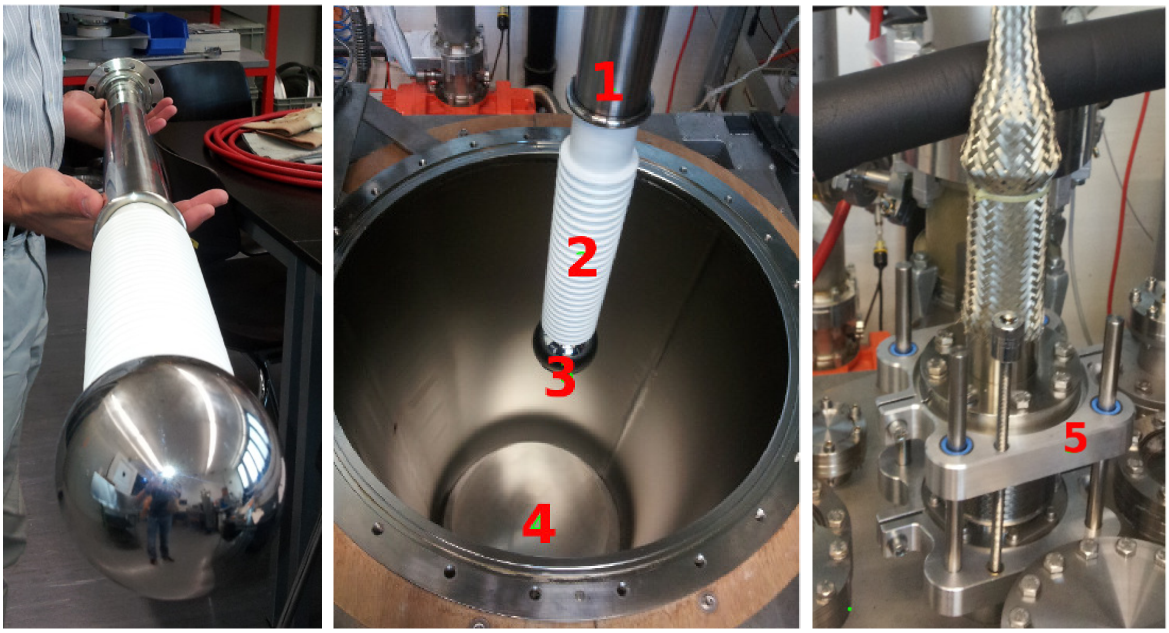

Figure 4.1.: Experimental setup used for the breakdown studies. Left: HV feedthrough with spherical cathode. Middle: feedthrough before insertion into the cryostat. 1. ground shield; 2. ribbed PET-C dielectric; 3. spherical cathode; 4. anode plate sitting on a tripod on the grounded cryostat bottom; two of the tripod legs are insulated while the third one contains a 50 Ω shunt resistor. Right: linear translation unit used to set the cathode-anode gap width (5).

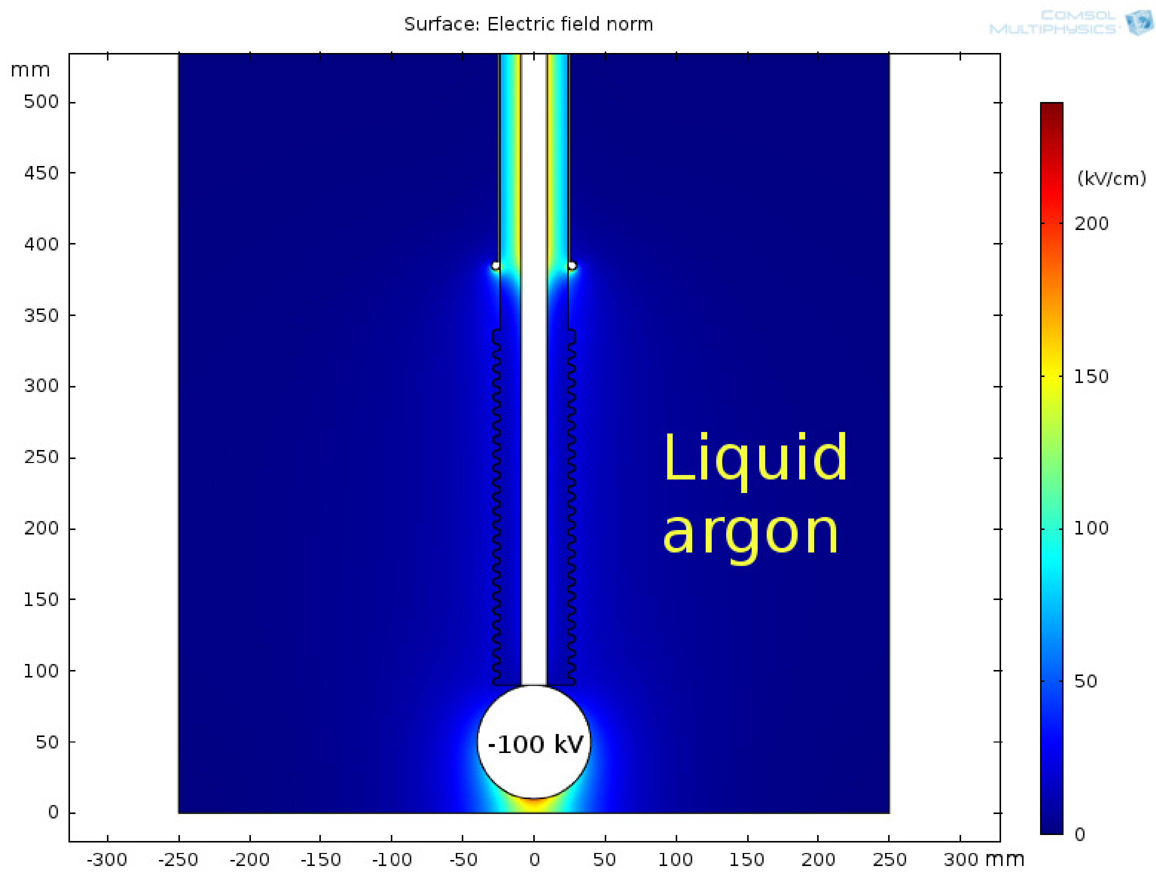

Figure 4.2.: Calculated electric field amplitude map for the test setup with −100 kV at the cathode and a cathode-anode distance of 1 cm.

in Figure 4.1. A spherical cathode and a planar anode form the discharge gap. Three different diameters of the cathode sphere were tested: 4 cm, 5 cm, and 8 cm. Two types of surface treatment were used in the cathode preparation, namely mechanical fine-polishing and electro-polishing. For the anode mechanical fine-polishing was used for all measurements. The anode-cathode gap width can be set in the range of 0 mm to 100 mm with a precision of 0.3 mm. An example of the field distribution in the setup is shown in Figure 4.2. The field map was calculated using the COMSOL Finite Element Method (FEM) package[1].

The argon purity after filling was estimated with a small TPC (according to the

[1]https://www.comsol.com

method described in [65]) to be ~ 1 ppb of oxygen-equivalent impurity concentration. More details on the setup can be found in [29].

The control circuit of the *Spellman SL130PN150* HV Power Supply Unit (PSU) [66] outputs two low voltages proportional to the voltage and the current at the output, respectively. These voltages are recorded with a *Tektronix DPO 3054* digital oscilloscope [67] controlled by a LabVIEW[2] program. The output polarity of the PSU can be switched by replacing the output HV multiplier module. To measure the discharge current a $50\,\Omega$ shunt resistor is placed between the anode plate and the vessel ground, which is connected to the ground return of the PSU. The voltage drop across the shunt resistor is transmitted to the oscilloscope via a matched coaxial line. Figure 4.3 shows the equivalent electric schematic of the setup. The voltage at V_{mon} corresponds to the PSU output HV divided by a factor K_{V}; the voltage at I_{mon} is related to the PSU output current. However, according to the manufacturer of the PSU, an accurate reconstruction of the output current for frequencies above 100 Hz is not possible because of a filtering circuit in the current control loop. Therefore, only the voltage drop across the shunt resistor is used for the measurement of the discharge current.

The oscilloscope is triggered by the channel connected to the shunt resistor. The breakdown discharge current is composed of the output current of the PSU and the discharge current of the setup capacitance C_{gap}, as $I_{\text{gap}} = I_{\text{out}} + C_{\text{gap}} \frac{\mathrm{d}V_{\text{gap}}}{\mathrm{d}t}$. To limit the PSU output current an additional resistor R_{lim} is inserted into the HV output circuit. The measured values for the circuit parameters are summarised in Table 4.1. The knowledge of these parameters allows the calculation of the voltage across the gap during breakdown.

In addition, the setup is equipped with an *AOS Technologies S-PRI* high-speed camera [68] to observe the development of the discharge. The camera is capable of recording 700×400 pixel Red Green Blue (RGB) images at 1230 fps. The camera comprises a frame ring buffer and is triggerable by an external Transistor-Transistor

[2] `https://www.ni.com/labview`

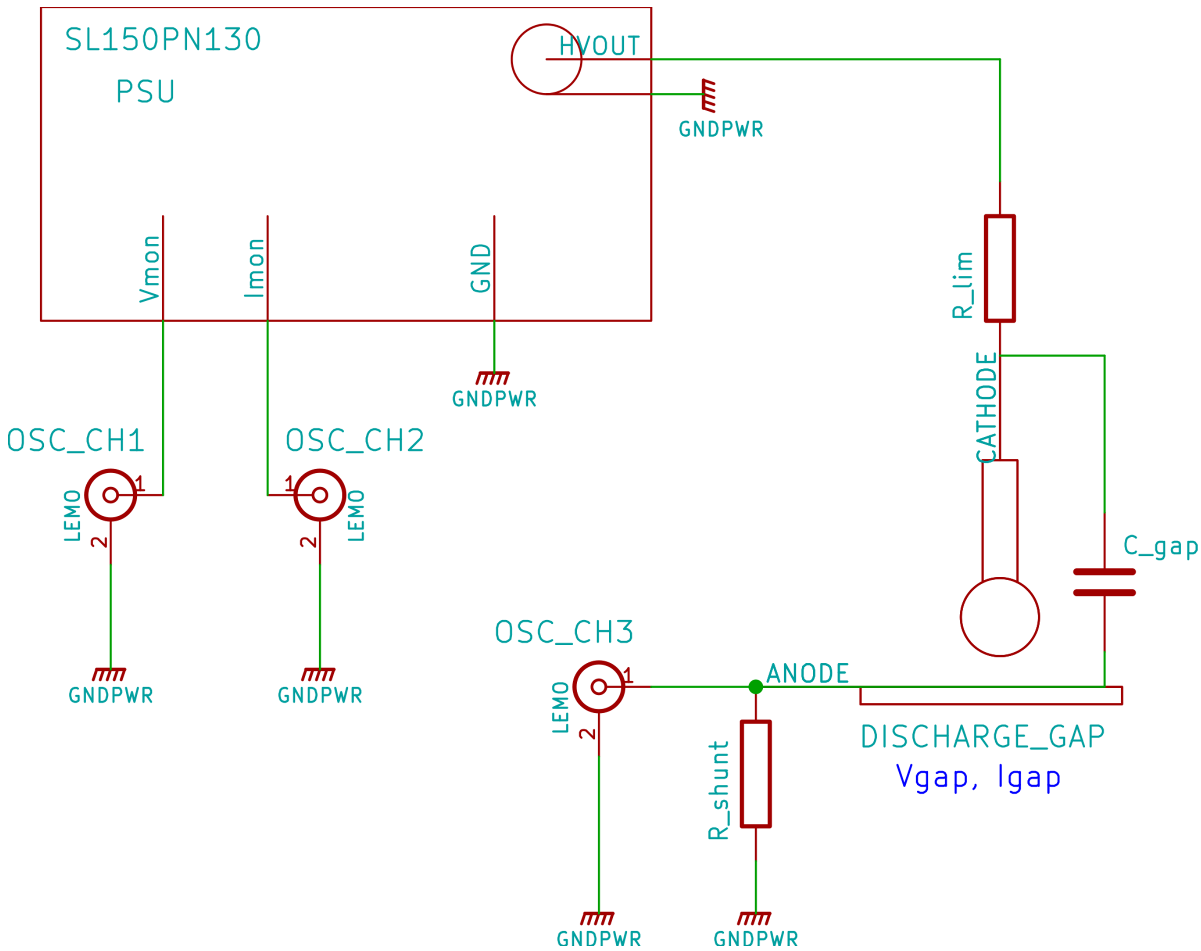

Figure 4.3.: Electric schematic of the experimental setup. The oscilloscope is connected to the control circuit of the HV power supply and to a shunt resistor on the ground return path. Discharge voltage and current can be derived from the recorded voltages.

Table 4.1.: Summary of the measured parameters of the test circuit.

Parameter	Value	Unit
K_V	42.3×10^{-6}	
R_{shunt}	50	Ω
R_{lim}	200	$M\Omega$
C_{gap}	370	pF

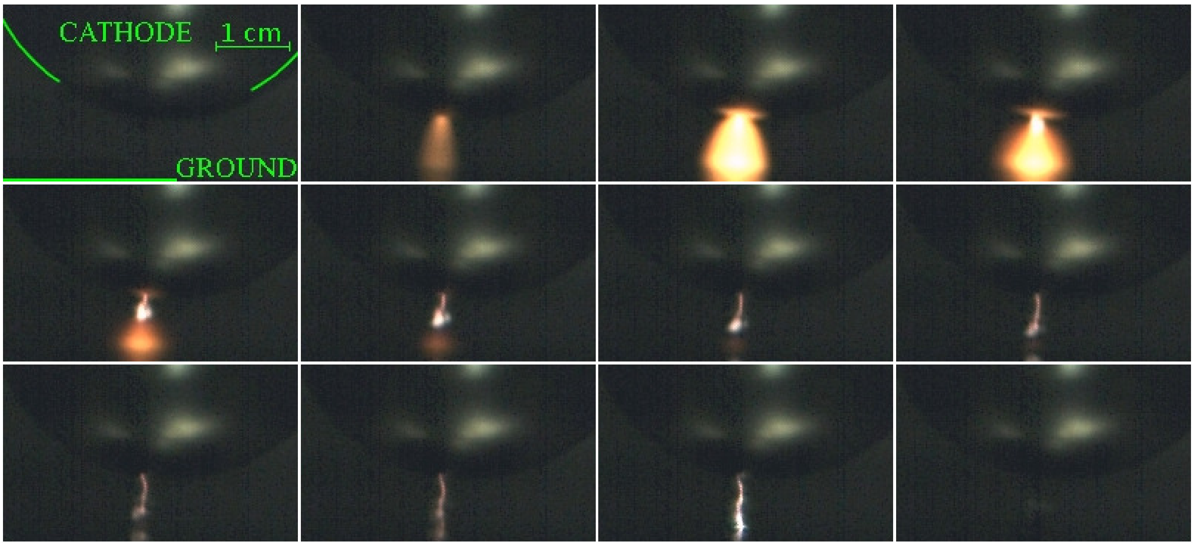

Figure 4.4.: Recorded camera image sequence for a breakdown from a 5 cm diameter cathode at −100 kV and 8.8 mm from the anode plate. The sequence is taken at 1250 fps, each frame takes 0.8 ms.

Logic (TTL) pulse. This allows a synchronous recording of the visual appearance of the discharge and its current-voltage characteristics. The camera is triggered from the trigger output of the oscilloscope. The luminous part of the discharge is analysed for each frame of the recorded sequence.

The camera is mounted above a 5 cm diameter glass view port, located at the top flange of the cryostat, and is looking downward. To observe a discharge from the side a glass mirror plate is installed at the edge of the cathode plane, located 20 cm from the cathode in such a way as to not perturb the electric field in the discharge gap.

Finally, a custom built optical spectrometer is used to analyse the light emission of the discharges. The spectrometer is connected to an optical fibre entering the cryostat with its other end attached to the anode plate. The fibre is aligned such that its end directly faces the discharge gap, resulting in a high angular acceptance. As will be shown, the discharge emission spectra provide a better understanding of the processes at different stages of the discharge. This is due to the fact that the emission spectra of excited neutral, singly-ionised, and multiply-ionised argon atoms lay in different regions of the

Table 4.2.: Summary of the breakdown measurement runs.

Run	$\varnothing_{\text{Sphere}}$[cm]	Surface finish	Sphere polarity	Events	d_{Gap}[mm]	$V_{\text{Breakdown}}$[kV]
1	4	Mech. polished	Cathode (−)	1086	0.5 to 8.0	3 to 130
2	5	Mech. polished	Cathode (−)	900	0.2 to 12.0	2 to 130
3	8	Mech. polished	Cathode (−)	2434	0.1 to 70.0	1 to 130
4	5	Mech. polished	Anode (+)	102	4.0 to 5.0	5 to 114
5	5	Electro-polished	Cathode (−)	1141	0.1 to 10.0	1 to 130

visible spectrum.

The possibility of creating gas bubbles near the discharge gap is inhibited by keeping the pressure in the inner vessel at 100 mbar above atmospheric pressure, plus an additional 100 mbar due to the hydrostatic pressure. The outer bath is opened to the atmosphere, thus keeping the inner vessel temperature constant and well below the boiling point. No boiling was detected anywhere near the discharge gap region during the measurements.

In earlier measurements [29] sporadic discharges were experienced across the ribs of the dielectric of the HV feedthrough. It was possible to suppress these discharges completely by rising the level of the LAr by about 20 cm. This improved the cooling of the feedthrough and reduced bubble production near the bottom of the feedthrough grounded shield, placed 60 cm below the liquid surface.

The measurement campaign comprised 5 runs with a total of more than 5000 measured discharges, for various sphere diameters, surface treatments, and polarities. A summary is shown in Table 4.2. A typical recorded camera image sequence for a breakdown from a 5 cm diameter cathode at −100 kV and 8.0 mm from the anode plate is shown in Figure 4.4. The movie can be found as *movie1.webm* in the ancillary files[3] of [6].

[3] `https://arxiv.org/src/1512.05968v2/anc/movie1.webm`

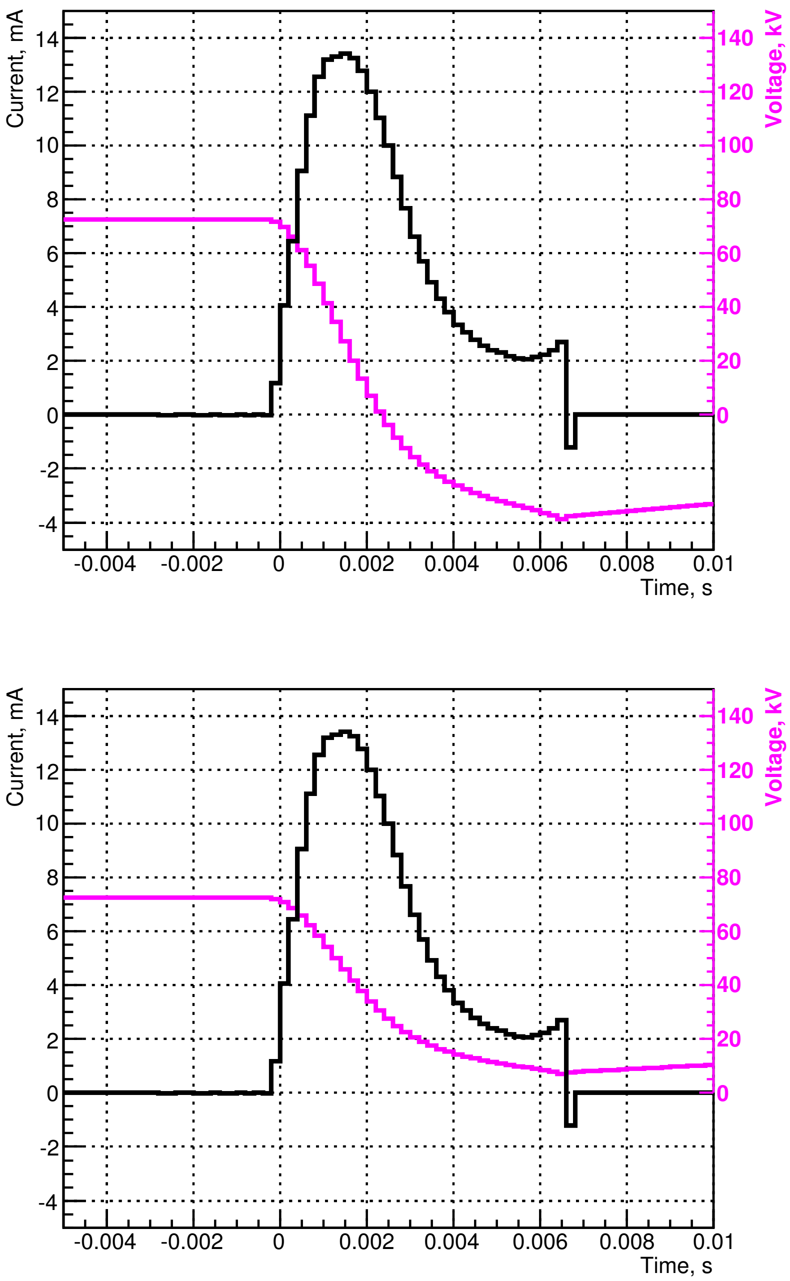

Figure 4.5.: Measured current through the gap (black) and voltage across the gap (magenta) for a typical breakdown at 6.0 mm distance between a 4 cm diameter cathode and the anode plate. The top plot shows the voltage obtained using the measured values of the protection resistor and the gap capacitance while the bottom plot uses the tuned values.

Figure 4.5 shows the current and voltage features of a similar breakdown from a 4 cm diameter cathode at 6.0 mm from the anode plate. The current was directly measured by observing the voltage drop across the shunt resistor while the voltage was obtained by integrating the current, taking into account the gap capacitance, protection resistor, and output voltage of the power supply. Using the measured values of Table 4.1 for capacitance and resistance results in a negative voltage at the end of most discharges. This is an unphysical result, as can be seen in the top plot of Figure 4.5. The behaviour may be attributed to poor knowledge of the effective values of the current-limiting resistor and the setup capacitance in the frequency domain of the discharge. In order to better approximate these parameters they are tuned in such a way that the minimum voltage approaches zero for a maximum number of discharges. The best result was achieved by lowering the resistance by a factor of 1.7 and increasing the capacitance by the same factor. Interestingly, this result leaves the RC characteristics of the system unchanged. The bottom plot of Figure 4.5 shows the result obtained by using the tuned values for capacitance and resistance.

Most of the discharges are localised in the area of high field concentration between the tip of the sphere and the anode plane. However, in rare cases the discharge is initiated far from that region, sometimes at the side surface of the sphere. An example of such a discharge is shown in Figure 4.6, and the corresponding movie can be found as *movie2.webm* in the ancillary files[4] of [6].

As shown in [69, 70], experimental data on breakdowns in liquefied noble gases suggests the following dependence for the maximum breakdown field: $E_{\max} = CA^p$, where C is a material-dependent constant, A is the stressed cathode area with an electric field intensity above 90 % of its maximum, and $p \approx -0.25$. Figure 4.7 combines data available in literature with data obtained from the measurements in this thesis and earlier measurements performed at LHEP. Each data point is the mean value of all measurements

[4] `https://arxiv.org/src/1512.05968v2/anc/movie2.webm`

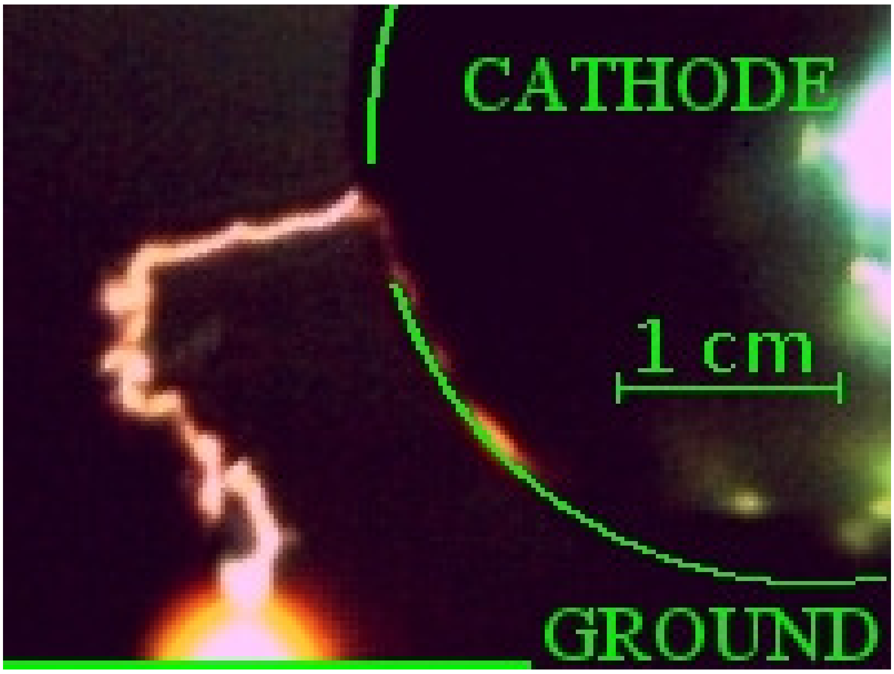

Figure 4.6.: An image of the streamer stage of the discharge, initiated at the side surface of a 5 cm cathode sphere at −121.5 kV and 8.0 mm from the anode plate. The cone of electrons emitted from the streamer tip towards the anode (lower edge of the image) produces a bright orange luminescence in LAr.

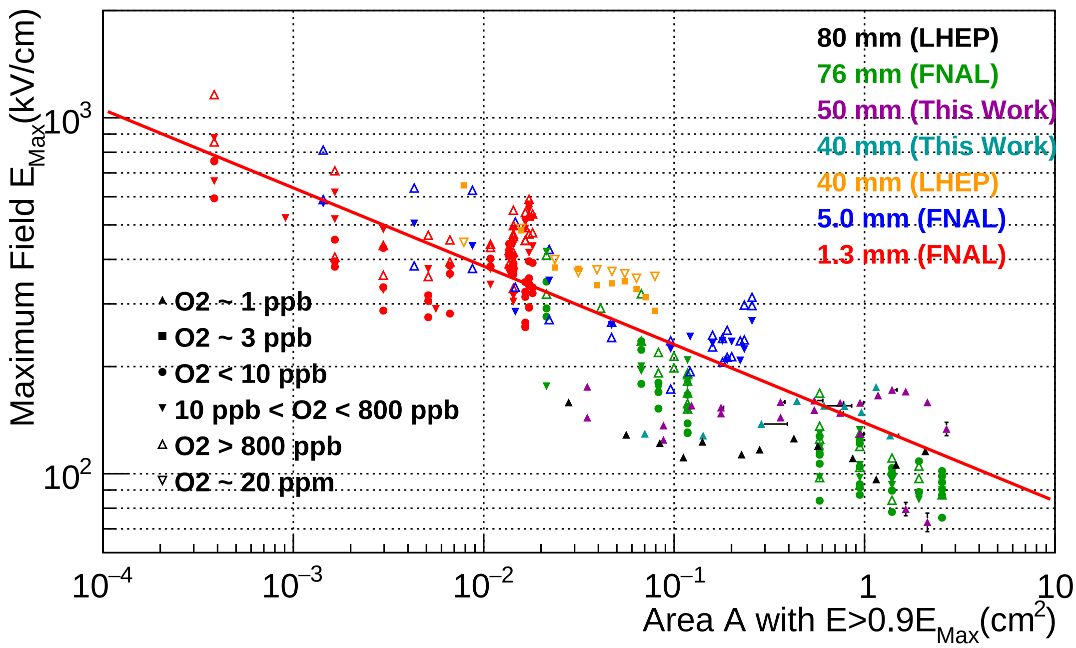

Figure 4.7.: Breakdown field versus stressed cathode area. The stressed area A is defined as the area with an electric field intensity greater than 90 % of the maximum electric field intensity in the gap. The fit line represents the dependence $E_{max} = CA^p$ with $C = 139 \pm 5$ and $p = -0.22 \pm 0.01$. The colours correspond to different cathode sphere diameters while the marker styles correspond to different oxygen-equivalent impurity concentrations. Data taken from [69] (FNAL), [29] (LHEP), and [6] (this work).

of one run taken at the same gap distance and therefore stressed area. The global best fit gives the following values for the parameters: $C = 139 \pm 5$ and $p = -0.22 \pm 0.01$. The statistical uncertainties represented by the error bars (smaller than the marker where not shown) are small compared to the unknown systematic uncertainties. Indications for this are the high spread of the points around the fit line and the high reduced chi-square of 7283.

Figure 4.8 shows the recorded spectra of a typical event. The spectra are integrated over 1 ms and approximately correspond to frames 3 (blue) and 8 (red) in Figure 4.4. Three phases of breakdown development can be distinguished from the observation of

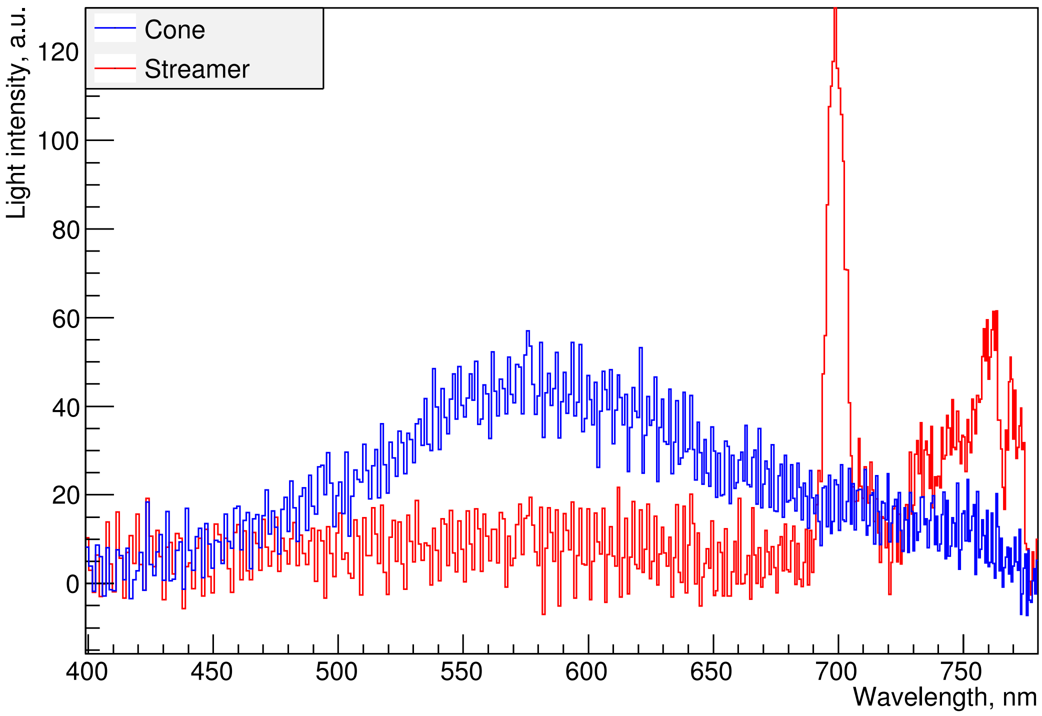

Figure 4.8.: Spectra of the field emission cone (blue) and the streamer (red) for a breakdown from a 4 cm diameter cathode at −56.2 kV and 3.0 mm from the anode plate. The spectra were integrated over a time of 1 ms with the spectrum of the streamer taken 2 ms after the spectrum of the cone. The blue curve is a broad continuum, similar to the scintillation spectrum of LAr, while the red curve features a distinct peak around 700 nm, which is attributed the the $3p^5 4p$–$3p^5 4s$ transition of neutral argon gas.

the emitted light spectra and discharge appearance: field emission, streamer, and spark. The first phase starts with the field emission of electrons from a point of the cathode metal surface. The emitted electrons drift towards the anode, ionising and exciting argon atoms. Frames 2 and 3 of Figure 4.4, the broad current peak of the current in Figure 4.5, and the blue curve in Figure 4.8 show the development of the emission. Evidence for the presence of ionisation comes from the analysis of the emission spectrum in the cone formed by drifting electrons.

The emission of light by charged particles drifting in noble liquids under the influence of an electric field (electro-luminescence) has gained great interest lately. Recent studies in this field are well covered by [71–73] and references therein. The red electro-luminescence (the peak around 700 nm of the red curve in Figure 4.8) produced by electrons drifting in argon gas is attributed to the $3p^5 4p$–$3p^5 4s$ transition of neutral argon [74]. The energy needed for the excitation of the electrons from the ground state to the $3p^5 4p$ states in argon gas is 12.9 eV to 13.5 eV. The ionisation potential of LAr is 13.84 eV [65]. For the condensed state only the scintillation spectrum under ionisation by high-energy charged particles has been described in literature so far [75]. The electro-luminescence spectrum measured (blue curve in Figure 4.8) exhibits a broad continuum, similar to the scintillation spectrum. However, the centre value at about 580 nm does not correspond to any of the electron transitions of neutral, singly-, or doubly-ionised argon atoms. The nearest candidate for such an emission is the residual oxygen with its strong 557.7 nm emission line. However, if attributable to oxygen, this line has to be observed also at the later stages of the discharge, which does not take place in the measurements.

The broad width of the spectrum could be explained by smearing the energy levels into bands due to inter-atomic interactions in liquid and by the formation of exciton clusters [76, 77]. If the energy band structure of excitons in LAr is continuous, as suggested by the scintillation spectrum, there might be a significant overlap of the band corresponding to the $3p^5 4p$ atomic levels and the conduction band above 13.84 eV. The presence of an observable emission at about 580 nm, in this case, is therefore inevitably linked to a presence of ionised states.

Another signature of avalanche ionisation in this phase of the breakdown is the increase of the cone brightness as it develops from the cathode towards the anode. Figure 4.9 shows this increase together with the fitted avalanche multiplication parameter $\alpha = (0.15 \pm 0.03)\,\mathrm{mm}^{-1}$ for the following gap conditions: voltage $V = 54.0\,\mathrm{kV}$ across a gap of 7.0 mm, cathode diameter of 4 cm, maximum field in the gap $E_{\mathrm{max}} = 96.1\,\mathrm{kV\,cm}^{-1}$,

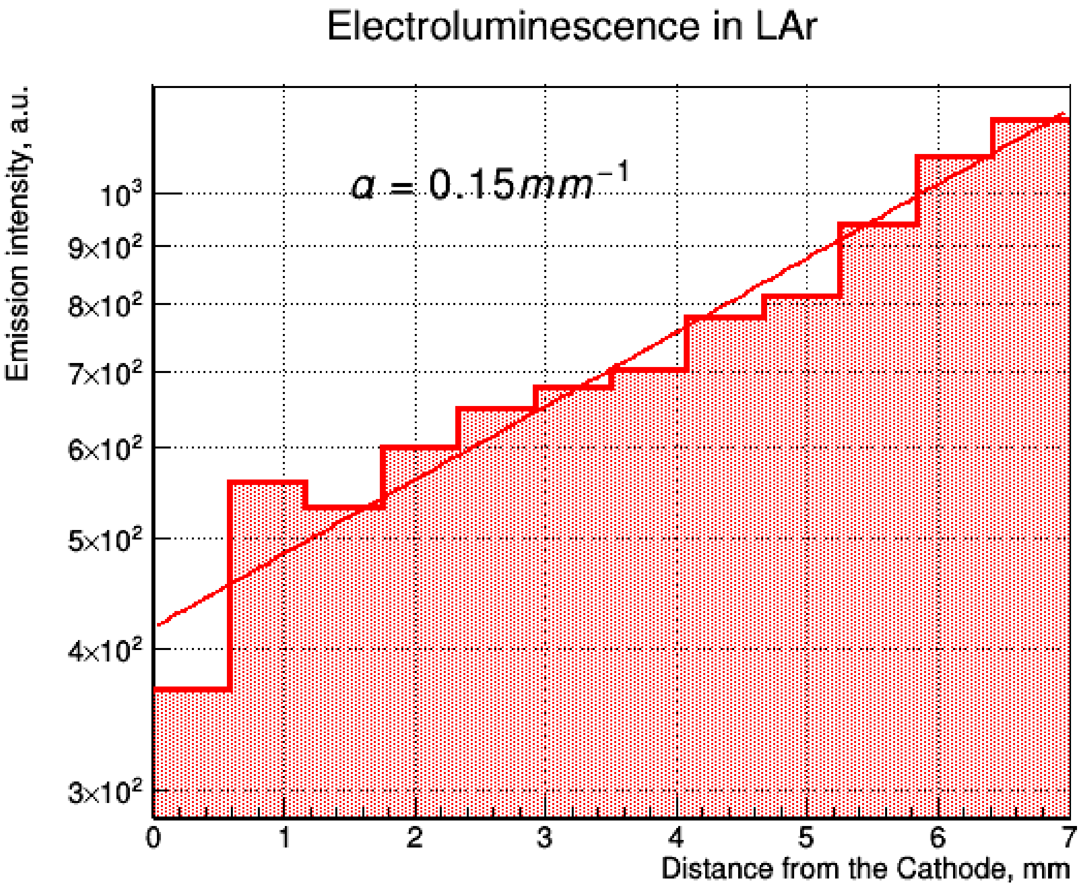

Figure 4.9.: Increasing brightness of the electro-luminescence cone as it develops towards the anode. The line represents the exponent with a fitted avalanche multiplication parameter $\alpha = (0.15 \pm 0.03)\,\mathrm{mm}^{-1}$ for gap conditions: voltage $V = 54.0\,\mathrm{kV}$ across a gap of 7.0 mm, cathode diameter of 4 cm, maximum field in the gap $E_{\mathrm{max}} = 96.1\,\mathrm{kV\,cm}^{-1}$, mean field in the gap $\langle E \rangle = 87.0\,\mathrm{kV\,cm}^{-1}$.

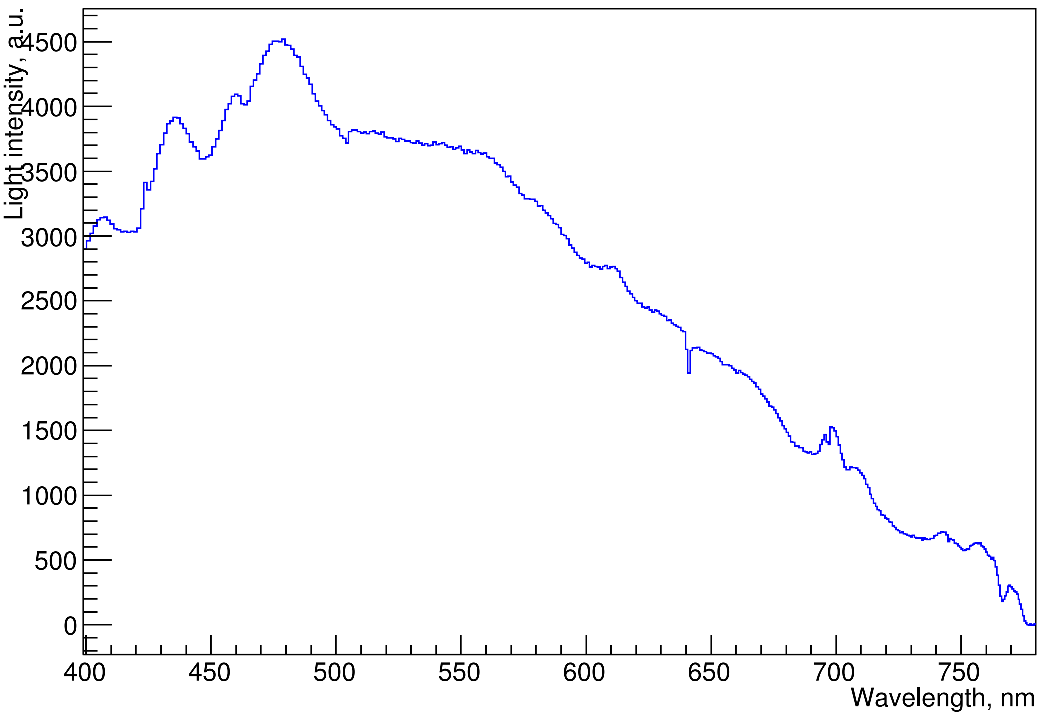

Figure 4.10.: Spectrum of the spark for a breakdown from a 4 cm diameter cathode at −39.7 kV and 4.0 mm from the anode plate. The spectrum was integrated over a time of 1 ms.

mean field in the gap $\langle E \rangle = 87.0\,\mathrm{kV\,cm^{-1}}$. To calculate the emission intensity the raw values of all pixels of the camera image in a row perpendicular to the cone direction were summed up. The distance from the cathode can be derived from the known gap distance. The given statistical uncertainty of α was obtained from the fit. As only one measurement was taken, it is not possible to state anything about unknown systematic uncertainties (for instance the calibration of the camera).

As suggested in [29], positive ions produced by the avalanche ionisation drift towards the cathode, raising the surface field and provoking a rapid increase of the field emission current to $\sim 1\,\mathrm{mA}$. Ions bombarding the cathode surface raise the local temperature and, after 1 ms to 2 ms, the liquid near the initial discharge point transitions to a gas phase, forming a bubble. Both the first and the second avalanche multiplication coefficients are a few orders of magnitude higher in gas than in liquid. Therefore, the ionisation density in the gas bubble quickly rises along with the conductivity of the formed plasma. This leads to a decrease of the electric field in the close vicinity of the field emission point, and to the suppression of a further growth of the field emission current. Accelerated electrons of the gas plasma hit the gas-liquid interface, forcing the bubble to elongate and grow into a streamer-like filament. In the region behind its head this streamer is collapsed to a diameter below 200 µm (the spatial resolution of the camera) by surface tension and electrostriction forces. This second phase of the discharge is characterised by the growth of the streamer in LAr. In Figure 4.4 (frames 4 to 10) one can see the development of such a streamer. Unlike the electrons in the first phase the streamer does not follow the electrostatic field lines but it rather meanders around their direction, being subject to thermodynamic fluctuations at the tip of the growing streamer, where the liquid-gas transition occurs. The spectrum of the light emitted by the streamer has a distinct line at about 700 nm, a characteristic feature of plasma in argon gas.

Finally, when the streamer reaches the anode, a short peak of light emission is registered (frame 11 in Figure 4.4) with the blue-green spectral component dominating (Figure 4.10). This phase is characterised by an acoustic shock and a massive production of gas bubbles in the region of the discharge. These effects are typical for an arc discharge in argon gas. The spectrum of the light emission in this phase is shown in Figure 4.10.

As demonstrated in [75], the transition from the liquid phase to the gas phase for scintillation manifests itself by the appearance of sharp spectral lines while in liquid the emission spectrum is continuous and without features. This behaviour is also suggested by the two spectra in Figure 4.8. While the spectrum is continuous during the field emission phase, there is a distinct peak at around 700 nm several ms later.

It is worth mentioning that not every streamer results in a spark phase. For those streamers started from the side of the cathode sphere the charge needed for streamer

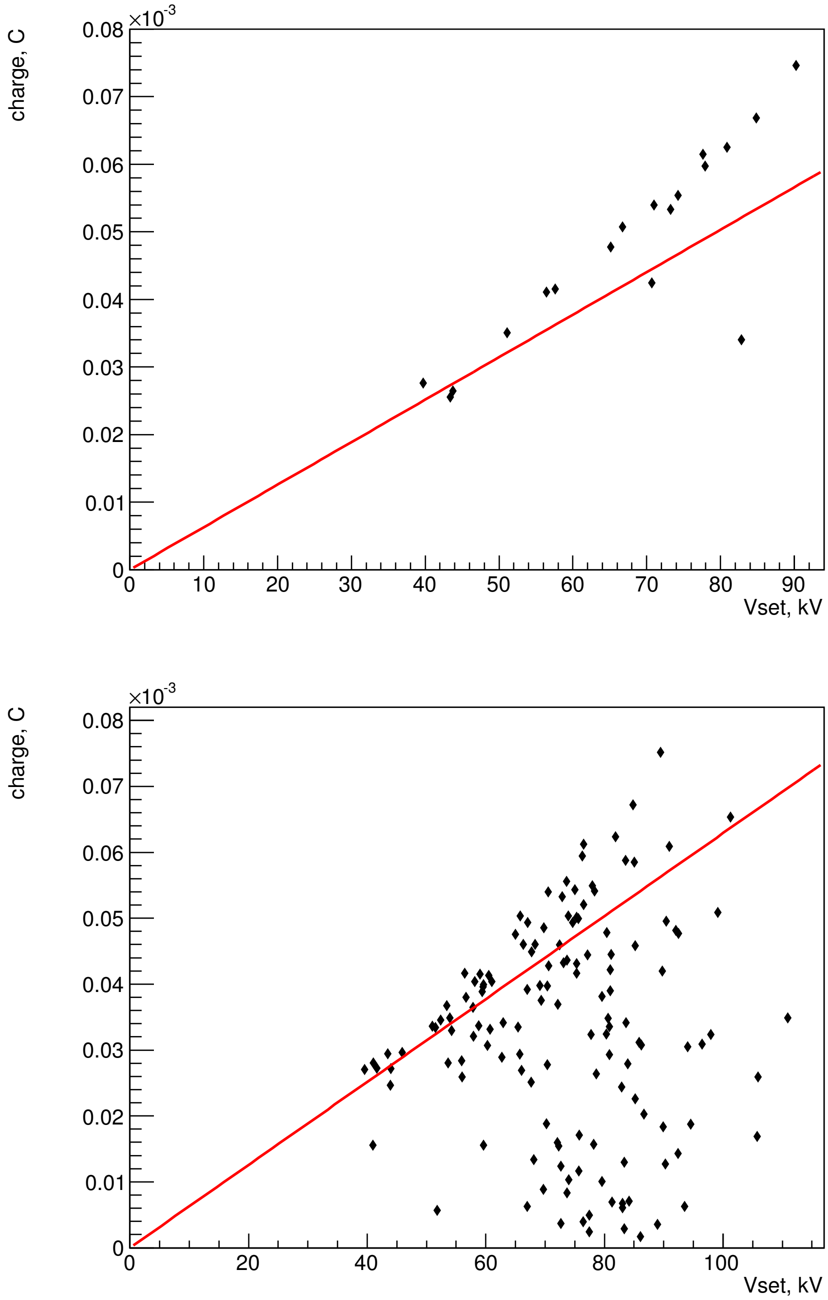

Figure 4.11.: Correlations between integrated charge and breakdown voltage *Vset* for the selected events with distinguishable slow streamer phase (top) and for all events with recorded current characteristics (bottom). The red line represents the charge stored in the gap capacitance using the tuned value of the latter.

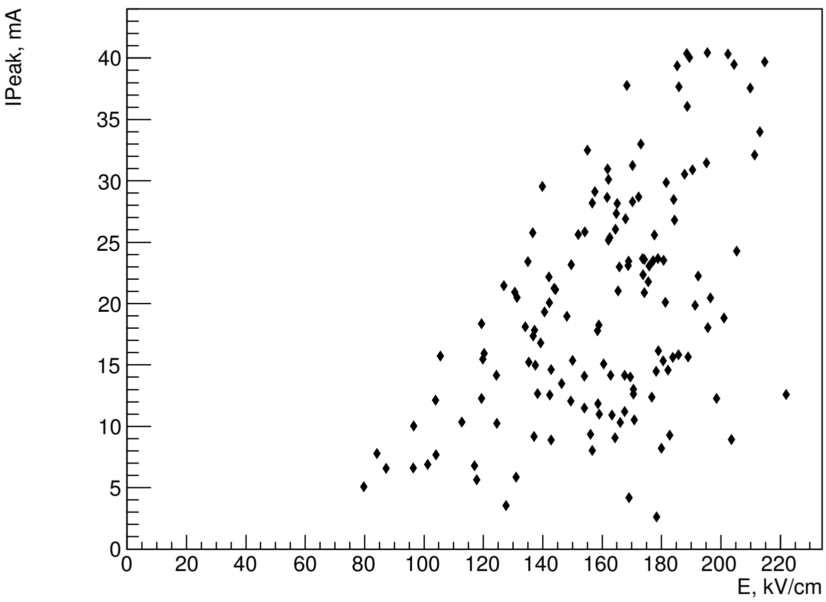

Figure 4.12.: Correlations between peak current *IPeak* and maximum breakdown field *E* for all events with recorded current characteristics.

growth might exceed the total charge available in the system. Such streamers extinguish before reaching the anode without an acoustic shock or any other additional effects. On the other hand, in some cases the filament quickly transits to a third stage before it reaches the anode. One possible explanation for this is that, if the filament current exceeds a given threshold, the filament loses its thermodynamic stability and expands into a gas bubble, in which the arc discharge quickly develops.

In Figures 4.11 to 4.15 several correlations of measured and calculated parameters of the breakdowns are shown. For some of these plots 18 events were selected with recorded current characteristics similar to Figure 4.5. As a comparison, the bottom plot of Figure 4.11 shows the data of all events with current characteristics, including events not possessing a distinct plateau as the one visible in Figure 4.5. The reduced number of events compared to Table 4.2 arises, on the one hand, because the shunt resistor was installed only in the last run and, on the other hand, since the resistor was damaged

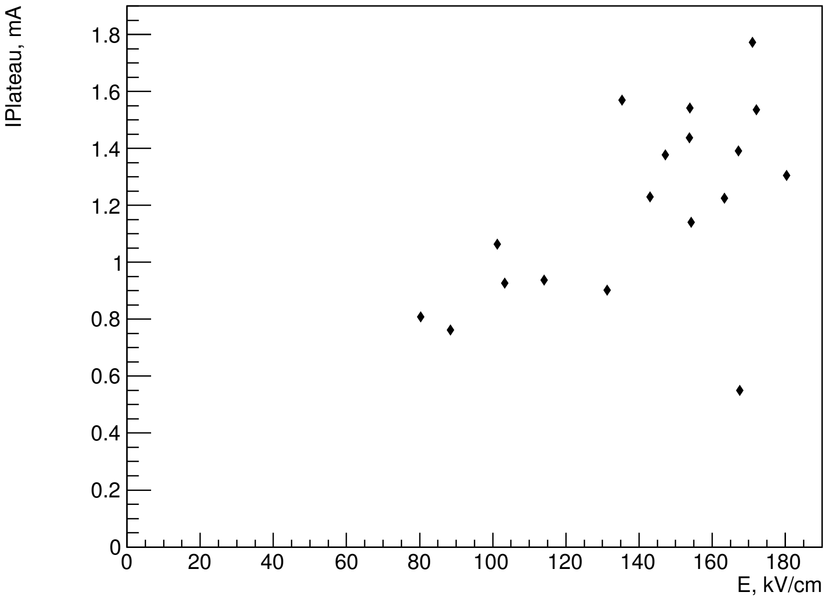

Figure 4.13.: Correlations between plateau current *IPlateau* and maximum breakdown field E for the selected events.

after the events shown in the bottom plot of Figure 4.11. The low number of events in the selection is due to the fact that an automated analysis of the current characteristics can only detect very long streamers. This also explains the behaviour of the charge in Figure 4.11: The selected streamers last for several ms, almost always consume the whole charge in the system, and then cease without transitioning to a spark. The slight excess in charge compared to the charge in the gap capacitance (red line) is likely supplied by the PSU before tripping. Contrary to this the bottom plot showing all the events contains many events that do not consume all the stored charge and result in a spark. The good match between the red curve and the data points serves as a cross-check of the tuned capacitance.

Figure 4.12 shows the behaviour of the peak current versus the breakdown field, suggesting a proportionality between the two with a coefficient of about $60\,\mu\mathrm{A\,cm\,kV^{-1}}$. The field was calculated by dividing the breakdown voltage by the gap distance. Therefore,

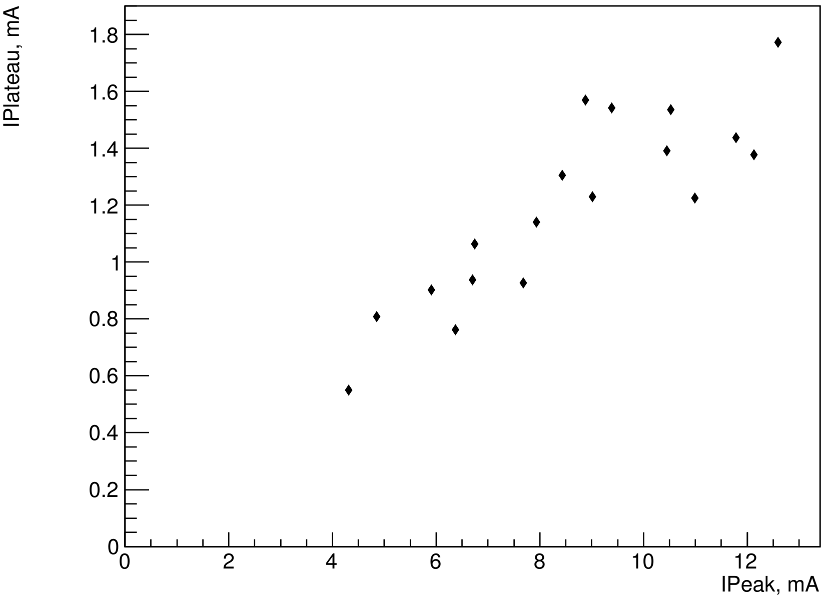

Figure 4.14.: Correlations between plateau current *IPlateau* and peak current *IPeak* for the selected events.

this is a mean value along the shortest path and only an upper limit for most of the selected events because the streamer often emerged from the side of the sphere.

Figures 4.13 and 4.14 show the correlation of the current during the streamer phase (the plateau in Figure 4.5) with the breakdown field and peak current, respectively. The plateau current clearly rises with both breakdown field and peak current. Together with Figure 4.12 this indicates that for higher fields higher currents flow during the field emission phase as well as the streamer phase. As mentioned above, the plateau current could only be reliably detected for the selected events, which is why these plots are not shown for all events.

Finally, Figure 4.15 depicts the dependence of the streamer velocity on the breakdown field. Again, the velocity is only a lower limit as it was calculated by dividing the gap distance by the duration of the streamer, which is not correct for streamers emerging from the side of the sphere. There are two distinct types of events: While the selected

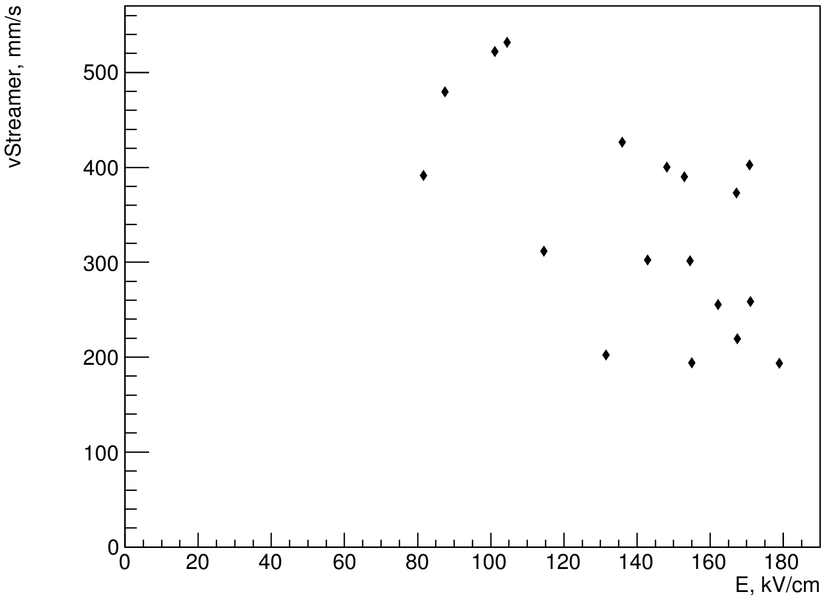

Figure 4.15.: Correlations between minimum streamer velocity *vStreamer* and maximum breakdown field E for the selected events with a distinguishable slow streamer phase.

streamers are rather slow (velocity $\approx 300\,\mathrm{mm\,s^{-1}}$, independent of the field), the whole data set contains much faster events with the total time in the ns scale (not shown). The knowledge of the streamer velocity can be applied in the design of protection circuits for future LArTPCs. If a breakdown condition is detected during the streamer phase, the HV can be killed prior to a disruptive spark phase potentially damaging sensitive detector electronics.

4.2. A Method to Suppress Electric Breakdowns in Liquid Argon

As a result of the thorough characterisation of breakdowns in LAr, a method was developed to suppress them by coating HV components with latex. It was possible to

Table 4.3.: Summary of the breakdown test measurements with 200 µm and 450 µm thick polyisoprene layers deposited on 5 cm and 4 cm diameter spherical cathodes, respectively.

d_{Gap}[mm]	$E_{\text{max}}\left[\text{kV cm}^{-1}\right]$	$\varnothing_{\text{Sphere}}$[cm]	Polyisoprene thickness [µm]	Breakdown
5.0	298	4	450	no
4.0	358	4	450	no
3.0	412	4	450	yes
3.0	296	5	200	yes

increase the voltage by a factor of 10 using this technique. This study has been published in [7].

The setup was the same as the one used to study the breakdowns, described in Section 4.1. Additionally, the cathode sphere was coated by a layer of polymer. In order to effectively suppress electric breakdowns the coating needs to have a high dielectric strength while at the same time staying elastic at cryogenic temperatures (87 K for a LAr detector). Furthermore, the excess electron mobility of the coating needs to be significantly lower than the one of LAr. If this is the case, electrons emitted by the cathode via field emission can accumulate inside the coating layer and in turn locally reduce high fields and thus quench the field emission.

Natural polyisoprene (latex rubber) is a polymer that satisfies the above requirements. Its dielectric strength is reported to be in the range of $1\,\text{MV}\,\text{cm}^{-1}$ to $2\,\text{MV}\,\text{cm}^{-1}$ [78], its dielectric constant is 2.1 which is close to the 1.6 of LAr, and its room temperature resistivity is $1 \times 10^{16}\,\Omega\,\text{cm}$. A polyisoprene layer of several 100 µm can be deposited on the sphere by dipping the latter in purified latex milk. After drying at room temperature the coating is leached in deionised water for several hours and finally vulcanised at 70 °C for one hour. Leaching is needed to remove all soluble pollutants contained in natural latex while the vulcanisation increases the tear strength of the coating. Like this the polyisoprene layer keeps its integrity and does not crack even after multiple fast cool-down and warm-up cycles to 87 K and back to room temperature, respectively.

In the first measurement a 4 cm cathode sphere coated with 450 µm of polyisoprene was used. The test was started at a cathode anode gap width of 5 mm and the voltage was ramped up from 0 kV to 130 kV at 50 V s^{-1}. After no breakdown could be observed for several hours, the gap width was decreased to 4 mm. The voltage was ramped down for the gap adjustment and ramped back up afterwards. Again, no breakdown occurred for several hours and subsequently the gap was decreased to 3 mm. During the third ramp-up there was a breakdown at 112 kV. This corresponds to a maximum electric field intensity across the gap of 412 kV cm^{-1}, which is more than one order of magnitude higher than the required value to provoke breakdowns from an uncoated cathode [6, 29]. A summary of the results is given in Table 4.3.

4.3. High Voltage Summary

A study of the visible light emission by electrical breakdowns in LAr was performed, near its boiling point with cathode-anode distances ranging from 0.1 mm to 10.0 mm with a spherical cathode and a planar anode geometry. Three distinct discharge development phases were identified by observing the discharge appearance and the time development of the visible light emission. The dependence of several breakdown parameters on the critical field was also studied. For the first time it was found that the streamer propagation velocity is about 300 mm s^{-1} and independent of the field intensity. The streamer phase is characterised by a current peak between 5 mA and 15 mA depending on the breakdown field, followed by a plateau at an approximately ten times lower current level.

The deposition of a few hundred µm thick polyisoprene (latex) layer on the surface of the cathode serves to efficiently suppress field emission of electrons from the cathode surface. As a result, significantly higher electric field intensities can be reached for cathode-ground distances of several mm. A field strength as high as 412 kV cm^{-1} was reached. This solution enables the operation of LArTPCs with a LAr volume outside the electron drift region much smaller compared to LArTPCs with non-coated HV components.

However, it was also found that the employed latex coating is very fragile. In particular, it loses its protective function after a single breakdown. This makes an application in a physics experiment impractical. Currently, a safe LArTPC operation can only be guaranteed by keeping electric fields below $40\,\mathrm{kV\,cm^{-1}}$ at all points in the detector. Therefore, either low cathode voltages or large inactive volumes around the cathode are required.

4.4. A More Robust Approach to TPC Readout Wires

As outlined in Section 3.6, classical wire readouts pose two big challenges to future LArTPCs: ambiguities and mechanical stability. A possible solution to the mechanical problems with wires is to not use actual wires but instead print thin coper tracks on a support structure. I investigated this solution and provide a proof of concept in this section.

In a classical wire readout plane the induction signal is produced by drifting the charge through one or multiple induction wire grids. With the proposed scheme of copper tracks on a support structure it is no longer possible for the charge to actually drift through the induction plane(s). Therefore, induction is only produced by the approach of the charge. One consequence of this is that induction signals are no longer bipolar. As opposed to the classic design, the collection plane is even in front of the induction plane(s). This means that the charge can only approach the induction plane(s) until it is collected by the collection plane on the top layer of the support structure. That is why it is crucial to make the support structure as thin as possible in order to get induction signals as high as possible. Using a Flame Retardant 4 (FR4) structure as in classical Printed Circuit Board (PCB) designs is not a viable option. Very thin support structures can be

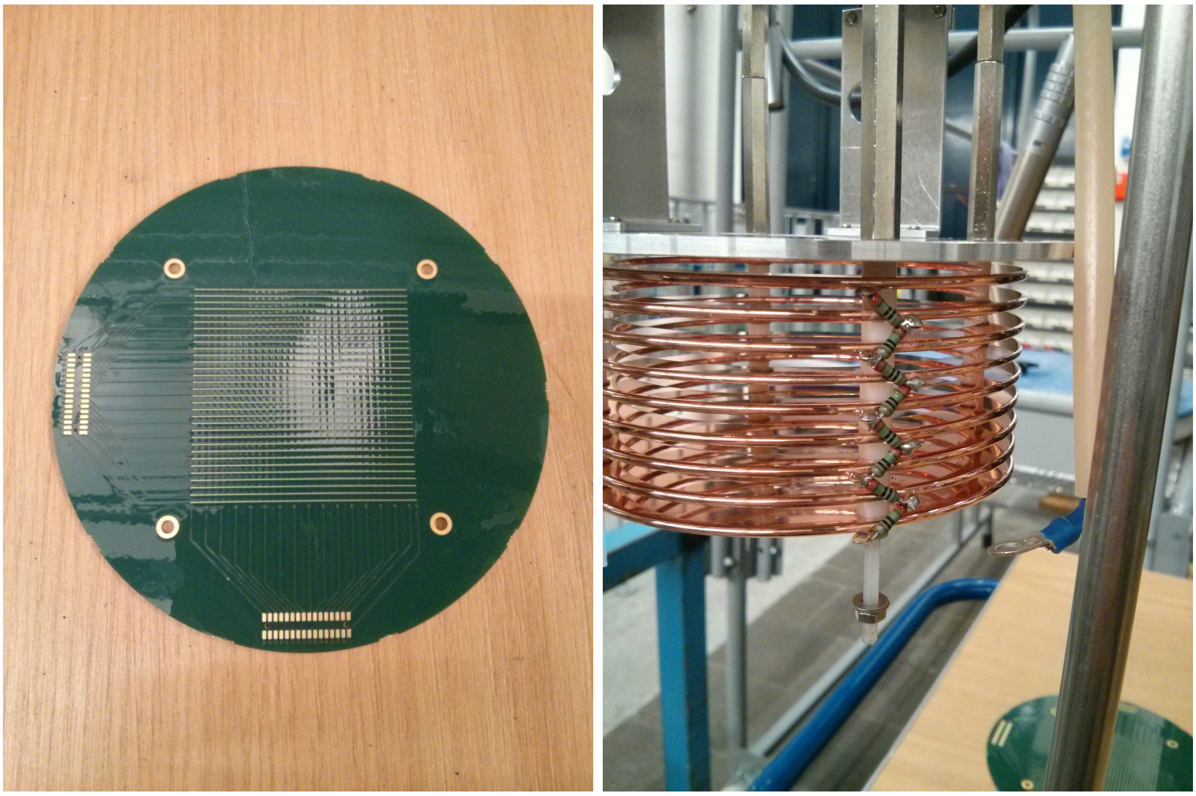

Figure 4.16.: Copper on Kapton readout plane (left) and TPC used to test it (right).

provided by using a flexible PCB made from Kapton instead of FR4. These can be made as thin as a few 10 µm. For this test a Kapton layer of 50 µm was used with a single induction plane on the back (Figure 4.16). The Kapton layer is supported by an FR4 frame for mounting on the TPC.

The test was performed in a small vacuum-insulated double-bath cryostat with an inner volume of 15 cm diameter and 60.8 cm height. Prior to filling the cryostat was evacuated using a turbo-molecular pump and then purged with argon gas and evacuated a second time. From earlier experiments [65] the purity can be assumed to be ~ 1 ppb after filling. The cryostat is sealed using rubber O-rings, which lose tightness at cryogenic temperatures. Therefore, and due to the fact that no purification system was available, the purity degraded slowly in the course of the experiment. Figure 4.16 shows the TPC I built to test the new readout. The 8 cm long field cage consists of 8 copper rings of 8 cm

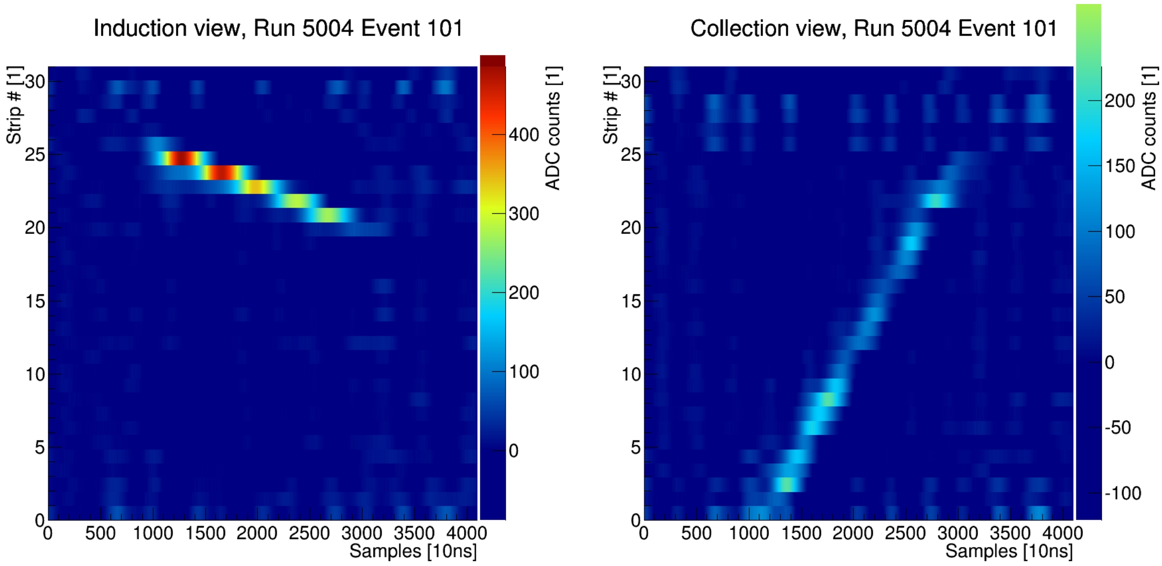

Figure 4.17.: Cosmic muon event recorded using the copper on Kapton readout.

diameter terminated by a copper plate cathode. A field of $1\,\mathrm{kV\,cm^{-1}}$ is generated using a resistive divider.

The charge readout electronics were adopted from ARGONTUBE without modifications. Charge signals are amplified by cryogenic charge amplifiers and then digitised at room temperature. More details can be found in Section 4.8.

No internal light trigger system could be used due to the limited space inside the cryostat. Instead, the digitisers were either triggered on one of the charge collection channels or by an external muon telescope. The latter was formed of two scintillator panels with PMTs above and below the cryostat, respectively. Triggering directly on charge collection channels has the potential disadvantage of recording events only partially. If the triggering channel does not receive the first charge pulse of the event, all earlier pulses are lost, unless the DAQ implements a pre-trigger ring buffer of sufficient size. It is therefore preferable to trigger on the external muon telescope.

Using the above-described setup cosmic muons were recorded over the course of multiple hours. A typical event is depicted in Figure 4.17. It can be seen that due to the event being almost parallel to the induction strips the induction signal is in fact stronger than the collection signal. The reason for the bad SNR is improper grounding of the setup and high noise levels in the lab from the nearby train station and air conditioning. No further analysis was performed on this data due to time constraints and the upcoming test of a pixelated readout described in Chapter 6. Anyhow, the fact that cosmic muons could be seen using this setup proves that there is no inherent problem with having the induction plane a few 10 µm behind the collection plane.

While this technique can potentially solve the mechanical problems of classical wire readouts, it does not reduce the ambiguities inherent to 2D projective readouts outlined in Section 3.6. Therefore, I decided not to further investigate copper on Kapton readouts, and instead focus on pixelated readouts for LArTPCs, providing real 3D data.

4.5. Pixelated Charge Readouts

Wire readouts are not suitable for LArTPCs the size of the envisioned future neutrino detectors, as has been outlined in Section 3.6. The ambiguities caused by the nature of wire readouts can be eliminated by using a fully pixelated readout. Such a readout will record a true 2D image of the charge for every time slice and thus directly produce 3D space points of the event. On the other hand, this will increase the required number of DAQ channels and therefore the data throughput. To illustrate this let us imagine a readout plane of $1\,\mathrm{m} \times 1\,\mathrm{m}$ and a desired resolution of $5\,\mathrm{mm}$. For a conventional wire readout with two planes this results in

$$\left(\frac{1\,\mathrm{m}}{5\,\mathrm{mm}}\right) \times 2 = 40 \tag{4.1}$$

wires and thus DAQ channels. In order to reduce ambiguities one can use more than two planes which will increase the number of channels linearly with the number of planes. For a pixelated readout

$$\left(\frac{1\,\mathrm{m}}{5\,\mathrm{mm}}\right)^2 = 400 \tag{4.2}$$

DAQ channels are required. Scaling this up to the needed detector size leads to an enormous number of DAQ channels and data throughput.

It is possible to reduce the number of channels by employing some form of multiplexing. There are multiple options one could imagine for this:

- Digital multiplexing
- Genetic multiplexing
- Regions Of Interest (ROIs)

Digital multiplexing means digitising all channels as close as possible to the readout plane and then multiplexing the digital data onto a high-speed digital link. An advantage of this technique is that the technology already exists and is well established in information technology. Ideally, one would feed the data stream into an optical fibre, which additionally provides galvanic isolation of the readout from the DAQ. The challenging part is that all of this needs to happen at cryogenic temperatures, which is far from trivial because most off-the-shelf components are not made for this. A detailed description of upcoming electronics capable of cold digitisation and multiplexing is given in Section 4.9. In contrast, genetic multiplexing and ROIs are forms of analogue multiplexing. The difference to digital multiplexing is that multiple readout channels are combined into a single analogue link before digitising them at room temperature outside the cryostat. In the two schemes described here this happens by connecting multiple readout channels to a single DAQ channel.

In genetic multiplexing [79] the connections are done in a way that a certain event type (a single straight track for instance) forms a distinct pattern of DAQ channels activated. For simple events it is possible to recover the full event from the pattern. Naturally, this reintroduces new ambiguities. Depending on the complexity of the event topology and the degree of multiplexing they can potentially be resolved during reconstruction. In any case, if the event is too complex, it cannot be reconstructed properly. While genetic multiplexing has been shown to work for 1D readouts (wires), there is no known solution for two dimensions (pixels).

A third technique is to subdivide a pixelated readout plane into ROIs. This scheme was tested for an earlier PhD thesis at LHEP using a Micro-Mesh Gaseous Structure (MicroMeGaS) in a xenon gas TPC [8]. All pixels at the same relative position inside the ROIs are connected to the same DAQ channel. For instance, let us assume squared ROIs. One DAQ channel would connect to all the pixels in the top left corners of the ROIs. Another channel would connect to all the pixels in the top right corner and so on. To explain this a little better let us assume a square pixel plane of $N \times N$ pixels, where $N = n^2$ and n integer. Then, we divide the plane into $n \times n = N$ ROIs, each consisting of $n \times n = N$ pixels. For such a readout we need N DAQ channels for the ROIs and another N channels for the pixels. We need only as many pixel channels as we have pixels per ROI because all the pixels at the same relative position inside the ROIs are connected together to one DAQ channel. This means that we can read out a $N \times N$ pixel plane using only $2N$ DAQ channels; the same number required by a conventional 2-plane wire readout of the same size and pitch. If there is a signal on a certain DAQ channel, the position inside the ROI is known but not the ROI. To determine the full position each ROI has its own inductive grid in between the pixels. The grid is biased such that the charge is fully focussed onto the pixels and does not collect any charge. It is possible to disentangle the true position by combining the bipolar pulse on the ROI grid with the collection pulse from the pixels. Again, the drawback of this approach is that it is not free of ambiguities. It fails for multiple simultaneous hits when it is impossible to say which pixel pulse belongs to which ROI pulse.

Independently of the amount of data one needs to bring out of the detector a second problem is heat dissipation. The more of the readout chain is sitting inside of the detector, the more serious this problem becomes. It is especially problematic for digital multiplexing which requires a lot of cryogenic electronics. A possible solution to this is to power only that part of the readout that is actually needed. This would require a means to wake up the part of the readout where the charge is arriving before it is collected. Provided the wake-up time is short enough, inductive grids on ROIs could allow precisely for this.

4.6. Charge Readout Summary

Replacing a classical wire readout by copper strips on a thin ($\sim 10\,\mu$m) layer of Kapton can alleviate the mechanical challenges met by the charge readout. However, this does not change the projective nature of the readout, introducing ambiguities in event reconstruction. A pixelated readout can provide true 3D information at the price of an increased number of channels. Due to the lack of bespoke pixel electronics able to readout so many channels (see Section 4.9) I implemented a form of analogue multiplexing. As the ROI approach had already been demonstrated in a gas TPC, it was chosen for the first prototype of a pixelated LArTPC. The readout plane can be realised as a conventional PCB because the detector is a single-phase LArTPC, and thus no gas amplification as in MicroMeGaS is needed. Alongside the PCB I designed a new TPC which can be reused for future prototyping efforts. The design of PCB and TPC as well as the results from the first tests will be described in Section 5.1.

4.7. Noise in Charge Readout Electronics

For a heavy MIP with $\frac{\mathrm{d}E}{\mathrm{d}x} \approx 2.1\,\mathrm{MeV\,cm^{-1}}$ a LArTPC has a charge yield of $\sim 1\,\mathrm{fC\,mm^{-1}}$ as explained in Chapter 3. The readout electronics need to be able to reliably digitise this charge. One of the biggest challenges to detect such low charges is the Signal-To-Noise Ratio (SNR). This section gives a theoretical overview of various noise sources and mitigation techniques. Noise can originate from a plethora of sources. They can be divided into internal, originating inside the electronic components, and pick-up from external sources.

The most important internal source is the *Johnson-Nyquist* noise. It is generated by the intrinsic motion of the charge carriers at non-zero temperature and therefore often called thermal noise. In statistical thermodynamics the energy of a system with one degree of freedom,

$$E = \frac{kT}{2}, \tag{4.3}$$

is proportional to its temperature T by the Boltzmann constant k. The stored energy in a capacitor is given by

$$E = \frac{CV^2}{2}, \tag{4.4}$$

where C is the capacitance of and V the voltage across the capacitor. Therefore, the voltage generated by the thermal noise inside an isolated ideal capacitor is

$$V = \sqrt{\frac{kT}{C}}. \tag{4.5}$$

Combining this with the charge in the capacitor,

$$Q = CV = \sqrt{kTC}, \tag{4.6}$$

yields the equivalent noise charge due to the capacitor's temperature. [80]

Equation (4.6) has two important consequences for charge detectors: Noise scales with temperature and detector capacitance. The temperature dependence is one of the main reasons to operate all analogue electronics at cryogenic temperatures. Noise levels on pixels are significantly lower compared to wires due to the much smaller capacitance.

Another internal noise source are resonances in the signal path that can start to oscillate. Resonances can occur from the combination of the impedance of electronic components such as cables and input impedances. The main culprits are usually parasitic impedances not taken into account during the design of the circuit. The resulting oscillations are superimposed on the signal.

An example of such a resonance is the behaviour of the cryogenic LARASIC preamplifiers used for ARGONTUBE, described in Section 4.8. They include a user-configurable shaping filter. With its change the input capacitance of the amplifier changes as well. Some configurations can form resonances with the circuit at the input. Most passive electronic components change their values more or less significantly with temperature. Therefore, the resonance behaviour of the detector circuit is different at room temperature and in LAr. Additionally, every deviation from the final setup potentially changes parasitic impedances. As a result, it is quite challenging to debug such resonances in the signal path.

External sources can induce voltages on the signal path via variable magnetic fields, as predicted by Faraday's law. Particularly prone to this are ground loops, any closed circuit supposed to be entirely at ground potential. If the resistance at one place of the loop is high enough, the induction results in a voltage difference along the loop. If the

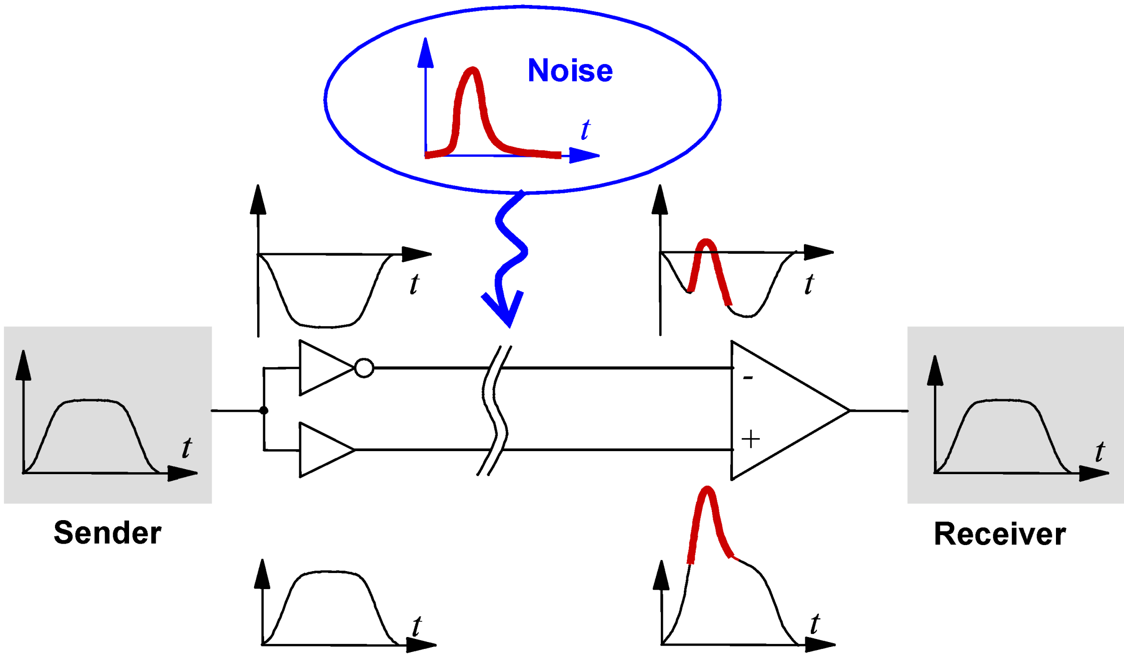

Figure 4.18.: Noise reduction using differential signalling. [81]

same part of the loop is used as reference of a signal carrying connection, the difference in the ground reference between signal source and sink will affect the signal.

There are several possibilities to make a circuit more resilient to external noise sources. An obvious one is shielding all sensitive parts from external magnetic fields using a Faraday cage. Implementing this effectively is extremely complicated and often not practical for small experiments. Another approach is hardening the signal path itself by using current-coupled and/or symmetric signals. Current-coupled signals are much less sensitive to induced voltages, as long as the voltages are small enough and do not result in significant current across parasitic impedances. An example is Nuclear Instrumentation Module (NIM) logic.

In conventional single-ended signalling the signal is measured as the voltage or current difference between a signal conductor and a ground common to signal source and sink. Using a common ground as signal return path can have several undesired effects. The signal conductor is usually enclosed in a ground shield. If the shield is connected on both sides, a ground loop can result in combination with a shared power supply ground, for instance. Ground loops can pick up noise through induction if the resistance along the loop is high enough. A second way to couple noise into a single-ended system is by shifting the potential on the common ground away from the reference voltage or current, for instance due to high currents flowing through a lossy ground connection. The signal will be distorted because it is always measured against the common ground. In symmetric or differential signalling the signal is not measured between a signal conductor and ground, but instead between two signal conductors. This works by putting an inverted (symmetric) waveform of the signal on a second conductor. The signal is recovered by forming the difference between the two signal conductors. As a result, the signal sink needs not be connected to the same ground as the signal source because the signal is independent of ground. Ground loops in the signal path can thus be avoided. Furthermore, the effect of noise pick-up on the signal lines is drastically reduced. Inductive noise pick-up is equal on both signal conductors due to the completely symmetric signal path, as opposed to single-ended signals where the signal path is not symmetric. In the signal sink the difference between the two symmetric signal conductors is formed and everything that is present on both of them, such as the inductively picked up noise, cancels out.

Disentangling the three different sources of noise (thermal noise, resonances, and external pick-up) is not easy. Hints can often be found in the spectrum of the noise. Thermal noise is equal and uncorrelated over the full frequency spectrum. Resonances usually occur at specific frequencies and thus produce regular patterns, such as a sine, at the resonance frequency. External sources are more difficult to identify. If the source produces EM fields at known frequencies (e.g. harmonics of a switched power supply) the noise spectrum can be scanned for them. Debugging is much more complex if the source is unknown.

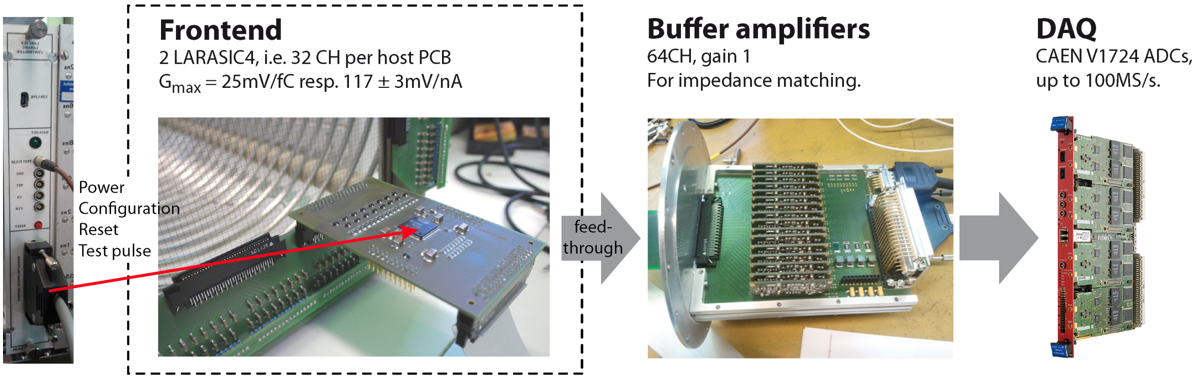

Figure 4.19.: Scheme of the ARGONTUBE charge readout chain. From left to right: preamplifier power and control NIM module, LARASIC preamplifiers on wire readout plane, buffer amplifiers, CAEN V1724 digitisers. The dashed rectangle denotes the cold part of the chain. [82]

4.8. ARGONTUBE Charge Readout Chain

Contemporary electronics schemes are introduced by looking at the existing readout chain at LHEP. It was originally designed for the ARGONTUBE experiment and a more detailed description can be found in [82]. I successfully upgraded the chain to partial differential signalling, significantly improving the SNR.

The charge collected by the readout plane is amplified by LARASIC4* [83] cryogenic charge amplifiers developed by BNL for the Micro Booster Neutrino Experiment (MicroBooNE) [32]. A performance characterisation of these Application-Specific Integrated Circuits (ASICs) can be found in [82]. Their main features include:

- 16 channels per ASIC
- low noise charge amplifier incorporating high-order filters
- per channel programmable gain of $4.7\,\mathrm{mV\,fC^{-1}}$, $7.8\,\mathrm{mV\,fC^{-1}}$, $14\,\mathrm{mV\,fC^{-1}}$, or $25\,\mathrm{mV\,fC^{-1}}$
- per channel programmable filter peaking time of $0.5\,\mathrm{\mu s}$, $1.0\,\mathrm{\mu s}$, $2.0\,\mathrm{\mu s}$, or $3.0\,\mathrm{\mu s}$

- built-in test capacitance connected to dedicated external test pulse input for calibration

- power dissipation $< 10\,\mathrm{mW}$ per channel

The cryogenic preamplifiers are mounted as close as possible to the readout in order to minimise noise pick-up on these very sensitive lines. LARASICs can be programmed to the different aforementioned configurations via a Serial Peripheral Interface bus (SPI). For this purpose they are connected to a bespoke NIM module housing an SPI controller, a test pulse generator, and multiple low-noise voltage regulators providing power to the LARASICs. A standard PC controls the NIM module via Universal Serial Bus (USB). The output of the preamplifiers is fed to buffer amplifiers mounted on top of the cryostat signal feedthrough by means of flexible Kapton ribbon cables. The buffers operate at room temperature, have a unity gain, and match the output impedance of the LARASICs to the $50\,\Omega$ input impedance of the downstream digitisers. From the buffers the signals are routed via $50\,\Omega$ coaxial lines to *CAEN V1724* digitisers [84] mounted in a VERSAmodule Eurocard (VME) crate. For debugging purposes the output of the buffers can be routed to an oscilloscope via a coaxial T-piece. Finally, the digital data is read out from the VME crate via a fibre-optic link by a standard PC. Figure 4.19 depicts the entire readout chain. The complete analogue signal path from the pixel plane to the VME digitisers is single-ended and thus prone to ground loops and all associated noise problems.

During the first pixelated readout measurement campaign (see Section 5.1) it became apparent that the data was significantly impaired by noise. As can be seen in Figure 4.20, the noise amplitude is similar over multiple channels. This implies a common-mode component that cannot originate from inductive pick-up. Instead, the noise is likely generated by self-oscillating parts of the signal path due to ground loops and parasitic impedances. For the second measurement campaign different steps were taken to mitigate

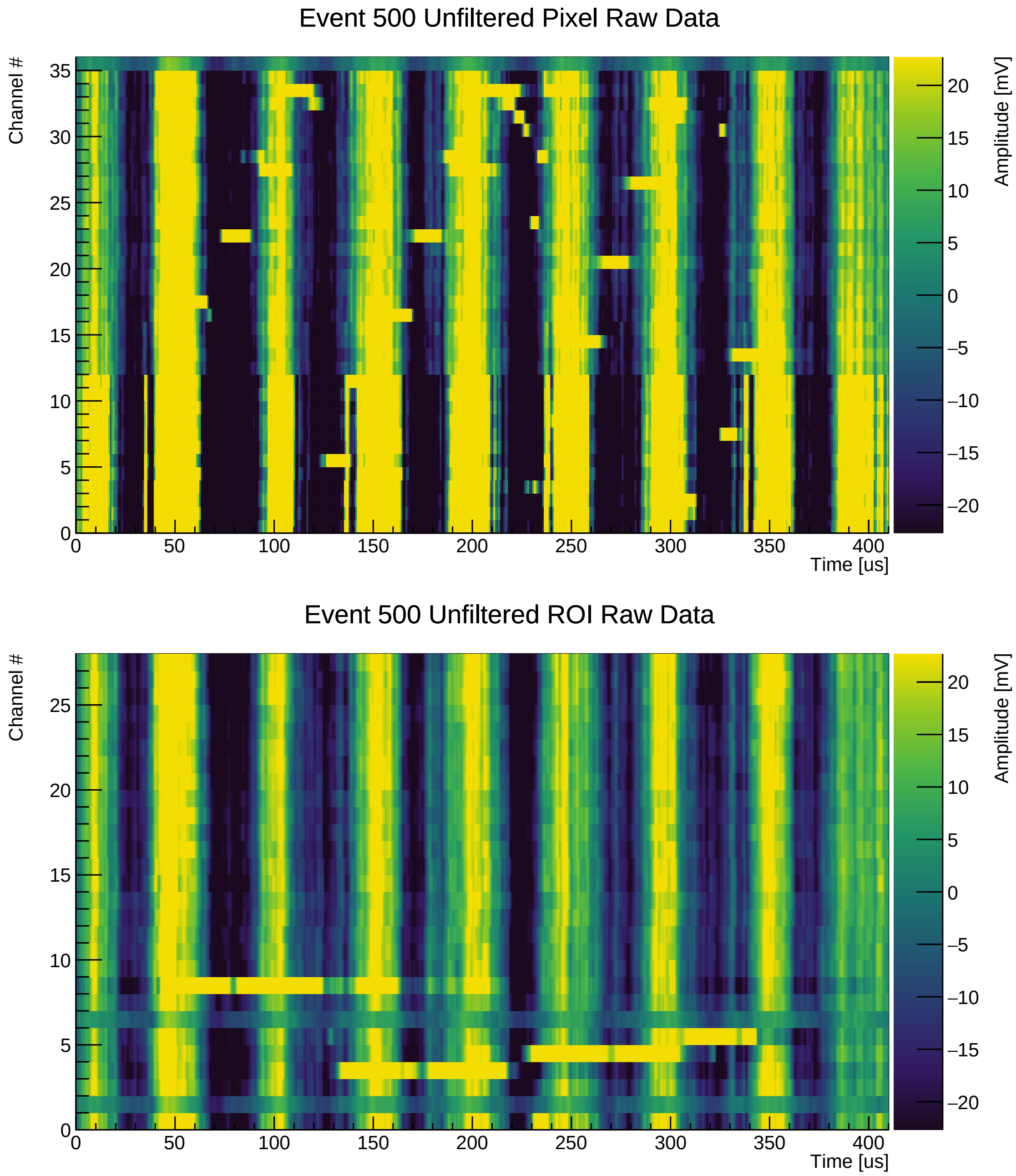

Figure 4.20.: Event from the first pixel demonstrator measurement campaign. The top plot shows pixel data while the bottom plot shows ROI data. Note that the colour scale does not represent the full available dynamic range.

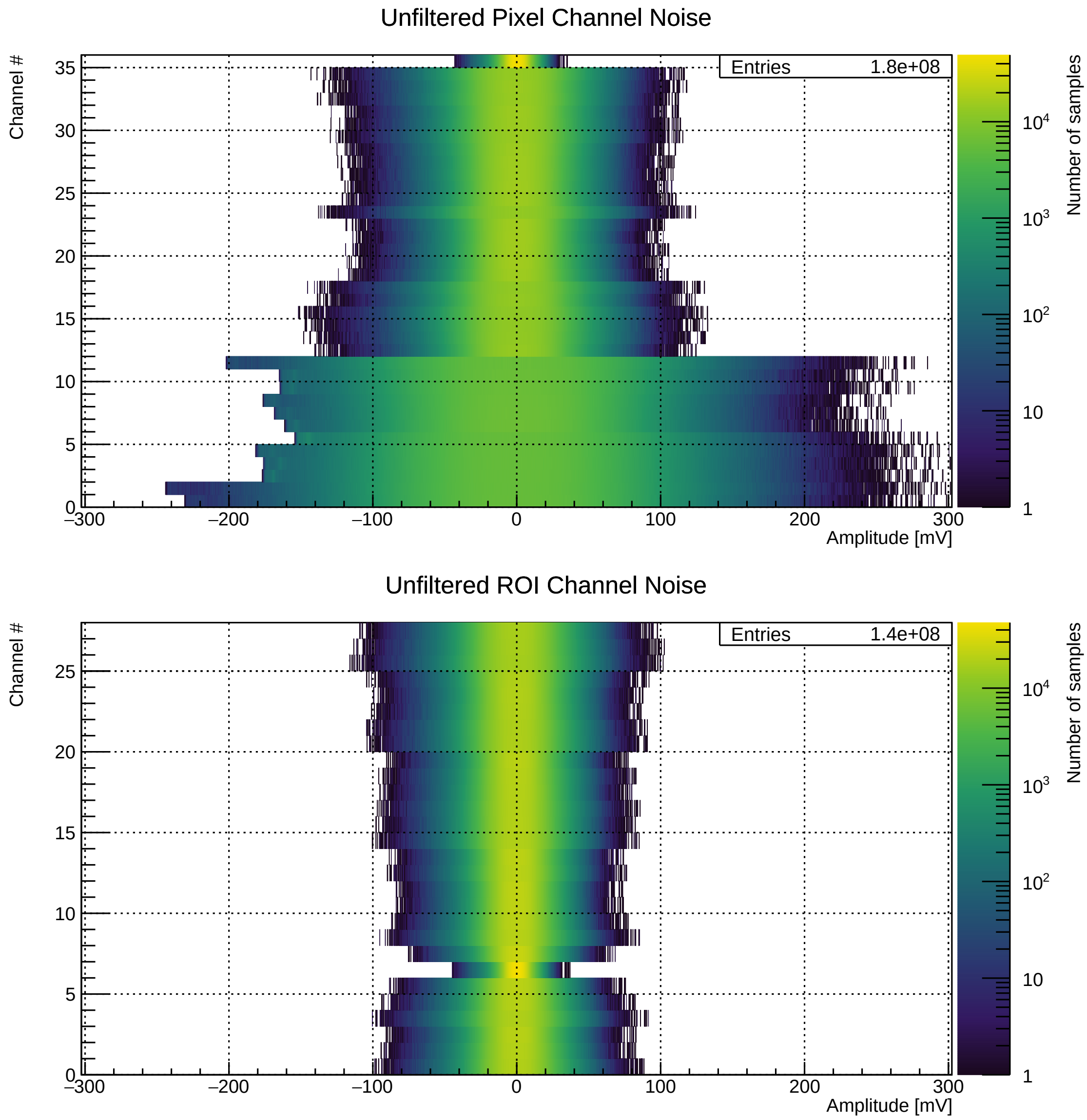

Figure 4.21.: Noise amplitude distributions of pixel (top) and ROI (bottom) channels from the first pixel demonstrator measurement campaign. 5000 events from a 5 Hz random trigger, with 1000 410 ns samples each, were combined.

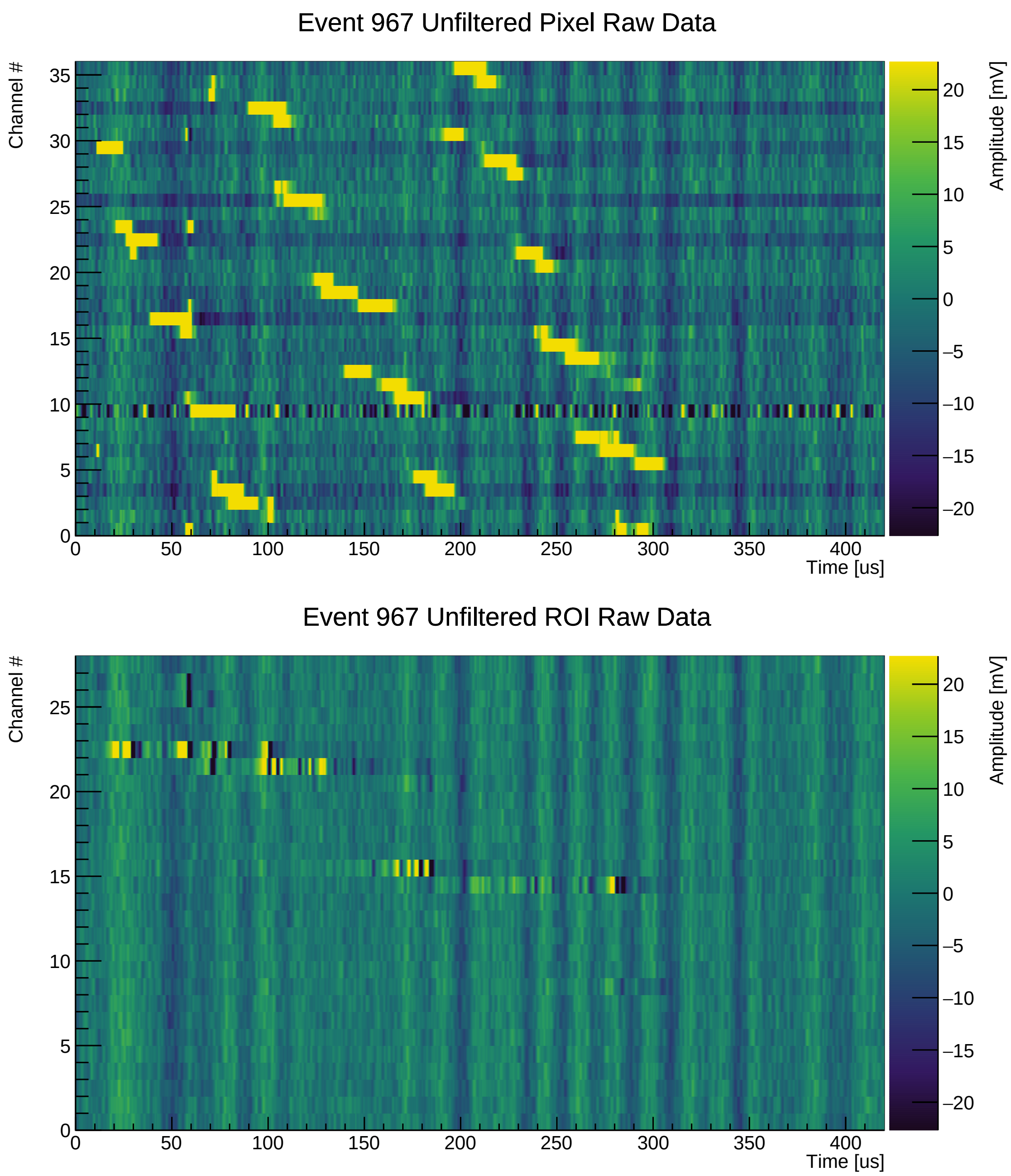

Figure 4.22.: Event from the second pixel demonstrator measurement campaign, after implementing hardware noise mitigation measures. The top plot shows pixel data while the bottom plot shows ROI data. Note that the colour scale does not represent the full available dynamic range.

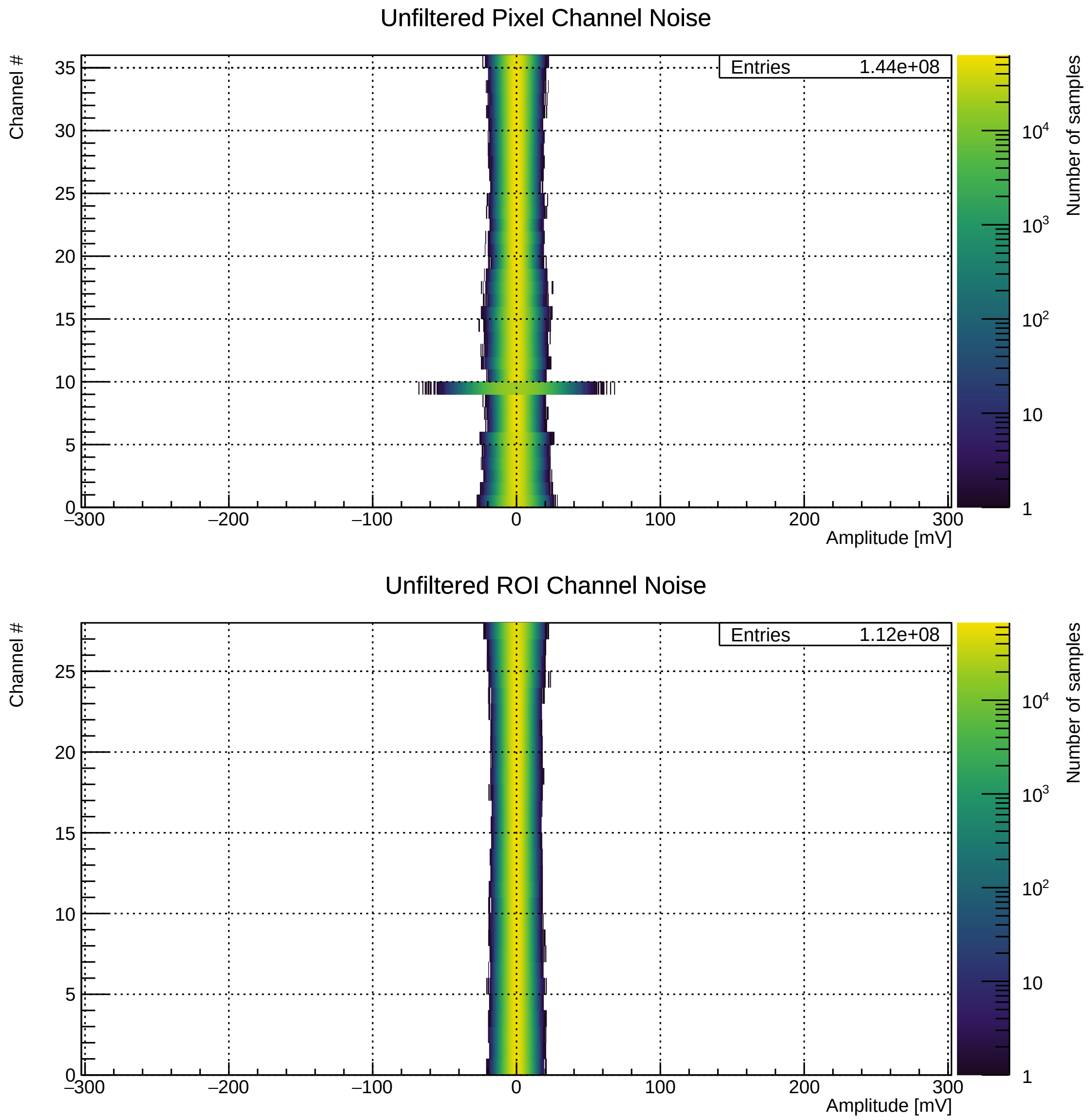

Figure 4.23.: Noise amplitude distributions of pixel (top) and ROI (bottom) channels from the second pixel demonstrator measurement campaign, after implementing hardware noise mitigation measures. 2000 events from a 5 Hz random trigger, with 2000 210 ns samples each, were combined.

this behaviour through modifications to detector location, power supply, signal path, and intrinsic capacitance.

A correlation between noise levels and the running state of the air conditioning system in the utility room next to the lab was found. Therefore, the experimental setup was moved away from the wall facing the utility room.

A decoupled clean power grid was built in the lab. A Motor Generator set (MG) separates the lab grid mechanically from the building power supply. Thus, any noise present on the latter is prevented from entering the experimental setup. Furthermore, this decouples the lab grid entirely from the building ground preventing ground loops via electric mains.

The signal path from the impedance-matching buffer amplifiers to the digitisers—i.e. the warm signal path—was changed from single-ended to differential signalling. This was achieved by replacing the buffer amplifiers by single-ended-to-differential amplifiers, and inserting another stage upstream of the digitisers to change the signal back to $50\,\Omega$ single-ended, matching the input of the digitisers. Like this noise pick-up outside the cryostat could be reduced as well as sensitivity to ground loops between the detector and the DAQ rack. The design for the two buffer stages was kindly provided by the Liquid Argon In A Testbeam (LArIAT) collaboration (see Section 5.3 and [85]).

A source of noise was identified in the layout of the pixel readout plane. It was found that due to several ground planes and long traces in the PCB parasitic capacitances were very high. Pixel channels are particularly affected due to the increased total trace lengths from connecting multiple pixels to the same DAQ channel. This is problematic because the input is shorted to ground for high enough frequencies (determined by RC), creating a ground loop. Through the capacitive coupling to ground the system can start to oscillate. One evidence for this is that the noise is equal over multiple channels, implying a common-mode component. More specifically, the noise is equal for two respective groups of channels (see Figure 4.20). Investigating this, I found out that these groups correspond to channels of roughly equal parasitic capacitance: (150 ± 5) pF and (95 ± 5) pF. The noise amplitude is higher on channels with higher capacitance (see Figure 4.21). To solve this problem the PCB design was optimised by removing unnecessary ground planes, routing signal tracks outside necessary ground planes, and increasing the thickness of the PCB. Pixel capacitance could be improved to (65 ± 5) pF for all channels. ROI capacitance improved only slightly from (25 ± 10) pF to (20 ± 10) pF, which confirms the hypothesis that the long traces due to pixel multiplexing were the culprits. The reason for the higher spread of the ROI capacitances is the larger difference in trace length between the different ROIs. For the sake of completeness it should be noted here that the old PCB was not populated for the capacitance measurements while the new one was populated as described in Section 5.1. However, the installed capacitors are either not connected to ground or in series with a $10\,\mathrm{M\Omega}$ resistor. Therefore, their influence on the measurements is negligible.

As can be seen from Figures 4.20 and 4.22, there was a significant decrease in noise after applying all of the above improvements to the readout chain. This can also be seen from Figures 4.21 and 4.23, depicting the noise amplitude distributions of the two measurement campaigns. The data for the noise distributions (5000 events in the first and 2000 events in the second campaign) was taken employing a 5 Hz random trigger. A more detailed assessment of the noise after the implementation of the described noise mitigation measures can be found in Section 5.1.

4.9. Improved Cold Electronics for Pixelated Charge Readouts

This section describes the challenges met by electronics for pixelated LArTPCs and possible solutions. I evaluated the cryogenic Analogue-to-Digital Converters (ADCs) for the DUNE FD, developed by BNL, and found that they are unsuitable for a pixelated ND. The neutrino group at Lawrence Berkeley National Laboratory (LBNL) is developing bespoke pixel electronics for the ND, the Liquid Argon Pixel readout ASIC (LArPix). Based on my experience I advised the LBNL group on the testing of their new readout electronics.

As mentioned in Section 3.5, cold digitisation can improve noise because of both shorter analogue signal paths and reduced thermal noise of the electronics. Furthermore, it enables data multiplexing on high-speed digital links, reducing the number of needed signal cables and cryostat feedthroughs. However, designing reliable electronics at cryogenic temperatures is not an easy task. ADCs require very stable reference voltages for proper analogue-to-digital conversion, making them susceptible to voltage fluctuations. A further important aspect is power dissipation. All power dissipated by cryogenic electronics needs to be compensated for in order to prevent the LAr from boiling. This is particularly problematic for a pixelated readout that requires a much higher number of readout channels than a wire readout (see Section 4.5). Another problem arises from the fact that digital electronics in general require clocks with sharp edges for proper timing, usually realised as a square wave. According to Fourier analysis a square wave produces a high level of harmonics. This is particularly problematic in the case of readout wires that can act as antennae and pick up these clock signals.

BNL is developing cold charge readout electronics for the DUNE FD [86]. The plan is to accompany the cryogenic LARASIC charge preamplifiers by cryogenic ADCs. They

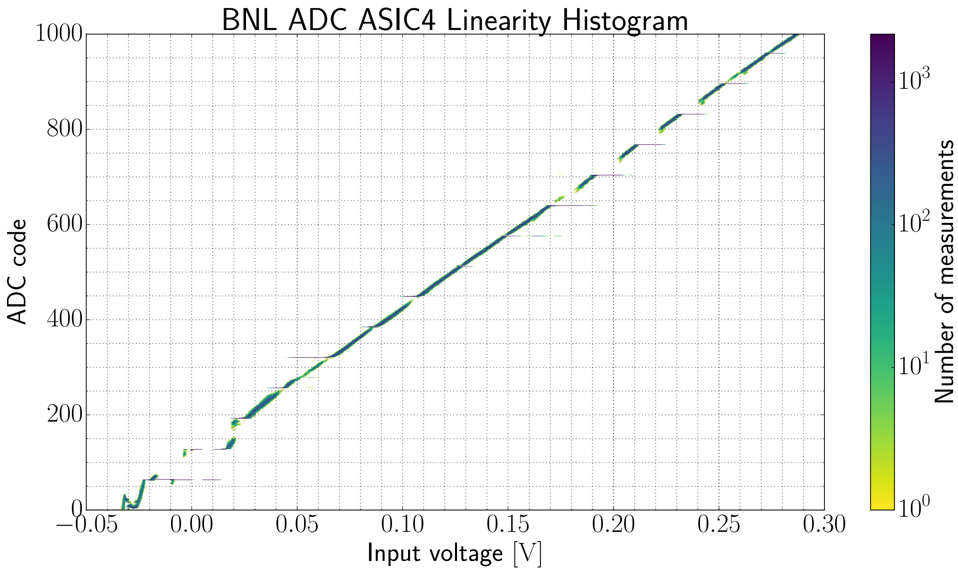

Figure 4.24.: Linearity measurement of the BNL cryogenic ADC ASICs with input voltage on the x-axis and ADC value (code) on the y-axis. Colour represents the number of measurements. The measurements were performed in liquid nitrogen.

have 16 inputs, each capable of digitising the TPC signals at 2 MS/s and 12 bit with input characteristics optimised for the LARASIC output. A more detailed description is given in [87].

In the course of this work, the cryogenic ADC ASICs developed by BNL were evaluated to be used in the ND as well. I joined the team at BNL in cold tests of the devices. One of the results of these tests is presented here to illustrate the difficulties of cryogenic ADCs. As a disclaimer, it should be noted that this is by no means the status of the ADCs at the time of writing. The described tests were performed in autumn 2016 at BNL.

An important characteristic of an ADC is linearity. It describes the relation between the applied input voltage and the calculated digital number, the *ADC code*, at the output. In case of the BNL ADCs this relation is expected to be strictly linear. To test this a voltage ramp is applied to the input and the converted digital values are recorded.

Table 4.4.: LArPix specifications for a 10 MHz external clock. [88]

Specification	Value	Unit
Number of analogue inputs (channels)	32	
Noise at 88 K	300	e
Noise at 300 K	500	e
Channel gain	4 or 45	$\mu V\, e^{-1}$
Time resolution	2	µs
Analogue dynamic range	≈1300	mV
ADC resolution	8	bit
Threshold range	0 to 1.8	V
Threshold resolution	<1	mV
Channel linearity	1	%
Operating temperature range	80 to 300	K
Event memory depth	2048	
Nominal output signalling level (CMOS)	3.3	V
Digital data rate	5	$\text{Mbit}\, s^{-1}$
Event readout time	≈11	µs
Power dissipation per channel at 1 Hz event rate	∼100	µW

A typical measurement is shown in Figure 4.24. The expected shape is one straight diagonal line from the bottom left to the top right, i.e. a linear relationship between input voltage and ADC value. Two particular deviations from this are visible: gaps accompanied by horizontal lines and a wobbly response around zero. Upon close inspection it can be seen that the gaps have the same voltage range as the horizontal lines. The meaning of this is that the ADC output is *stuck* at the same value for the corresponding input voltage range. Both effects result in a non-linear detector response to detected charge and thus energy deposition. While some non-linearities can be compensated in offline data analysis, this is not possible for the sticking ADC values because they correspond to a range of input voltages. This impairs the energy resolution of the detector.

The cause for the non-linearities is rooted in the electronic design of the ASIC. It was not fully understood at the time of these tests. Therefore, an explanation is out of the scope of this work and not given here. The measurements are shown to illustrate the difficulties of designing a reliable cryogenic ADC.

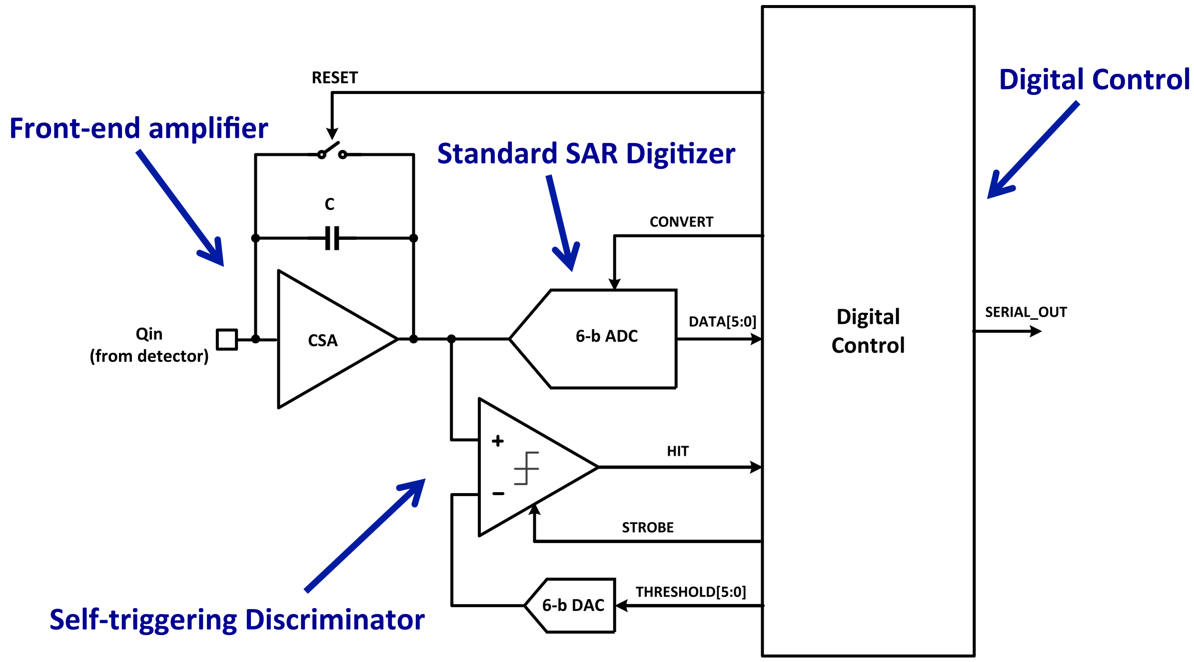

Figure 4.25.: Conceptual block diagram of a LArPix channel. [89]

Leaving aside the non-linear response, the BNL ADCs are not suitable for use in conjunction with a pixelated LArTPC charge readout. Being designed for wire readouts, no strong focus was laid on power dissipation, which is $\approx 5\,\mathrm{mW}$ per channel. Combined with the one of the LARASIC ($10\,\mathrm{mW}$) [83] a total of $\approx 15\,\mathrm{mW}$ is dissipated. A pixelated DUNE ND with a $3\,\mathrm{mm}$ pitch and the dimensions given in Section 6.2 will need $\gtrsim 10^7$ channels. The resulting required cooling power would be $\gtrsim 150\,\mathrm{kW}$ for $84\,\mathrm{t}$ of LAr. In comparison, MicroBooNE has a total cooling power of $\approx 20\,\mathrm{kW}$ for $170\,\mathrm{t}$ of LAr [32].

Due to their smaller geometric extent pixels have a much lower capacitance ($\approx 4\,\mathrm{pF}$ for vias [88]) than wires ($\approx 200\,\mathrm{pF}$ [86]). According to Equation (4.6) this reduces the intrinsic noise present on a pixelated readout. LArPix, being developed by LBNL [88, 90], exploits this fact to significantly reduce the complexity of the cold electronics. Two key points distinguish them from the BNL design for the wire-equipped FD. The complex shaping preamplifier required by wires for noise filtering can be replaced by a simple charge integrator. Additionally, the low noise levels allow for a smart zero suppression scheme; charge arriving at the LArPix is only digitised if it is above a predefined threshold. This reduces the duty cycle and thus power dissipation of the ADC. If noise levels are well below the set threshold, power dissipation becomes primarily a function of charge flux rate in the detector.

In addition, the digital circuitry of LArPix operates at lower frequencies than the BNL design. For an Alternating Current (AC) of frequency f, the resistance presented by a conductor is not simply given by its Ohmic resistance. There is an additional component proportional to $\sqrt{f}$ caused by the *skin effect* [91]. HF currents do not flow in the bulk of the conductor but only in a finite layer (skin) at its surface. Therefore, the conductivity is no longer proportional to the cross-section area but rather the circumference of the conductor. The result of the skin effect is more power dissipation at higher frequencies for the same conductor geometry. By operating at lower frequencies the power dissipation of LArPix can be lowered further. The cost is a decrease in data transmission rates.

With its power dissipation dependent on the charge flux and the lowered data transmission rate LArPix is susceptible to high event rates. The same goes for noise levels due to the self-triggered digitisation. For the successful operation of LArPix it is of paramount importance to keep event rates and noise levels low. The latter can be achieved by minimising detector capacitance. To lower the susceptibility to high event rates the DUNE ND design orientates the TPC drift direction perpendicular to beam direction. This reduces the amount of charge per event arriving simultaneously at the readout. Furthermore, LArPix is equipped with a First In First Out (FIFO) buffer capable of holding 2048 charge pulses to cope with short peaks in event rate.

To accommodate the elevated channel number of a pixelated readout the first LArPix prototype chip has 32 inputs. Its resolution in time and charge are 2 µs and 8 bit, respectively. While currently inferior to the BNL design, these specifications are planned to be improved in the next design iteration. The first LArPix version aims to demonstrate

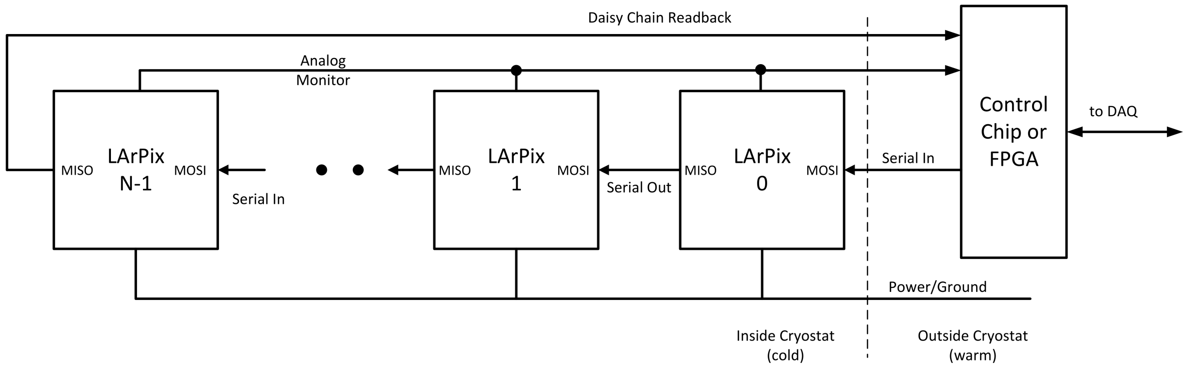

Figure 4.26.: LArPix daisy chain configuration. [88]

two critical aspects [89]:

1. Low noise and low power dissipation (see Table 4.4)
2. MIP track detection capability in a test TPC

Another goal is to assess the optimal size of the FIFO event buffer [92]. The most important LArPix specifications are given in Table 4.4.

Figure 4.25 shows the block diagram of a single LArPix channel. The incoming charge is converted to a voltage by a Charge-Sensitive Amplifier (CSA) via integration on the feedback capacitance C. To minimise power dissipation the output of the CSA is only digitised if it is above a digitally configurable threshold. This is realised by discriminating the signal against a Digital-to-Analogue Converter (DAC) output. If the signal is above threshold, the discriminator triggers a digitisation and then a reset of the CSA. Each channel can be connected individually to an analogue monitor bus shared between multiple LArPix chips (see Figure 4.26). The LArPix controller outside the cryostat can probe the analogue monitor bus to set the thresholds correctly (see the datasheet [88] for a detailed procedure).

Digitisation is performed by a standard Successive Approximation Register (SAR) digitiser. It works as follows [91]. The input signal is compared to the output of a DAC controlled by a register. At the start of the conversion all bits in the register are set to 0.

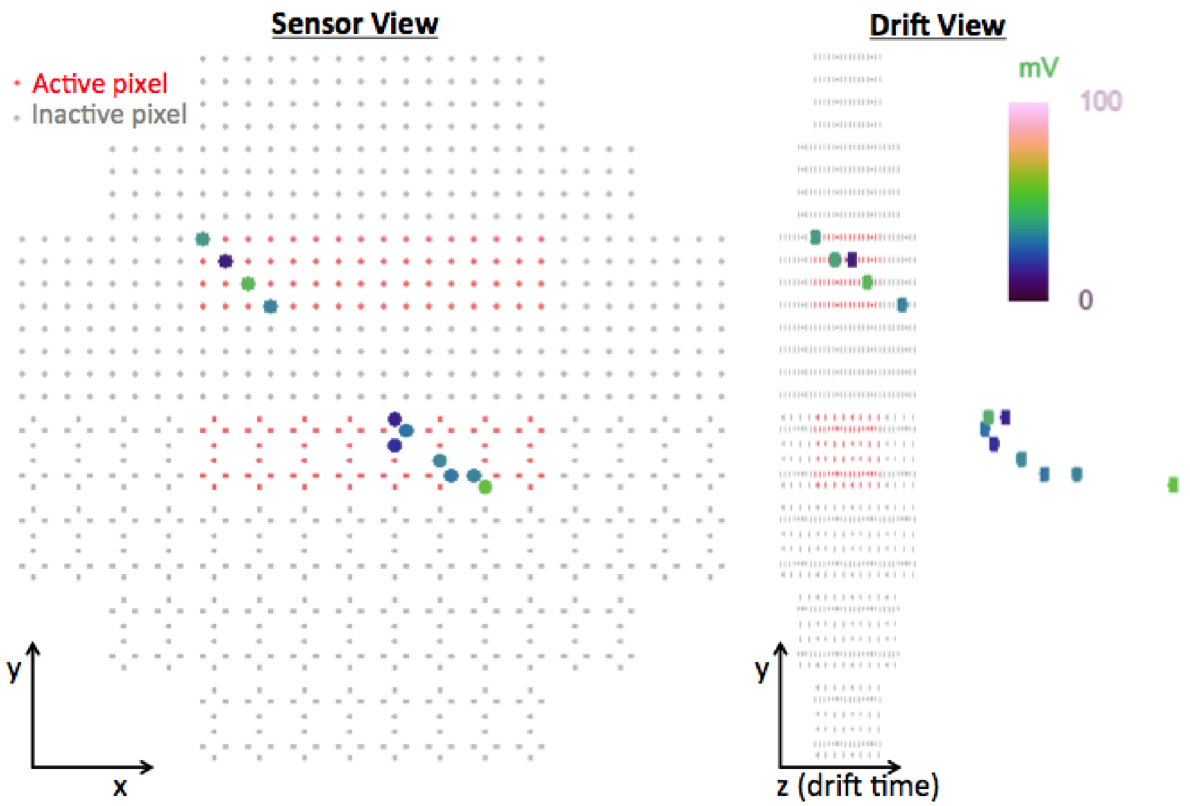

Figure 4.27.: Cosmic muon track recorded with the first LArPix prototype. The left projection is perpendicular to the pixel plane while the right one is almost parallel to it. Note that only red pixels are instrumented. [92]

Then, the most significant bit is set to 1. If the DAC output is above the analogue input, the bit is set back to 0. Otherwise, it is kept at 1. The procedure is successively repeated for all bits. After the least significant bit has been set, the conversion is complete and the value of the register is output to the digital event buffer (FIFO). The whole conversion requires the same number of clock cycles as the number of DAC (and therefore ADC) bits.

LArPix uses a Universal Asynchronous Receiver-Transmitter (UART) connected by SPI for communication. This allows to daisy chain up to 256 LArPix chips as depicted in Figure 4.26. The daisy chain is connected to a LArPix controller outside the cryostat, which can be a Field-Programmable Gate Array (FPGA) or any other digital controller capable of handling the expected data rate. Chips are identified by means of a hard-coded

Identifier (ID). During data taking each LArPix chip constantly transmits the events present in its FIFO buffer to the controller via SPI. One data packet or event consists of 54 bit of data, containing a single ADC value, chip and channel ID, and a timestamp. Configuration of the LArPix chips (e.g. threshold setting) happens via the same SPI line.

LArPix does not have its own oscillator. All timing signals are derived from an external clock signal supplied by the controller and shared between multiple chips. In particular, this clock defines the time resolution of the digitisation and the SPI data rate. Furthermore, the event timestamp generated inside LArPix is derived from this clock. The specifications in Table 4.4 are given for a 10 MHz, clock resulting in a time resolution of 2 µs. This is the nominal configuration for the first prototype. Later chip designs will be optimised to allow for a better time resolution.

Each LArPix chip has an integrated test pulse generator. It consists of a DAC that can be connected to one or more inputs via a coupling capacitor. Charge can be injected into the selected inputs by switching the level of the DAC. This allows to characterise and/or debug the charge readout chain in a similar fashion to the LARASIC preamplifiers described in Section 4.8.

One design goal of LArPix is to reach a power dissipation of 100 µW per channel. Using the same numbers as above this results in a total power dissipation of ~ 1 kW for a pixelated DUNE ND. Most of the supply voltages of LArPix can be reduced from their nominal value. This allows to further decrease power dissipation in addition to the smart zero suppression and reduced clock frequency. Attention has to be paid to adjust the SPI signalling levels accordingly. More information on this can be found in the datasheet [88].

The first LArPix prototype was successfully tested at LBNL in a shorter version of the pixel demonstrator TPC described in Section 5.1. In particular, the noise and power dissipation levels given in Table 4.4 were reached [93]. Figure 4.27 shows a recorded cosmic muon track. Note that only the red pixels are instrumented, explaining the segmented track.

4.10. Charge Readout Electronics Summary

Pixelated LArTPCs place high demands on the charge readout electronics. The very high number of readout channels required makes digitisation outside of the cryostat impractical due to the resulting number of cable feedthroughs. Cold digitisation inside the cryostat reduces the number of cables by channel aggregation on digital high-speed links. However, this worsens the problem of heat dissipation inside the LAr. I evaluated the cold digitisers developed for the charge readout wire planes of the DUNE FD, but found them to be unsuitable for a pixelated LArTPC due to their high power dissipation. LArPix is a bespoke cold digitiser for pixelated LArTPCs. It is currently under development at LBNL and designed to meet the stringent heat dissipation requirements by means of a smart zero suppression.

4.11. Cryogenic SiPM Light Readout

For the ArgonCube detector concept, detailed in Section 5.4, a compact light readout is needed. PhotoMultiplier Tubes (PMTs) are not suitable because they occupy a lot of space and thus would require mounting on top of a module, which in turn would reduce their efficiency. That is why the photon detectors of choice for such a detector are Silicon PhotoMultipliers (SiPMs).

A novel light readout system based on SiPMs in LAr was implemented for the ArgonCube pixel demonstrator described in Section 5.1. Acrylic rings placed in between the aluminium field-shaping rings of the TPC provide the light collection; their inner surfaces are machine-polished and coated with the WLS TPB. The coating method is based on [94]. 0.5 g of TPB and 0.5 g of acrylic flakes were dissolved in 50 mL of toluene and then mixed with 12 mL of ethanol, which serves to increase the coating homogeneity. Three layers of the coating were applied by hand with a fine brush.

1 mm diameter WLS fibres, *Kuraray Y11(200)M* [95], couple the acrylic rings to four *Hamamatsu S12825-050P* SiPMs [96] mounted close to the anode (see Figure 5.5). The SiPMs and their front-end electronics were adapted from those developed at LHEP for the Cosmic Ray Taggers (CRTs) used in MicroBooNE and the Short Baseline Neutrino Detector (SBND) [97, 98]. Residing on the cryostat top flange at room temperature, the Front-End Board (FEB) is connected to the SiPMs via Teflon insulated coaxial cables. For operation in LAr the SiPM bias voltages has to be reduced from $\approx 70\,\mathrm{V}$ to $53\,\mathrm{V}$, in order to compensate for change of breakdown voltage.

The peak of scintillation light emission in LAr lies at 128 nm (see Table 3.1) while the sensitivity wavelength peak of the SiPM is at 450 nm. Therefore, the scintillation light needs to be shifted before it can be detected by the SiPMs. This happens in two stages. For the first shift TPB is applied to the inside of the acrylic rings. Their outside is not coated to reduce the collected amount of scintillation light that originates outside the TPC while their inside is machined to optimise light collection. TPB absorbs the 128 nm scintillation light and re-emits it with a peak at 440 nm [99]. The light emitted by the TPB is then propagated through the acrylic and coupled into the WLS fibre which has an absorption peak at 430 nm and an emission peak at 476 nm.

In the FEB two coincidences ($\wedge$) of two out of four SiPMs are formed and combined by means of a logic *OR* ($\vee$) operation. The trigger pattern is thus

$$T = (S_1 \wedge S_2) \vee (S_3 \wedge S_4) \tag{4.7}$$

for SiPMs S_1 through S_4. To improve trigger purity we tried to change the firmware to trigger on the coincidence of all four fibres in the TPC. Due to a firmware bug however this was not successful.

The light readout scheme described above was successfully used to trigger and record several thousand cosmic muon interactions with the ArgonCube pixel demonstrator, as will be explained in Section 5.1. However, when compared to a measurement triggered on the charge readout directly, it became apparent that the efficiency of this light readout was very poor. No quantitative measurement of the trigger efficiency was performed due to limitations in the experimental setup. Triggering on the charge readout was only possible using an oscilloscope because the used DAQ system was not capable of self-triggering. Therefore, the channel number was limited to four which would have enabled charge readout triggering only on a subset of the readout area. An external reference trigger source, such as a muon telescope, was not available during the measurements. After warming up the experiment, we discovered that all four fibres were damaged because the acrylic rings had fallen out of their mounting brackets and squeezed or even broken the fibres.

Another drawback of the design is the optical coupling between the acrylic rings and the LAr. A lot of light escapes from the rings and is lost because the refractive indices are very close. Many other low-volume light readout systems based on light guides have been developed for LAr [100–106], all suffering from the same problem. A dedicated light readout system for ArgonCube was developed at LHEP to address these issues.

4.12. ArCLight

Most of the following has been published in [9]. The ArgonCube Light readout system (ArCLight) is designed to minimise the occupied volume while maximising the area coverage of SiPMs. This is achieved by coupling them to a passive light collector. As mentioned above, principles based on full reflection on a polymer-LAr interface are not suitable. Instead, ArCLight is based on the light trapping principle of the Argon R&D Advanced Program at UniCamp (ARAPUCA) sensor [107]. ARAPUCA works by

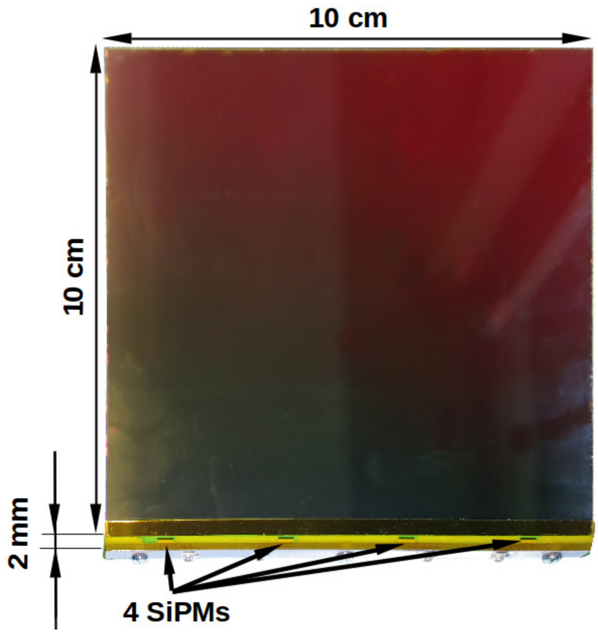

Figure 4.28.: 10 cm × 10 cm ArCLight prototype. Four SiPMs can be seen at the lower side, soldered to a narrow PCB providing coaxial connectors for signal readout. The rest of the sensor area is dielectric.

trapping the photons inside a cavity made of walls covered by highly reflective materials. One of the walls is formed of a dichroic film, a material transparent to certain wavelengths while highly reflective to others. On the outside this film is coated with TPB, which shifts the LAr scintillation light to the blue range, where the dichroic film is transparent. The inner surface of the film is covered by a second WLS, shifting the light to green, which is reflected by the dichroic film and therefore trapped inside the cavity. One or more SiPMs are mounted inside the cavity to collect the trapped photons. ArCLight improves the ARAPUCA design by replacing the empty cavity with a solid transparent polymer sheet doped with a WLS dye. This makes it substantially more robust and compact, especially when scaled up to larger areas.

A 10 cm × 10 cm ArCLight prototype is shown in Figure 4.28. The ratio of sensitive area to total area is 98 % with the remaining 2 % occupied by a PCB carrying four *Hamamatsu S13360-3050VE* SiPMs [108] with a sensitive area of 3 mm × 3 mm each.

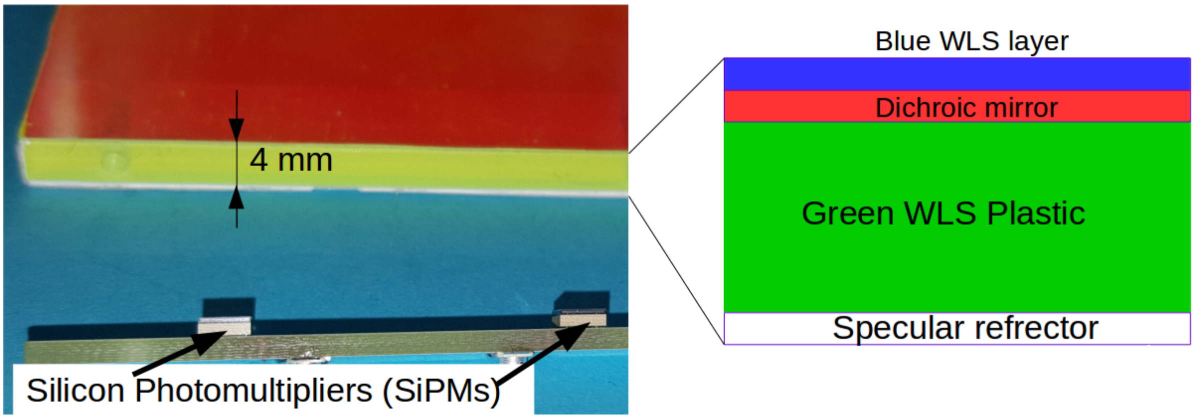

Figure 4.29.: ArCLight light collector cross-section near a corner. The structure is mechanically supported by a 4 mm thick WLS plastic. Its front is covered with a dichroic mirror film while the edges and the back face are covered with a dielectric specular reflector foil. The outer surface of the dichroic mirror is coated with TPB to shift the LAr VUV scintillation light to the blue range, where the dichroic film is transparent. At the bottom of the left picture two of the four SiPMs mounted to the carrier PCB are visible.

The inside of ArCLight is made of a 4 mm thick *Eljen Technology EJ-280* WLS plate [109]. Its sides are laminated with reflective films. The back face and the edges are covered with a *3M Vikuiti ESR* dielectric specular reflector foil [110] having $\approx 98\,\%$ reflectance in the visible light range. A *3M DF-PA Chill* dichroic mirror [111] covers the front face. It is transparent in the blue and has a high reflectance in the green spectral range. Both films are held in place by thin layers of transparent adhesive. To shift the VUV scintillation light produced in LAr to the blue transparent range of the dichroic mirror its outer surface is coated with TPB. A cross-section of the structure of ArCLight is depicted in Figure 4.29.

The Photon Detection Efficiency (PDE) was measured at room temperature using an ^{241}Am source, previously calibrated with a PMT. A PDE of 0.8 % to 2.2 % was measured. Figure 4.30 shows the PDE as a function of the position on the light collector, overlaid on a picture of the prototype for reference. The increase in PDE near the SiPMs is likely caused by photons hitting the SiPMs directly with no prior reflection from the

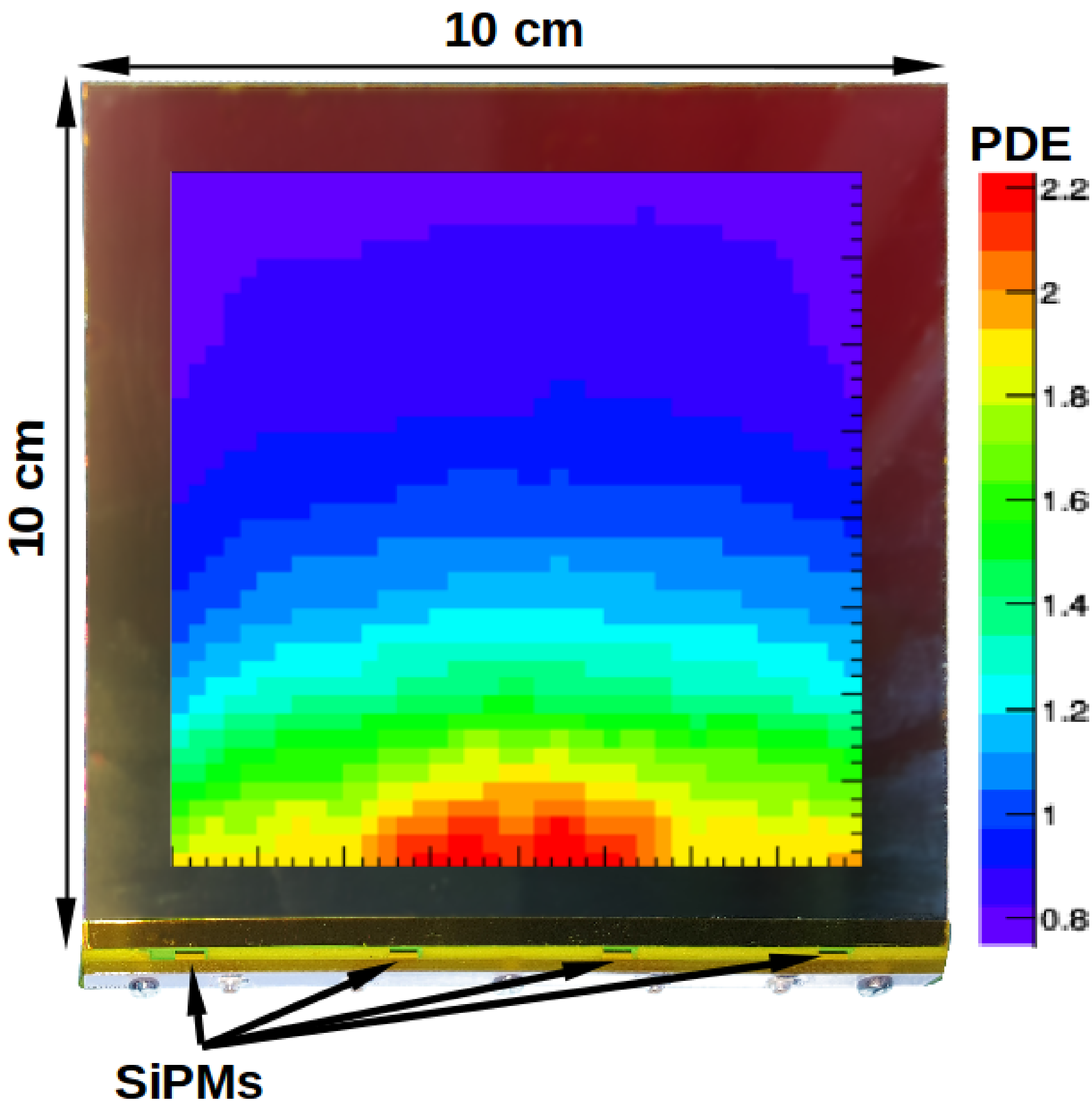

Figure 4.30.: Measured PDE for the 10 cm × 10 cm ArCLight prototype (background image), at room temperature. The PDE is given in %.

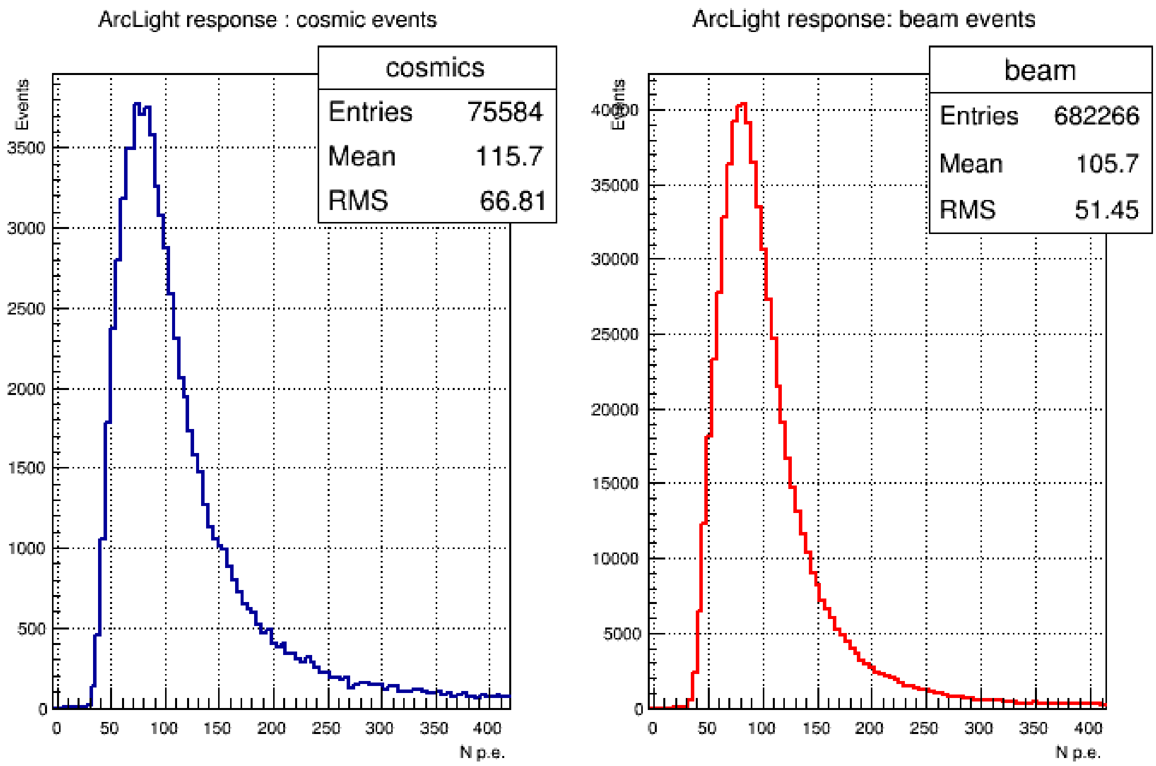

Figure 4.31.: Distribution of observed number of photo-electrons (N p.e.) per event by the ArCLight module in the PixLAr test beam demonstrator at FNAL. The response is shown for cosmic (blue) and beam events (red).

dichoic mirror. Due to the angular dependence of the dichroic mirror's reflectance about 30 % of the light is lost during the first reflection. Once reflected, a photon is trapped inside ArCLight because of the specular nature of the reflection on all faces. Additionally, the average PDE was calculated from theory to be $(0.7 \pm 0.4)\,\%$, in agreement with the measurements. More details on the calculations and the calibration of the measurement can be found in [9].

The measurements described above were performed at room temperature. A 43 cm × 15 cm ArCLight module was successfully operated at LAr temperatures in the PixLAr test beam demonstrator at FNAL, described in Section 5.3. Figure 4.31 shows the response for beam (red) and cosmic events (blue). Cosmic events yield a mean of 115.7 photo-electrons while beam events produce slightly less light with a mean of 105.7

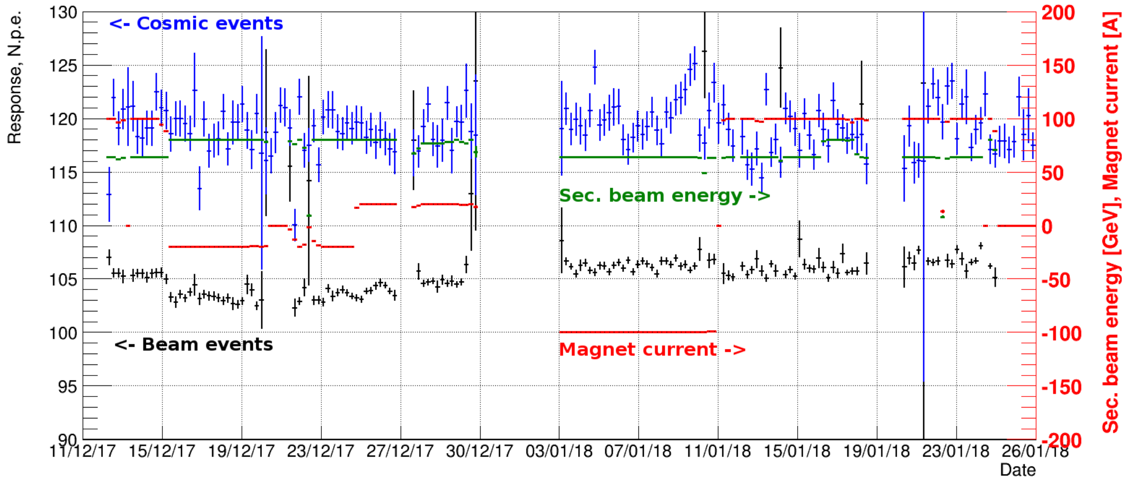

Figure 4.32.: Mean observed number of photo-electrons (N p.e.) per event by the ArCLight module in the PixLAr test beam demonstrator at FNAL, over several weeks. The response is shown for cosmic (blue) and beam events (black). For reference the secondary beam energy (green) and the bending magnet current (red) are shown.

photo-electrons. The time evolution of the mean photo-electron yield per event in beam (magenta) and cosmic ray (blue) mode is depicted in Figure 4.32. Secondary beam energy and bending magnet current, selecting the momentum range of the tertiary beam, are also plotted for reference. It can be seen that the photo-electron yield is approximately constant over several weeks. The jumps in the response to beam events can be explained by the switching between different beam configurations.

4.13. Light Readout Summary

Classic PMT-based light readout schemes for LArTPCs occupy large inactive volumes. SiPMs are much smaller but so is their sensitive area. I successfully used a cold SiPM-based light readout to trigger the charge readout of a pixelated LArTPC prototype. ArCLight is a new light readout system based on the ARAPUCA light trap principle to increase the sensitive area of SiPMs. Initial characterisations indicate a PDE of $\sim 1\,\%$.

It can be installed inside the field cage of a LArTPC due to its low volume and the dielectric nature of the light collector.

5. A Novel Implementation of the LArTPC Technology

While the theory and improvements of individual LArTPC subsystems were discussed in Chapter 4, this chapter presents the amalgamation of all my findings into a new LArTPC concept, ArgonCube, aligned to the needs of future LArTPC neutrino detectors. The results of the ArgonCube pixel demonstrator are presented, alongside a reconstruction framework I developed, yielding fully reconstructed 3D cosmic muon tracks. Both have been published in [10, 11]. Afterwards, the ArgonCube modular LArTPC concept is introduced.

5.1. ArgonCube Pixel Demonstrator

This section describes the results obtained from the pixel demonstrator for the ArgonCube project (see Chapter 5.4). A particular focus is put on the reconstruction of the recorded cosmic ray events.

The pixelated anode plane, shown in Figure 5.1, was produced as a conventional PCB. It implements the ROI-based analogue multiplexing scheme introduced in Section 4.5. The pixelated area is 100 mm across, the pixels are formed of 900 µm vias with a pitch of 2.54 mm. An inductive focusing grid surrounds the pixels, it is made from 152.4 µm

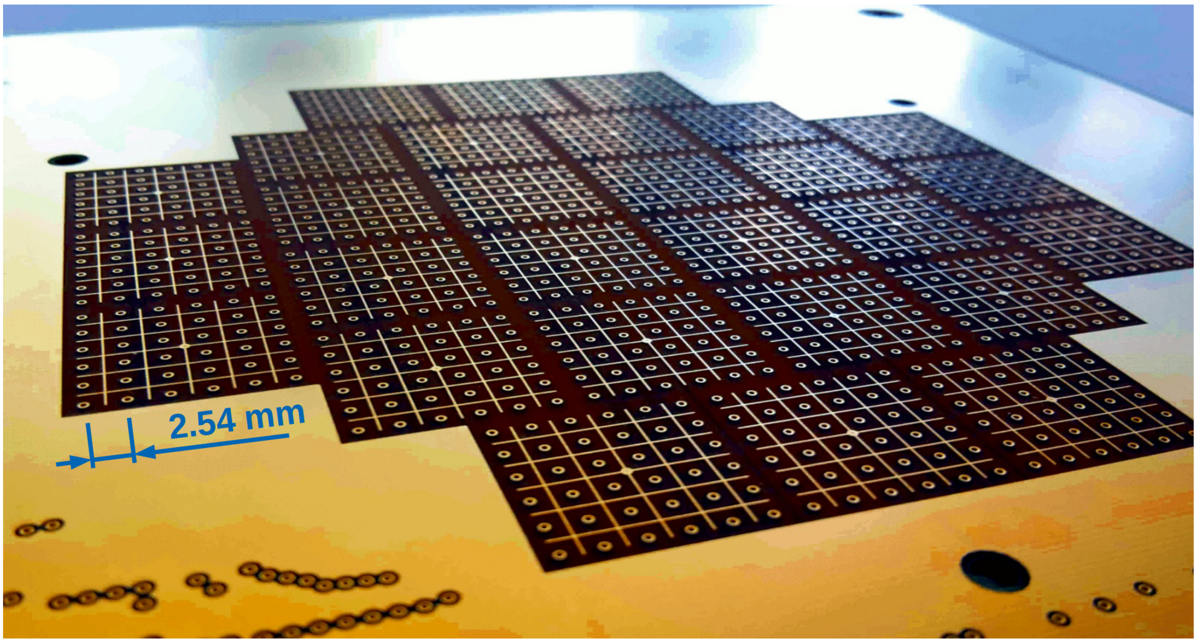

Figure 5.1.: First (high-capacitance) version of the pixelated anode PCB. The pixelated readout area is 100 mm in diameter. Each charge collection pixel is a 900 µm via, at a pitch of 2.54 mm. Inductive focusing grids formed of 152.4 µm copper traces surround the pixels. There are 28 inductive focusing grids with 36 pixels per region, a total of 1008 pixels.

copper traces split into 28 regions. There are 6×6 pixels per region, giving a total of 1008 pixels.

Vias were used for pixels instead of pads in order to minimise capacitance. As detailed in Section 4.7, it is important to minimise capacitance of a charge readout. To further minimise parasitic capacitances the PCB design was optimised by removing unnecessary ground planes, routing signal tracks outside necessary ground planes, and increasing the thickness of the PCB to 3.5 mm from an initial 1.75 mm. The resulting capacitance at each pixel is ≈ 65 pF (see Section 4.8).

The pixels are directly connected to the preamplifiers while the inductive focusing grids are decoupled via 10 nF capacitors. Additionally, the bias voltage is filtered at the input by another 10 nF and 10 MΩ. The full schematic of the bias circuit is depicted in Figure 5.2.

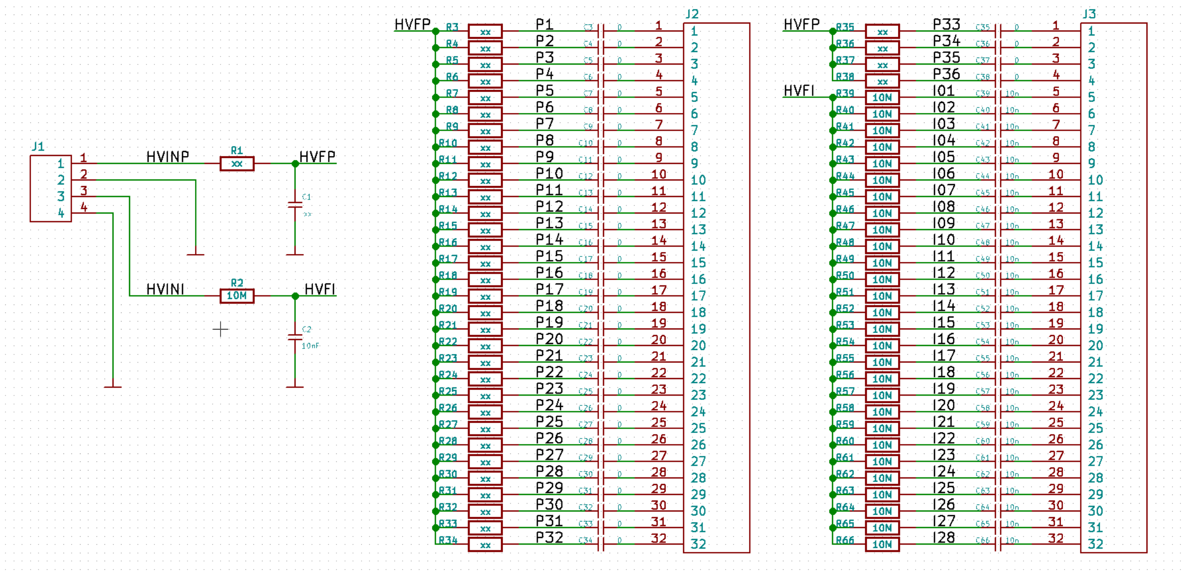

Figure 5.2.: Schematic of the bias circuit for the ArgonCube pixel demonstrator PCB. On the left the pin header connected to the bias HV power supply is shown. In the middle and on the right are the connections to the pixels and inductive ROI grids. The connections to the preamplifier inputs are located at the positions of labels P1–P36 (pixels) and I1–I28 (ROIs). For simplicity and universality the same circuit was used for both pixels and ROIs even though only the inductive ROI grids were biased for the measurements described here. Therefore, the ROIs are connected as depicted (R2 and R39–R66, C2 and C39–C66). The pixels are directly connected to the preamplifiers by leaving R3–R38 unpopulated and replacing C3–C38 by 0 Ω resistors because no pixel bias is needed. Additionally, R1 is 0 Ω and C1 unpopulated, and all unused PCB traces are grounded by connecting pin 1 of J1 to ground.

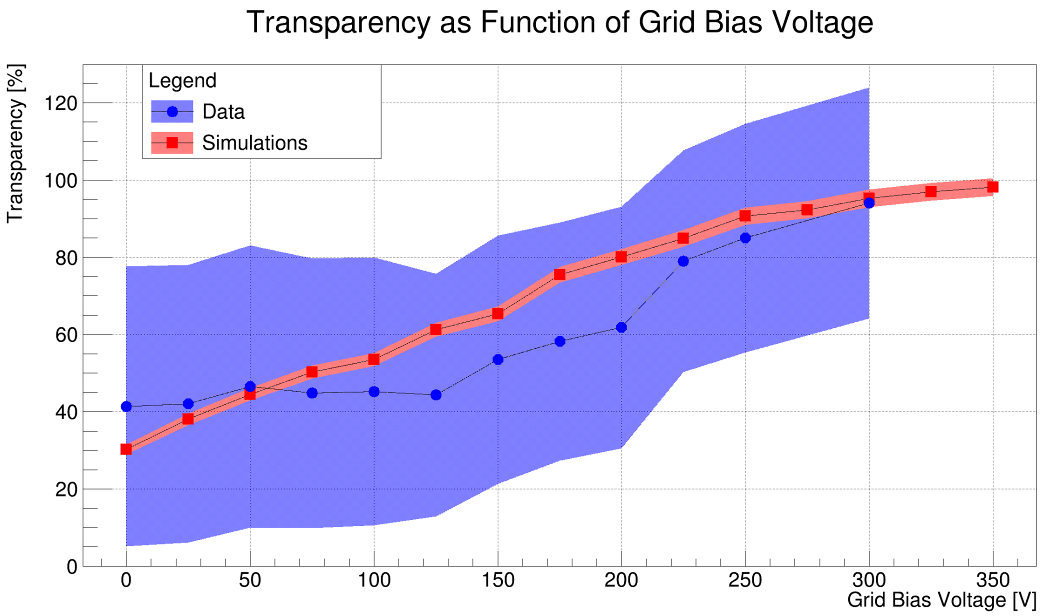

Figure 5.3.: Measured and simulated transparency versus bias voltage of the ArgonCube pixel demonstrator. [112]

The bias on the inductive focusing grids has to be sufficient to allow full charge transparency (all charge collected by the pixels), yet low enough to minimise any risk of damaging the cold coupling capacitors. It was increased incrementally until transparency was observed at 300 V. Simulations suggest this was only 95 % transparency, with 100 % at 350 V (see Figure 5.3). The simulations available at the time of the measurement contained a bug resulting in an underestimation of the bias voltage required for full transparency. During the measurements the bug became apparent and full transparency had to be estimated by looking at live data from the detector. Due to the limited accuracy of this method measurements were not taken up to the bias voltage for full transparency suggested by the (corrected) simulation. [112]

The pixel demonstrator TPC, shown in Figures 5.4 and 5.5, is cylindrical with an inner diameter of 101 mm and a 590 mm drift length. The TPC operated with a drift field of $1\,\mathrm{kV\,cm^{-1}}$, corresponding to a total drift time of 281 µs at $2.1\,\mathrm{mm\,\mu s^{-1}}$ [113].

The field-cage consists of aluminium rings supported by clear acrylic rings, with a

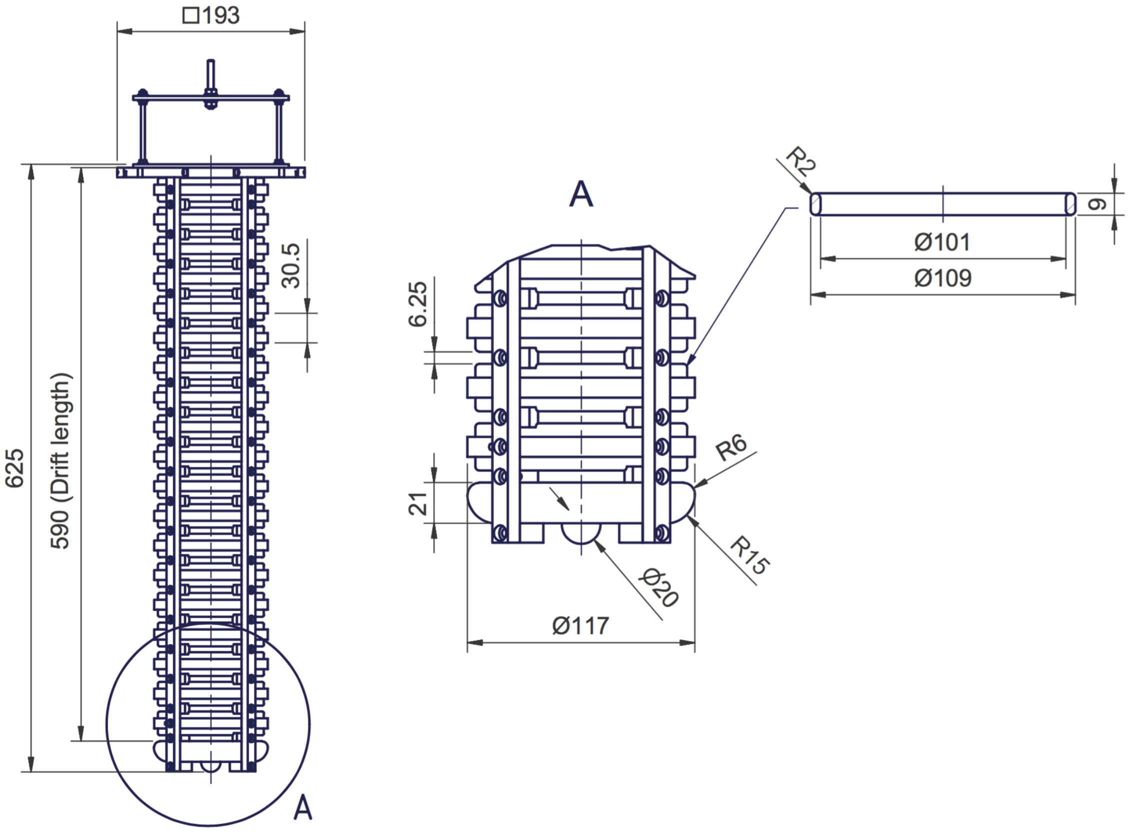

Figure 5.4.: Engineering drawing of the pixel demonstration TPC; 590 mm drift length; 6.25 mm field cage spacing; 101 mm internal diameter.

cathode formed of a brass disc. The dimensions of the field-cage and cathode are shown in Figure 5.4. Alternating acrylic rings are split to allow for the circulation of purified LAr within the TPC volume. Four square section PolyAmide-Imide (PAI) uprights support the cathode and field cage, with PolyEther Ether Ketone (PEEK) screws fixing the pillars to the acrylic rings. The four PAI uprights connect to a PAI frame which supports the anode plane and the light readout SiPMs, see Figure 5.5.

The resistive divider consists of a chain of 100 MΩ *Vishay ROX100100MFKEL* metal oxide resistors [114]. Each resistor is soldered to its neighbour and fixed to the field cage at each joint with an M3 screw.

The acrylic rings provide the light collection; their inner surfaces are machine-polished and coated with the WLS TPB. 1 mm diameter WLS fibres couple the acrylic rings to four SiPMs mounted close to the anode (see Figure 5.5). The SiPMs and their front-end electronics were adapted from those developed at LHEP for the CRTs used in MicroBooNE and SBND [97, 98]. A more detailed description of the light readout system is given in Section 4.11.

The pixel demonstration TPC is housed in a double-bath vacuum-insulated cryostat with the outer bath open to atmosphere. A diameter of 50 cm and a height of 110 cm give an inner volume of $\approx 200\,\mathrm{l}$ of LAr. This is the same cryostat that was used for the HV studies described in Section 4.1. The LAr filtering method is the same as described in [65], with LAr filtered first on filling through a pair of Oxysorb-Hydrosorb filters, and then recirculated through a single custom-made filter containing both activated copper and silica gel. LAr purity is estimated to be in accordance with [65], with impurity concentrations ~ 1 ppb of oxygen-equivalent, which corresponds to a charge lifetime of $(290 \pm 30)\,\mu\mathrm{s}$.

The Crystalline PolyEthylene Terephthalate (PET-C) HV feedthrough capable of potentials as high as -130 kV remains unchanged from the breakdown studies (Section 4.1). I added a low-pass filter between the power supply and feedthrough, which consists of an 800 pF decoupling capacitor grounded between two 100 MΩ resistors connected in series; i.e. a Resistor Capacitor (RC) low-pass filter with an additional protection resistor at the output. For proper insulation the filter circuit is submerged in transformer oil.

Dedicated noise data was taken to assess the SNR, employing a 5 Hz random trigger. Drift, focusing, and SiPM bias voltages were turned off for these measurements. The data of 5000 events was combined. Subsequently, all pixel and ROI channels were combined separately and filled into respective amplitude distribution histograms. Finally, the standard deviation of the noise was calculated by fitting a Gaussian to the amplitude distribution. This value was used to calculate the SNR for pixel and ROI channels

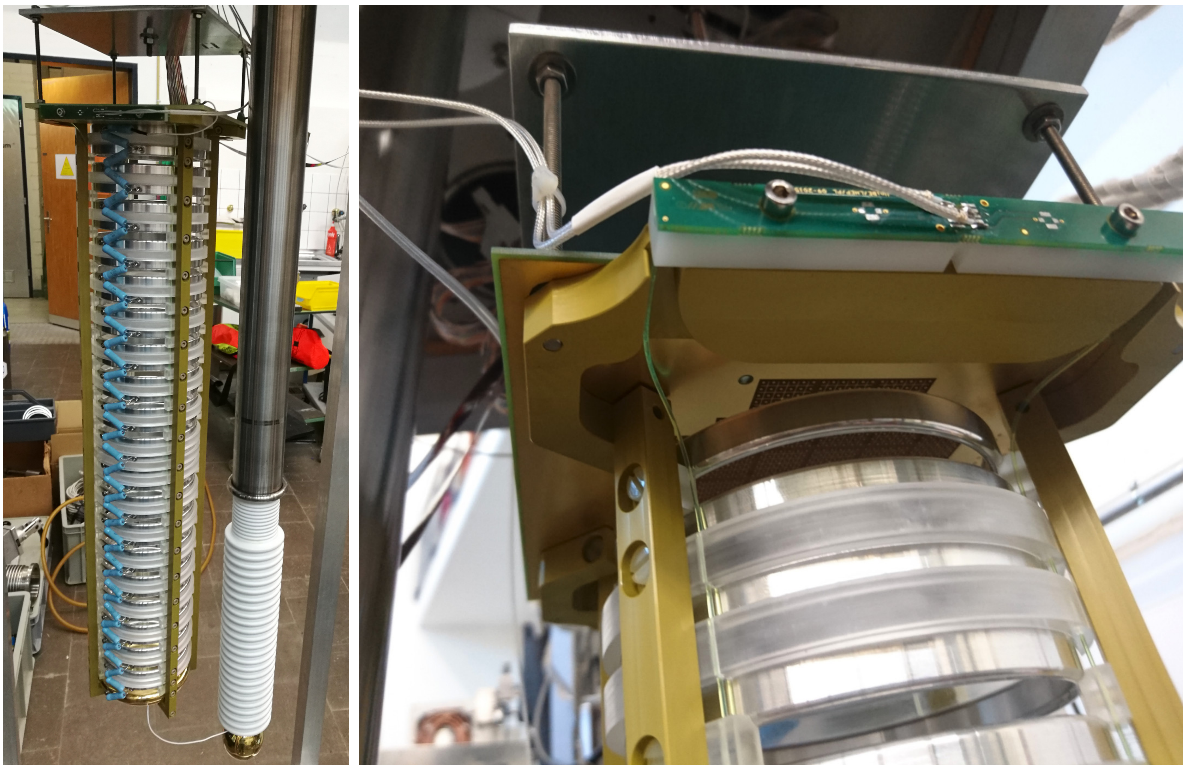

Figure 5.5.: Left: Photograph of the pixel demonstrator TPC at LHEP, with the HV feedthrough. Right: Close-up of the light collection system, showing WLS fibres coupling the SiPMs to the TPB-coated light guides.

Table 5.1.: SNR values obtained from Equation (5.1). The signal was calculated from theory assuming a MIP at the readout plane or cathode, respectively. The average equivalent noise charge was obtained from measurements for pixel and ROI channels, respectively.

Channel	MIP at	SNR
Pixel	Readout plane	14
Pixel	Cathode	5.5
ROI	Readout plane	16
ROI	Cathode	6.1

according to

$$\mathrm{SNR} = \frac{S}{\sigma}, \tag{5.1}$$

where S is the signal and σ is the noise standard deviation from the Gaussian fit. As can be seen in the top plot in Figure 5.6 (and also 4.23), one of the pixel channels is significantly noisier in comparison to the others, likely caused by a broken preamplifier. Therefore, this channel was blinded for the SNR calculations. The resulting equivalent noise charge is $1095\,e$ for the pixel channels and $982\,e$ for the inductive ROI channels. The noise amplitude distributions are shown in Figure 4.23.

The signal S is often taken for a MIP as this is at the lower end of the signal range interesting for neutrino physics. Obtaining a clean MIP signal from experimental data requires a calibrated reconstruction which was not available at the time of writing. Therefore, the MIP signal is estimated from theory assuming an energy loss of $2.1\,\mathrm{MeV\,cm^{-1}}$ (see Section 2.5). This can be converted to charge loss using the energy required to produce one electron-ion pair from Table 3.1: $W_\mathrm{i} = 23.6\,\mathrm{eV}\,e^{-1}$. Additionally, charge recombination, diffusion, and lifetime need to be taken into account (see Section 3.1). The recombination factor was measured by the Imaging Cosmic And Rare Underground Signals (ICARUS) [115] and Argon Neutrino Test (ArgonNeuT) [116] experiments, and found to be $R_\mathrm{c} \approx 0.7$ for a drift field of $1\,\mathrm{kV\,cm^{-1}}$. With

ARGONTUBE [62] LHEP measured a transverse diffusion coefficient $D_\mathrm{T} = 5.3\,\mathrm{cm}^2\,\mathrm{s}^{-1}$ at $0.25\,\mathrm{kV\,cm}^{-1}$ while Gushchin et al. [117] report a value of $D_\mathrm{T} = 13\,\mathrm{cm}^2\,\mathrm{s}^{-1}$ at $1\,\mathrm{kV\,cm}^{-1}$. Even using the more conservative value results in a transverse spread of $\approx 0.9\,\mathrm{mm}$ for the pixel demonstrator drift time of $t = 281\,\mathrm{\mu s}$, according to Equation (3.2). This value lies well below the pixel pitch of $d_\mathrm{p} = 2.54\,\mathrm{mm}$. Considering that the longitudinal component is smaller than the transverse [60], diffusion is neglected completely for these calculations. Finally, the lifetime of $290\,\mathrm{\mu s}$ results in the reduction of charge by a factor of ≈ 0.38 over the full drift distance (Equation (3.3)). Combining this, the signal is

$$S = \frac{\mathrm{d}E}{\mathrm{d}x}_{\mathrm{MIP}} \frac{R_\mathrm{c} d_\mathrm{p}}{W_\mathrm{i}} = 15\,821\,e \tag{5.2}$$

for a charge deposited adjacent to the readout plane, and $S = 6004\,e$ for a charge deposited adjacent to the cathode. Table 5.1 lists the SNR values obtained from these signal values and the aforementioned measured equivalent noise charge, using Equation (5.1).

5.2. 3D Track Reconstruction

To demonstrate 3D track reconstruction several thousand cosmic ray events were collected with the ArgonCube pixel demonstrator described in Section 5.1, many of which are MIPs, mostly muons. The pixelated charge readout was triggered by the cold SiPM light readout described in Section 4.11.

Official event reconstruction tools were only available for LArTPCs read out by wire planes[1]. Therefore, I developed a new framework from scratch[2]. The reconstruction procedure comprises five steps: noise filtering, hit finding, hit matching, ambiguity rejection, and track fitting. These steps are explained in the following and depicted in Figures 5.6 through 5.10, all taken from the same MIP (cosmic muon) event.

[1] `http://larsoft.org`
[2] `https://github.com/70rc/pixy_roimux`

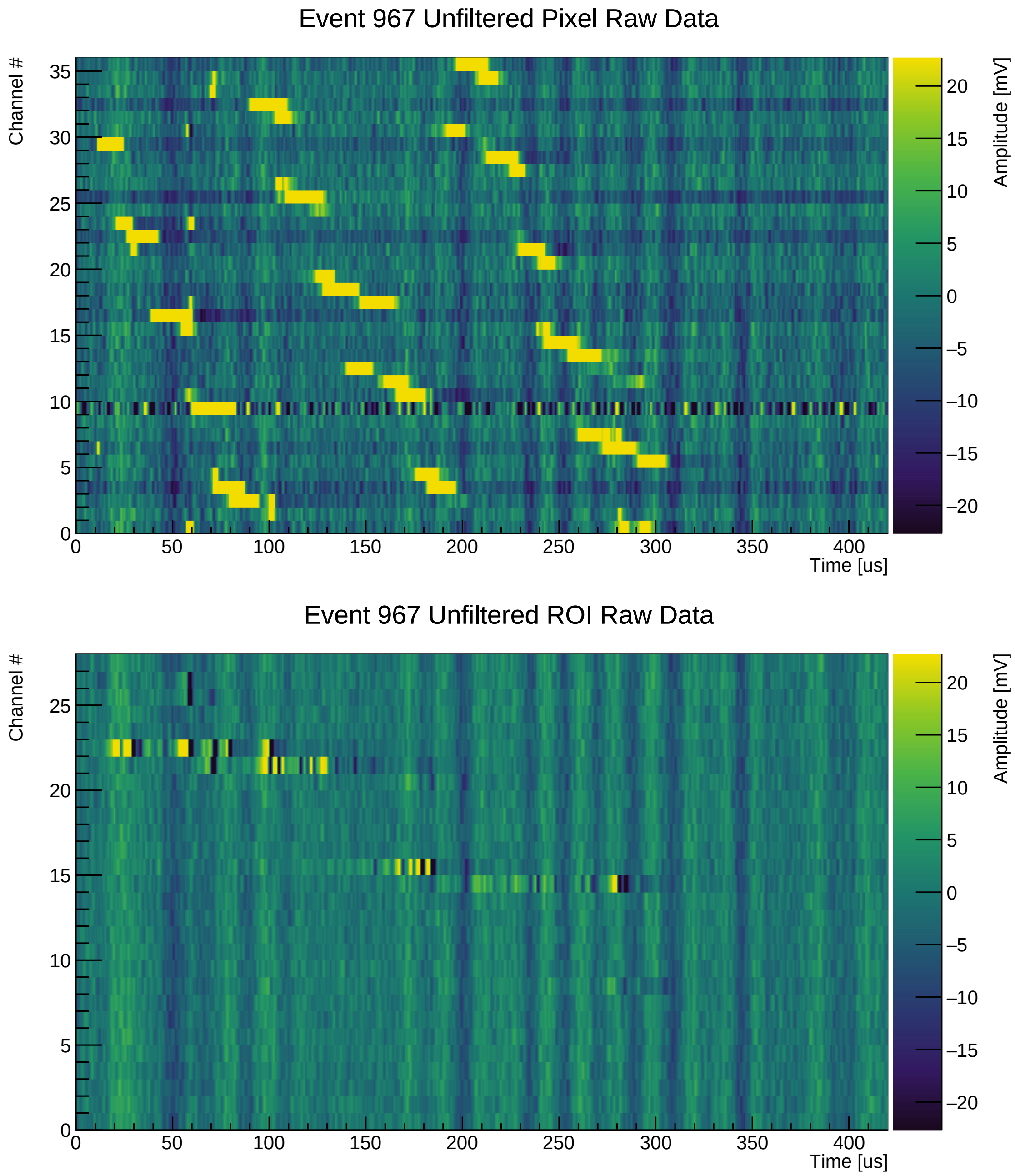

Figure 5.6.: Unfiltered raw data of a typical MIP event (the same for Figures 5.6 through 5.10). The top plot shows pixel data while the bottom plot shows ROI data. Note that the colour scale was adjusted to highlight the charge signals. Therefore, most signal peaks are above/below the maximum/minimum of the colour scale. The full range of a typical signal can be seen in Figure 5.8.

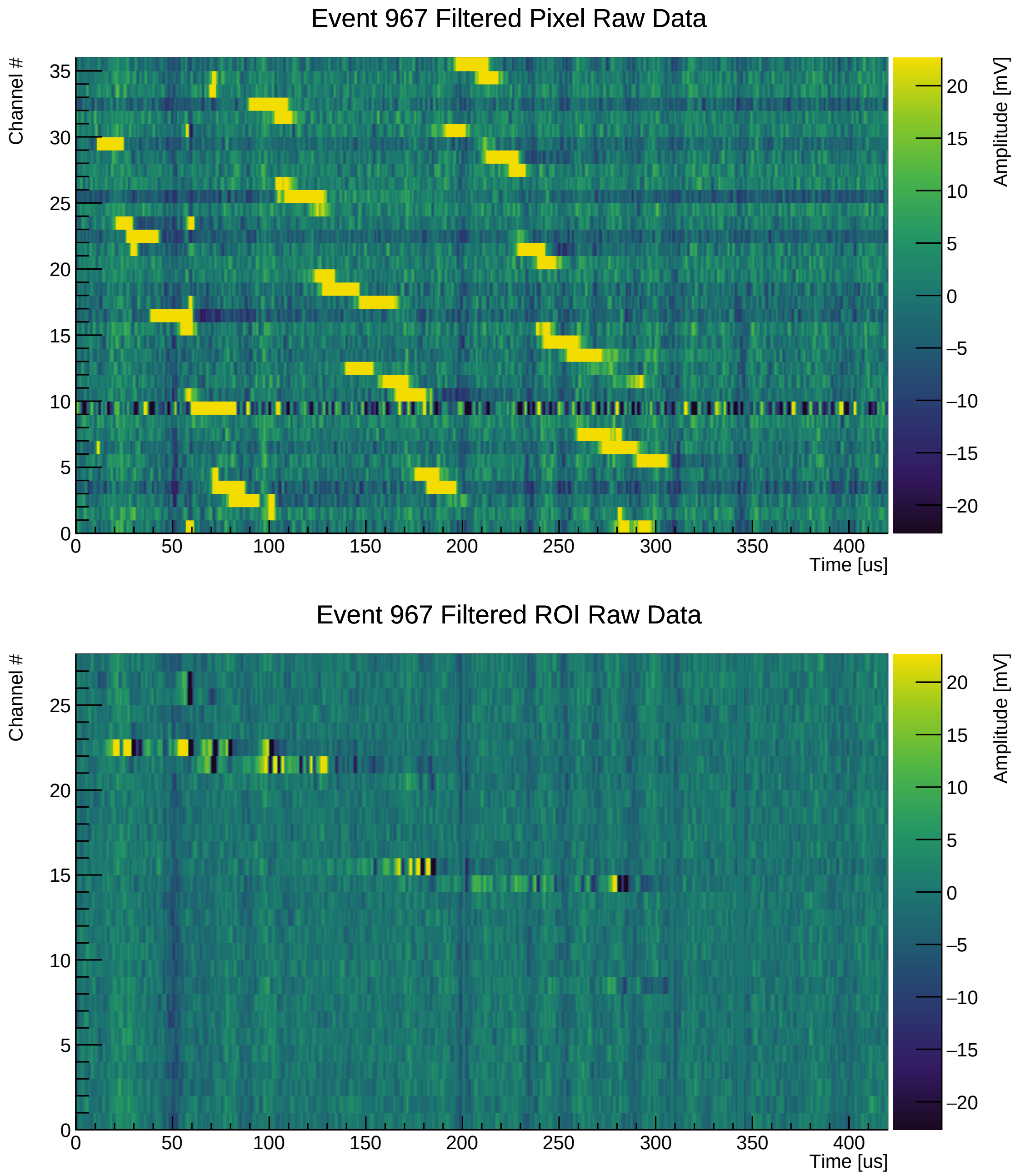

Figure 5.7.: Filtered data of a typical MIP event (the same for Figures 5.6 through 5.10). The top plot shows pixel data while the bottom plot shows ROI data. Note that the colour scale was adjusted to highlight the charge signals. Therefore, most signal peaks are above/below the maximum/minimum of the colour scale. The full range of a typical signal can be seen in Figure 5.8.

In the first step a noise-filtering algorithm is applied to the raw data. As can be seen from Figure 5.6, the noise is largely correlated across all the channels. This common-mode correlation can be exploited by the noise filter algorithm. The following is done separately for the all pixel and ROI channels of each event. Similarly to the SNR calculation all samples are filled into an amplitude distribution histogram for each channel and subsequently fitted with a Gaussian. A noise band is defined per channel with its centre equal to the mean of the Gaussian and its width equal to the standard deviation multiplied by a tunable scaling factor. The amplitudes of all channels within the corresponding noise band are then averaged for each sample. Finally, this average is subtracted from each channel at the corresponding sample. This technique was chosen because it effectively suppresses the dominating common-mode noise. At the same time spurious signals, produced by actual charge collection signals distorting the average, are kept to a minimum by only accepting values within the noise band. The effectiveness of the filtering can be seen in Figure 5.7, which shows the same data as Figure 5.6 post filtering.

The second step applies a recursive pulse finding algorithm. Three types of thresholds are used: peak, edge, and zero-crossing thresholds. The zero-crossing threshold is equal to the noise mean, as defined above. Peak and edge thresholds are calculated by adding the noise standard deviation multiplied by a respective scaling factor to the noise mean. The following is performed for each channel independently. Noise mean and standard deviation are recalculated from the noise-filtered data. Using these all thresholds are calculated. Then, the sample with the highest amplitude is found. If it is below the peak threshold, the process stops and proceeds to the next channel. Otherwise, the pulse is scanned in positive and negative directions until it crosses the edge threshold in both directions. Next, the whole pulse is deleted from the data, and the process starts over with finding the new maximum sample and checking it against the peak threshold.

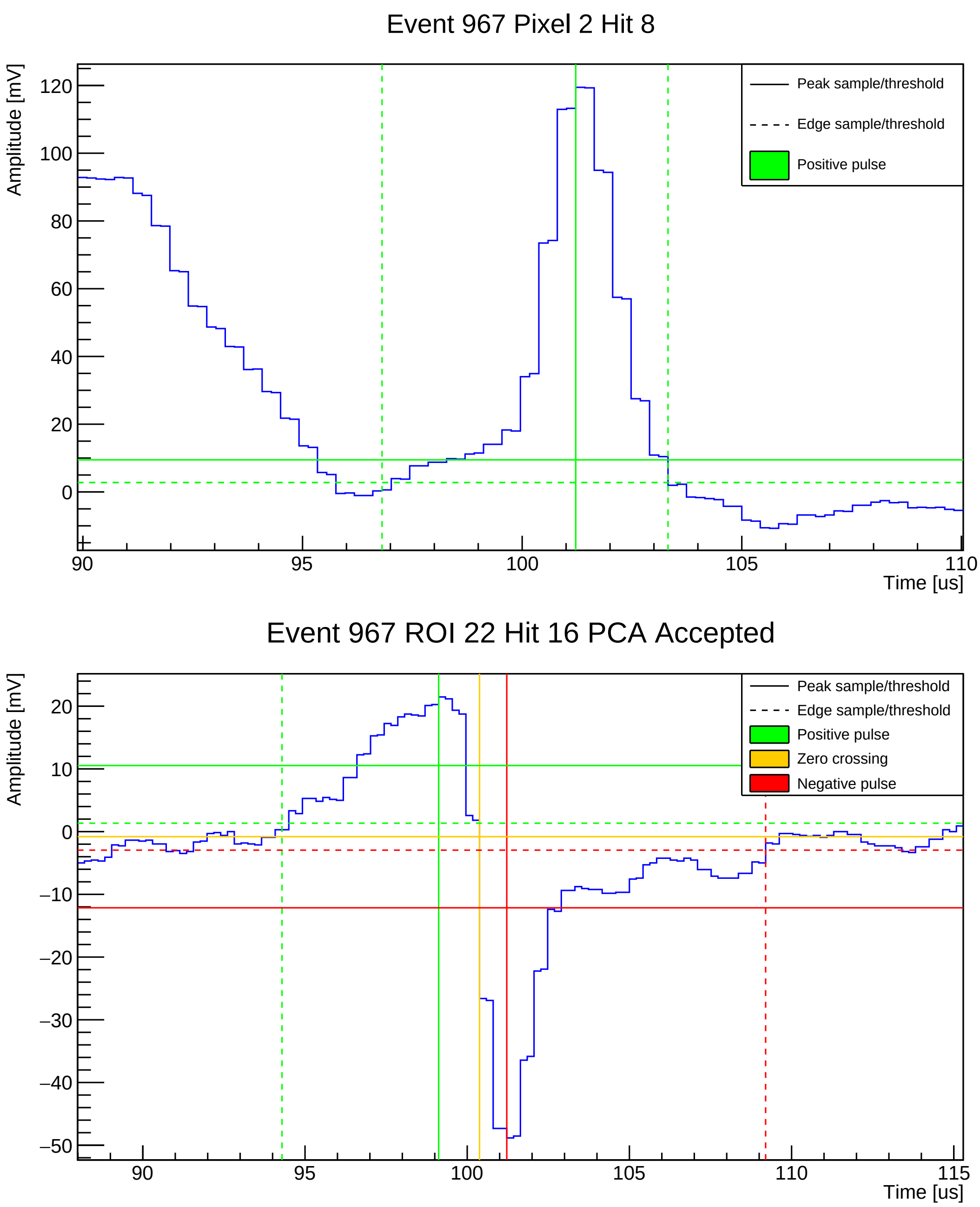

Figure 5.8.: Pulse shapes of a single pixel (top) and ROI (bottom) hit of a typical MIP event (the same for Figures 5.6 through 5.10). Superimposed are the thresholds of the hit finder algorithm. Horizontal lines represent thresholds: solid is the minimum threshold required to be crossed for a pulse to be detected, and dashed are the thresholds used to detect the pulse edges. Vertical lines represent the corresponding detected peak/edge samples. Colour indicates a positive (green) or negative (red) pulse, or a zero crossing (yellow).

For stability reasons the peak threshold relative to noise levels is compared against an absolute peak threshold and the higher of the two is applied. The search is extended to the negative pulse for the bipolar ROI pulses, using the zero-crossing threshold and respective negative peak and edge thresholds. The different thresholds employed and samples found by this process are illustrated in Figure 5.8.

Identified pulses are then combined to 3D hit candidates by matching pixel pulses to coincident ROI pulses. Looking at Figure 5.8, a pixel and ROI pulse are matched if their time slices, defined by the vertical dashed lines, overlap. This matching algorithm minimises the number of missed hits at the price of a rather high number of ambiguous matches.

To resolve the ambiguities a Principal Component Analysis (PCA) is applied to the 3D space points in a fourth step. This technique is well established and described in literature, e.g. [118]. Therefore, it is only briefly summarised here. The basic idea is to calculate three orthogonal eigenvectors of the 3D space point cloud. A graphic interpretation of these eigenvectors are the three axes of an ellipsoid fitted to the data points. If the points form a track, one of these eigenvectors will have a much higher eigenvalue than the other two. This eigenvector is taken as an estimate for the track direction. Ambiguities can be resolved by selecting the hit candidates closest to the track estimate. A similar procedure is used to recursively reject outliers, by forming a cylinder around the track estimate with a radius proportional to the second largest eigenvalue. All hits outside the cylinder are rejected. The outlier rejection is recursively repeated for an optimal result. In a later stage of reconstructing more complex events this algorithm can potentially be used to cluster 3D space points in order to separate multiple tracks. The PCA ambiguity rejection is illustrated in Figure 5.9.

The final step consists of a Kalman filter. For this the well-established Generic track-Fitting toolkit (GENFIT) [119, 120] was used. Ionisation losses and MCS in LAr are

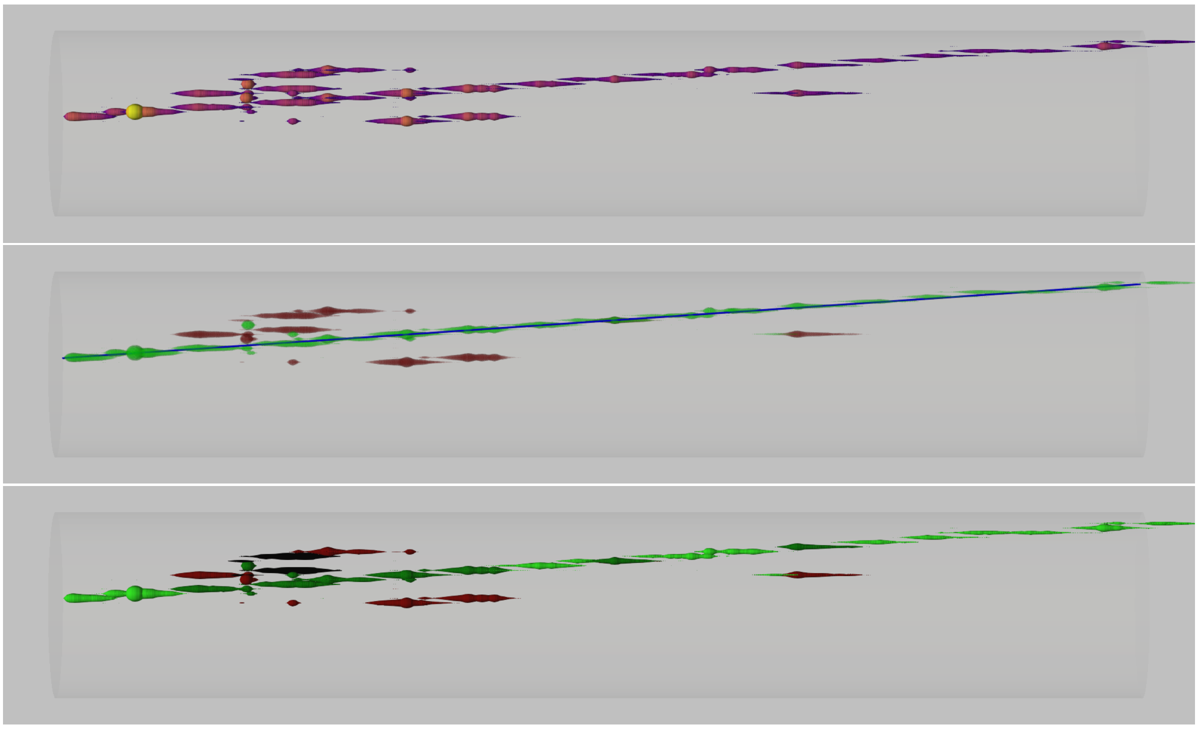

Figure 5.9.: Reconstructed 3D hit candidates from the hit finder. The passing particle is most likely a cosmic μ (the same for Figures 5.6 through 5.10) entering from the left. Drift direction is from right to left. Pulse shape is encoded as thickness. In the top plot colour codes the amount of collected charge. The middle plot illustrates the ambiguity resolution employing a PCA. Green hit candidates are accepted while dark red ones are rejected. This is achieved by selecting the candidate closest to the eigenvector of the point cloud with the largest eigenvalue, represented by the blue line. In the bottom plot the degree of ambiguity is colour-coded: Light green are unambiguous hits while dark green are selected candidates of ambiguous hits. Dark red through black are rejected candidates of ambiguous hits, where darker colour represents a higher degree of ambiguity. As this is quite a clean track with only a few short δ rays, there are no outliers rejected other than the multiplexing ambiguities. Interactive versions of these event displays are available online[a].

[a] https://70rc.github.io/ac_pix_3d

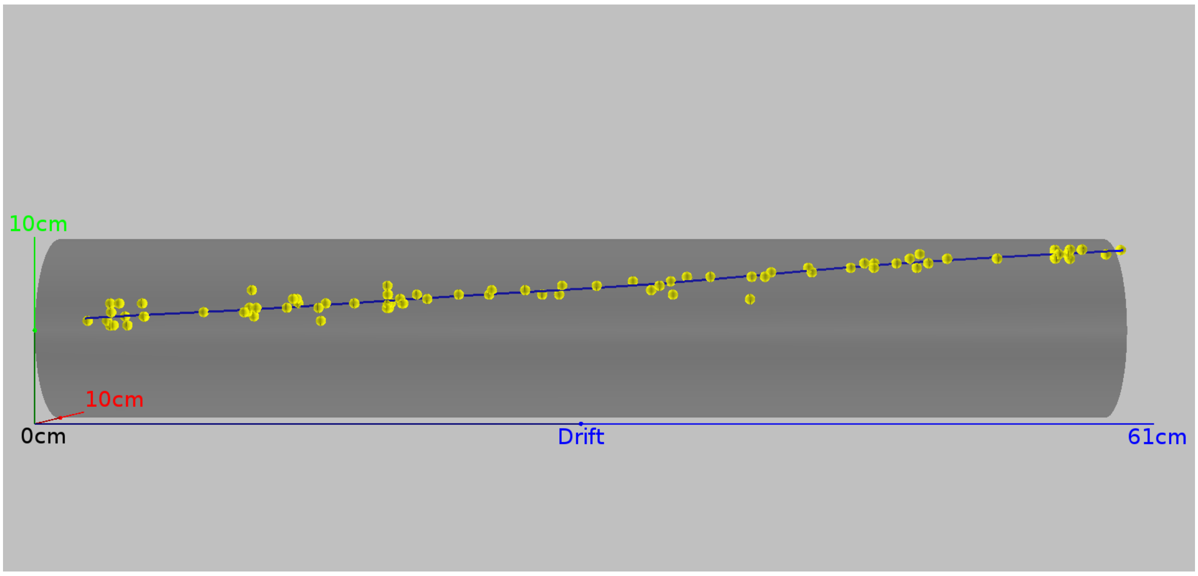

Figure 5.10.: Track fitted by the Kalman filter. The shaded volume represents the TPC. The passing particle is most likely a cosmic μ (the same for Figures 5.6 through 5.10) entering from the left. Drift direction is from right to left. The yellow points are the input to the Kalman filter, the accepted hits from the PCA. Blue is the output, a fitted track taking into account ionisation losses and MCS in LAr.

taken into account. The particle is assumed to be a minimum-ionising muon with an initial momentum of $260\,\mathrm{MeV}\,c^{-1}$ in the direction of the track estimate from the PCA. A recursive algorithm capable of dealing with outliers was chosen, a so-called *deterministic annealing filter*. It rejects outliers by assigning successively lower weights to them with each recursion step. For more details see the respective publications [119, 120]. The resulting track is shown in Figure 5.10.

Technically, the Kalman filter would be capable of fitting the particle momentum or even particle type to the data. At the time of writing this is not implemented yet. In particular, the momentum stays roughly at the initial guess of $260\,\mathrm{MeV}\,c^{-1}$, assuming a minimum ionising muon in LAr. A potential explanation for this is that the resolution of the detector is too low to estimate momentum from MCS. Another explanation might be the hit finder missing hits due to non-optimal tuning. Proper tuning of the reconstruction requires a full simulation chain of the detector which is not yet available. Using data to tune the reconstruction is prone to the introduction of circular biases. On the other hand, most of the difficulties emerge from the multiplexing ambiguities and their resolution. While the presented almost full 3D readout has already reduced the reconstruction complexity compared to a classical wire readout, an ambiguity-free readout will make reconstruction another big step easier by completely eliminating the need to resolve ambiguities. My results described above triggered the development of the LArPix pixel readout electronics at LBNL, described in Section 4.9.

5.3. PixLAr

After my successful test with cosmic muons at LHEP, a scaled-up prototype of the pixel readout, employing the same multiplexing scheme, was built for a beam exposure in the LArIAT experiment [85] at FNAL. LArIAT consists of the former ArgonNeuT [121] cryostat and LArTPC placed in a test beam. The tertiary beam line produces mainly pions and protons, as well as electrons, muons, and kaons at a lower rate. Their momentum spectrum can be tuned from $0.2\,\mathrm{GeV}\,c^{-1}$ to $2.0\,\mathrm{GeV}\,c^{-1}$ by means of bending magnets. 550 l of LAr are contained in a cylindrical cryostat. It houses a TPC with 47 cm drift length and a $40\,\mathrm{cm} \times 90\,\mathrm{cm}$ readout plane parallel to the beam direction, resulting in an active volume of 170 l. For the pixel test, called PixLAr, the original wire planes were replaced by a 120×240 pixel readout. At 3 mm pitch this gives an instrumented area of $36\,\mathrm{cm} \times 72\,\mathrm{cm}$. The readout plane had to be split into two mirror-symmetric, electrically independent half planes due to constraints from the PCB manufacturer. Each 120×120 pixel half plane is divided into 8×15 ROIs of 15×8 pixels each. The ROIs are oriented with their longer dimension parallel to the beam direction to reduce the multiplexing ambiguities. One of the noise mitigation measures implemented for the LHEP pixel demonstrator was to use the same differential warm signal path as used by LArIAT. Therefore, the charge readout electronics used in PixLAr are quite similar

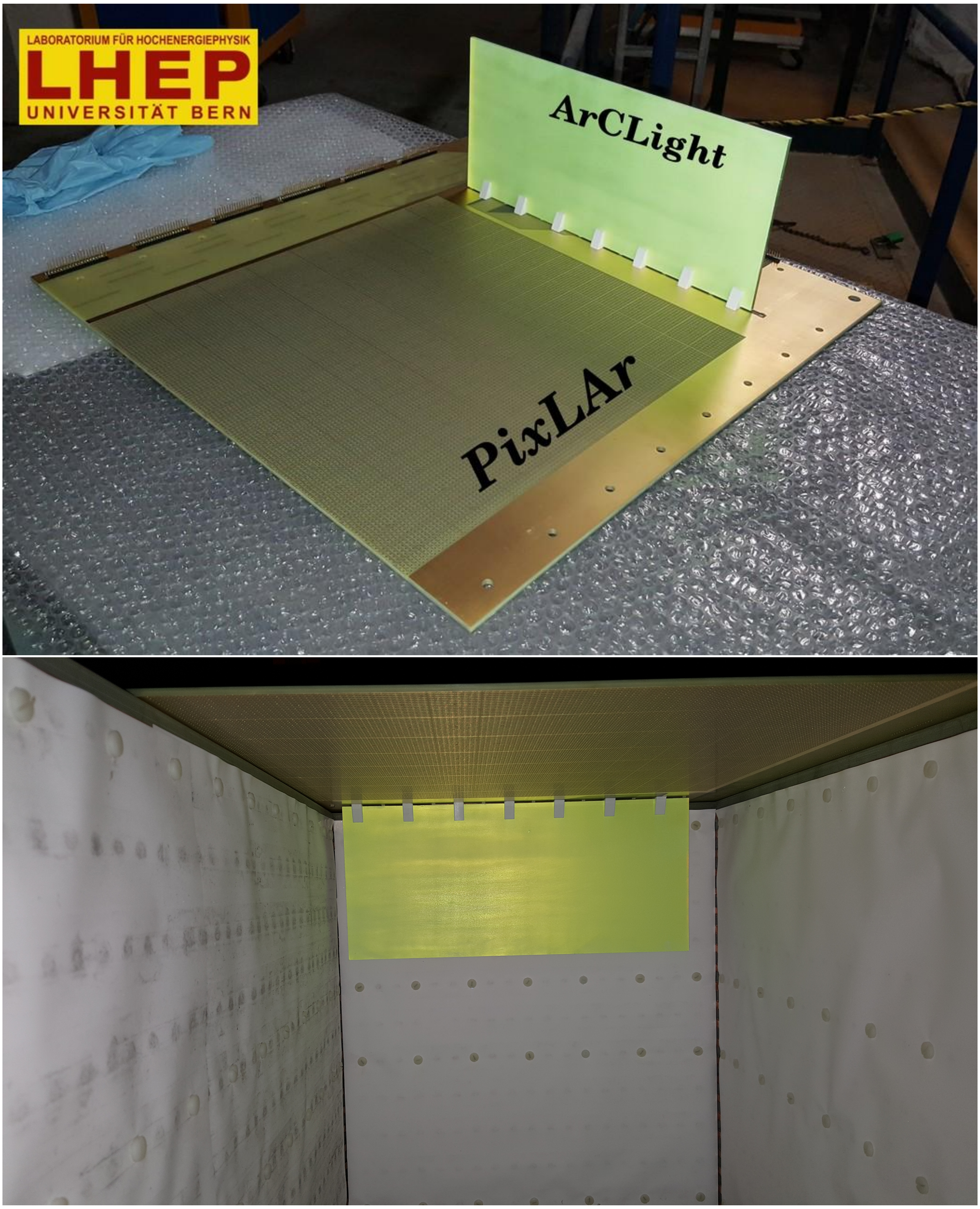

Figure 5.11.: One of the two PixLAr readout half planes with the ArCLight module attached. The bottom picture shows the inside of the LArIAT TPC with the PixLAr ArCLight assembly installed.

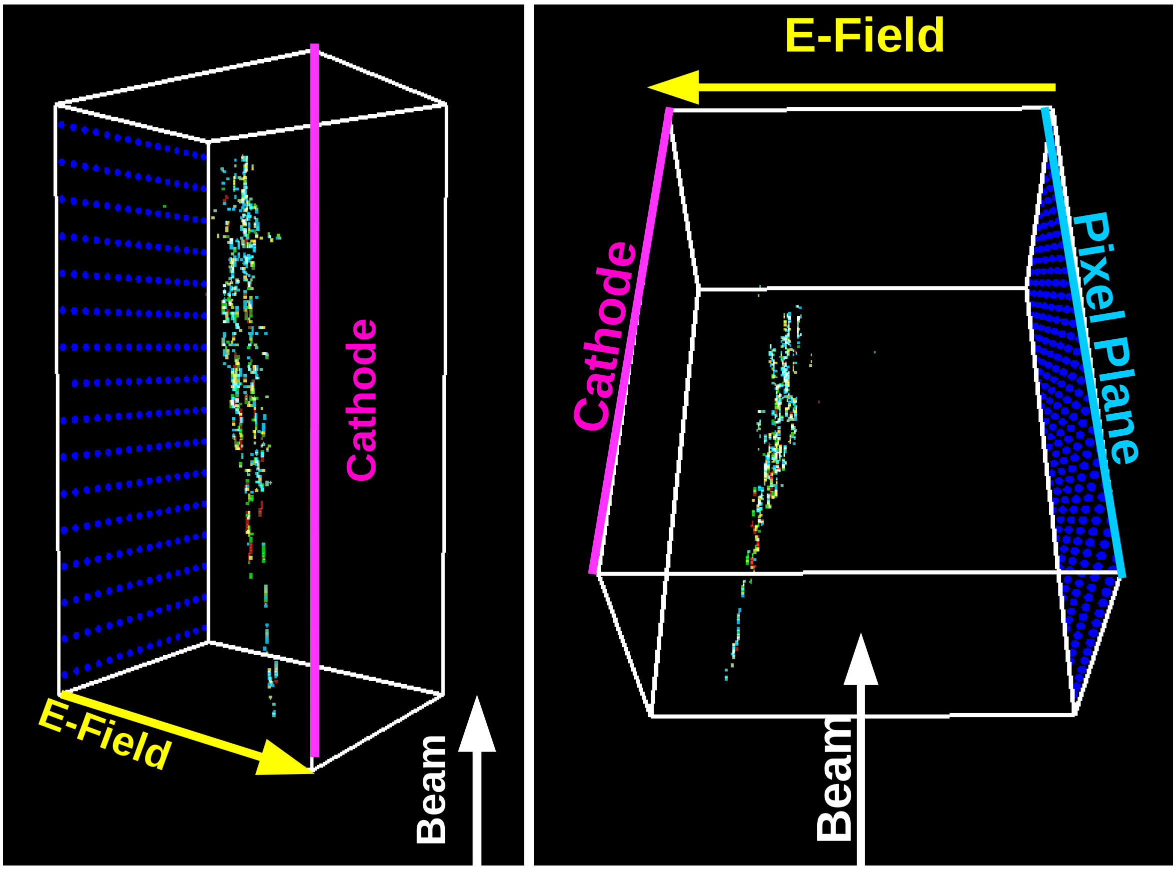

Figure 5.12.: PixLAr beam event.

to the ARGONTUBE chain described in Section 4.8 after the upgrades. To trigger on scintillation light one end of the TPC is equipped with a 43 cm × 15 cm ArCLight module (see Section 4.12) while the other end features an ARAPUCA [107] detector for comparison. Figure 5.11 shows one of the readout half planes with the ArCLight module attached.

Over several weeks beam and cosmic muon data was taken. At the time of writing no official results were available. Nevertheless, preliminary analyses indicate a successful scale-up of the pixelated LArTPC concept. The achieved SNR is comparable to what was reached with the prototype at LHEP (see Section 5.1). A recorded beam event is shown in Figure 5.12.

5.4. The ArgonCube Approach

LHEP has formed the ArgonCube collaboration with the goal of developing a novel fully modular type of LArTPC addressing the challenges mentioned in Section 3.6. Modularity reduces pile-up and allows for shorter drift-times and thus slackens the requirements on argon purity and HV. A modular detector furthermore reduces event pile-up because the acquisition time is reduced to the size of one half module. Maintenance and upgrading of a modular detector is much easier than for a monolithic one. In case of a fault condition, the affected module(s) can be shut down and repaired or replaced individually without affecting the rest of the detector. During construction data-taking can be commenced as soon as the first module is operational without waiting for the commissioning of the whole detector. Finally, trigger purity profits from a modular approach because scintillation light is contained within each module, allowing for a localised trigger.

ArgonCube is made of self-contained TPC modules sharing a common cryostat. A module is made of a rectangular box with a square footprint and the height required by physics goals and/or sensitivity constraints. The top and bottom flanges are made of stainless steel while the side walls are made from 1 cm G10 sheets. G10 is a glass-reinforced epoxy composite formerly used for PCBs [122]. Its EM radiation length ($X_0 = 19.4\,\mathrm{cm}$) and hadronic interaction length ($\lambda_{\mathrm{int}} = 53.1\,\mathrm{cm}$) [123] are both comparable to LAr (see Table 3.1). This makes G10 structures in LAr almost transparent for passing particles allowing for a performance comparable to a monolithic detector. The module walls produce gaps in particle tracks traversing multiple modules similar to dead wires in classic LArTPC readouts. Algorithms to join such segmented tracks already exist [124]. However, a detailed study of the influence of module walls on reconstruction efficiency still needs to be performed. At the same time, inactive volume is drastically reduced compared to a monolithic design due to the comparably low cathode voltage. The modules are placed side-by-side in a bath of LAr where they can be extracted and reinserted as

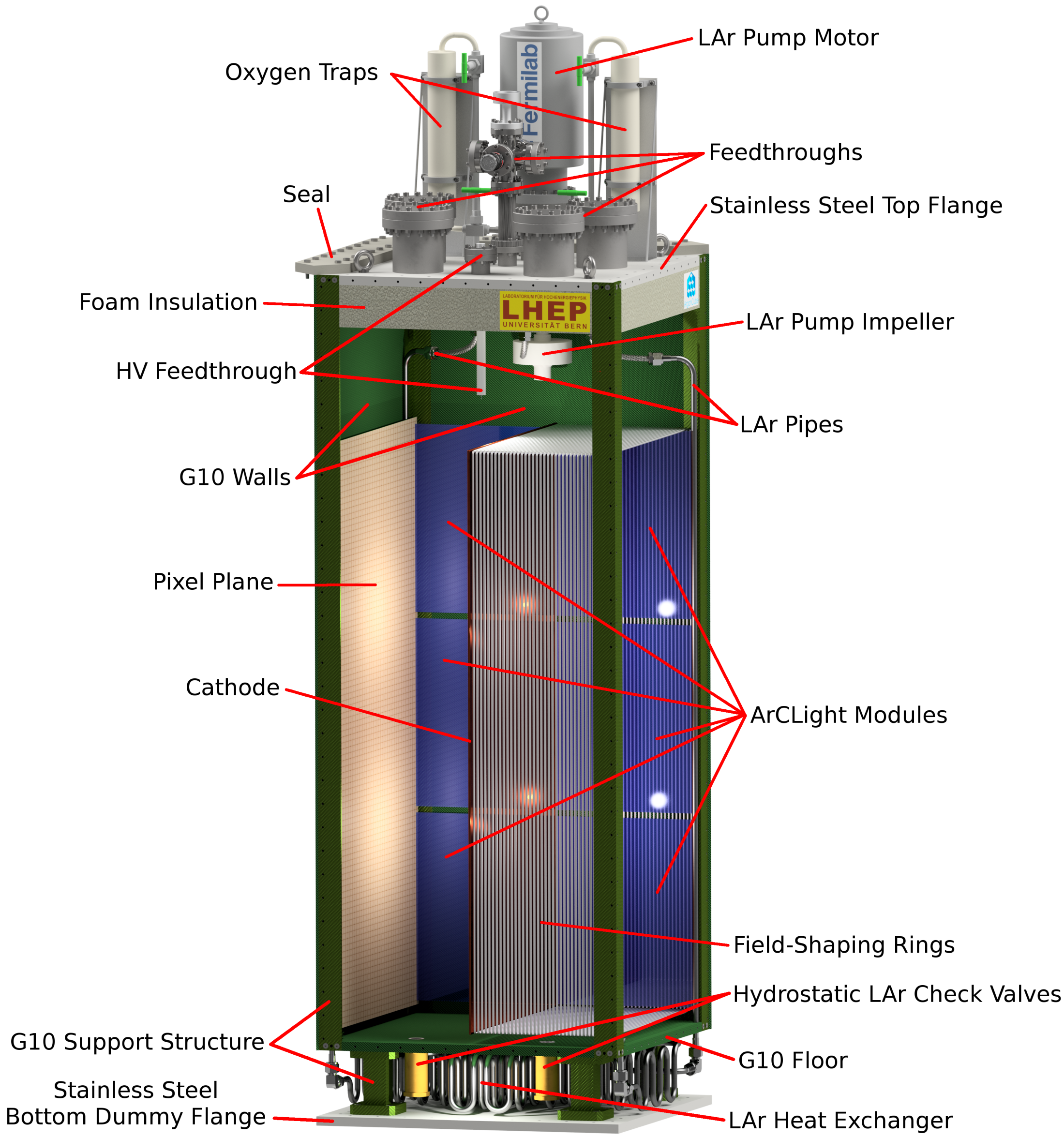

Figure 5.13.: Engineering drawing of a 0.67 m $\times$ 0.67 m $\times$ 1.81 m ArgonCube module for the 2 $\times$ 2 module prototype at LHEP (see Section 6.1).

needed. Pressure inside the modules is kept close to the bath pressure putting almost no hydrostatic force on the module walls. Purity of the LAr is maintained within each module by means of a recirculation system. As a result, the argon surrounding the modules needs not meet as stringent purity requirements as the argon inside. Under normal operation conditions all modules are inserted with only clearance distances between modules, and adjacent top flanges sealed using indium. An engineering drawing of an ArgonCube module is shown in Figure 5.13.

To extract a module the indium seal around the flange in question is removed. The module is then slowly lifted up by a crane and the LAr is drained to the surrounding bath through a hydrostatic outlet valve at the module bottom by means of gravity. A dummy flange is located at the bottom of each module, with equal dimensions as the top flange but without any feedthroughs. When the bottom flange reaches the original position of the top flange, it is resealed with indium and then detached from the module, which is now free and can be brought to its destination. Upon reinsertion the procedure is reversed. First, the module is reattached to the dummy flange and the indium seal is removed. Then, it is slowly inserted into the argon bath while being filled through a hydrostatic inlet valve at its bottom by means of hydrostatic pressure. As soon as the top flange of the module reaches the top flanges of the other modules, the indium seal is reinstalled. Figure 5.14 illustrates the sealing of the argon bath for all modules inserted (left) and one module extracted (right), in the 2×2 prototype at LHEP (see Section 6.1).

During module insertion and extraction the argon flow is controlled by hydrostatic check valves located at the module bottom. They require a minimal differential pressure to open. Purity inside to modules is maintained by means of continuous LAr recirculation through oxygen traps. The dirty argon is sucked in at the module top and then pushed through the oxygen traps. The clean argon is first routed through a heat exchanger, located below the module inside the outer bath, for cooling and then re-enters the module at the bottom. For optimal heat transport the argon flow is directed along the cold electronics. To prevent dirty argon from the bath entering the modules their interior is held at a slight overpressure, just below the opening pressure of the check valves. Cooling power to the bath is supplied by cryocoolers located in unistrumented volumes at the side of the detector called service volumes.

There are two slightly different options for the recirculation system. To maximise module autonomy each module can be equipped with its own oxygen trap and LAr pump. One drawback of this is the very high cost of LAr pumps. Additionally, the DUNE ND complex is planned to consist of a magnetised detector besides an unmagnetised LArTPC. The resulting magnetic stray fields might interfere with the electric motors of LAr pumps on top of the modules. Using a shared recirculation circuit is more economic but reduces module autonomy. An external system comprising pumps and oxygen traps can be located outside the argon bath (and potential magnetic stray fields), connected to the modules via tubes.

One big problem that can be solved by a modular TPC design is the high cathode voltage required for large monolithic detectors, and the resulting stored energy. As each module contains its own TPCs independent of all other modules, the required cathode potential only depends on the module size, not the detector size. To minimise the cathode voltage the drift field is applied along one of the short edges of a module. In addition, the module is split in two half TPCs by the cathode, reducing the voltage by another factor of two. Thus, for a module footprint of $1\,\mathrm{m} \times 1\,\mathrm{m}$ and an electric field of $1\,\mathrm{kV\,cm^{-1}}$ a cathode potential of only $50\,\mathrm{kV}$ is required. Operating a LArTPC at this voltage is challenging but feasible without a prohibitive loss in active volume [62]. The HV is brought into the module using a feedthrough similar to the one used for the breakdown studies presented in Section 4.1. Owing to the moderate cathode voltage

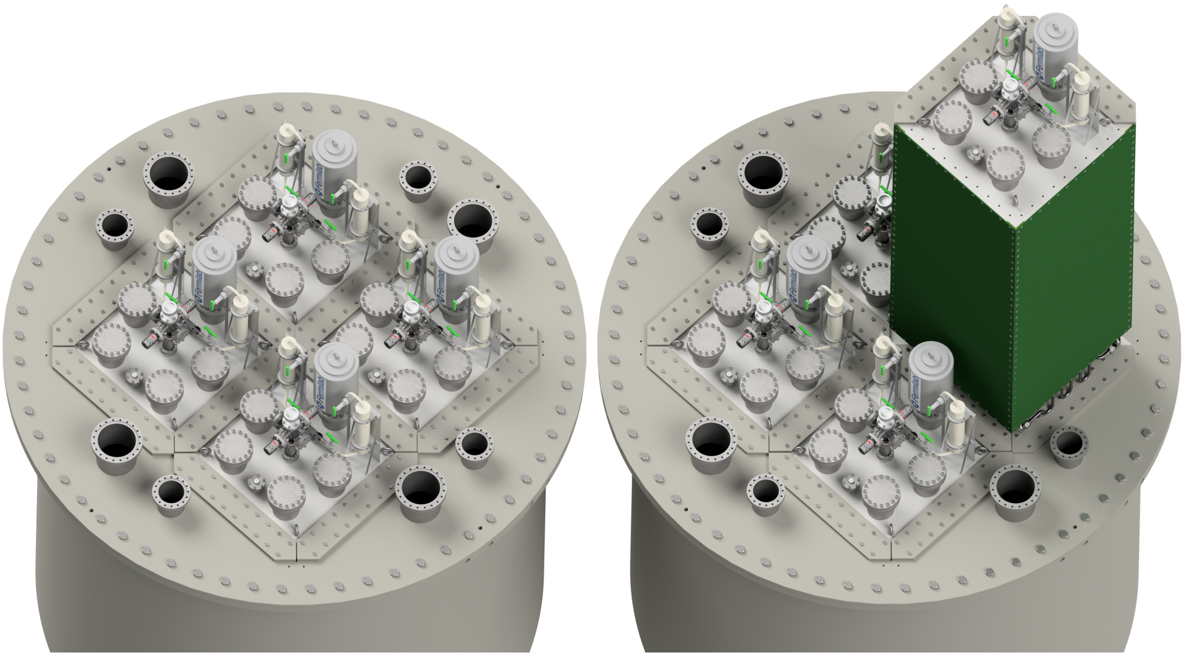

Figure 5.14.: Inserted (left) and extracted (right) ArgonCube module in the 2×2 module prototype at LHEP (see Section 6.1). The bottom dummy flange of the extracted module seals the LAr bath.

commercial alternatives are also available. Field-shaping rings can be realised as copper traces printed directly on the G10 module walls using conventional PCB techniques. They are connected via HV resistors in the same fashion as for a classic LArTPC. An improved solution with a continuous resistive-plane field cage is under investigation. This could provide a very homogeneous field paired with simple mechanics. The difficulty is to find a material with the required sheet resistivity of $\sim 1\,\mathrm{G\Omega/sq}$[3] that is stable at cryogenic temperatures and depositable on G10.

The high rates present in an ND environment will lead to a significant amount of event pile-up. Disentangling the individual neutrino events requires a highly capable charge readout. Solving this task with a projective wire readout is more than doubtful. To enable true 3D tracking the modules are equipped with a pixelated charge readout very

[3]Sheet resistivity only depends on the aspect ratio of the sheet but not its area. It is therefore quantified as a resistance per square.

similar to the one described in Section 4.5. Pixelated anode planes are located on the two module walls parallel to the cathode. The bespoke LArPix cryogenic electronics, described in Section 4.9, are used to digitise the signals in cold to achieve unambiguous 3D information.

One of the main challenges for the light readout are again the high rates faced by an ND. To get proper timing for the third spatial coordinate scintillation signals need to be correctly matched to charge signals (flash matching). Furthermore, attenuation due to Rayleigh scattering becomes a problem for large detectors (see Table 3.1). Both problems are greatly alleviated by using an opaque cathode and module walls, containing the scintillation light inside a single module half (TPC). Therein, pile-up is reduced due to the smaller volume. Having a position-resolving light readout helps as well. However, a modular TPC introduces a new challenge: The dead spaces in between adjacent TPCs have to be kept to a minimum because they introduce gaps in the recorded event topologies accompanied by lost energy. Classic PMTs could therefore only be mounted at the top and/or bottom of the module, but they would still waste active argon volume. Additionally, the light would be collected at the far ends of a long narrow volume, reducing efficiency. Finally, due to their operating principle PMTs do not work well in high electric fields, such as near the field cage at the module top and bottom. Therefore, ArgonCube modules are instrumented with the ArCLight light collection system described in Section 4.12. With its light trap design it allows light collection from a large area with a minimal dead volume. The location of the SiPMs at the edges of a dielectric sheet makes most of the light detector immune to electric fields. Splitting ArCLight into several horizontal strips stacked vertically gives some spatial resolution in the vertical direction. ArCLight sheets are mounted in between cathode and anode, parallel to the field cage, with the SiPMs directly attached to the charge readout PCB. The additional dead volume of a few mm is similar to the one caused by the charge readout PCBs in perpendicular direction.

6. Towards the DUNE Near Detector

While Section 5.4 gave a general overview of the ArgonCube concept, this chapter focuses on the detailed implementation for the DUNE Near Detector (ND). After I established the required key technologies with this work, the next step is a 2×2 module prototype at LHEP. The current status of an ArgonCube LArTPC component for the DUNE ND complex is also described. Finally, I provide a proof that ArgonCube can handle the expected high event rates.

6.1. 2×2 Module ArgonCube Prototype

The goals of this prototype are testing the mechanical design and cryogenic systems, comparing different charge and light readout systems, and studying module insertion and extraction procedures with a focus on their influence on purity. For comparison, one of the four modules will be equipped with a classic wire readout. To investigate purity first tests will be performed with the ArgonCube demonstrator TPC described in Section 5.1. The TPC will be mounted inside an otherwise empty module, hanging from an intermediate support layer. This will also serve as a first cryogenic stress-test of the module structure and LAr purification.

The four modules will be housed in an existing cylindrical, vacuum-insulated cryostat at LHEP. An artistic view is shown in Figure 5.14. With its approximately 2 m diameter by 2 m height the cryostat provides a LAr bath volume of roughly $6\,\mathrm{m}^3$. To fit inside

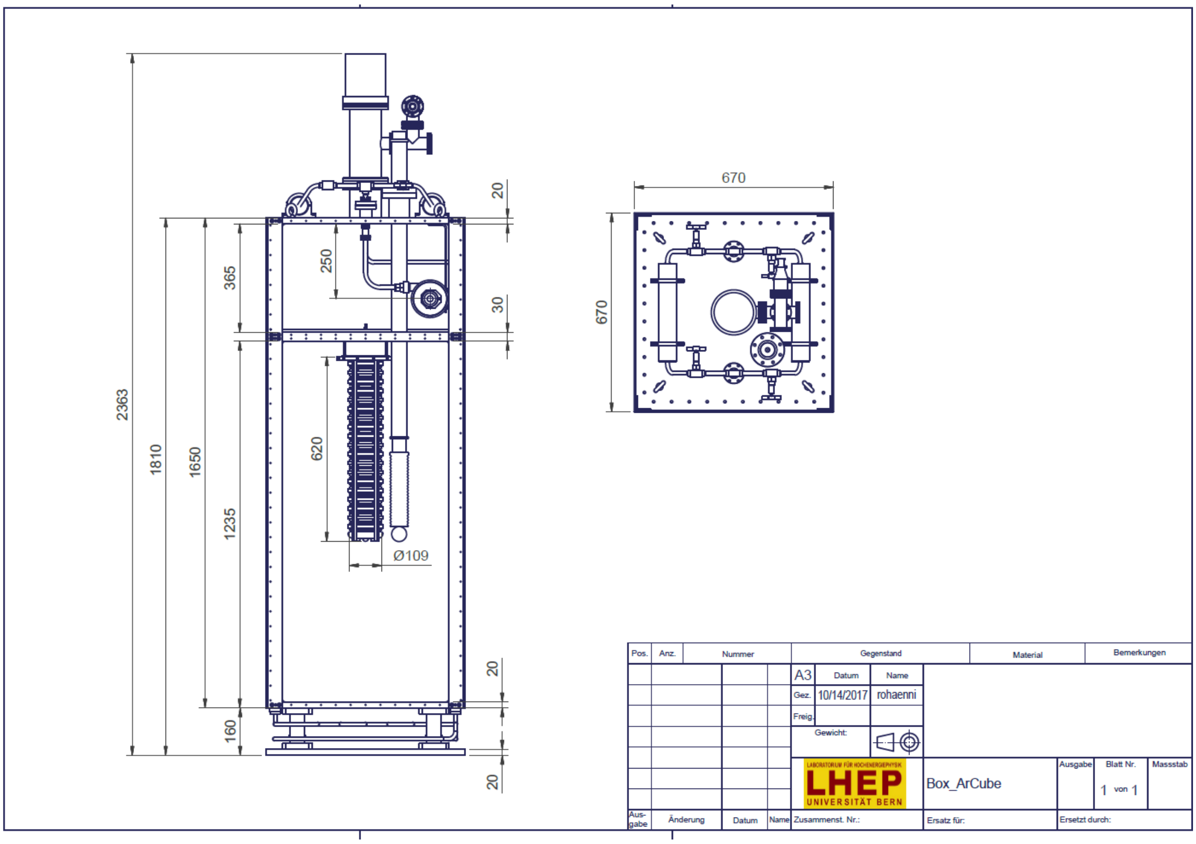

Figure 6.1.: Dimensions of a 0.67 m × 0.67 m × 1.81 m module, equipped with the pixel demonstrator TPC, for the 2 × 2 module ArgonCube prototype at LHEP.

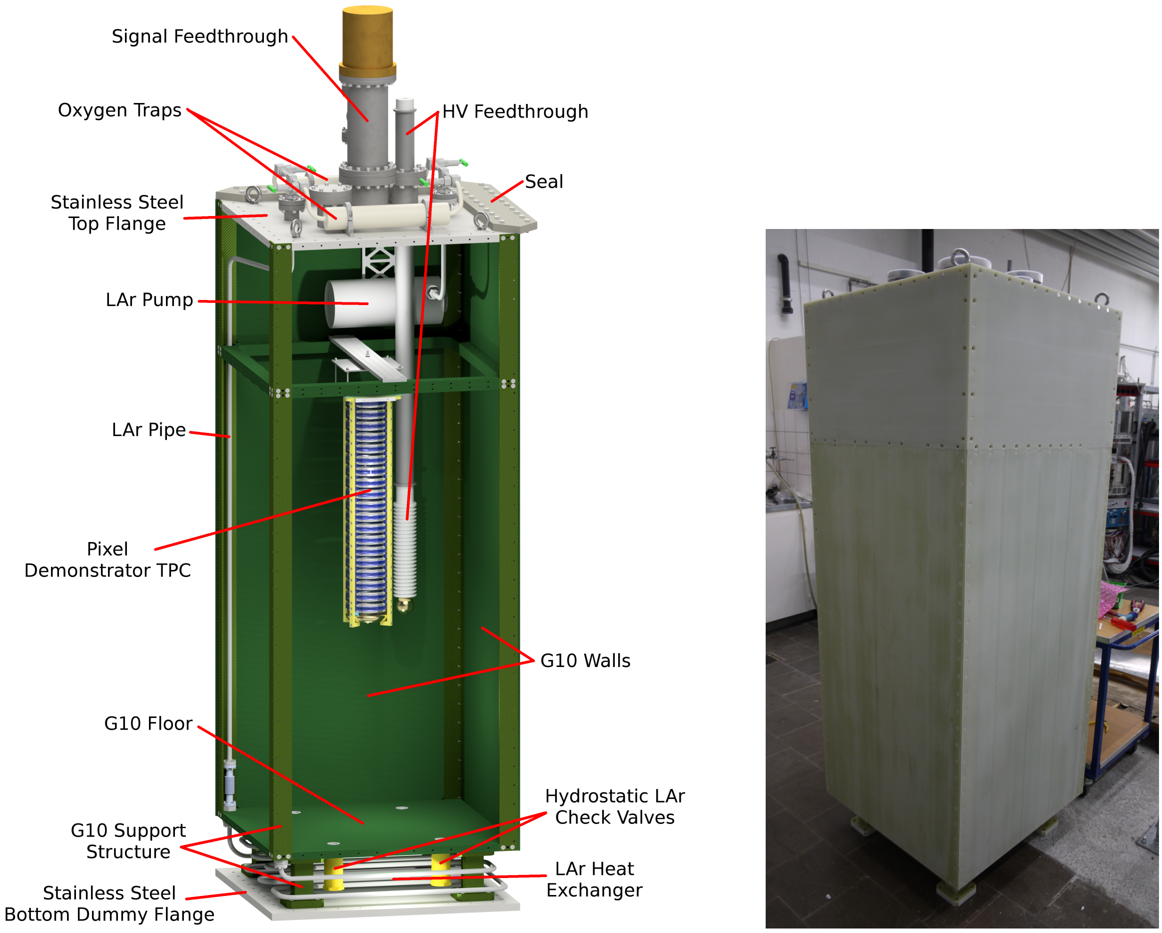

Figure 6.2.: Engineering drawing (left) and picture (right) of a 0.67 m × 0.67 m × 1.81 m module, equipped with the pixel demonstrator TPC, for the 2 × 2 module ArgonCube prototype at LHEP.

the bath the modules are scaled down to a footprint of 0.67 m × 0.67 m and a height of 1.81 m. Instead of service volumes cooling is provided by two turbo-cooling circuits attached to the inner cryostat wall inside the insulation vacuum. They cool the LAr bath via evaporation of liquid nitrogen. The nitrogen flow has to be regulated precisely to keep the LAr stable and prevent it from boiling or freezing.

The height of the actual TPC in a fully equipped module is 1235 mm. Due to the split-TPC design the resulting cathode voltage required for a $1\,\mathrm{kV\,cm^{-1}}$ field is below 35 kV. On the bottom 160 mm are occupied by the heat exchanger and check valves for LAr exchange with the bath upon insertion and extraction. The remaining room on

Table 6.1.: ArgonCube dimensions for the 2×2 prototype at LHEP and the preliminary DUNE ND design. Charge and light readout thicknesses are given per wall, i.e. the resulting dead space per module is twice as big. Both are preliminary estimates. For simplicity clearance between adjacent modules is included in these numbers.

Dimension	2×2	ND	Unit
Detector size	2×2	4×5	mod
Module footprint	0.670×0.670	1.000×1.000	m^2
Module height	1.810	3.500	m
TPC height	1.235	3.000	m
Total TPC volume	2.218	60.000	m^3
Flange thickness	0.020	0.020	m
Side wall thickness	0.010	0.010	m
Charge readout thickness	0.020	0.020	m
Light readout thickness	0.005	0.005	m
Total dead volume	0.289	5.292	m^3
Active volume fraction	87.0	91.2	%

top of the TPC is filled up by the HV feedthrough, a buffer gas phase, and an optional recirculation pump. All support structures except for the flanges at the module top and bottom are made from *Amsler & Frey HGW 2372* G10 [122], including most of the screws. The thickness of the side walls is 10 mm while the flanges are made of 20 mm stainless steel plates. An engineering drawing of a 2×2 prototype module is given in Figure 5.13. It uses a LAr pump donated by FNAL in combination with oxygen traps mounted on top of the module.

Figure 6.1 gives the detailed dimensions of a prototype module. It depicts the first module, which will be equipped with the demonstrator TPC. For this test an internal pump salvaged from ARGONTUBE will be used. An engineering drawing together with a picture of the pixel demonstrator module is given in Figure 6.2.

Table 6.1 gives an overview of the most important dimensions of the 2×2 module prototype at LHEP and the preliminary DUNE ND design (see Section 6.2). In particular, the table contains a rough estimate of dead space, caused by the modular design, and the corresponding active volume fraction. For these calculations a total charge readout thickness of 20 mm and a total light readout thickness of 5 mm were assumed. The difference is caused by the fact that charge readout electronics are located directly behind the readout while the SiPMs are only mounted on the edges of the ArCLight modules. Additionally, a few mm clearance between the anode plane and the module wall are required for convection cooling of the LArPix electronics. Readout thicknesses also include the clearance between adjacent modules (~ 1 mm). The resulting total fraction of active volume is 87.0 % for the 2×2 module prototype.

In a first phase the 2×2 prototype will be operated in the Grosslabor of LHEP, taking cosmic ray data. After a successful test of all subsystems, it is planned to be installed in a test beam at either CERN or FNAL to investigate the influence of the module walls on calorimetry and tracking.

6.2. Preliminary ArgonCube Near Detector Design

The ArgonCube ND design is based on a scaled-up version of the 2×2 module prototype design described in Section 6.1. Modules will have a footprint of 1 m $\times$ 1 m and a height of 3.5 m. Again, 0.1 m at the bottom are occupied by the heat exchanger and valves while 0.4 m at the top are taken up by feedthroughs and the gas phase. This results in a TPC size of 1 m $\times$ 1 m $\times$ 3 m, split in two half TPCs by a cathode at a potential of 50 kV. The full detector will consist of 4×5 modules with the longer dimension in beam direction.

Detector dimensions were optimised for maximum hadron containment by means of simulations done by the neutrino group at LBNL [125]. While horizontal dimensions are unproblematic, the vertical 3 m are at the lower limit. According to the simulations, 2.5 m would be sufficient but provide no safety margin at all. Reducing the height by another 0.25 m results in a significant loss of hadron containment already. Figure 6.3

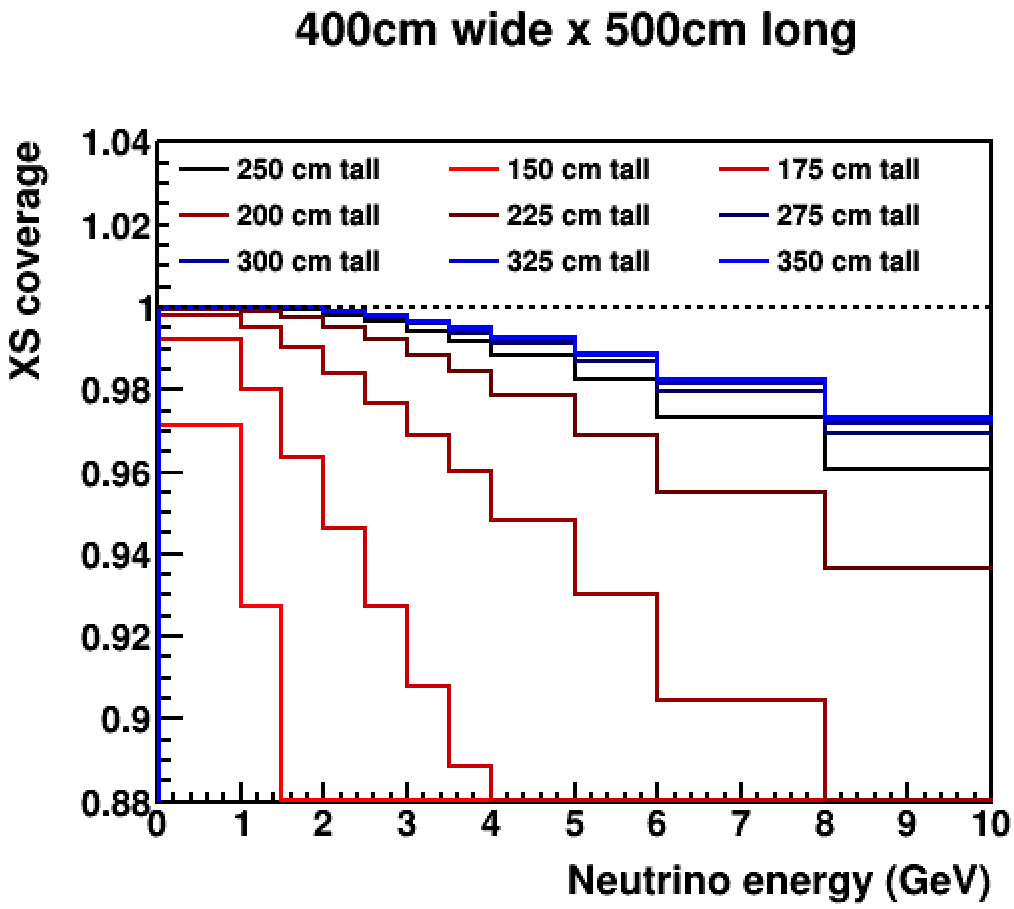

Figure 6.3.: Influence of the LArTPC size in the DUNE ND complex on hadron containment. Given in cross-section coverage as a function of neutrino energy. Horizontal dimensions are held constant at their nominal values of 4 m × 5 m. Height is indicated by colour. See text for explanation of cross-section coverage. [125]

illustrates this by means of the cross-section coverage as a function of neutrino energy. Cross-section coverage is similar to containment efficiency but should not be confused with the latter. To assess the efficiency a detector of the corresponding size in the neutrino beam is simulated. While this indeed provides a good measure of the efficiency of the detector to contain different events, it is not necessarily a good quantity to assess the required detector size. Many events are simply not contained because of their specific location and/or orientation inside the detector. Cross-section coverage remedies this deficiency by looking at the actual extent of the event instead of its containment at a random position inside a realistic detector. On the other hand, an event extending through the full detector will very likely never be contained in a real detector due to the low probability of it exactly happening in the right location. Therefore, the maximum event size needs to be selected smaller than the full detector size. For the ND simulation this buffer was chosen as 0.5 m in all directions; i.e. an event can have a maximum extent of $2\,\mathrm{m} \times 3\,\mathrm{m} \times 4\,\mathrm{m}$ to be counted as contained in a nominal size detector. Like this cross-section coverage allows to probe for phase space regions inaccessible to a particular detector configuration. In Figure 6.3 it can be seen that cross-section coverage decreases rapidly for detector heights below 2.5 m. A height of 3 m is therefore preferable to have some buffer for yet unknown uncertainties in the simulation.

A pixel pitch of 3 mm was chosen. This value has been field-tested in a physics experiment, MicroBooNE [32], and is below the $\approx$ 5 mm wire pitch of the DUNE FDs [28]. The LArPix electronics described in Section 4.9 are designed to be capable of handling the data rates and power consumption expected for a 3 mm pixel pitch ArgonCube ND component. Therefore, a sufficient spatial resolution from a physics point of view is provided while keeping the power and data rate demands on the readout electronics under control.

Inspired by the design of the DUNE 35 t prototype at FNAL [28] the LAr bath is

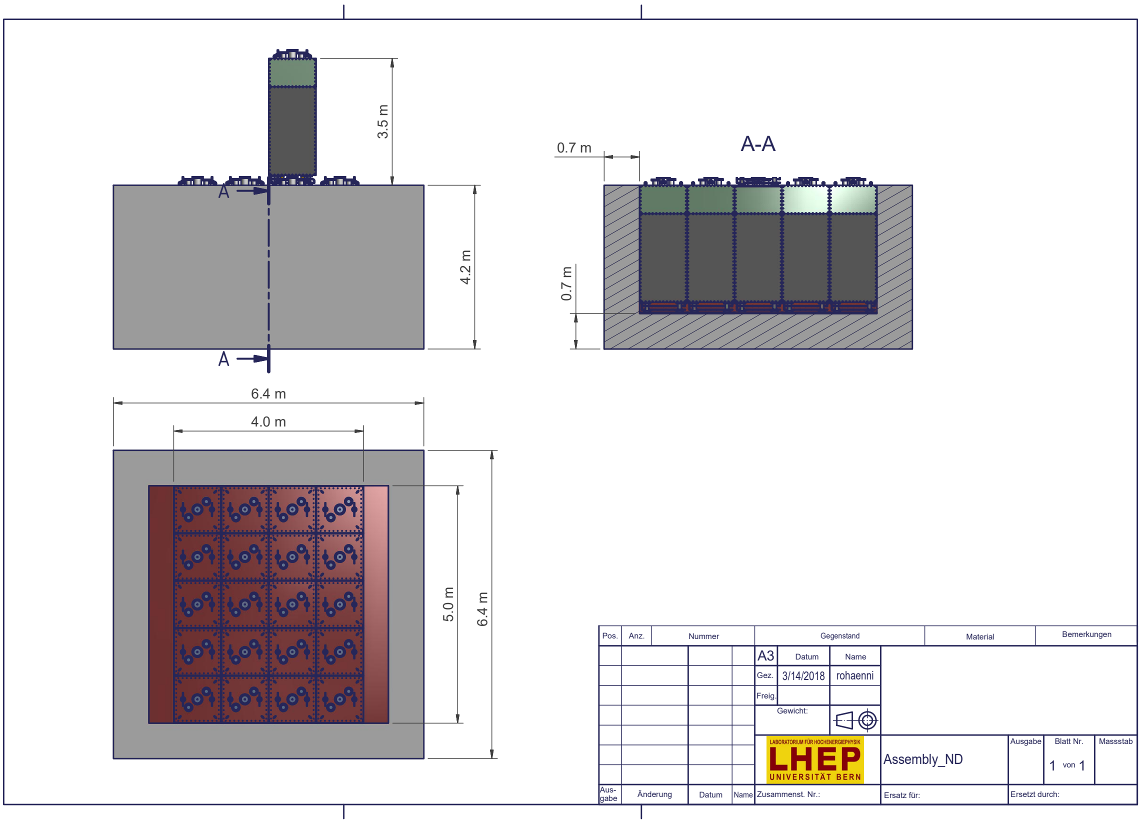

Figure 6.4.: Preliminary engineering drawing of ArgonCube in the DUNE ND. 4×5 modules with the longer dimension in beam direction. Service volumes make up the remainder of the $5\,\mathrm{m} \times 5\,\mathrm{m}$ LAr bath contained within a low-radiation-length foam-insulated membrane cryostat.

contained within a foam-insulated membrane cryostat. The outer support structure is a 0.3 m thick steel-reinforced concrete layer, followed by a 0.4 m thick polyurethane foam layer for thermal insulation. Inside of this is a 2 mm thick stainless steel membrane sealing the LAr bath from the environment. There are several other support layers, all of which with a thickness of ~ 1 mm, with a more detailed description in [28]. The total thickness of the cryostat wall amounts to 2.88 radiation lengths. Cooling is provided by 10 uninstrumented 0.5 m $\times$ 1 m service volumes equipped with cryocoolers, arranged along the two detector edges parallel to beam direction. The total required cryostat footprint is therefore 5 m $\times$ 5 m.

Table 6.1 gives an overview of the most important ArgonCube ND dimensions, in comparison to the 2×2 module prototype at LHEP. Due to the bigger modules the total fraction of active volume is increased to 91.2 %. Drift direction is perpendicular to beam direction to reduce the hit rate on single pixels. If drift direction is parallel to beam direction, particle tracks highly parallel to drift direction lead to a very high rate on single channels, potentially leading to a buffer overflow and thus data loss in the LArPix chip. In addition, power dissipation increases proportionally to the pixel hit rate due to the smart zero suppression scheme of LArPix. Another advantage is that dead space in beam direction between adjacent modules will only be 30 mm due to the very slim dimensions of ArCLight. Figure 6.4 shows a preliminary engineering drawing of the ArgonCube ND component.

6.3. Event Pile-up in the Near Detector

With ArgonCube proposed as the LAr component of the DUNE ND complex there were two main questions that needed to be addressed:

1. Is a pixelated LArTPC feasible?

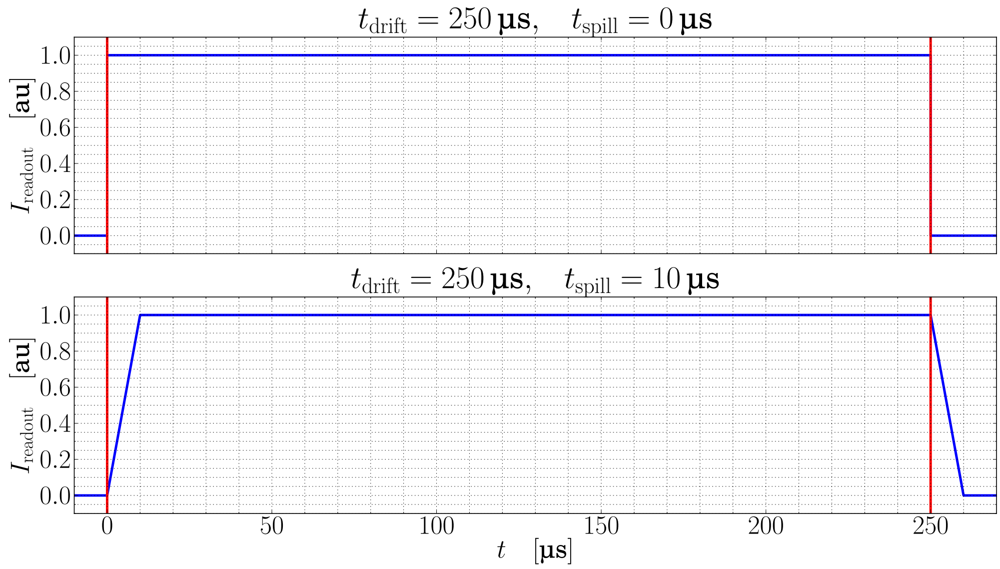

Figure 6.5.: Average current collected for one beam spill as a function of time. The current is given in arbitrary but equal units for both plots. Anode and cathode are represented by the vertical red lines, relative to the trigger timestamp. The upper plot assumes the whole charge is deposited instantaneously while for the lower plot the actual spill duration from [26] is used.

2. Can the LAr detector handle the high rates?

Number one was addressed in Section 5.1. This and the next section will address question number two. As described in Section 2.3, the DUNE beam will have an intensity of 2 MW. Paired with the slow (ms) nature of LArTPCs described in Chapter 3 this will result in multiple neutrinos interacting inside the detector for each beam spill, so-called event pile-up. A more precise phrasing of question number two is therefore: Can a LArTPC disentangle these piled up events? To assess this one of the most difficult reconstruction tasks—π^0-induced EM showers—was simulated in an ArgonCube ND component (see Section 6.2).

LArTPCs are intrinsically slow detectors with a readout time of $\approx 0.5\,\mathrm{ms\,m^{-1}}$ for a $1\,\mathrm{kV\,cm^{-1}}$ drift field (see Chapter 3). This causes a pile-up of events in the detector; if the readout was infinitely fast, all neutrino interactions could be separated in time. In reality even the ArgonCube TPCs with a drift length of only 0.5 m, corresponding to a full readout cycle of 250 µs, are significantly slower than the spill duration of 10 µs of the DUNE beamline design (see Table 2.2). Figure 6.5 visualises this effect. The charge arriving at the readout is represented as an average current in arbitrary units (same for both plots). Anode and cathode are represented by the vertical red lines, relative to the trigger timestamp. The amplitude of the readout current is a direct measure for event pile-up in the corresponding time slice. For simplicity an infinitely short spill duration was assumed for the pile-up study (top), i.e. the whole ionisation charge produced by one beam spill is deposited instantaneously inside the TPC volume. As the time in between beam spills is $\sim 1\,\mathrm{s}$, all this charge can be read out within one drift time. In this case the average current (pile-up) seen by the readout is constant over the whole readout cycle. The realistic case with the spill duration of the DUNE beam is depicted in the bottom plot. At the beginning of the readout cycle there is no charge deposited yet, the current (pile-up) is zero. Over the duration of the beam spill ionisation charge accumulates inside the TPC volume while constantly being transported towards the readout by the drift field. After the beam spill is over the remainder of the initial drift volume (240 µs) contains a uniform charge density. Due to the finite spill duration there is an additional 10 µs (falling) ramp after the first 250 µs readout cycle, entering the next readout cycle. In short, a spill duration shorter than but comparable to the drift time results in the shape of the ionisation current (event pile-up) seen over time to become a trapezoid rather than a square. The integral, i.e. the total ionisation charge (deposited energy), is the same but part of it is shifted from the spill time slice to the beginning of the next readout cycle. In addition, the peak current (pile-up) stays unchanged as long as the spill duration is shorter than the drift time. If the spill duration becomes longer than the drift time, the charge is distributed over more than two readout cycles and the peak current (pile-up) begins to decrease. Therefore, the assumption of an infinitely short spill is a worst-case scenario slightly improved by the real, finite spill duration. However, for

Table 6.2.: Parameters of the π^0 pile-up simulation.

Parameter	Value	Unit
X-axis orientation	Drift	
Y-axis orientation	Vertical	
Z-axis orientation	Beam	
Resolution X	3	mm
Resolution Y	3	mm
Resolution Z	3	mm
Target volume X	−100 to 500	cm
Active volume X	0 to 400	cm
Fiducial volume X	30 to 370	cm
Target volume Y	−100 to 350	cm
Active volume Y	0 to 250	cm
Fiducial volume Y	30 to 220	cm
Target volume Z	−400 to 500	cm
Active volume Z	0 to 500	cm
Fiducial volume Z	30 to 470	cm
Detection threshold	0.1	MeV
Cone extent	10	X_0
Cone aperture (full angle)	30	°
Cylinder diameter	5	cm
Beam intensity	2.14	MW
Proton energy	80	GeV
Events per beam spill	0.21	$\mathrm{evt/t_{Ar}}$

96 % of the drift time (240 µs) pile-up is unchanged.

6.4. Feasibility Study of a Pixelated LArTPC in the Near Detector

Reconstruction complexity paired with potential impact on physics measurements make photons produced by π^0 decays a good sample to study the robustness to pile-up of a pixelated LArTPC in the DUNE ND environment. Energy misidentifications lead to a misreconstructed neutrino energy. The resulting discrepancy to the true neutrino energy has the potential to skew the measured energy spectrum and thus impact the oscillation measurements. A significant amount of π^0 are produced in various RES and COH neutrino interaction modes (see Table 2.3, Section 2.4, and [26]). They decay according to

$$\pi^0 \rightarrow \gamma\gamma \tag{6.1}$$

with a branching ratio of 98.8 % [20]. The photons subsequently produce EM showers in LAr (see Section 2.5). At the energies of the DUNE beam (see Figure 2.7) most showers do not deposit a homogeneous cone of charge but rather a lot of individually resolvable $e^{\pm}$ tracks. More importantly, there are often significant gaps in between these charge clusters. A main challenge of shower reconstruction is to associate these well separated charge blobs to the correct event.

One way to assess the performance of an analysis of experimental data is to run it on a simulated dataset. In the simulation the quantities to be measured by the experiment are known a priori. They are called truth information and can be compared to the output of the analysis run on the simulated dataset. To simulate the expected neutrino interactions in the ND the Argon Box[1] simulation tool was used. The neutrino group at LBNL is developing it with the goal of providing an easy-to-use simulation of particle interactions in the LAr component of the ND. Primary particles can either be provided by a particle gun (e.g. e^-, n, p, or μ^+) or in form of a *HEPEVT* file[2]. For this study 6.6×10^6 neutrino events, produced with the GENIE[3] neutrino event generator, were used. Secondary particle transport and interaction in Argon Box is performed by Geant4[4]. Finally, the energy deposition in LAr is voxelised and stored together with all the necessary ancillary information about the depositing particle. The data is stored

[1] `https://github.com/dadwyer/argon_box`
[2] A file format standard for passage of particle events between different simulation tools
[3] `https://genie.hepforge.org`
[4] `http://geant4.cern.ch`

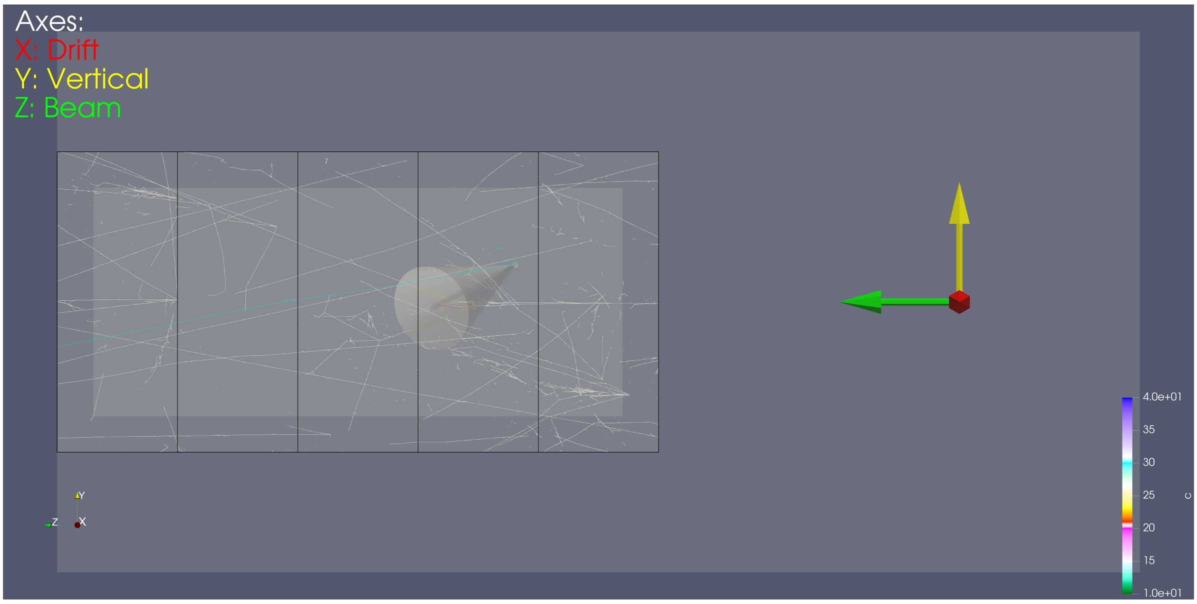

Figure 6.6.: Event display showing a simple π^0-induced EM shower reconstruction algorithm based on a cone-cylinder union, simulated for the ArgonCube ND component. Visible are the three different volumes used for the simulation. The outermost volume is used to simulate rock events. The active detector volume is represented by the intermediate volume, divided into modules by vertical black lines. In order to reduce the number of EM showers not depositing any energy inside the detector a fiducial volume (the innermost) is defined, and photons are required to be produced therein. Depicted is a side view of the detector, looking in drift direction. The detailed orientation is indicated by the coloured arrows.

in the tree format of the ROOT data analysis framework[5]. This allows for convenient further processing using ROOT.

To investigate the effects of pile-up on energy reconstruction a working reconstruction algorithm is necessary. However, at the time of writing official reconstruction tools were only available for LArTPCs read out by wire planes[6]. Therefore, I implemented a simple algorithm for true 3D space points, under the assumption that a positive outcome of such a pile-up study would imply an even better performance of a more sophisticated reconstruction. This algorithm is explained in the following, its parameters are listed in Table 6.2, an example of a simulated event is shown in Figures 6.6 and 6.7.

The basic underlying assumption is that a pixel readout without analogue multiplexing will yield unambiguous 3D space points of charge deposition with a given resolution, depending on the geometry of the pixel plane, time resolution of the readout electronics, and charge transport effects. In Section 5.1 I proved that this is feasible, provided the current reconstruction ambiguities can be eliminated by a successful deployment of the LArPix charge readout electronics described in Section 4.9. The spatial resolution of the pixel readout is assumed to be 3 mm in both directions, based on the ND design described in Section 6.2. A conservative value of 3 mm was chosen in drift direction. This has several advantages. Choosing the same resolution as the pixel pitch makes the simulation independent of the orientation of the TPC. MicroBooNE has achieved a resolution in drift direction < 3 mm [32], making it safe to assume LArPix will enable a similar performance with ArgonCube. A conservative value also accounts for charge diffusion.

Furthermore, it is assumed that EM showers can be identified and their starting point and direction reconstructed with negligible errors and inefficiencies, i.e. this information is taken from the simulation truth. In reality the direction and starting point can be

[5] https://root.cern
[6] http://larsoft.org

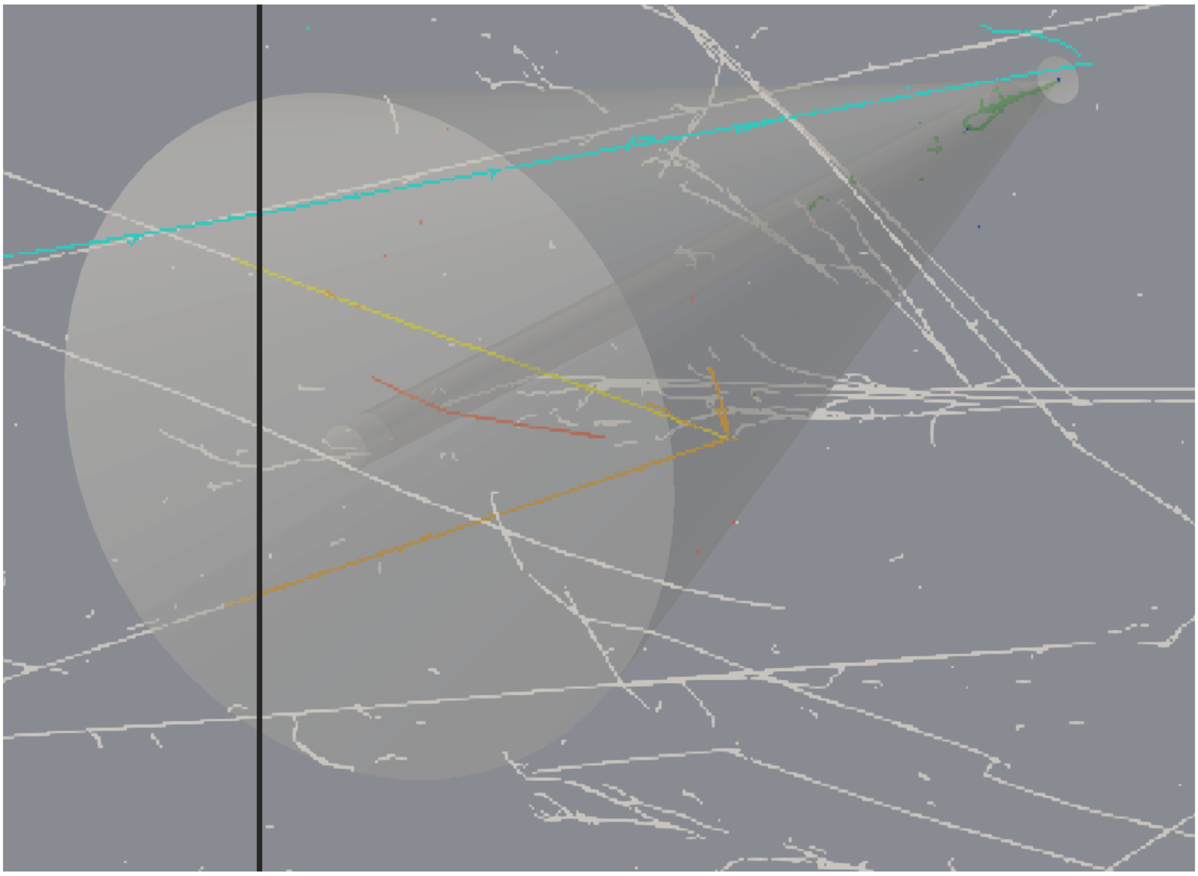

Figure 6.7.: Close-up view of the pile-up event shown in Figure 6.6. The acceptance volume is defined by the union of cone and cylinder. Charge depositions are depicted by white and coloured voxels whose size represents the applied resolution of 3 mm in all directions. Colour indicates type and acceptance of energy deposition. White: Different neutrino event, outside acceptance volume. Cyan: Correct neutrino event but not part of considered EM shower, outside acceptance volume. Dark blue: Correct neutrino event and EM shower, outside acceptance volume (missed energy). Green: Correct neutrino event and EM shower, inside acceptance volume. Magenta: Correct neutrino event but not part of considered EM shower, inside acceptance volume (not present in this example). Yellow (muons), red (γ, n, and descendants), orange (neither): Different neutrino event, inside acceptance volume (misidentified energy).

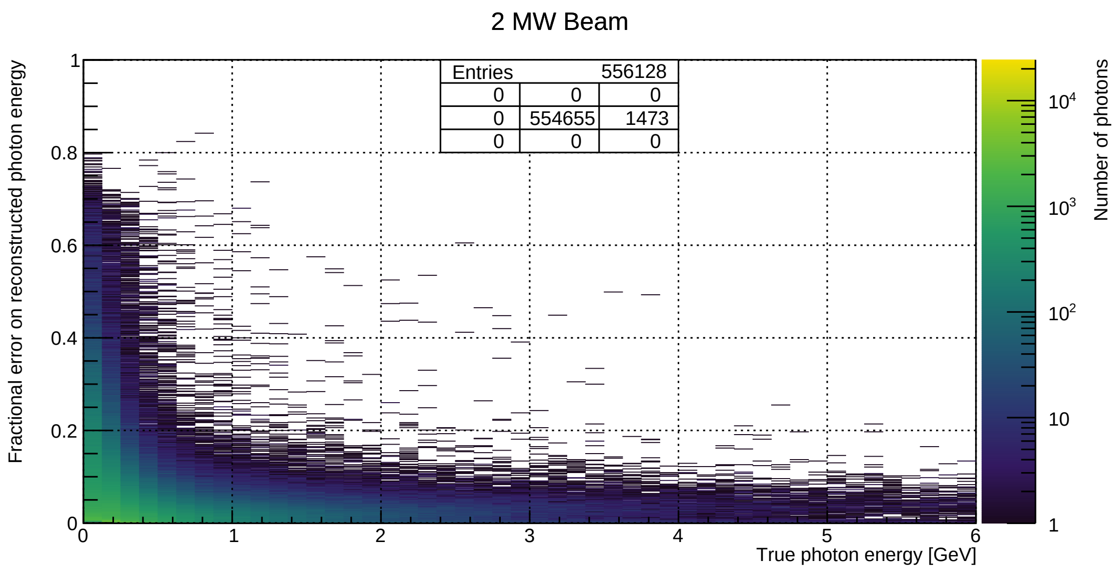

Figure 6.8.: Missed energy fraction versus true photon energy for a simple π^0-induced EM shower reconstruction algorithm based on a cone-cylinder union. All energy deposited outside of the cone-cylinder union is counted as missed. 2 MW beam of 80 GeV protons. Entries: Central cell shows plotted entries, other cells show overflow entries in direction w.r.t. central cell.

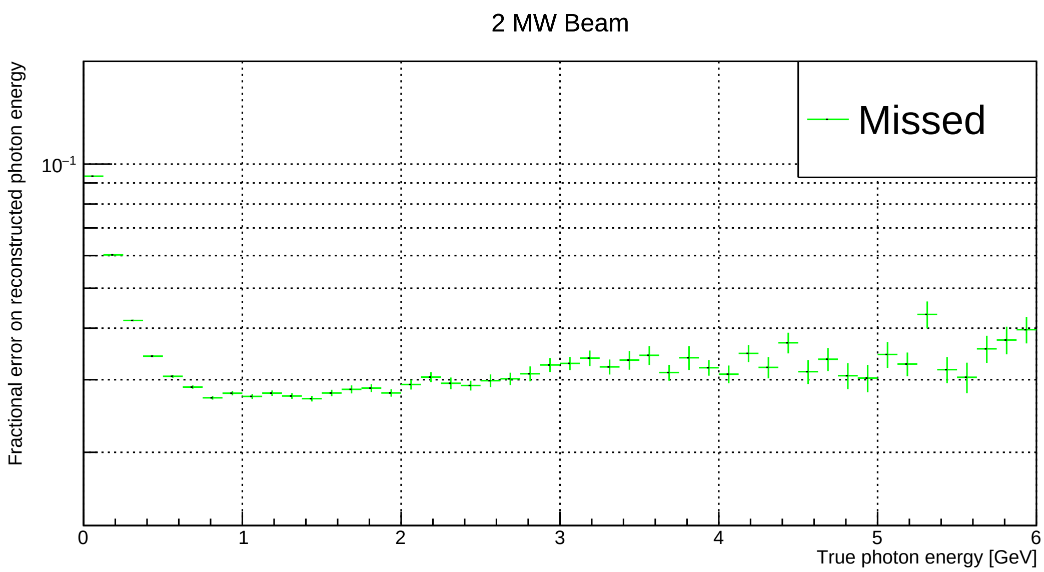

Figure 6.9.: Mean missed energy fraction versus true photon energy for a simple π^0-induced EM shower reconstruction algorithm based on a cone-cylinder union. All energy deposited outside of the cone-cylinder union is counted as missed. 2 MW beam of 80 GeV protons.

derived from the vertex producing the π^0, and a rough shower direction obtained from a pattern recognition. A cone is calculated in the direction of the shower with its tip at the first charge deposition of the initial photon. The opening angle and length of the cone were optimised by looking at the distributions of the distance from the starting point and the angle w.r.t. the direction of the shower. The finite resolution of the detector is emulated by voxelising (via rounding) the charge deposition with the corresponding resolution in all three spatial coordinates. This leads to problems near the tip of the cone, where the transversal extent is lower than the voxel dimensions. In particular, it can happen that most of the initial charge is shifted outside the cone. Furthermore, MCS at lower energies makes the cone model suboptimal near the tip. Therefore, the acceptance volume for the reconstruction is formed of the union of the cone with a cylinder of the same length, along the direction of the shower. The cylinder radius was tuned to optimise the trade-off between missed and misidentified energy deposition as defined below.

Argon Box propagates the neutrino interaction events it gets from GENIE through LAr, the output is a ROOT tree of neutrino interaction events. To get a realistic simulation of beam events in the detector these events need to be distributed randomly in time and space. Beam spills are simulated by drawing the number of events for each spill from a Poisson distribution whose mean is calculated from the beam intensity and the target mass according to the values in Table 2.2. The resulting number of events is taken from the Argon Box ROOT tree and their vertices are placed within the LAr volume at coordinates drawn from a uniform distribution. Combined with the target mass given in Table 6.2 this results in an equivalent of $\approx 1.5 \times 10^{19}$ POT. The seemingly low number (compared to Table 2.3) is the result of many neutrino interactions happening outside of the active detector.

Three different argon volumes are assumed for the simulation: target, active, and fiducial volume. The actual detector dimensions are represented by the active volume.

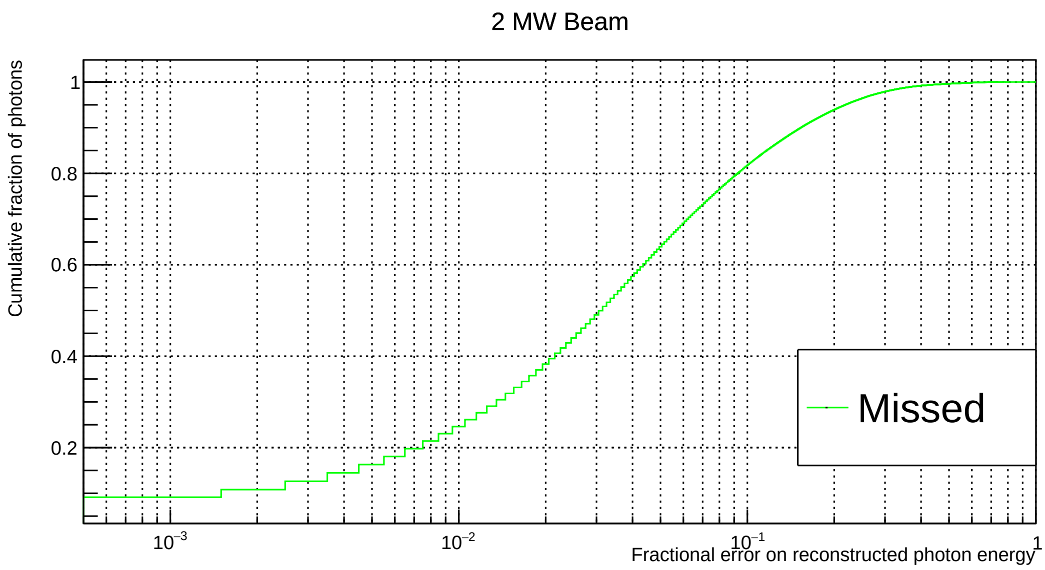

Figure 6.10.: Cumulative fraction of photons versus missed energy fraction for a simple π^0-induced EM shower reconstruction algorithm based on a cone-cylinder union. All energy deposited outside of the cone-cylinder union is counted as missed. The curve depicts the fraction of photons on the y-axis with a missed energy fraction equal to or lower than the corresponding value on the x-axis. 2 MW beam of 80 GeV protons.

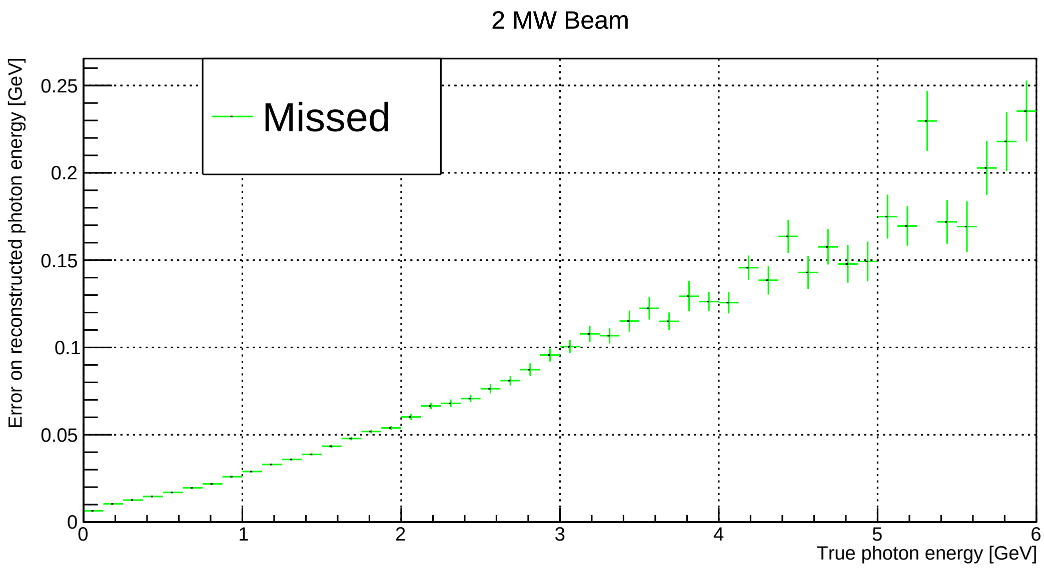

Figure 6.11.: Mean missed energy versus true photon energy for a simple π^0-induced EM shower reconstruction algorithm based on a cone-cylinder union. All energy deposited outside of the cone-cylinder union is counted as missed. 2 MW beam of 80 GeV protons.

It is inside the target volume which is the volume within which the neutrino vertices are placed randomly. This is done to crudely emulate rock events, secondary particles from beam neutrino interactions outside the detector volume. The additional target mass is 1 m in all four directions transverse to the beam and 4 m in upstream beam direction. According to Equations (2.57) and (2.58) hadronic showers up to 10 GeV are contained $> 95\,\%$ longitudinally and $> 50\,\%$ transversally (Equation (2.58) gives the radius for 95 % containment) in the additional volume. In other words, increasing the target volume further will not result in significantly more rock events entering the active volume. For transversal containment it is enough to use the radius for 95 % containment because the location of the shower is defined by its centre, i.e. showers further away than one 95 % radius from the detector only deposit a minimal amount of energy inside the detector. These numbers are supported by Geant4 simulations [126]. As mentioned in Section 2.5, EM interactions happen on smaller scales than hadronic interactions. The big exception are muons due to their high range. However, it makes sense to ignore pile-up from muons due to their high reconstruction efficiency, as will be explained below. Finally, a fiducial volume 30 cm ($\approx 2\,X_0$) smaller than the active volume on all six faces is defined. Without fiducialisation there is a significant number of photons produced by π^0 decays inside the detector but only showering outside the detector. This selection results in $\approx 5.5 \times 10^5$ processed π^0 photons from the initial 6.6×10^6 neutrino events. Table 6.2 contains a summary of all the LAr volume dimensions, Figure 6.6 shows an example event with all three volumes drawn.

Active volume dimensions are taken from the preliminary DUNE ND design described in Section 6.2. Note that the height was taken as 2.5 m as opposed to the 3 m of the ND design. The reason is that another 0.5 m safety margin were added after this pile-up simulation had been completed. The hadron containment studies described in Section 6.2 indicated that 2.5 m height is the bare minimum. A safety margin was added to account

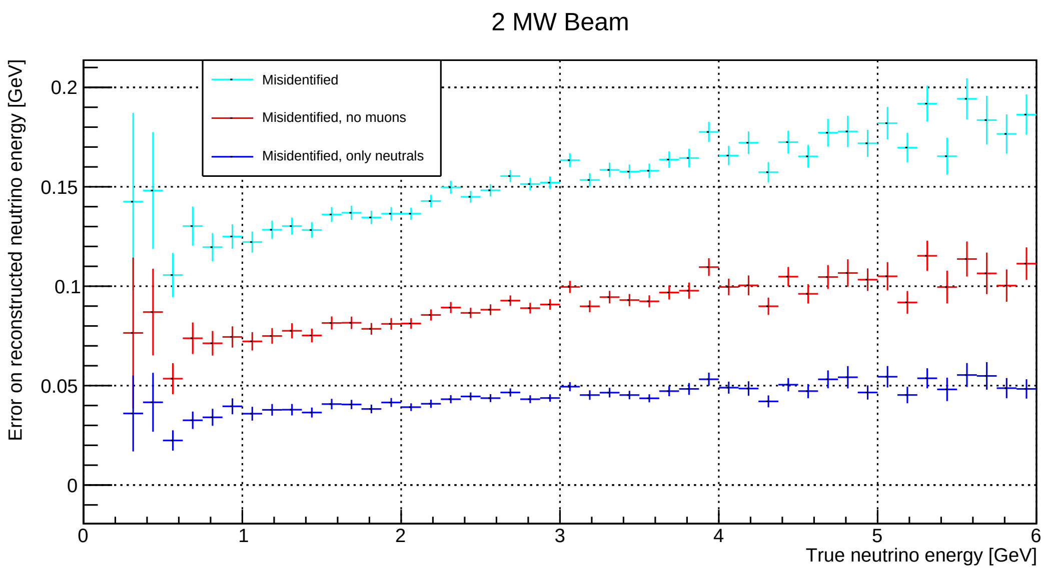

Figure 6.12.: Mean misidentified energy versus true neutrino energy for a simple π^0-induced EM shower reconstruction algorithm based on a cone-cylinder union. All energy deposited inside the cone-cylinder union by descendants of neutrinos different from the parent of the corresponding π^0 photon is counted as misidentified. Colour indicates different selections of misidentified energy: total (cyan); excluding depositions from muons (red); deposition from photons, neutrons, and their descendants only (blue). 2 MW beam of 80 GeV protons.

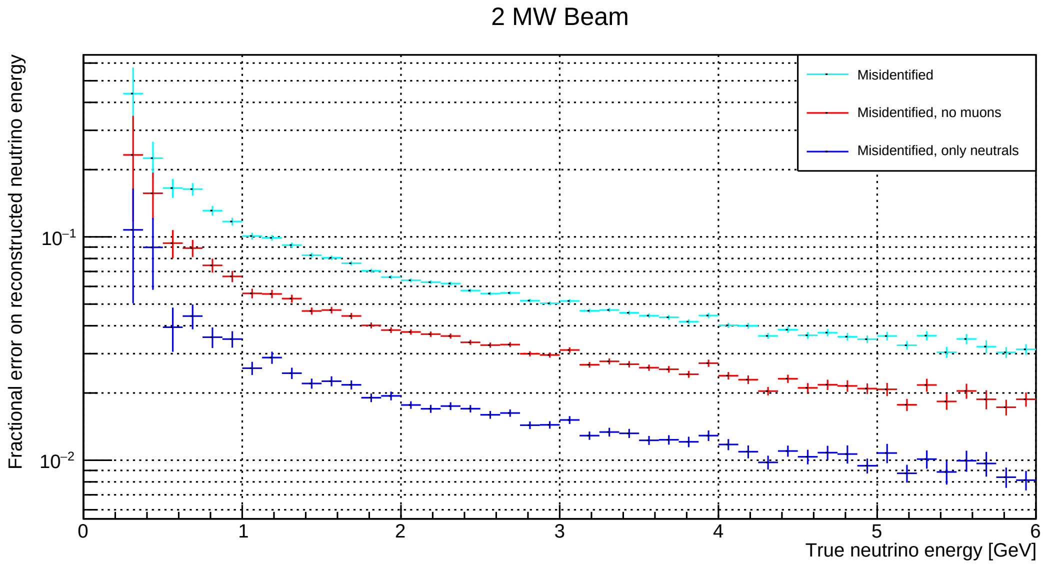

Figure 6.13.: Mean misidentified energy fraction versus true neutrino energy for a simple π^0-induced EM shower reconstruction algorithm based on a cone-cylinder union. All energy deposited inside the cone-cylinder union by descendants of neutrinos different from the parent of the corresponding π^0 photon is counted as misidentified. Colour indicates different selections of misidentified energy: total (cyan); excluding depositions from muons (red); deposition from photons, neutrons, and their descendants only (blue). 2 MW beam of 80 GeV protons.

for unknown uncertainties in the simulation. However, the same simulation framework was used for both the containment and the pile-up study. Therefore, the 2.5 m height is sufficient for the pile-up study.

Cosmic ray backgrounds are neglected for the following reasons. The ND hall will have an overburden of 53 m, 33 m of rock ($2.43\,\mathrm{g\,cm^{-3}}$) plus 20 m of dirt ($1.7\,\mathrm{g\,cm^{-3}}$). Simulations predict a muon rate of $2.7\,\mathrm{Hz\,m^{-2}}$ at the top of the hall [127]. Scaled up to the ArgonCube ND footprint of $4\,\mathrm{m} \times 5\,\mathrm{m}$, this results in a rate of 54 Hz for the whole LArTPC component. However, the majority of these events can be rejected by means of a beam spill trigger gate. Looking at Figure 6.5, the total readout time for one beam spill is 260 µs. Events outside of this window cannot originate from beam neutrinos. On average this results in 0.014 cosmic events per beam spill, compared to 14.7 beam

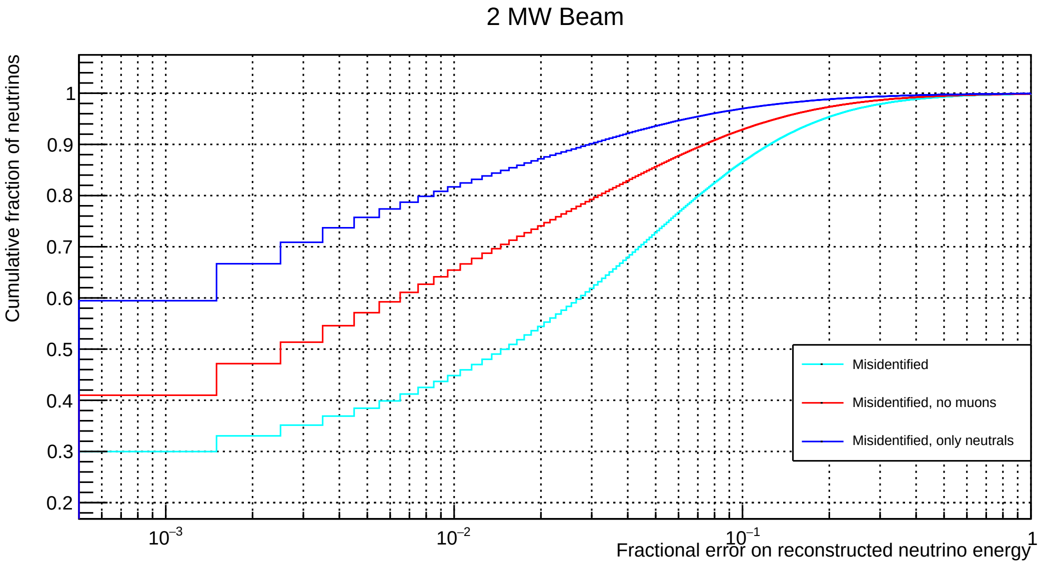

Figure 6.14.: Cumulative fraction of neutrinos versus misidentified energy fraction for a simple π^0-induced EM shower reconstruction algorithm based on a cone-cylinder union. All energy deposited inside the cone-cylinder union by descendants of neutrinos different from the parent of the corresponding π^0 photon is counted as misidentified. Colour indicates different selections of misidentified energy: total (cyan); excluding depositions from muons (red); deposition from photons, neutrons, and their descendants only (blue). The curve depicts the fraction of neutrinos on the y-axis with a misidentified energy fraction equal to or lower than the corresponding value on the x-axis. 2 MW beam of 80 GeV protons.

events in the simulated detector. Therefore, contributions from cosmic rays can be safely neglected.

After all events of one spill are placed inside the target volume, all π^0 photons produced inside the fiducial volume are reconstructed using the cone-cylinder algorithm. All energy depositions inside the active volume are considered. To assess the performance of the algorithm and the influence of pile-up on neutrino energy reconstruction the following two errors on the reconstructed energy are calculated for each π^0 photon:

Missed energy is the energy deposited by the corresponding π^0 photon (or its descendants) that is outside the cone-cylinder union and therefore "missed" by the algorithm. This is a measure of the reconstruction performance and can be used to ensure optimum tuning of the union parameters.

Misidentified energy is the energy inside the cone-cylinder union deposited by descendants of a different ("wrong") parent neutrino. This is a measure of event pile-up: the higher the charge deposition by other events inside the union, the higher the event pile-up.

Using this general definition of misidentified energy leads to quite mediocre results. However, there are some assumptions that can be taken even without knowing the actual reconstruction algorithm. From results of earlier experiments [124] the muon reconstruction can be assumed to be very efficient. Assuming 100 % reconstruction efficiency for muons and 0 % for all other particles can therefore serve as an upper limit for misidentified energy. It can be calculated by ignoring energy deposited by muons originating from other parent neutrinos. A lower limit for misidentified energy can be calculated by assuming 100 % reconstruction efficiency for all charged particles and 0 % for neutral particles (γ and n). This is calculated by only taking into account misidentified energy deposited by neutral particles. Even assuming 0 % reconstruction efficiency for neutral particles is potentially too pessimistic. Future, more sophisticated reconstruction algorithms (e.g. based on machine learning) might be able to partially reconstruct the topology of charge depositions originating from neutral particles and thus prevent their misidentification. Therefore, it can be assumed that the actual pile-up-related energy reconstruction error is closer to the lower limit and potentially even below. It should be noted that the upper limit excludes only energy deposited by muons directly and not by their descendants (e.g. δ rays or Michel electrons). Whereas the lower limit excludes charge deposited by photons, neutrons, and any of their descendants. Figure 6.7 illustrates the distinction of various energy depositions for an example event. In particular, it can be seen that δ rays (orange) are not counted towards energy deposited by muons (yellow). The long red track is an example of a deposition originating from a photon or

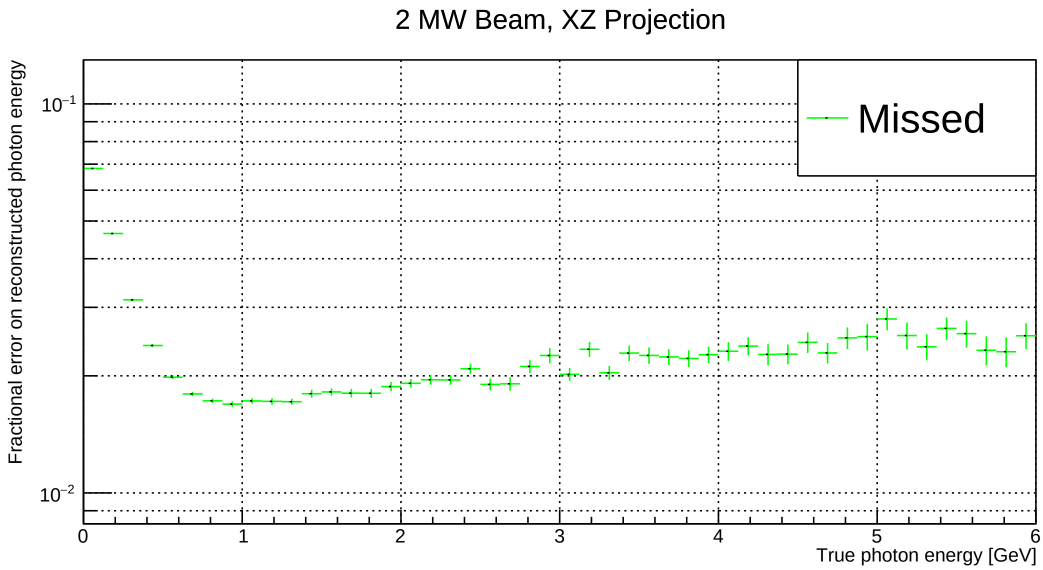

Figure 6.15.: Mean missed energy fraction versus true photon energy for a simple π^0-induced EM shower reconstruction algorithm based on a cone-cylinder union. All energy deposited outside of the cone-cylinder union is counted as missed. 2 MW beam of 80 GeV protons. As a primitive simulation of a 2D wire readout, only X- and Z-coordinates are used for the energy reconstruction.

neutron (descendant) included in the lower limit sample but very likely reconstructible by future algorithms.

Missed and misidentified energy by the cone-cylinder union are analysed as a function of true photon and neutrino energy, respectively. As mentioned above, the missed energy is used to measure the performance of the employed photon reconstruction algorithm. Therefore, it is sensible to compare it to the true photon energy rather than the true energy of its parent neutrino. On the other hand, the primary goal of this study is to assess the effect of event pile-up on the neutrino energy spectrum. The misidentified energy is thus compared to the true neutrino energy. For this the total misidentified energy of each neutrino event is first calculated by summing up the contributions of all descending π^0 photons. Additionally, it is illustrative to look at the fraction of events with a certain misidentified or missed energy. For misidentified energy this is the fraction of neutrino events containing π^0-induced EM showers, not the fraction of all neutrino events. All the aforementioned information is contained in 2D histograms of all events with the true neutrino (photon) energy on one axis and the misidentified (missed) energy on the other axis. The energy dependence of the error can be obtained by looking at the true energy axis and calculating the mean misidentified (missed) energy for each bin (a profile of the 2D histogram). Looking at the misidentified (missed) energy axis and summing over all true energy bins yields the number of events with the corresponding misidentified (missed) energy (a projection of the 2D histogram). The corresponding fraction of events is obtained by normalising the histogram, i.e. dividing every bin by the total number of entries. It should be noted that for the projections all values in the corresponding y-bin are taken into account, including the ones outside the boundaries of the histogram (under- and overflow). For the profiles, only events with energies from 0 GeV to 6 GeV or energy fractions from 0 to 1 are taken into account.

The results for a 2 MW beam at 80 GeV proton energy are shown in Figures 6.8 through 6.14. To illustrate the relation between the different histograms all of them are shown for the missed energy in Figures 6.8 through 6.10. The initial 2D histogram is shown in Figure 6.8. Note that it actually depicts the missed photon energy as a fraction of the true photon energy rather than an absolute value. Figure 6.9 is the profile of the x-axis, i.e. the mean missed energy fraction for each true energy bin. The projection of the y-axis is depicted in Figure 6.10. This is the fraction of photons with a certain missed energy. It is drawn as a cumulative fraction, which means that the curve represents the fraction of photons on the y-axis with a missed energy fraction equal to or lower than the corresponding value on the x-axis. A consequence of this is that the curve monotonically approaches one towards the right, 100 % of the reconstructed photons have a missed energy fraction of 100 % or less. For reference Figure 6.11 shows the mean absolute missed energy per true energy bin.

It can be seen that the absolute missed energy rises more or less linearly with the true

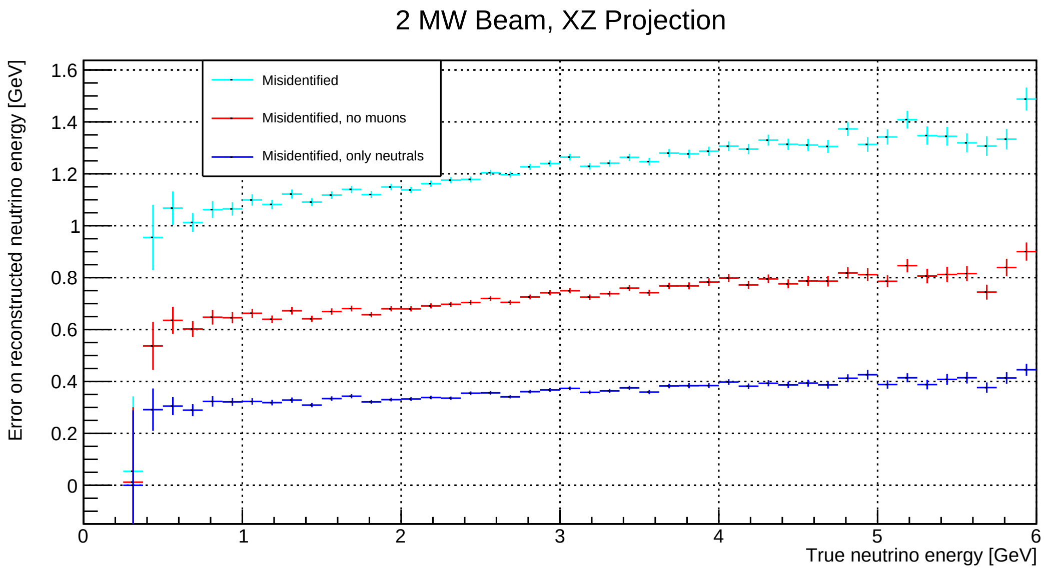

Figure 6.16.: Mean misidentified energy versus true neutrino energy for a simple π^0-induced EM shower reconstruction algorithm based on a cone-cylinder union. All energy deposited inside the cone-cylinder union by descendants of neutrinos different from the parent of the corresponding π^0 photon is counted as misidentified. Colour indicates different selections of misidentified energy: total (cyan); excluding depositions from muons (red); deposition from photons, neutrons, and their descendants only (blue). 2 MW beam of 80 GeV protons. As a primitive simulation of a 2D wire readout, only X- and Z-coordinates are used for the energy reconstruction.

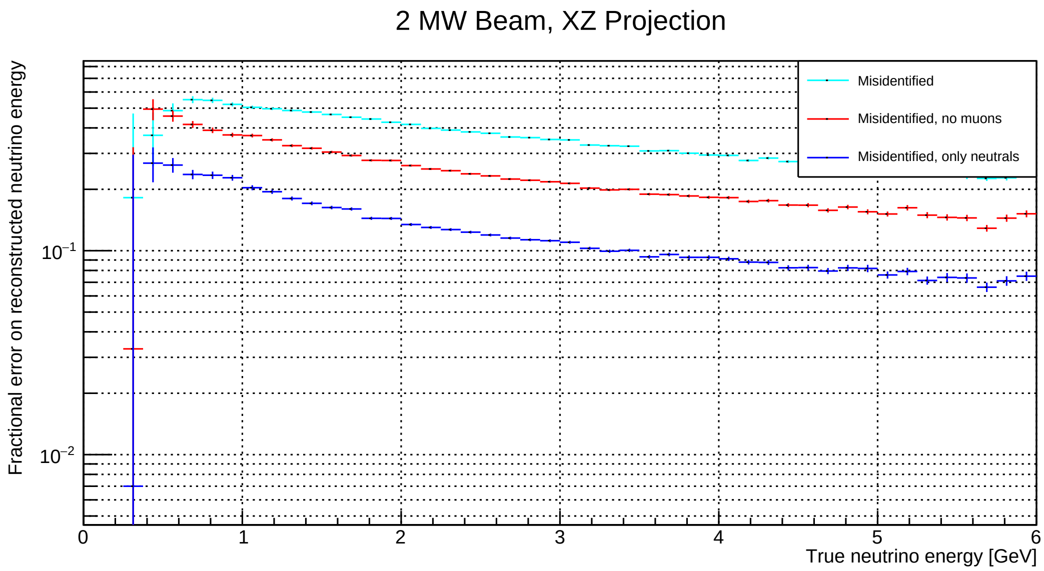

Figure 6.17.: Mean misidentified energy fraction versus true neutrino energy for a simple π^0-induced EM shower reconstruction algorithm based on a cone-cylinder union. All energy deposited inside the cone-cylinder union by descendants of neutrinos different from the parent of the corresponding π^0 photon is counted as misidentified. Colour indicates different selections of misidentified energy: total (cyan); excluding depositions from muons (red); deposition from photons, neutrons, and their descendants only (blue). 2 MW beam of 80 GeV protons. As a primitive simulation of a 2D wire readout, only X- and Z-coordinates are used for the energy reconstruction.

energy (Figure 6.11). This indicates that the cone models the shower well, as expected from theory (see Section 2.5). Indeed, it can be seen from Figure 6.9 that the missed energy fraction stays almost constant at 3 % from 1 GeV to 6 GeV. It starts to increase below 1 GeV, reaching almost 10 % in the lowest energy bin (0 MeV to 125 MeV). This can be explained by the increase in MCS at lower momenta. Similarly, the Compton scattering cross-section increases as well. Both these effects lead to a higher angular distribution of the energy deposited by electrons (and positrons) and photons. Consequentially, more energy is missed because the cone angle is independent of energy. From Figure 6.10 it can be seen that for roughly half of the photons 3 % of the energy is missed, indicating a symmetric distribution of missed energy around the mean value. It should be noted that energy deposited outside the detector, so-called leakage, is included in the missed energy. Despite the fiducial volume some events still exit the detector.

The behaviour of the misidentified energy is almost opposite to the missed energy: The absolute value is almost constant with the true neutrino energy (Figure 6.12) while the fraction of the total energy is inversely proportional to the true energy, accordingly (Figure 6.13). This is expected as the amount of charge deposited inside the cone originating from other neutrinos should only depend on the geometry of the acceptance volume (i.e. the parameters of the cone-cylinder union) and on the event rate, but not on the true energy of the reconstructed photon or its parent neutrino. The effect of the different misidentified energy selections can be seen well. As mentioned above, the actual error on the reconstructed neutrino energy is probably somewhere in between the red curve, only rejecting misidentified energy deposited by muons, and the dark blue curve, rejecting all but misidentified energy deposited by photons and neutrons or any of their descendants. From Figure 6.13 this can be determined to be about 2 % to 3 % at the flux peak (≈ 2.5 GeV, see Figure 2.7). The cumulative neutrino fraction versus the misidentified energy fraction reveals another interesting fact: It can be seen that about

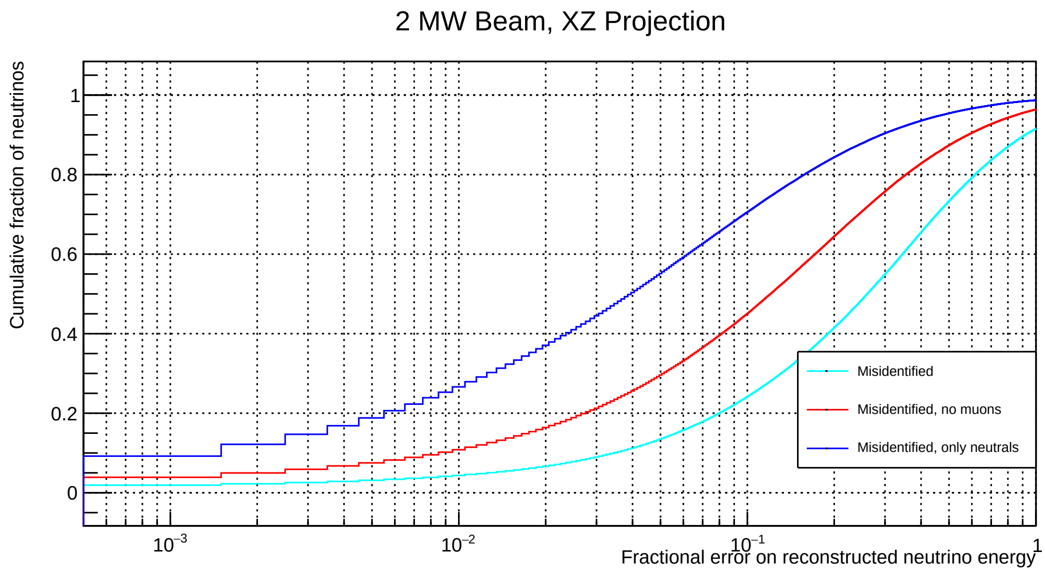

Figure 6.18.: Cumulative fraction of neutrinos versus misidentified energy fraction for a simple π^0-induced EM shower reconstruction algorithm based on a cone-cylinder union. All energy deposited inside the cone-cylinder union by descendants of neutrinos different from the parent of the corresponding π^0 photon is counted as misidentified. Colour indicates different selections of misidentified energy: total (cyan); excluding depositions from muons (red); deposition from photons, neutrons, and their descendants only (blue). The curve depicts the fraction of neutrinos on the y-axis with a misidentified energy fraction equal to or lower than the corresponding value on the x-axis. 2 MW beam of 80 GeV protons. As a primitive simulation of a 2D wire readout, only X- and Z-coordinates are used for the energy reconstruction.

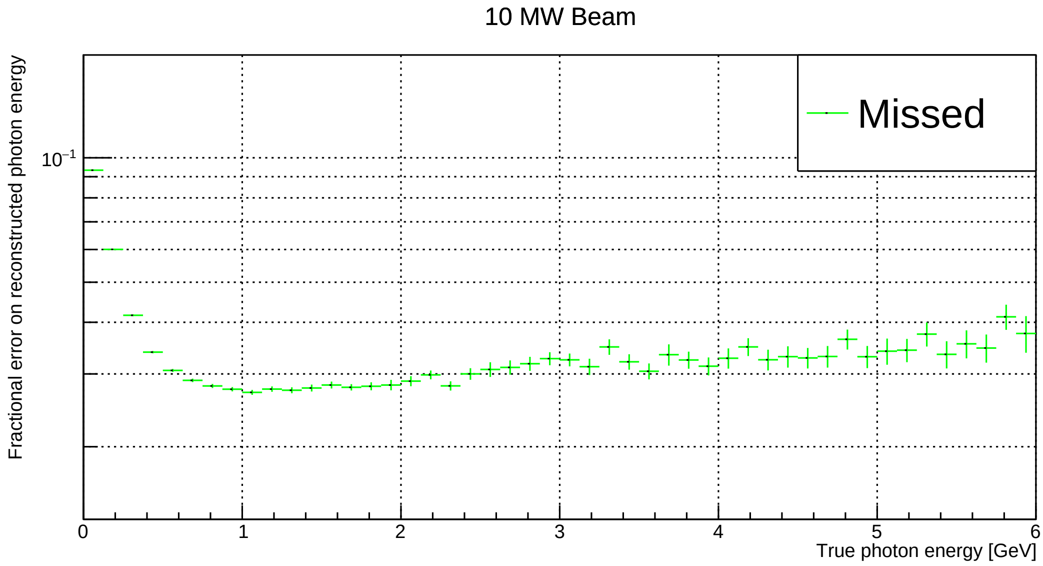

Figure 6.19.: Mean missed energy fraction versus true photon energy for a simple π^0-induced EM shower reconstruction algorithm based on a cone-cylinder union. All energy deposited outside of the cone-cylinder union is counted as missed. 10 MW beam of 80 GeV protons.

70 % of the events experience a pile-up-related error on reconstructed neutrino energy of 1 % or less. For roughly 50 % of the events it is even below 0.1 %. If it was possible to identify the other 50 % somehow in the real experiment, they could be ignored, giving an essentially pile-up-free sample. This would be easily affordable given the high event rates in the ND. In case of the cone-based algorithm described here, EM shower pile-up could be detected via overlapping cones for instance.

To get a rough idea of the performance of a 2D wire readout in an identical environment the same study was performed ignoring the Y-coordinate completely, leaving everything else untouched. Of course, this is a gross underestimation of the capabilities of existing reconstruction algorithms for 2D charge readout data. In particular, contemporary experiments use at least three 2D projections whereas only one was used here. Even though, doing this comparison serves to show that the simple cone-cylinder union reconstruction algorithm breaks down for two dimensions as can be seen in Figures 6.15 through 6.18. The fraction of events not suffering from pile-up is below 10 % while 50 %

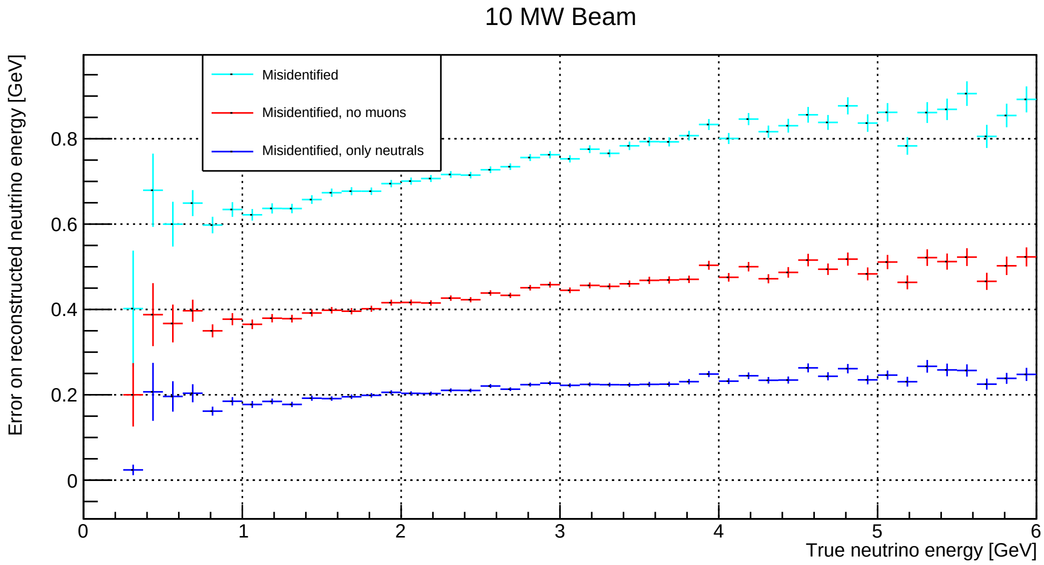

Figure 6.20.: Mean misidentified energy versus true neutrino energy for a simple π^0-induced EM shower reconstruction algorithm based on a cone-cylinder union. All energy deposited inside the cone-cylinder union by descendants of neutrinos different from the parent of the corresponding π^0 photon is counted as misidentified. Colour indicates different selections of misidentified energy: total (cyan); excluding depositions from muons (red); deposition from photons, neutrons, and their descendants only (blue). 10 MW beam of 80 GeV protons.

have 10 % or more misidentified energy (Figure 6.18). Similarly, the error on energy reconstruction has increased to 12 % to 23 % at the flux peak (Figure 6.17). On the other hand, the error due to missed energy has improved from 3 % to 2 % compared to 3D (Figure 6.15). An explanation for this is that all the energy in Y-direction was summed up due to the projection on XZ. Therefore, the cone (or rather triangle) cannot miss energy in the former direction.

Finally, as a cross-check the (3D) pile-up study was performed for a hypothetical 10 MW beam in Figures 6.19 through 6.22. As explained above, the missed energy only depends on the geometry of the acceptance volume, it should be independent of beam intensity. Therefore, it is expected to be very similar to the 2 MW case, as can be confirmed by comparing Figure 6.19 to Figure 6.9. As expected, the error due to misidentified energy

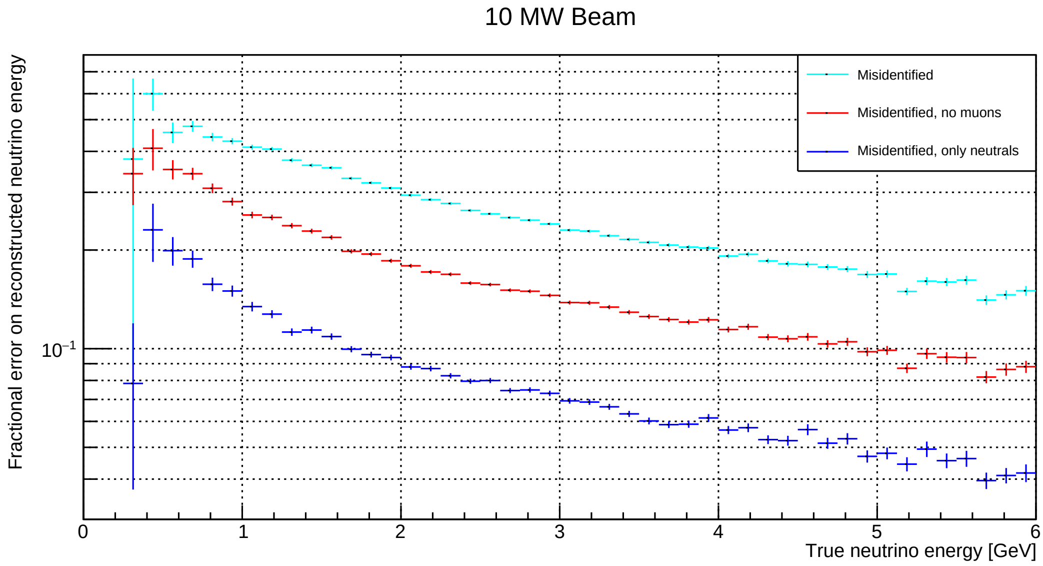

Figure 6.21.: Mean misidentified energy fraction versus true neutrino energy for a simple π^0-induced EM shower reconstruction algorithm based on a cone-cylinder union. All energy deposited inside the cone-cylinder union by descendants of neutrinos different from the parent of the corresponding π^0 photon is counted as misidentified. Colour indicates different selections of misidentified energy: total (cyan); excluding depositions from muons (red); deposition from photons, neutrons, and their descendants only (blue). 10 MW beam of 80 GeV protons.

is increased to 8 % to 15 % at the flux peak (Figure 6.21) but still better than for the XZ projection. Similarly, only about 10 % of the neutrino events remain pile-up free while 50 % suffer from more than 4 % misidentified energy (Figure 6.22).

In summary, I have shown that even a very simple EM shower reconstruction algorithm, employing a cone-cylinder union selection, performs well in the high-multiplicity environment of the DUNE ND, when fed with unambiguous 3D spatial coordinates of energy depositions. The mean deposited energy missed by the algorithm is less than 3 %. More importantly, the pile-up-related misidentification of energy depositions from other events has a mean of 2 % to 3 %. For more than 50 % of the neutrino events containing π^0-induced EM showers this error is even smaller than 0.1 %. If a way is found to flag the other 50 % as piled up during event reconstruction, a sample of neutrino

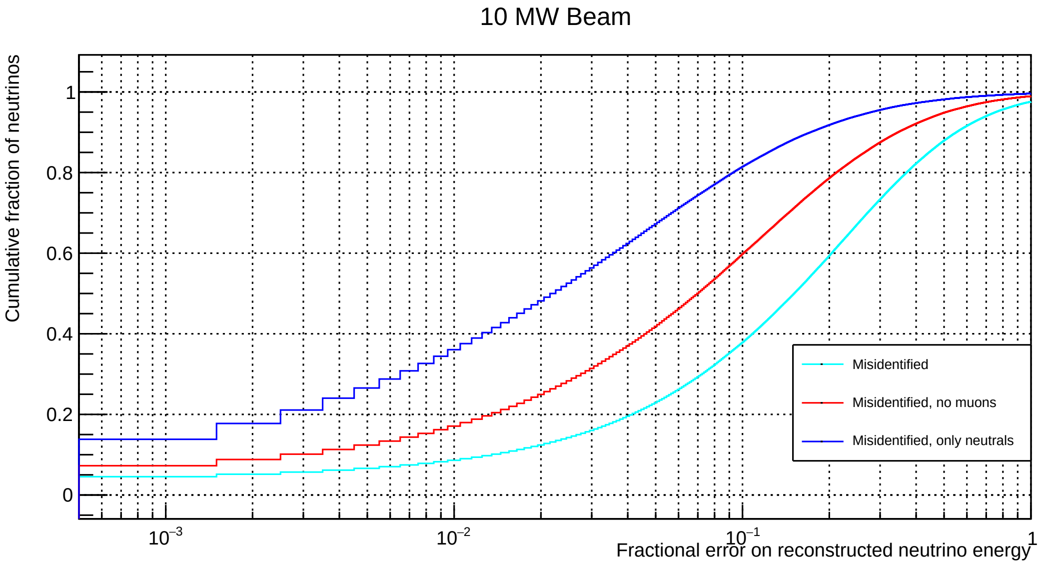

Figure 6.22.: Cumulative fraction of neutrinos versus misidentified energy fraction for a simple π^0-induced EM shower reconstruction algorithm based on a cone-cylinder union. All energy deposited inside the cone-cylinder union by descendants of neutrinos different from the parent of the corresponding π^0 photon is counted as misidentified. Colour indicates different selections of misidentified energy: total (cyan); excluding depositions from muons (red); deposition from photons, neutrons, and their descendants only (blue). The curve depicts the fraction of neutrinos on the y-axis with a misidentified energy fraction equal to or lower than the corresponding value on the x-axis. 10 MW beam of 80 GeV protons.

events almost free of pile-up can be generated. In comparison, the FD is required to have an energy resolution for stopping hadrons below 10 % and an electron energy resolution of $1\,\% \oplus 15\,\% \times \sqrt{\frac{1\,\mathrm{MeV}}{E}}$ [28]. Provided that a successful LArPix enables unambiguous 3D tracking information, ArgonCube will be capable of handling the high rates expected in the DUNE ND environment without significant contributions to the error budget. The employed reconstruction algorithm clearly fails when reduced to two dimensions or confronted with a much higher beam intensity.

7. Conclusion

DUNE is a long-baseline neutrino oscillation experiment aiming to discover CP violation in the lepton sector and determine the neutrino mass ordering. LArTPCs will be deployed in the FD complex due to their excellent tracking and calorimetric capabilities. A LArTPC component is also required in the ND complex to bring beam-related systematic uncertainties below the required 2 %. The ND environment will be very challenging due to the slow readout ($\approx 0.5\,\mathrm{ms\,m^{-1}}$) of LArTPCs compared to the beam spill duration ($10\,\mathrm{\mu s}$). The high beam intensity will therefore lead to 0.2 neutrino events per tonne of argon and beam spill. In this thesis most of the relevant challenges for LArTPCs in future high-multiplicity environments were studied alongside potential solutions, namely the dielectric strength of LAr, new charge and light readout methods, as well as the required next-generation charge readout electronics.

The ARGONTUBE detector demonstrator built at LHEP found the dielectric strength of LAr to be much lower than the predicted $\approx 1\,\mathrm{MV\,cm^{-1}}$. This led to a systematic study of dielectric breakdowns in LAr. In particular, we found that the dielectric strength is dependent on absolute dimensions. I recorded and analysed high-speed footage, current-voltage characteristics, and optical spectrometry of breakdowns. A conclusive theory of dielectric breakdowns in LAr at the centimetre scale was developed [6]. The phenomenon is governed by three distinct phases: field emission, streamer, and spark. Understanding the process enabled the development of a technique to mitigate breakdowns [7]. However, this solution proved to be unreliable. Only keeping fields below $40\,\mathrm{kV\,cm^{-1}}$ everywhere in the detector guarantees a safe operation. This can either be reached by decreasing cathode voltages or increasing uninstrumented clearance volumes around HV components. Avoiding additional dead LAr volume intrinsically motivates a segmented TPC design with lower cathode voltages.

Classical wire plane readouts of LArTPCs have significant drawbacks. Besides their mechanical fragility, they cripple the excellent 3D tracking capabilities of a TPC by reducing it to multiple 2D projections. This is highly problematic in high-multiplicity environments such as the DUNE ND due to the complex event topologies resulting from event pile-up. In a preliminary study I showed that the mechanical challenges met by wire plane charge readouts can be alleviated by replacing the wires with copper tracks printed on a thin Kapton layer. However, this does not solve the inherent ambiguities caused by wires. A true 2D readout in form of pixels is needed instead.

Realising a pixelated LArTPC is complicated by the high number of channels. Cold digitisation can help by aggregating many pixels on a single high-speed digital link, reducing the number of required cable feedthroughs out of the cryostat. I evaluated the cold digitisers foreseen for the DUNE FD and found them to be unsuitable for a pixelated ND. Being optimised for wire readouts their power dissipation is much too high given the required number of channels. With no suitable cold electronics at hand I implemented a form of analogue multiplexing to demonstrate a pixelated LArTPC at the price of introducing some ambiguities in the 3D spatial information. Like this it was possible to use the existing charge readout electronics from ARGONTUBE. The successful demonstration of pixels provides the basis for the charge readout in ArgonCube.

I designed and built a new prototype TPC to test the pixelated charge readout scheme. I extended the ARGONTUBE readout electronics by a differential warm signal path and reduced the parasitic capacitances in the pixel readout PCB. With this improvements an SNR of 14 was reached, proving pixels feasible for operation in real physics experiments.

Together with the LAr group of LHEP I successfully recorded several thousand cosmic muon tracks. These results triggered the development of bespoke cold pixel electronics, LArPix, by LBNL aimed to eventually enable an ambiguity-free pixelated charge readout in ArgonCube. LArPix uses a smart zero suppression scheme to meet the stringent power dissipation requirements of a pixelated charge readout.

I developed a new software framework to reconstruct the cosmic muon tracks recorded with the pixel demonstrator. The hit finder had to be written from scratch because all existing LArTPC reconstruction frameworks are optimised for wire readouts. A PCA was employed to solve the ambiguities stemming from the analogue multiplexing. Finally, the unambiguous 3D measurements were fed to GENFIT, an existing generic track-fitting toolkit based on a Kalman filter. Therewith, I obtained fully reconstructed cosmic muon tracks, illustrating the advantages of the ArgonCube approach over existing schemes. This software framework serves as a starting point for future efforts on the reconstruction of true 3D spatial information recorded with ArgonCube. Both pixel demonstration and 3D event reconstruction have been presented at conferences [10] by me and published in a paper [11] of which I am corresponding author.

The pixel demonstrator TPC was also used to test the operation of SiPMs in LAr for the light trigger system. Based on the findings LHEP developed ArCLight [9], a light trap maximising the area coverage of SiPMs while minimising the occupied volume. It provides a compact light readout for ArgonCube which cannot use a classic PMT-based light readout occupying large volumes. I contributed to the testing and characterisation of ArCLight.

Scaled up versions of both ArCLight and the pixelated charge readout were successfully tested in the PixLAr test beam experiment at FNAL. These results pave the way for an application of both technologies in ArgonCube.

Finally, I performed an event pile-up study using simulated π^0 decay photons to demonstrate the ability of a pixelated LArTPC to cope with the high event rates expected in the DUNE ND. At DUNE energies such photons produce EM showers consisting of a plethora of small disconnected charge depositions in the detector. Correctly associating these to the right neutrino event is one of the most difficult reconstruction tasks. At the same time, failure to reconstruct them properly significantly distorts the reconstructed neutrino energy spectrum. Based on the results from the pixel demonstrator I assumed unambiguous 3D position information for the charge depositions. I employed a simple cone-based algorithm to associate the charge to the corresponding photon. The mean deposited energy missed by the algorithm was found to be less than 3 %. More importantly the pile-up-related misidentification of energy depositions from other events was found to have a mean of 2 % to 3 %. For more than 50 % of the neutrino events this error is even smaller than 0.1 %. If a way is found to flag the other 50 % as piled-up events, a sample of neutrino events almost free of pile-up can be generated. In comparison, the FD is required to have an energy resolution for stopping hadrons below 10 % and an electron energy resolution of $1\,\% \oplus 15\,\% \times \sqrt{\frac{1\,\mathrm{MeV}}{E}}$. Therefore, a pixelated ArgonCube providing unambiguous 3D tracking information will be capable of handling the high rates expected in the DUNE ND environment without significant contributions to the error budget.

The combination of results from all of this work builds the groundwork for the ArgonCube, a novel fully modular LArTPC concept, addressing the most important challenges of future neutrino detectors, in particular the DUNE ND. High cathode voltages are prevented by splitting the detector into several small, self-contained TPCs requiring only a moderate 50 kV cathode voltage. A pixelated charge readout enables the true 3D tracking required to cope with the high event rates resulting from the high-intensity neutrino beam. The ArCLight readout minimises the occupied dead volume inside the modules resulting in a similar performance to a monolithic detector. At the same time, the scintillation light is contained within each module, simplifying association to the correct ionisation signals.

With the most important key technologies for ArgonCube tested the path is clear for the first modules in the 2×2 module prototype at LHEP, which will test the unification of all the pieces provided by this work. Cosmic ray events will be recorded and analysed with the developed reconstruction framework to characterise the physics performance of ArgonCube. After successful cosmic tests, beam tests will follow at either CERN or FNAL. The improvements I made allow LArTPCs to operate in high-multiplicity environments and led to ArgonCube being the baseline LAr component of the DUNE ND complex.

Several aspects of the presented work can be continued in the future to further improve LArTPC technology. Finding a more reliable coating material than latex for HV components could enable large monolithic detectors. A continuous resistive field cage has the potential to provide a highly uniform electric field with a simple mechanical structure. Recent tests indicate that the power dissipation of LArPix is low enough to make a pixelated DUNE FD conceivable. Even though not deemed a requirement as of today, this would simplify event reconstruction tremendously and improve sensitivities accordingly. Finally, the modular ArgonCube concept can easily be adapted to other experiments requiring a high-density, high-precision tracker and calorimeter.

Acknowledgements

I want to thank my supervisor **Antonio Ereditato** for making this thesis possible. In particular, you supported my decision to write a hardware thesis, which would not have been possible at many other institutions.

I would like to express my gratitude to my examiners **Hucheng Chen** and **Peter Wurz**.

Some of my biggest appreciations go towards **Igor Kreslo**, who taught me most of my detector physics knowledge and (almost) always had an answer to my questions. It was always enlightening and great pleasure discussing with you and being challenged by you.

I also want to thank **Michele Weber** for the many times he provided me with a simple solution to a seemingly complex problem, be it physical or organisational.

I am really grateful to **James Sinclair** for his guidance, in particular towards the end of my thesis. More than once, you prevented me from despairing or accidentally killing myself in the lab. Surprisingly, you never got tired of reading my thesis and fixing my abominations of the English language.

Without the input of **Yun-Tse Tsai** and **Tracy Usher** from SLAC I would not have succeeded at reconstructing the pixel data. Thank you!

A very big thank you to **Dean Shooltz** from LArIAT for providing the documentation of the differential warm signal path of LArIAT. This allowed me to tame our noise-haunted setup.

I am grateful to **Hucheng Chen**, **Gianluigi De Geronimo**, **Neena Nambiar**, **Emerson Vernon**, **Jack Fried**, **Shanshan Gao**, and **Linda Feierabend** for the great time I had at BNL and everything they taught me about electronics. I really enjoyed the company of **Aseem Gupta**, **Stefania Stucci**, and **Hannah Herde**.

I want to thank **Kam-Biu Luk** and the neutrino group at LBNL for hosting me. In particular, I am grateful to **Daniel Dwyer** for telling me everything about LArPix, and **Chris Marshall** for his guidance on the ND pile-up study.

None of this would have been possible without the excellent support of **Camilla Tognina** and **Pascal Lutz** from the LHEP electronics workshop, and **Roger Hänni**, **Jan Christen**, **Lorenzo Meier**, **Gregor Pfäffli**, and **Roger Liechti** from the LHEP mechanical workshop. Thank you!

I am really thankful to all the friends I have made at LHEP for the magnificent time: **Martin Auger**, **Matthias Lüthi**, **Christoph Urs Benjamin Rudolf von Rohr**, **James Sinclair**, **David Low Redshift survey at Calar Alto (LoRCA)**, **Camilla Tognina**, **Sabina Joos**, **Francesca Stocker**, **Yifan Chen**, **Sébastien Delaquis**, **Martti Nirkko**, **Lukas Bütikofer**, **Daniel Coderre**, **Marcel Häberli**, and **Martin Hierholzer**. Working (and having fun) with you never became boring.

Furthermore, I am grateful to **Ursula Witschi**, **Marcella Esposito**, and **Irene Neeser** from the LHEP secretariat for their patience with my inferior organisation.

I also appreciate the computing support from **Jeremy Singh**, **Gianfranco Sciacca**, and **Luis Martinez**.

My warmest thanks go towards all my friends for their continued support, even though I neglected them more than once during the last four years.

I am most grateful to my flatmate **Annette Mettler** and her husband **Raphaël Guillet** for bearing with me for the last years. You have become like family to me.

Most of all I want to thank my parents, **Brigitte** and **Willi Göldi**, and my brother,

Sebastian Göldi, for their (moral and financial) support. You taught me the most important lesson in science (and maybe also life): Always stay curious and question everything.

Bibliography

[1] C. Giunti and C. Kim. *Fundamentals of Neutrino Physics and Astrophysics*. OUP Oxford, 2007. ISBN: 9780191523229. URL: https://books.google.ch/books?id=2faTXKIDnfgC (cit. on p. ix).

[2] C. Grupen and B. Shwartz. *Particle Detectors*. Cambridge Monographs on Particle Physics, Nuclear Physics and Cosmology. Cambridge University Press, 2008. ISBN: 9781139469531. URL: https://books.google.ch/books?id=XCPlJTu3GQkC (cit. on pp. ix, 33, 35).

[3] N. Schmitz. *Neutrinophysik*. Teubner Studienbücher Physik. Vieweg+Teubner Verlag, 2013. ISBN: 9783322801142. URL: https://books.google.ch/books?id=Ud2SxVnGIgIC (cit. on p. ix).

[4] E. Aprile et al. *Noble Gas Detectors*. Wiley, 2007. ISBN: 9783527609635. URL: https://books.google.ch/books?id=tsnHM8x6cHAC (cit. on pp. ix, 42).

[5] M. Schenk. 'Study of cosmic muon and UV laser induced events with a large liquid argon TPC'. MA thesis. University of Bern, Switzerland, 2014 (cit. on pp. ix, 48).

[6] M. Auger et al. 'On the Electric Breakdown in Liquid Argon at Centimeter Scale'. In: *JINST* 11.03 (2016), P03017. DOI: 10.1088/1748-0221/11/03/P03017. arXiv: 1512.05968 [physics.ins-det] (cit. on pp. ix, 53, 59, 61, 63, 75, 172).

[7] M. Auger et al. 'A method to suppress dielectric breakdowns in liquid argon ionization detectors for cathode to ground distances of several millimeters'. In: *JINST* 9 (2014), P07023. DOI: `10.1088/1748-0221/9/07/P07023`. arXiv: `1406.3929 [physics.ins-det]` (cit. on pp. ix, 74, 172).

[8] M. Auger. 'New Micromegas based Readout techniques for Imaging in Time Projection Chambers'. PhD thesis. University of Bern, Switzerland, 2012 (cit. on pp. x, 81).

[9] M. Auger et al. 'ArCLight—A Compact Dielectric Large-Area Photon Detector'. In: *Instruments* 2.1 (2018), p. 3. ISSN: 2410-390X. DOI: `10.3390/instruments2010003`. URL: `http://www.mdpi.com/2410-390X/2/1/3` (cit. on pp. x, 105, 109, 174).

[10] J. Asaadi et al. 'A pixelated charge readout for Liquid Argon Time Projection Chambers'. In: *Journal of Instrumentation* 13.02 (2018), p. C02008. URL: `http://stacks.iop.org/1748-0221/13/i=02/a=C02008` (cit. on pp. x, 112, 174).

[11] J. Asaadi et al. 'First Demonstration of a Pixelated Charge Readout for Single-Phase Liquid Argon Time Projection Chambers'. In: (2018). arXiv: `1801.08884 [physics.ins-det]` (cit. on pp. x, 112, 174).

[12] W. Pauli. 'Dear radioactive ladies and gentlemen'. In: *Phys. Today* 31N9 (1978), p. 27 (cit. on pp. 1, 6).

[13] F. Reines et al. 'Detection of the Free Antineutrino'. In: *Phys. Rev.* 117 (1 Jan. 1960), pp. 159–173. DOI: `10.1103/PhysRev.117.159`. URL: `https://link.aps.org/doi/10.1103/PhysRev.117.159` (cit. on pp. 1, 2, 6).

[14] Y. Fukuda et al. 'Measurement of a small atmospheric ν_μ/ν_e ratio'. In: *Physics Letters B* 433.1 (1998), pp. 9–18. ISSN: 0370-2693. DOI: `http://dx.doi.org/`

10.1016/S0370-2693(98)00476-6. URL: http://www.sciencedirect.com/science/article/pii/S0370269398004766 (cit. on pp. 1, 2, 12).

[15] Y. Fukuda et al. 'Study of the atmospheric neutrino flux in the multi-GeV energy range'. In: *Physics Letters B* 436.1 (1998), pp. 33–41. ISSN: 0370-2693. DOI: http://dx.doi.org/10.1016/S0370-2693(98)00876-4. URL: http://www.sciencedirect.com/science/article/pii/S0370269398008764 (cit. on pp. 1, 2, 12).

[16] Q. R. Ahmad et al. 'Direct Evidence for Neutrino Flavor Transformation from Neutral-Current Interactions in the Sudbury Neutrino Observatory'. In: *Phys. Rev. Lett.* 89 (1 June 2002), p. 011301. DOI: 10.1103/PhysRevLett.89.011301. URL: https://link.aps.org/doi/10.1103/PhysRevLett.89.011301 (cit. on pp. 1, 2, 12).

[17] B. Pontecorvo. 'Inverse Beta Processes and Nonconservation of Lepton Charge'. In: *Journal of Experimental and Theoretical Physics* 7.1 (July 1958), p. 172. URL: http://www.jetp.ac.ru/cgi-bin/dn/e_007_01_0172.pdf (cit. on pp. 1, 15).

[18] Z. Maki, M. Nakagawa and S. Sakata. 'Remarks on the Unified Model of Elementary Particles'. In: *Progress of Theoretical Physics* 28.5 (1962), pp. 870–880. DOI: 10.1143/PTP.28.870. eprint: /oup/backfile/content_public/journal/ptp/28/5/10.1143/ptp.28.870/2/28-5-870.pdf. URL: +%20http://dx.doi.org/10.1143/PTP.28.870 (cit. on pp. 1, 15).

[19] E. Majorana. 'Teoria simmetrica dell'elettrone e del positrone'. In: *Il Nuovo Cimento (1924-1942)* 14.4 (Sept. 2008), p. 171. ISSN: 1827-6121. DOI: 10.1007/BF02961314. URL: https://doi.org/10.1007/BF02961314 (cit. on pp. 1, 15).

[20] C. Patrignani et al. 'Review of Particle Physics'. In: *Chinese Physics C* 40.10 (2016), p. 100001. URL: `http://stacks.iop.org/1674-1137/40/i=10/a=100001` (cit. on pp. 1, 21, 150).

[21] R. Davis, D. S. Harmer and K. C. Hoffman. 'Search for Neutrinos from the Sun'. In: *Phys. Rev. Lett.* 20 (21 May 1968), pp. 1205–1209. DOI: `10.1103/PhysRevLett.20.1205`. URL: `https://link.aps.org/doi/10.1103/PhysRevLett.20.1205` (cit. on pp. 2, 8).

[22] B. T. Cleveland et al. 'Measurement of the Solar Electron Neutrino Flux with the Homestake Chlorine Detector'. In: *The Astrophysical Journal* 496.1 (1998), p. 505. URL: `http://stacks.iop.org/0004-637X/496/i=1/a=505` (cit. on pp. 2, 8).

[23] F. P. An et al. 'Measurement of electron antineutrino oscillation based on 1230 days of operation of the Daya Bay experiment'. In: *Phys. Rev. D* 95 (7 Apr. 2017), p. 072006. DOI: `10.1103/PhysRevD.95.072006`. URL: `https://link.aps.org/doi/10.1103/PhysRevD.95.072006` (cit. on pp. 2, 14).

[24] K. Abe et al. 'Measurements of neutrino oscillation in appearance and disappearance channels by the T2K experiment with 6.6×10^{20} protons on target'. In: *Phys. Rev. D* 91 (7 Apr. 2015), p. 072010. DOI: `10.1103/PhysRevD.91.072010`. URL: `https://link.aps.org/doi/10.1103/PhysRevD.91.072010` (cit. on pp. 2, 14).

[25] R. Acciarri et al. 'Long-Baseline Neutrino Facility (LBNF) and Deep Underground Neutrino Experiment (DUNE): Volume 1: The LBNF and DUNE Projects'. In: (2016). arXiv: `1601.05471 [physics.ins-det]` (cit. on pp. 2, 20, 21).

[26] R. Acciarri et al. 'Long-Baseline Neutrino Facility (LBNF) and Deep Underground Neutrino Experiment (DUNE): Volume 2: The Physics Program for DUNE at LBNF'. In: (2015). arXiv: `1512.06148 [physics.ins-det]` (cit. on pp. 2, 20–22, 24–26, 28, 147, 150).

[27] J. Strait et al. 'Long-Baseline Neutrino Facility (LBNF) and Deep Underground Neutrino Experiment (DUNE): Volume 3: Long-Baseline Neutrino Facility for DUNE'. In: (2016). arXiv: `1601.05823 [physics.ins-det]` (cit. on pp. 2, 20, 22).

[28] R. Acciarri et al. 'Long-Baseline Neutrino Facility (LBNF) and Deep Underground Neutrino Experiment (DUNE): Volume 4: The DUNE Detectors at LBNF'. In: (2016). arXiv: `1601.02984 [physics.ins-det]` (cit. on pp. 2, 20, 144, 146, 171).

[29] A. Blatter et al. 'Experimental study of electric breakdowns in liquid argon at centimeter scale'. In: *Journal of Instrumentation* 9.04 (2014), P04006. URL: `http://stacks.iop.org/1748-0221/9/i=04/a=P04006` (cit. on pp. 3, 46, 53, 56, 59, 63, 67, 75).

[30] D. W. Swan and T. J. Lewis. 'Influence of Electrode Surface Conditions on the Electrical Strength of Liquified Gases'. In: *Journal of The Electrochemical Society* 107.3 (1960), pp. 180–185. DOI: `10.1149/1.2427647`. eprint: `http://jes.ecsdl.org/content/107/3/180.full.pdf+html`. URL: `http://jes.ecsdl.org/content/107/3/180.abstract` (cit. on pp. 4, 46, 53).

[31] D. W. Swan and T. J. Lewis. 'The Influence of Cathode and Anode Surfaces on the Electric Strength of Liquid Argon'. In: *Proceedings of the Physical Society* 78.3 (1961), p. 448. URL: `http://stacks.iop.org/0370-1328/78/i=3/a=314` (cit. on pp. 4, 46, 53).

[32] R. Acciarri et al. 'Design and construction of the MicroBooNE detector'. In: *Journal of Instrumentation* 12.02 (2017), P02017. URL: `http://stacks.iop.org/1748-0221/12/i=02/a=P02017` (cit. on pp. 4, 49, 87, 98, 144, 152).

[33] J. Chadwick. 'The intensity distribution in the magnetic spectrum of beta particles from radium (B + C)'. In: *Verh. Phys. Gesell.* 16 (1914), pp. 383–391 (cit. on p. 6).

[34] J. Chadwick. 'Possible Existence of a Neutron'. In: *Nature* 129 (1932), p. 312. DOI: 10.1038/129312a0 (cit. on p. 6).

[35] E. Fermi. 'Versuch einer Theorie der β-Strahlen. I'. In: *Zeitschrift für Physik* 88.3 (Mar. 1934), pp. 161–177. ISSN: 0044-3328. DOI: 10.1007/BF01351864. URL: https://doi.org/10.1007/BF01351864 (cit. on p. 6).

[36] G. Danby et al. 'Observation of High-Energy Neutrino Reactions and the Existence of Two Kinds of Neutrinos'. In: *Phys. Rev. Lett.* 9 (1 July 1962), pp. 36–44. DOI: 10.1103/PhysRevLett.9.36. URL: https://link.aps.org/doi/10.1103/PhysRevLett.9.36 (cit. on p. 7).

[37] D. Casper et al. 'Measurement of atmospheric neutrino composition with the IMB-3 detector'. In: *Phys. Rev. Lett.* 66 (20 May 1991), pp. 2561–2564. DOI: 10.1103/PhysRevLett.66.2561. URL: https://link.aps.org/doi/10.1103/PhysRevLett.66.2561 (cit. on p. 10).

[38] K. Hirata et al. 'Experimental study of the atmospheric neutrino flux'. In: *Physics Letters B* 205.2 (1988), pp. 416–420. ISSN: 0370-2693. DOI: http://dx.doi.org/10.1016/0370-2693(88)91690-5. URL: http://www.sciencedirect.com/science/article/pii/0370269388916905 (cit. on p. 10).

[39] K. S. Hirata et al. 'Real-time, directional measurement of ^{8}B solar neutrinos in the Kamiokande II detector'. In: *Phys. Rev. D* 44 (8 Oct. 1991), pp. 2241–2260. DOI: 10.1103/PhysRevD.44.2241. URL: https://link.aps.org/doi/10.1103/PhysRevD.44.2241 (cit. on p. 10).

[40] K. Kodama et al. 'Observation of tau neutrino interactions'. In: *Physics Letters B* 504.3 (2001), pp. 218–224. ISSN: 0370-2693. DOI: http://dx.doi.org/10.1016/S0370-2693(01)00307-0. URL: http://www.sciencedirect.com/science/article/pii/S0370269301003070 (cit. on p. 13).

[41] A. Gando et al. 'Reactor on-off antineutrino measurement with KamLAND'. In: *Phys. Rev. D* 88 (3 Aug. 2013), p. 033001. DOI: 10.1103/PhysRevD.88.033001. URL: https://link.aps.org/doi/10.1103/PhysRevD.88.033001 (cit. on p. 14).

[42] N. Agafonova et al. 'Discovery of τ Neutrino Appearance in the CNGS Neutrino Beam with the OPERA Experiment'. In: *Phys. Rev. Lett.* 115 (12 Sept. 2015), p. 121802. DOI: 10.1103/PhysRevLett.115.121802. URL: https://link.aps.org/doi/10.1103/PhysRevLett.115.121802 (cit. on p. 14).

[43] S. King. 'Unified models of neutrinos, flavour and CP Violation'. In: *Progress in Particle and Nuclear Physics* 94.Supplement C (2017), pp. 217–256. ISSN: 0146-6410. DOI: https://doi.org/10.1016/j.ppnp.2017.01.003. URL: http://www.sciencedirect.com/science/article/pii/S0146641017300042 (cit. on pp. 17–19, 22).

[44] E. K. Akhmedov and A. Y. Smirnov. 'Paradoxes of neutrino oscillations'. In: *Physics of Atomic Nuclei* 72.8 (Aug. 2009), pp. 1363–1381. ISSN: 1562-692X. DOI: 10.1134/S1063778809080122. URL: https://doi.org/10.1134/S1063778809080122 (cit. on p. 18).

[45] S. P. Mikheyev and A. Y. Smirnov. 'Resonance enhancement of oscillations in matter and solar neutrino spectroscopy'. In: *Yadernaya Fizika* 42 (1985), pp. 1441–1448 (cit. on p. 20).

[46] L. Wolfenstein. 'Neutrino oscillations in matter'. In: *Phys. Rev. D* 17 (9 May 1978), pp. 2369–2374. DOI: `10.1103/PhysRevD.17.2369`. URL: `https://link.aps.org/doi/10.1103/PhysRevD.17.2369` (cit. on p. 20).

[47] L. Fields. Personal Memo. Fermi National Accelerator Laboratory, Batavia, IL, USA. Jan. 2018 (cit. on pp. 22, 30).

[48] P. Ballett et al. 'Sensitivities and synergies of DUNE and T2HK'. In: *Phys. Rev. D* 96 (3 Aug. 2017), p. 033003. DOI: `10.1103/PhysRevD.96.033003`. URL: `https://link.aps.org/doi/10.1103/PhysRevD.96.033003` (cit. on p. 22).

[49] X. Qian and P. Vogel. 'Neutrino mass hierarchy'. In: *Progress in Particle and Nuclear Physics* 83.Supplement C (2015), pp. 1–30. ISSN: 0146-6410. DOI: `https://doi.org/10.1016/j.ppnp.2015.05.002`. URL: `http://www.sciencedirect.com/science/article/pii/S0146641015000307` (cit. on pp. 22, 23).

[50] L. Aliaga et al. 'Design, calibration, and performance of the MINERvA detector'. In: *Nuclear Instruments and Methods in Physics Research Section A: Accelerators, Spectrometers, Detectors and Associated Equipment* 743 (2014), pp. 130–159. ISSN: 0168-9002. DOI: `https://doi.org/10.1016/j.nima.2013.12.053`. URL: `http://www.sciencedirect.com/science/article/pii/S0168900214000035` (cit. on p. 28).

[51] P. Adamson et al. 'First measurement of muon-neutrino disappearance in NOvA'. In: *Phys. Rev. D* 93 (5 Mar. 2016), p. 051104. DOI: `10.1103/PhysRevD.93.051104`. URL: `https://link.aps.org/doi/10.1103/PhysRevD.93.051104` (cit. on p. 28).

[52] L. Pickering and C. Wilkinson. Personal Memo. Michigan State University, MI, USA; University of Bern, Switzerland. Mar. 2018 (cit. on p. 30).

[53] C. W. Fabjan and T. Ludlam. 'Calorimetry in High-Energy Physics'. In: *Annual Review of Nuclear and Particle Science* 32.1 (1982), pp. 335–389. DOI: 10.1146/annurev.ns.32.120182.002003. eprint: https://doi.org/10.1146/annurev.ns.32.120182.002003. URL: https://doi.org/10.1146/annurev.ns.32.120182.002003 (cit. on p. 40).

[54] G. Charpak et al. 'The use of multiwire proportional counters to select and localize charged particles'. In: *Nuclear Instruments and Methods* 62.3 (1968), pp. 262–268. ISSN: 0029-554X. DOI: http://dx.doi.org/10.1016/0029-554X(68)90371-6. URL: http://www.sciencedirect.com/science/article/pii/0029554X68903716 (cit. on p. 41).

[55] D. R. Nygren. 'The Time Projection Chamber: A New 4 pi Detector for Charged Particles'. In: *eConf* C740805 (1974), p. 58 (cit. on p. 41).

[56] C. Rubbia. *The Liquid Argon Time Projection Chamber: A New Concept for Neutrino Detectors*. Tech. rep. CERN-EP-INT-77-08. CERN, 1977 (cit. on p. 41).

[57] R. L. Amey and R. H. Cole. 'Dielectric Constants of Liquefied Noble Gases and Methane'. In: *The Journal of Chemical Physics* 40.1 (1964), pp. 146–148. DOI: 10.1063/1.1724850. eprint: https://doi.org/10.1063/1.1724850. URL: https://doi.org/10.1063/1.1724850 (cit. on p. 42).

[58] J. Thomas and D. A. Imel. 'Recombination of electron-ion pairs in liquid argon and liquid xenon'. In: *Phys. Rev. A* 36 (2 July 1987), pp. 614–616. DOI: 10.1103/PhysRevA.36.614. URL: https://link.aps.org/doi/10.1103/PhysRevA.36.614 (cit. on p. 43).

[59] M. Zeller et al. 'Ionization signals from electrons and alpha-particles in mixtures of liquid Argon and Nitrogen – perspectives on protons for Gamma Resonant Nuclear Absorption applications'. In: *Journal of Instrumentation* 5.10 (2010),

P10009. URL: http://stacks.iop.org/1748-0221/5/i=10/a=P10009 (cit. on p. 44).

[60] V. Chepel and H. Araújo. 'Liquid noble gas detectors for low energy particle physics'. In: *Journal of Instrumentation* 8.04 (2013), R04001. URL: http://stacks.iop.org/1748-0221/8/i=04/a=R04001 (cit. on pp. 45, 120).

[61] A. Ereditato et al. 'Measurement of the drift field in the ARGONTUBE LAr TPC with 266 nm pulsed laser beams'. In: *Journal of Instrumentation* 9.11 (2014), P11010. URL: http://stacks.iop.org/1748-0221/9/i=11/a=P11010 (cit. on pp. 47, 48).

[62] M. Zeller et al. 'First measurements with ARGONTUBE, a 5 m long drift Liquid Argon TPC'. In: *Nuclear Instruments and Methods in Physics Research Section A: Accelerators, Spectrometers, Detectors and Associated Equipment* 718 (2013). Proceedings of the 12th Pisa Meeting on Advanced DetectorsLa Biodola, Isola d'Elba, Italy, May 20 – 26, 2012, pp. 454–458. ISSN: 0168-9002. DOI: https://doi.org/10.1016/j.nima.2012.11.181. URL: http://www.sciencedirect.com/science/article/pii/S0168900212015288 (cit. on pp. 46, 53, 120, 134).

[63] M. Zeller. 'Advances in liquid argon TPCs for particle detectors'. PhD thesis. University of Bern, Switzerland, 2013 (cit. on p. 48).

[64] S. Amerio et al. 'Design, construction and tests of the ICARUS T600 detector'. In: *Nuclear Instruments and Methods in Physics Research Section A: Accelerators, Spectrometers, Detectors and Associated Equipment* 527.3 (2004), pp. 329–410. ISSN: 0168-9002. DOI: https://doi.org/10.1016/j.nima.2004.02.044. URL: http://www.sciencedirect.com/science/article/pii/S0168900204004966 (cit. on p. 49).

[65] I. Badhrees et al. ‘Measurement of the two-photon absorption cross-section of liquid argon with a time projection chamber’. In: *New Journal of Physics* 12.11 (2010), p. 113024. URL: http://stacks.iop.org/1367-2630/12/i=11/a=113024 (cit. on pp. 56, 65, 77, 117).

[66] *SL 10W to 1200W COMPACT HV POWER SOURCE*. Datasheet 128009-001. Spellman High Voltage Electronics Corporation, 2001. URL: https://web.archive.org/web/20180228175907/https://www.spellmanhv.com/-/media/en/Products/SL.pdf (cit. on p. 56).

[67] *Mixed Signal Oscilloscopes MSO3000 Series, DPO3000 Series*. Datasheet. Tektronix, Inc., Feb. 2016. URL: https://web.archive.org/web/20180228181052/http://download.tek.com/datasheet/MSO3000-DPO3000-Mixed-Signal-Oscilloscope-Datasheet-3GW2136412.pdf (cit. on p. 56).

[68] *S-PRI – High Speed Camera*. Product Leaflet. AOS Technologies AG, 2014. URL: https://web.archive.org/web/20180228183102/http://www.aostechnologies.com/fileadmin/user_upload/PDFs/Highspeed/AOS_S-PRI_en.pdf (cit. on p. 56).

[69] R. Acciarri et al. ‘Liquid argon dielectric breakdown studies with the MicroBooNE purification system’. In: *Journal of Instrumentation* 9.11 (2014), P11001. URL: http://stacks.iop.org/1748-0221/9/i=11/a=P11001 (cit. on pp. 61, 63).

[70] J. Gerhold, M. Hubmann and E. Telser. ‘Gap size effect on liquid helium breakdown’. In: *Cryogenics* 34.7 (1994), pp. 579–586. ISSN: 0011-2275. DOI: http://dx.doi.org/10.1016/0011-2275(94)90183-X. URL: http://www.sciencedirect.com/science/article/pii/001122759490183X (cit. on p. 61).

[71] A. Bondar et al. ‘Study of infrared scintillations in gaseous and liquid argon. Part I: methodology and time measurements’. In: *Journal of Instrumentation* 7.06

(2012), P06015. URL: `http://stacks.iop.org/1748-0221/7/i=06/a=P06015` (cit. on p. 65).

[72] A. Bondar et al. ‘Study of infrared scintillations in gaseous and liquid argon. Part II: light yield and possible applications’. In: *Journal of Instrumentation* 7.06 (2012), P06014. URL: `http://stacks.iop.org/1748-0221/7/i=06/a=P06014` (cit. on p. 65).

[73] A. Buzulutskov. ‘Advances in Cryogenic Avalanche Detectors’. In: *Journal of Instrumentation* 7.02 (2012), p. C02025. URL: `http://stacks.iop.org/1748-0221/7/i=02/a=C02025` (cit. on p. 65).

[74] J. B. Boffard et al. ‘Electron-impact excitation of argon: Optical emission cross sections in the range of 300-2500 nm’. In: *Atomic Data and Nuclear Data Tables* 93.6 (Nov. 2007). DOI: `10.1016/j.adt.2007.06.004` (cit. on p. 65).

[75] T. Heindl et al. ‘The scintillation of liquid argon’. In: *EPL (Europhysics Letters)* 91.6 (2010), p. 62002. URL: `http://stacks.iop.org/0295-5075/91/i=6/a=62002` (cit. on pp. 65, 68).

[76] P. Laporte et al. ‘Evolution of intermediate excitons in fluid argon and krypton’. In: *Phys. Rev. B* 35 (12 Apr. 1987), pp. 6270–6280. DOI: `10.1103/PhysRevB.35.6270`. URL: `https://link.aps.org/doi/10.1103/PhysRevB.35.6270` (cit. on p. 65).

[77] M. Förstel et al. ‘Energy band dispersion in photoemission spectra of argon clusters’. In: *Journal of Electron Spectroscopy and Related Phenomena* 184.3–6 (2011). Advances in Vacuum Ultraviolet and X-ray PhysicsThe 37th International Conference on Vacuum Ultraviolet and X-ray Physics (VUVX2010), pp. 107–112. ISSN: 0368-2048. DOI: `http://doi.org/10.1016/j.elspec.2010.09.001`. URL: `http://www.sciencedirect.com/science/article/pii/S0368204810001969` (cit. on p. 65).

[78] G. I. Skanavi. *Fizika Dielektrikov; Oblast Silnykh Polei (Physics of dielectrics; Strong Fields)*. Moscow: Gos. Izd. Fiz. Mat. Nauk (State Publ. Hause for Phys. and Math. Scis.), 1958 (cit. on p. 74).

[79] S. Procureur, R. Dupré and S. Aune. 'Genetic multiplexing and first results with a 50×50cm2 Micromegas'. In: *Nuclear Instruments and Methods in Physics Research Section A: Accelerators, Spectrometers, Detectors and Associated Equipment* 729 (2013), pp. 888–894. ISSN: 0168-9002. DOI: `https://doi.org/10.1016/j.nima.2013.08.071`. URL: `http://www.sciencedirect.com/science/article/pii/S0168900213012126` (cit. on p. 81).

[80] R. Sarpeshkar, T. Delbruck and C. A. Mead. 'White noise in MOS transistors and resistors'. In: *IEEE Circuits and Devices Magazine* 9.6 (Nov. 1993), pp. 23–29. ISSN: 8755-3996. DOI: `10.1109/101.261888` (cit. on p. 84).

[81] Linear77. *Noise reduction using differential signaling*. Wikimedia Commons. Feb. 2012. URL: `https://commons.wikimedia.org/wiki/File:DiffSignaling.png` (cit. on p. 85).

[82] A. Ereditato et al. 'Performance of cryogenic charge readout electronics with the ARGONTUBE LAr TPC'. In: *Journal of Instrumentation* 9.11 (2014), P11022. URL: `http://stacks.iop.org/1748-0221/9/i=11/a=P11022` (cit. on p. 87).

[83] G. D. Geronimo et al. 'Front-End ASIC for a Liquid Argon TPC'. In: *IEEE Transactions on Nuclear Science* 58.3 (June 2011), pp. 1376–1385. ISSN: 0018-9499. DOI: `10.1109/TNS.2011.2127487` (cit. on pp. 87, 98).

[84] *V1724 8 Channel 14 bit 100 MS/s Digitizer*. CAEN S.p.A. Feb. 2018. URL: `https://web.archive.org/web/20180228184516/http://www.caen.it/csite/CaenProd.jsp?parent=11&idmod=483` (cit. on p. 88).

[85] F. Cavanna et al. ‘LArIAT: Liquid Argon In A Testbeam’. In: (2014). arXiv: `1406.5560 [physics.ins-det]` (cit. on pp. 93, 128).

[86] B. Abi et al. ‘The Single-Phase ProtoDUNE Technical Design Report’. In: (2017). arXiv: `1706.07081 [physics.ins-det]` (cit. on pp. 95, 98).

[87] C. Thorn et al. ‘Cold Electronics Development for the LBNE LAr TPC’. In: *Physics Procedia* 37 (2012). Proceedings of the 2nd International Conference on Technology and Instrumentation in Particle Physics (TIPP 2011), pp. 1295–1302. ISSN: 1875-3892. DOI: `https://doi.org/10.1016/j.phpro.2012.02.473`. URL: `http://www.sciencedirect.com/science/article/pii/S187538921201838X` (cit. on p. 96).

[88] C. Grace, A. Krieger and D. Gnani. *LArPix Datasheet*. LBNL IC Group Design Note. Lawrence Berkeley National Laboratory, Nov. 2017 (cit. on pp. 97, 98, 100, 102).

[89] D. Dwyer. ‘Front End Electronics (LArPix)’. In: *ArgonCube Collaboration Meeting*. Oct. 2017. URL: `https://indico.cern.ch/event/665009/contributions/2734411` (cit. on pp. 98, 100).

[90] A. Krieger et al. ‘A micropower readout ASIC for pixelated liquid Ar TPCs’. In: *Topical Workshop on Electronics for Particle Physics*. 2017. URL: `https://pos.sissa.it/313` (cit. on p. 98).

[91] P. Horowitz and W. Hill. *The Art of Electronics*. Cambridge University Press, 2015. ISBN: 9780521809269. URL: `https://books.google.ch/books?id=LAiWPwAACAAJ` (cit. on pp. 99, 100).

[92] D. A. Dwyer. Personal Memo. Lawrence Berkeley National Laboratory, Berkeley, CA, USA. Feb. 2018 (cit. on pp. 100, 101).

[93] D. Dwyer. 'LArTPC - Pixel R/O electronics'. In: *DUNE Collaboration Meeting*. Feb. 2018. URL: https://indico.fnal.gov/event/14581/session/5/contribution/85 (cit. on p. 102).

[94] Z. Moss et al. 'A Factor of Four Increase in Attenuation Length of Dipped Lightguides for Liquid Argon TPCs Through Improved Coating'. In: (2016). arXiv: 1604.03103 [physics.ins-det] (cit. on p. 103).

[95] *Plastic Scintillating Fibers*. Datasheet. Kuraray Co., Ltd., 2018. URL: https://web.archive.org/web/20180228143348/http://kuraraypsf.jp/pdf/all.pdf (cit. on p. 104).

[96] *MPPC (Multi-Pixel Photon Counter) S12825-050C, S12825-050P*. Datasheet KSX-I50017-E_S12825. Hamamatsu Photonics K.K., Nov. 2013. URL: http://www.hamamatsu.com (cit. on p. 104).

[97] M. Auger et al. 'A Novel Cosmic Ray Tagger System for Liquid Argon TPC Neutrino Detectors'. In: *Instruments* 1.1 (2017), p. 2. ISSN: 2410-390X. DOI: 10.3390/instruments1010002. URL: http://www.mdpi.com/2410-390X/1/1/2 (cit. on pp. 104, 117).

[98] M. Auger et al. 'Multi-channel front-end board for SiPM readout'. In: *Journal of Instrumentation* 11.10 (2016), P10005. URL: http://stacks.iop.org/1748-0221/11/i=10/a=P10005 (cit. on pp. 104, 117).

[99] R. Francini et al. 'VUV-Vis optical characterization of Tetraphenyl-butadiene films on glass and specular reflector substrates from room to liquid Argon temperature'. In: *Journal of Instrumentation* 8.09 (2013), P09006. URL: http://stacks.iop.org/1748-0221/8/i=09/a=P09006 (cit. on p. 104).

[100] B. Howard et al. 'A Novel Use of Light Guides and Wavelength Shifting Plates for the Detection of Scintillation Photons in Large Liquid Argon Detectors'. In: (2017). arXiv: `1710.11233 [physics.ins-det]` (cit. on p. 105).

[101] Z. Moss et al. 'Improved TPB-coated light guides for liquid argon TPC light detection systems'. In: *Journal of Instrumentation* 10.08 (2015), P08017. URL: `http://stacks.iop.org/1748-0221/10/i=08/a=P08017` (cit. on p. 105).

[102] C. Ignarra. 'A Demonstration of Light Guides for Light Detection in Liquid Argon TPCs'. In: *Physics Procedia* 37 (2012). Proceedings of the 2nd International Conference on Technology and Instrumentation in Particle Physics (TIPP 2011), pp. 1217–1222. ISSN: 1875-3892. DOI: `https://doi.org/10.1016/j.phpro.2012.02.455`. URL: `http://www.sciencedirect.com/science/article/pii/S1875389212018160` (cit. on p. 105).

[103] B. Baptista et al. 'Benchmarking TPB-coated Light Guides for Liquid Argon TPC Light Detection Systems'. In: (2012). arXiv: `1210.3793 [physics.ins-det]` (cit. on p. 105).

[104] B. J. P. Jones. 'A simulation of the optical attenuation of TPB coated light-guide detectors'. In: *Journal of Instrumentation* 8.10 (2013), p. C10015. URL: `http://stacks.iop.org/1748-0221/8/i=10/a=C10015` (cit. on p. 105).

[105] L. Bugel et al. 'Demonstration of a lightguide detector for liquid argon TPCs'. In: *Nuclear Instruments and Methods in Physics Research Section A: Accelerators, Spectrometers, Detectors and Associated Equipment* 640.1 (2011), pp. 69–75. ISSN: 0168-9002. DOI: `https://doi.org/10.1016/j.nima.2011.03.003`. URL: `http://www.sciencedirect.com/science/article/pii/S0168900211005158` (cit. on p. 105).

[106] D. Whittington. ‘Photon detection system designs for the Deep Underground Neutrino Experiment’. In: *Journal of Instrumentation* 11.05 (2016), p. C05019. URL: `http://stacks.iop.org/1748-0221/11/i=05/a=C05019` (cit. on p. 105).

[107] A. Machado and E. Segreto. ‘ARAPUCA a new device for liquid argon scintillation light detection’. In: *Journal of Instrumentation* 11.02 (2016), p. C02004. URL: `http://stacks.iop.org/1748-0221/11/i=02/a=C02004` (cit. on pp. 105, 130).

[108] *MPPC (Multi-Pixel Photon Counter) S13360-2050VE/-3050VE/-6050VE*. Datasheet. Hamamatsu Photonics K.K., June 2016. URL: `https://web.archive.org/web/20180228153950/http://www.hamamatsu.com/resources/pdf/ssd/s13360-2050ve_etc_kapd1053e.pdf` (cit. on p. 106).

[109] *WAVELENGTH SHIFTING PLASTICS EJ-280, EJ-282, EJ-284, EJ-286*. Datasheet. Eljen Technology, Aug. 2016. URL: `https://web.archive.org/web/20180228155546/http://www.eljentechnology.com/images/products/data_sheets/EJ-280_EJ-282_EJ-284_EJ-286.pdf` (cit. on p. 107).

[110] *Vikuiti Enhanced Specular Reflector (ESR)*. Brochure. 3M Optical Systems Division, 2010. URL: `https://web.archive.org/web/20180228165054/http://multimedia.3m.com/mws/media/374730O/vikuiti-tm-esr-sales-literature.pdf?fn=ESR%20ss2.pdf` (cit. on p. 107).

[111] *DICHROIC Glass Finishes DF-PA Blaze & Chill*. Technical Data Sheet. 3M, 2017. URL: `https://web.archive.org/web/20180228170351/https://multimedia.3m.com/mws/media/876651O/3mtm-dichroic-glass-finish-df-pa-data-sheet.pdf` (cit. on p. 107).

[112] F. Stocker. ‘A Novel Approach to Liquid Argon Time Projection Chambers’. MA thesis. University of Bern, Switzerland, 2017 (cit. on p. 115).

[113] B. Rossi et al. ‘A prototype liquid Argon Time Projection Chamber for the study of UV laser multi-photonic ionization’. In: *Journal of Instrumentation* 4.07 (2009), P07011. URL: http://stacks.iop.org/1748-0221/4/i=07/a=P07011 (cit. on p. 115).

[114] *ROX - Metal Oxide Resistors, Special Purpose, High Voltage*. Datasheet 31033. Vishay Intertechnology, Inc., Jan. 2017. URL: https://web.archive.org/web/20180313151436/http://www.vishay.com/docs/31033/rox.pdf (cit. on p. 116).

[115] S. Amoruso et al. ‘Study of electron recombination in liquid argon with the ICARUS TPC’. In: *Nuclear Instruments and Methods in Physics Research Section A: Accelerators, Spectrometers, Detectors and Associated Equipment* 523.3 (2004), pp. 275–286. ISSN: 0168-9002. DOI: https://doi.org/10.1016/j.nima.2003.11.423. URL: http://www.sciencedirect.com/science/article/pii/S0168900204000506 (cit. on p. 119).

[116] R. Acciarri et al. ‘A study of electron recombination using highly ionizing particles in the ArgoNeuT Liquid Argon TPC’. In: *Journal of Instrumentation* 8.08 (2013), P08005. URL: http://stacks.iop.org/1748-0221/8/i=08/a=P08005 (cit. on p. 119).

[117] E. M. Gushchin, A. A. Kruglov and I. M. Obodovskil. ‘Electron dynamics in condensed argon and xenon’. In: *Journal of Experimental and Theoretical Physics* 55.4 (Apr. 1982), p. 650 (cit. on p. 120).

[118] I. Jolliffe. *Principal Component Analysis*. Springer Series in Statistics. Springer, 2002. ISBN: 9780387954424. URL: https://books.google.ch/books?id=%5C_olByCrhjwIC (cit. on p. 125).

[119] C. Höppner et al. 'A novel generic framework for track fitting in complex detector systems'. In: *Nuclear Instruments and Methods in Physics Research Section A: Accelerators, Spectrometers, Detectors and Associated Equipment* 620.2 (2010), pp. 518–525. ISSN: 0168-9002. DOI: `https://doi.org/10.1016/j.nima.2010.03.136`. URL: `http://www.sciencedirect.com/science/article/pii/S0168900210007473` (cit. on pp. 125, 127).

[120] J. Rauch and T. Schlüter. 'GENFIT — a Generic Track-Fitting Toolkit'. In: *Journal of Physics: Conference Series* 608.1 (2015), p. 012042. URL: `http://stacks.iop.org/1742-6596/608/i=1/a=012042` (cit. on pp. 125, 127).

[121] C. Anderson et al. 'The ArgoNeuT detector in the NuMI low-energy beam line at Fermilab'. In: *Journal of Instrumentation* 7.10 (2012), P10019. URL: `http://stacks.iop.org/1748-0221/7/i=10/a=P10019` (cit. on p. 128).

[122] *HGW 2372 GLASHARTGEWEBE / G10 / EP GC 201.* Technisches Datenblatt. Amsler & Frey AG, Dec. 2015. URL: `https://web.archive.org/web/20180228172229/https://shop.amsler-frey.ch/downloads/datenblaetter/td_hgw2372.pdf` (cit. on pp. 131, 141).

[123] W.-M. Yao et al. 'Review of Particle Physics'. In: *Journal of Physics G* 33 (2006), pp. 1+. URL: `http://pdg.lbl.gov` (cit. on p. 131).

[124] R. Acciarri et al. 'The Pandora multi-algorithm approach to automated pattern recognition of cosmic-ray muon and neutrino events in the MicroBooNE detector'. In: *The European Physical Journal C* 78.1 (Jan. 2018), p. 82. ISSN: 1434-6052. DOI: `10.1140/epjc/s10052-017-5481-6`. URL: `https://doi.org/10.1140/epjc/s10052-017-5481-6` (cit. on pp. 131, 161).

[125] C. M. Marshall. ‘LArTPC - optimal height of detector’. In: *DUNE Collaboration Meeting*. Feb. 2018. URL: https://indico.fnal.gov/event/14581/session/5/contribution/86 (cit. on pp. 142, 143).

[126] C. M. Marshall. ‘Containment, acceptance, and event rates in LAr’. In: *3rd DUNE Near Detector Workshop*. Nov. 2017. URL: https://indico.fnal.gov/event/14737/session/2/contribution/28 (cit. on p. 157).

[127] T. Alion et al. *DUNE Near Detector Task Force Report*. DUNE document 1792. DUNE, 2017. URL: https://web.archive.org/web/20180224162141/http://www.neutrino.bnl.gov/q/DUNE/DUNE-doc-1792-v2.pdf (cit. on p. 159).

A. DUNE ND Event Pile-up Study Data

A.1. $2\,\mathrm{MW}$ Beam at $80\,\mathrm{GeV}$ Proton Energy

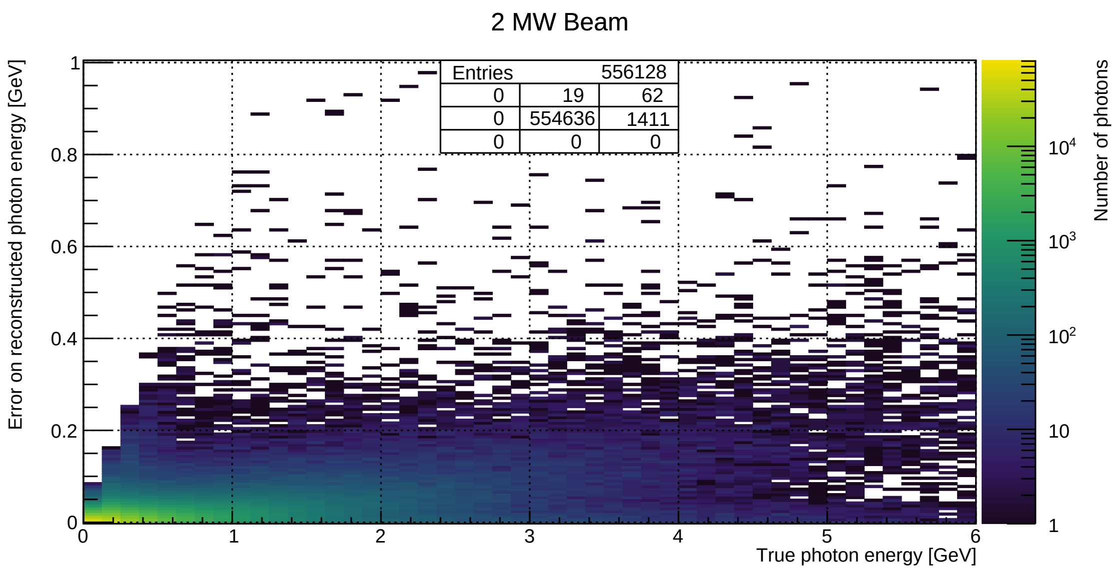

Figure A.1.: Missed energy versus true photon energy for a simple π^0-induced EM shower reconstruction algorithm based on a cone-cylinder union. All energy deposited outside of the cone-cylinder union is counted as missed. $2\,\mathrm{MW}$ beam of $80\,\mathrm{GeV}$ protons. Entries: Central cell shows plotted entries, other cells show overflow entries in direction w.r.t. central cell.

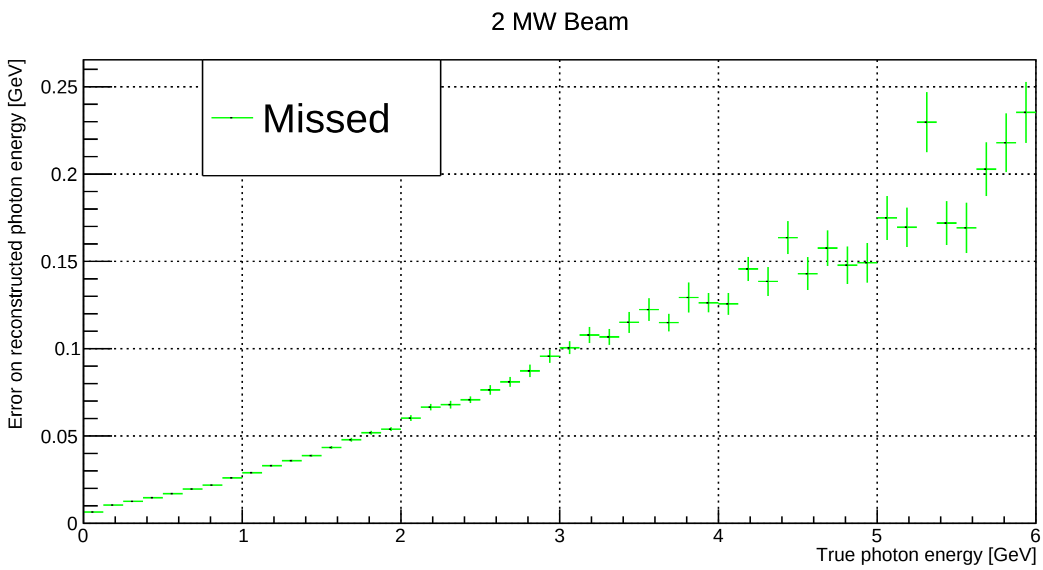

Figure A.2.: Mean missed energy versus true photon energy for a simple π^0-induced EM shower reconstruction algorithm based on a cone-cylinder union. All energy deposited outside of the cone-cylinder union is counted as missed. 2 MW beam of 80 GeV protons.

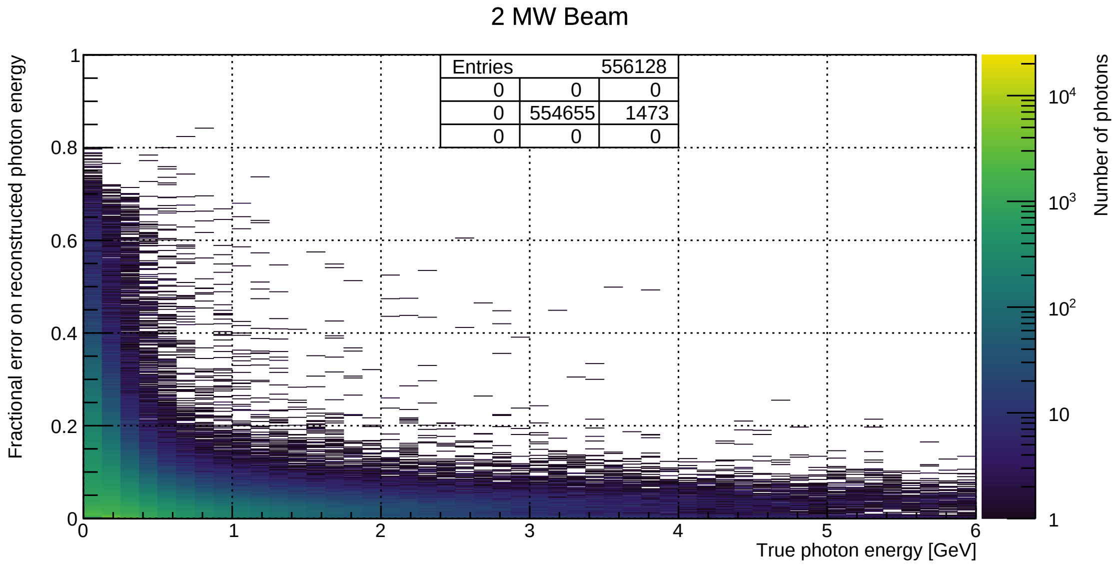

Figure A.3.: Missed energy fraction versus true photon energy for a simple π^0-induced EM shower reconstruction algorithm based on a cone-cylinder union. All energy deposited outside of the cone-cylinder union is counted as missed. 2 MW beam of 80 GeV protons. Entries: Central cell shows plotted entries, other cells show overflow entries in direction w.r.t. central cell.

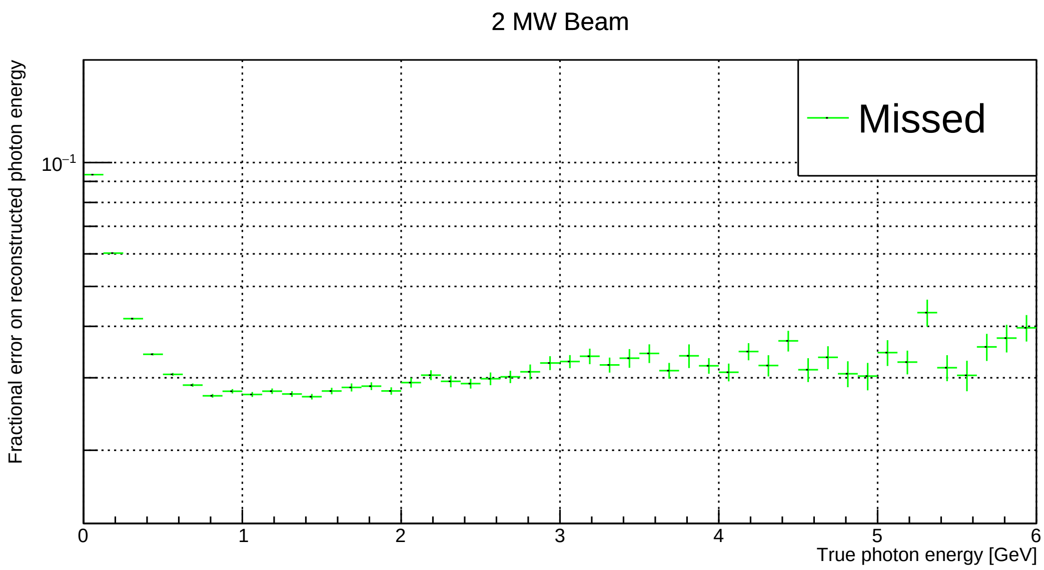

Figure A.4.: Mean missed energy fraction versus true photon energy for a simple π^0-induced EM shower reconstruction algorithm based on a cone-cylinder union. All energy deposited outside of the cone-cylinder union is counted as missed. 2 MW beam of 80 GeV protons.

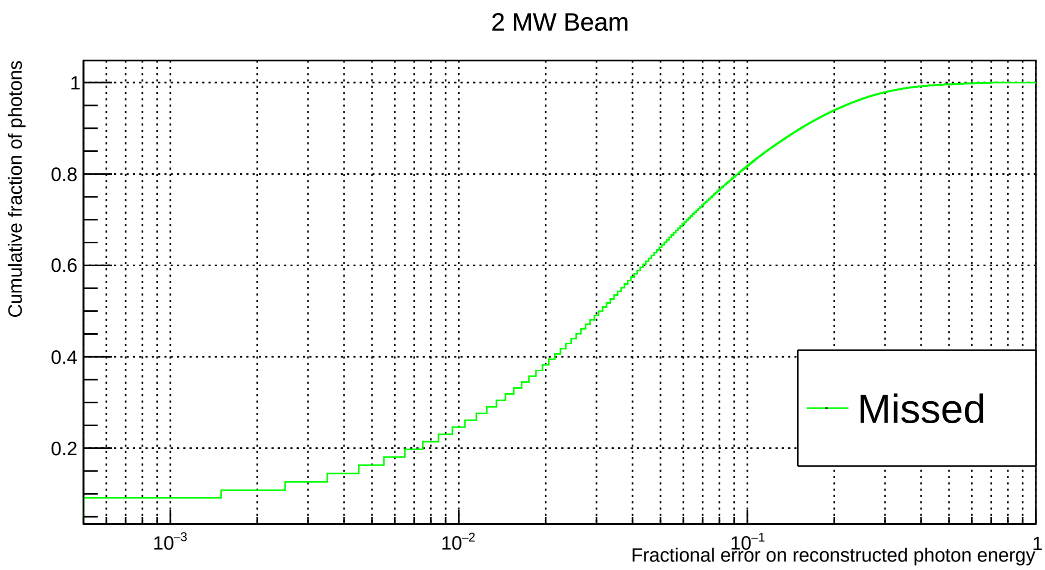

Figure A.5.: Cumulative fraction of photons versus missed energy fraction for a simple π^0-induced EM shower reconstruction algorithm based on a cone-cylinder union. All energy deposited outside of the cone-cylinder union is counted as missed. The curve depicts the fraction of photons on the y-axis with a missed energy fraction equal to or lower than the corresponding value on the x-axis. 2 MW beam of 80 GeV protons.

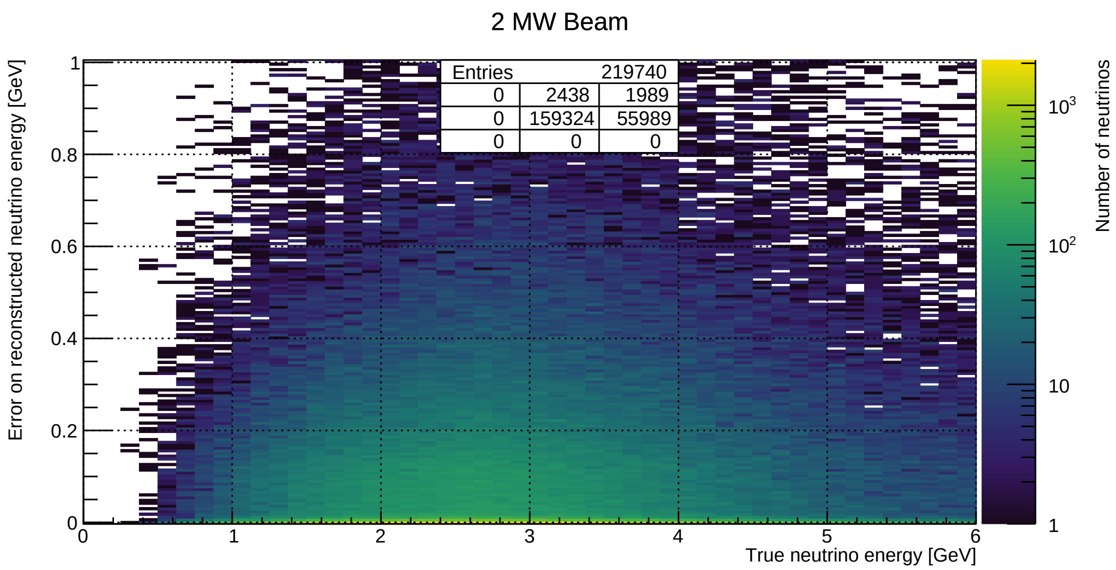

Figure A.6.: Misidentified energy versus true neutrino energy for a simple π^0-induced EM shower reconstruction algorithm based on a cone-cylinder union. All energy deposited inside the cone-cylinder union by descendants of neutrinos different from the parent of the corresponding π^0 photon is counted as misidentified. 2 MW beam of 80 GeV protons. Entries: Central cell shows plotted entries, other cells show overflow entries in direction w.r.t. central cell.

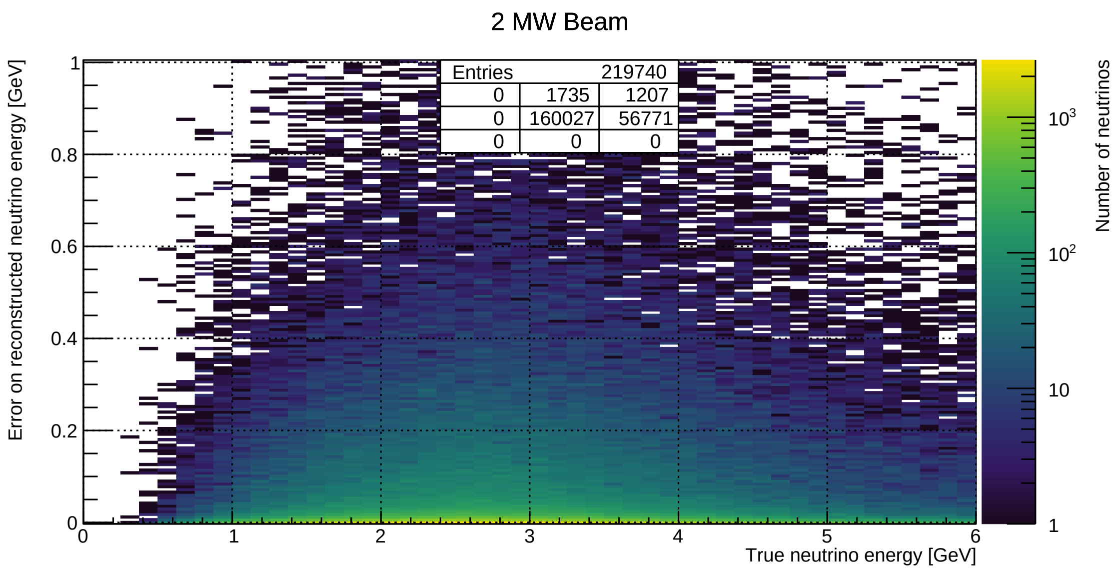

Figure A.7.: Misidentified energy versus true neutrino energy for a simple π^0-induced EM shower reconstruction algorithm based on a cone-cylinder union. Energy deposited inside the cone-cylinder union by descendants of neutrinos different from the parent of the corresponding π^0 photon is counted as misidentified. Any energy deposited by muons is excluded. 2 MW beam of 80 GeV protons. Entries: Central cell shows plotted entries, other cells show overflow entries in direction w.r.t. central cell.

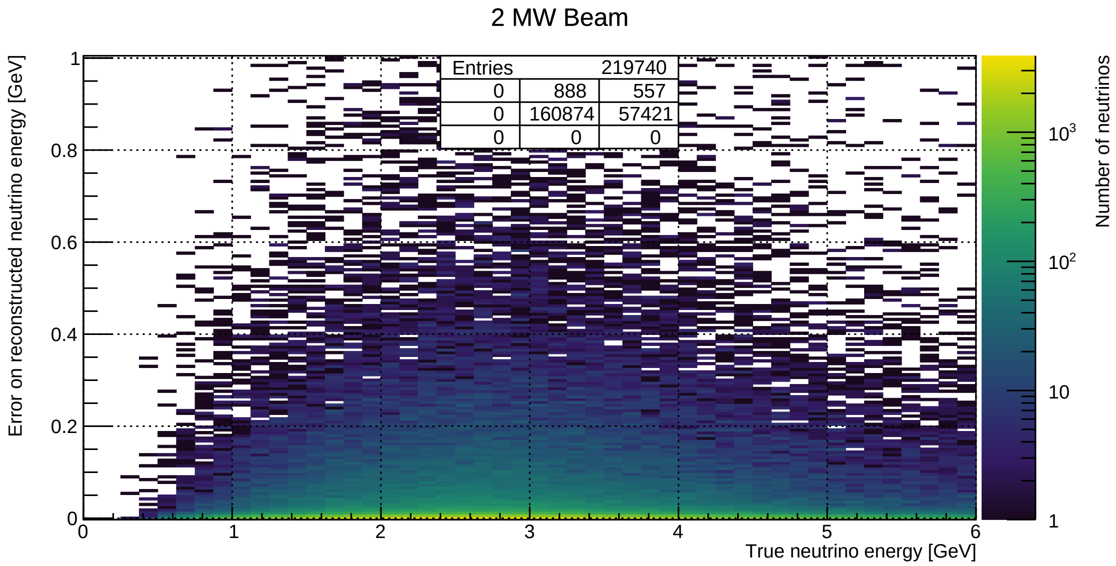

Figure A.8.: Misidentified energy versus true neutrino energy for a simple π^0-induced EM shower reconstruction algorithm based on a cone-cylinder union. Energy deposited inside the cone-cylinder union by descendants of neutrinos different from the parent of the corresponding π^0 photon is counted as misidentified. Only energy deposited by photons, neutrons, or any of their descendants is included. 2 MW beam of 80 GeV protons. Entries: Central cell shows plotted entries, other cells show overflow entries in direction w.r.t. central cell.

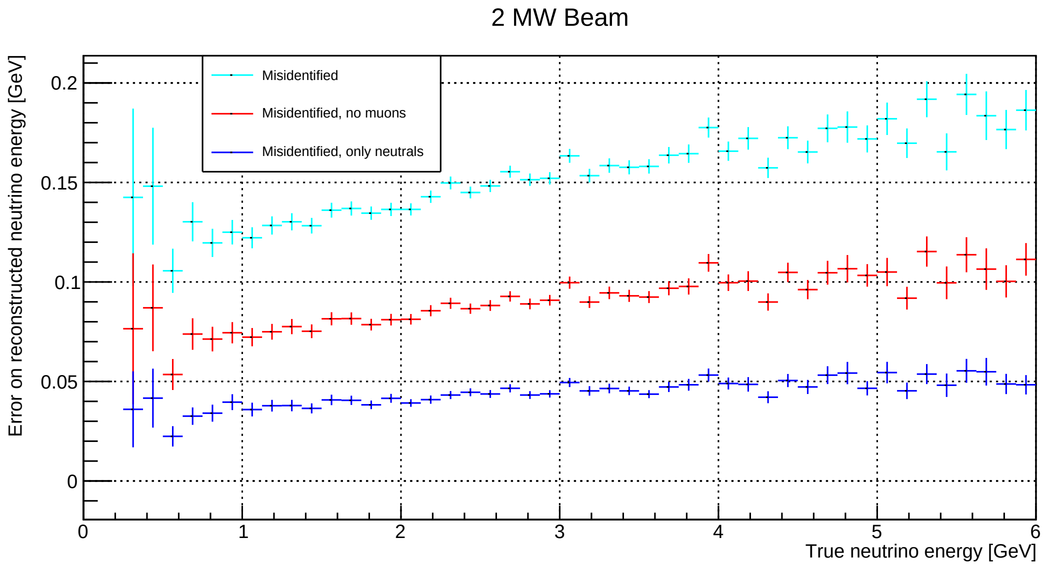

Figure A.9.: Mean misidentified energy versus true neutrino energy for a simple π^0-induced EM shower reconstruction algorithm based on a cone-cylinder union. All energy deposited inside the cone-cylinder union by descendants of neutrinos different from the parent of the corresponding π^0 photon is counted as misidentified. Colour indicates different selections of misidentified energy: total (cyan); excluding depositions from muons (red); deposition from photons, neutrons, and their descendants only (blue). 2 MW beam of 80 GeV protons.

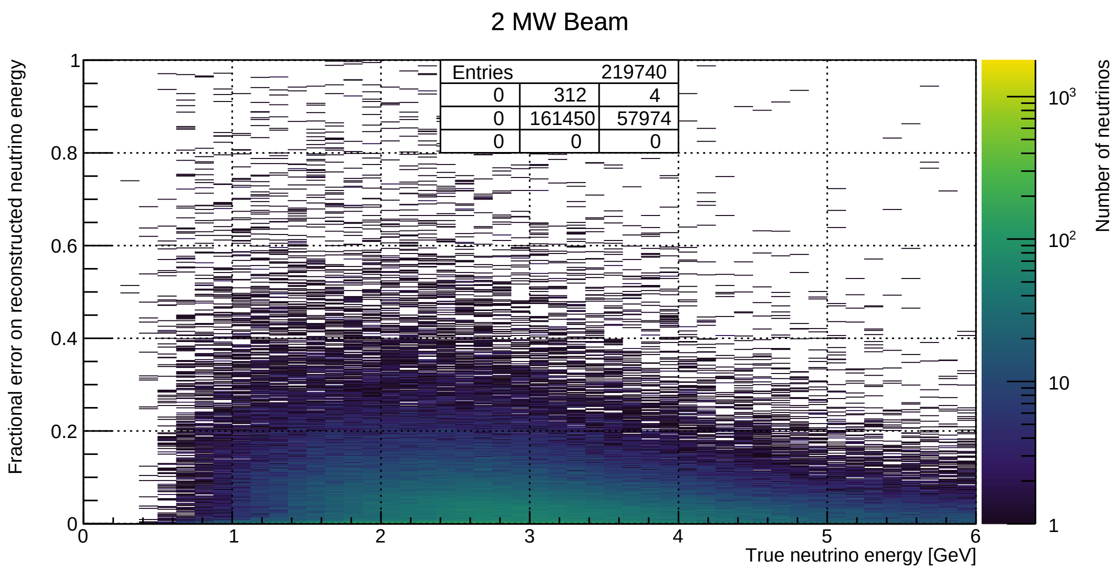

Figure A.10.: Misidentified energy fraction versus true neutrino energy for a simple π^0-induced EM shower reconstruction algorithm based on a cone-cylinder union. All energy deposited inside the cone-cylinder union by descendants of neutrinos different from the parent of the corresponding π^0 photon is counted as misidentified. 2 MW beam of 80 GeV protons. Entries: Central cell shows plotted entries, other cells show overflow entries in direction w.r.t. central cell.

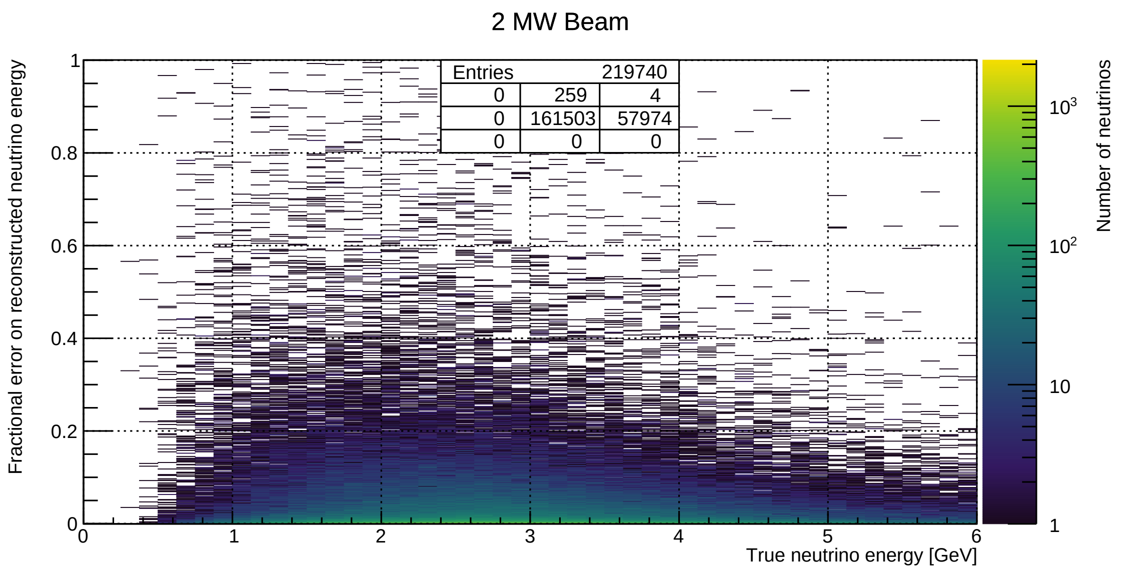

Figure A.11.: Misidentified energy fraction versus true neutrino energy for a simple π^0-induced EM shower reconstruction algorithm based on a cone-cylinder union. Energy deposited inside the cone-cylinder union by descendants of neutrinos different from the parent of the corresponding π^0 photon is counted as misidentified. Any energy deposited by muons is excluded. 2 MW beam of 80 GeV protons. Entries: Central cell shows plotted entries, other cells show overflow entries in direction w.r.t. central cell.

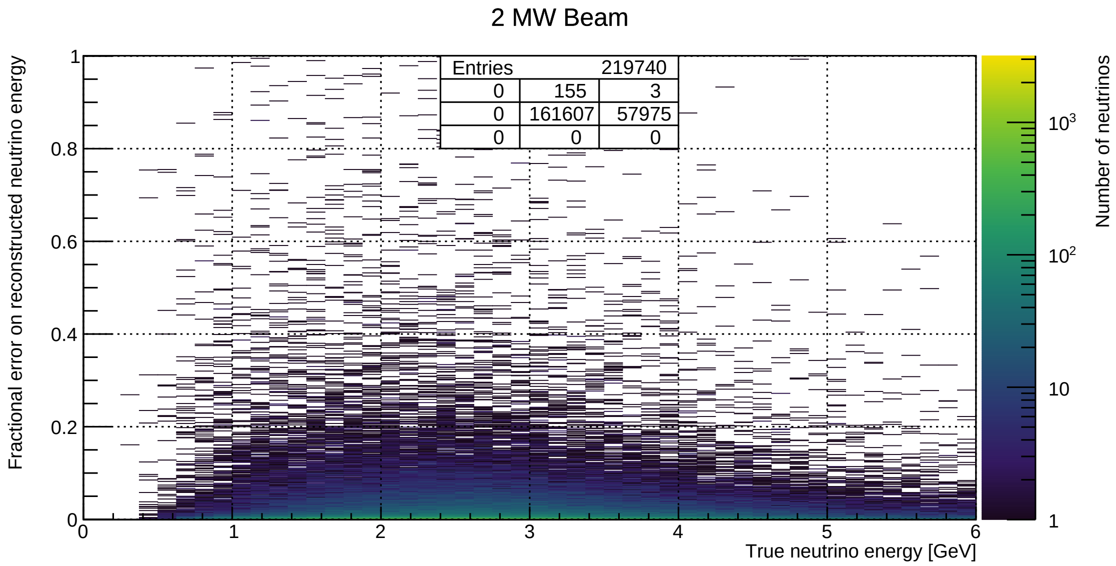

Figure A.12.: Misidentified energy fraction versus true neutrino energy for a simple π^0-induced EM shower reconstruction algorithm based on a cone-cylinder union. Energy deposited inside the cone-cylinder union by descendants of neutrinos different from the parent of the corresponding π^0 photon is counted as misidentified. Only energy deposited by photons, neutrons, or any of their descendants is included. 2 MW beam of 80 GeV protons. Entries: Central cell shows plotted entries, other cells show overflow entries in direction w.r.t. central cell.

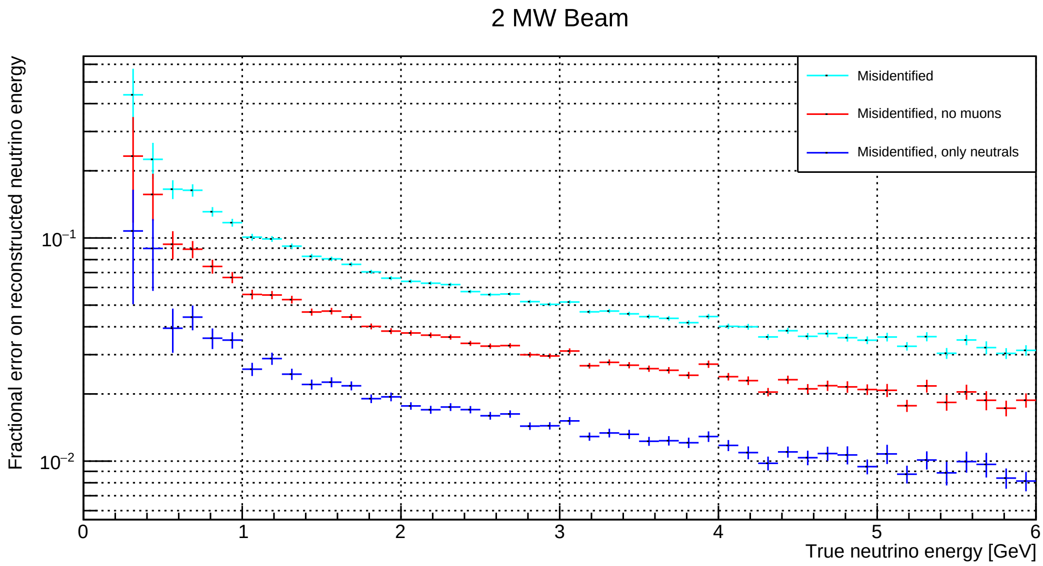

Figure A.13.: Mean misidentified energy fraction versus true neutrino energy for a simple π^0-induced EM shower reconstruction algorithm based on a cone-cylinder union. All energy deposited inside the cone-cylinder union by descendants of neutrinos different from the parent of the corresponding π^0 photon is counted as misidentified. Colour indicates different selections of misidentified energy: total (cyan); excluding depositions from muons (red); deposition from photons, neutrons, and their descendants only (blue). 2 MW beam of 80 GeV protons.

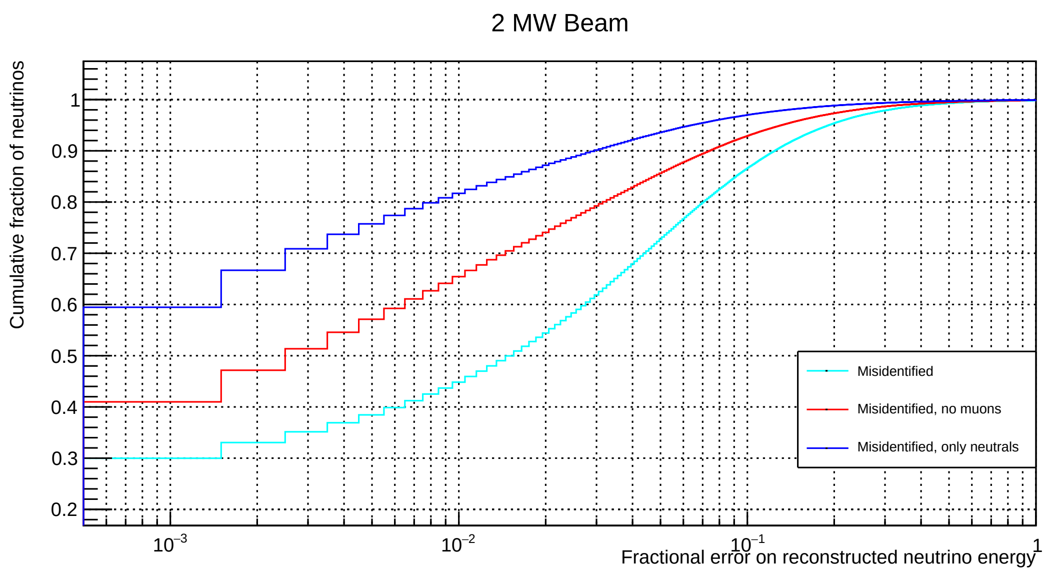

Figure A.14.: Cumulative fraction of neutrinos versus misidentified energy fraction for a simple π^0-induced EM shower reconstruction algorithm based on a cone-cylinder union. All energy deposited inside the cone-cylinder union by descendants of neutrinos different from the parent of the corresponding π^0 photon is counted as misidentified. Colour indicates different selections of misidentified energy: total (cyan); excluding depositions from muons (red); deposition from photons, neutrons, and their descendants only (blue). The curve depicts the fraction of neutrinos on the y-axis with a misidentified energy fraction equal to or lower than the corresponding value on the x-axis. 2 MW beam of 80 GeV protons.

A.2. 2 MW Beam at 80 GeV Proton Energy, XZ Projection

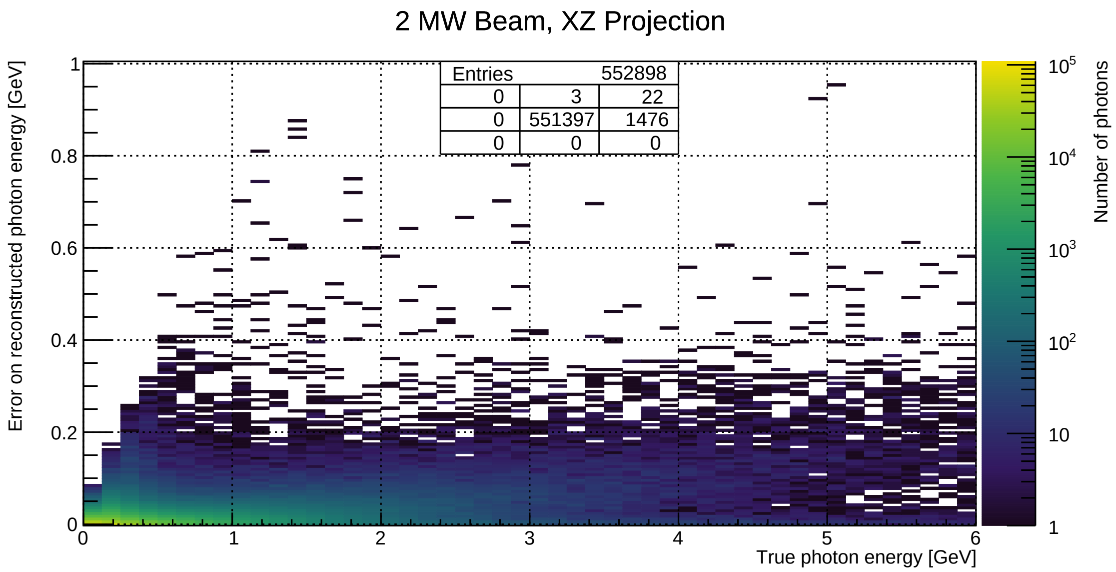

Figure A.15.: Missed energy versus true photon energy for a simple π^0-induced EM shower reconstruction algorithm based on a cone-cylinder union. All energy deposited outside of the cone-cylinder union is counted as missed. 2 MW beam of 80 GeV protons. As a primitive simulation of a 2D wire readout, only X- and Z-coordinates are used for the energy reconstruction. Entries: Central cell shows plotted entries, other cells show overflow entries in direction w.r.t. central cell.

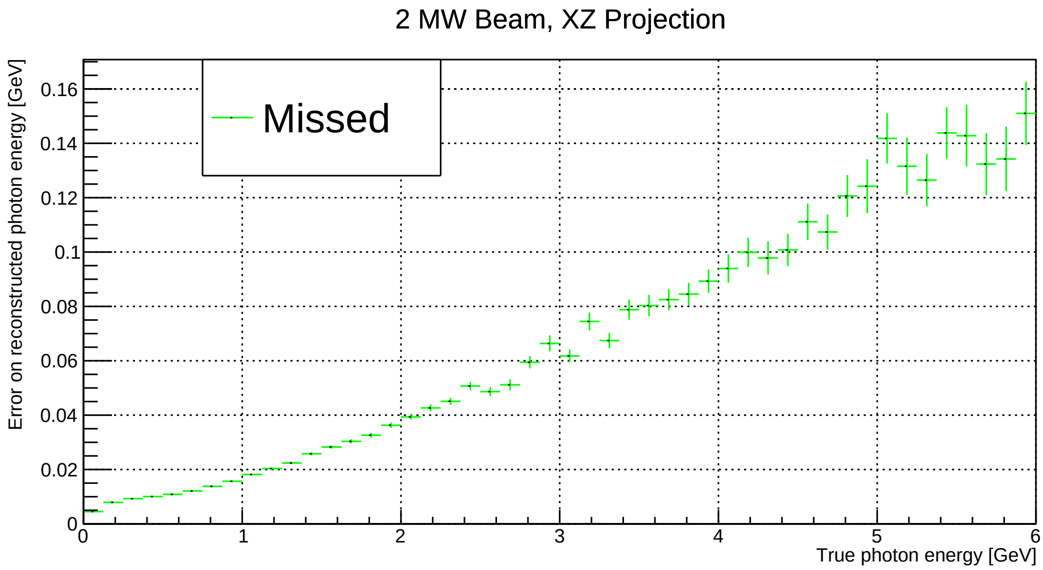

Figure A.16.: Mean missed energy versus true photon energy for a simple π^0-induced EM shower reconstruction algorithm based on a cone-cylinder union. All energy deposited outside of the cone-cylinder union is counted as missed. 2 MW beam of 80 GeV protons. As a primitive simulation of a 2D wire readout, only X- and Z-coordinates are used for the energy reconstruction.

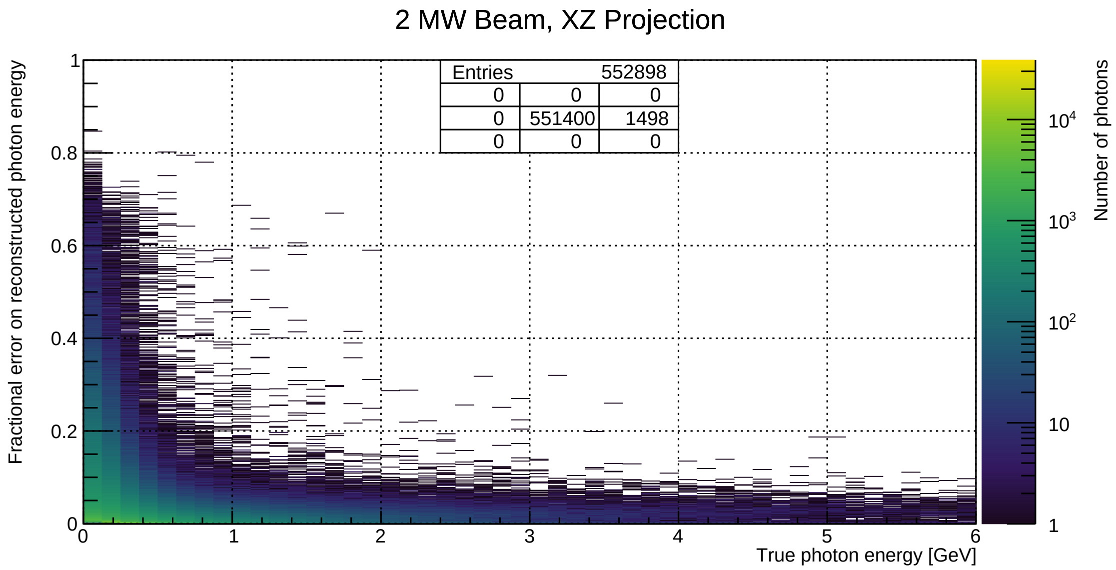

Figure A.17.: Missed energy fraction versus true photon energy for a simple π^0-induced EM shower reconstruction algorithm based on a cone-cylinder union. All energy deposited outside of the cone-cylinder union is counted as missed. 2 MW beam of 80 GeV protons. As a primitive simulation of a 2D wire readout, only X- and Z-coordinates are used for the energy reconstruction. Entries: Central cell shows plotted entries, other cells show overflow entries in direction w.r.t. central cell.

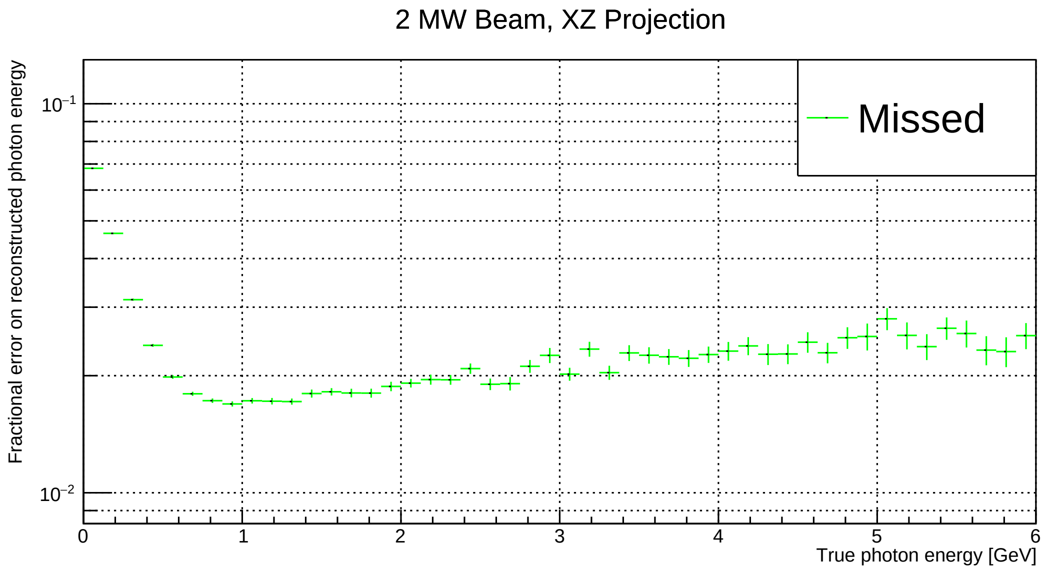

Figure A.18.: Mean missed energy fraction versus true photon energy for a simple π^0-induced EM shower reconstruction algorithm based on a cone-cylinder union. All energy deposited outside of the cone-cylinder union is counted as missed. 2 MW beam of 80 GeV protons. As a primitive simulation of a 2D wire readout, only X- and Z-coordinates are used for the energy reconstruction.

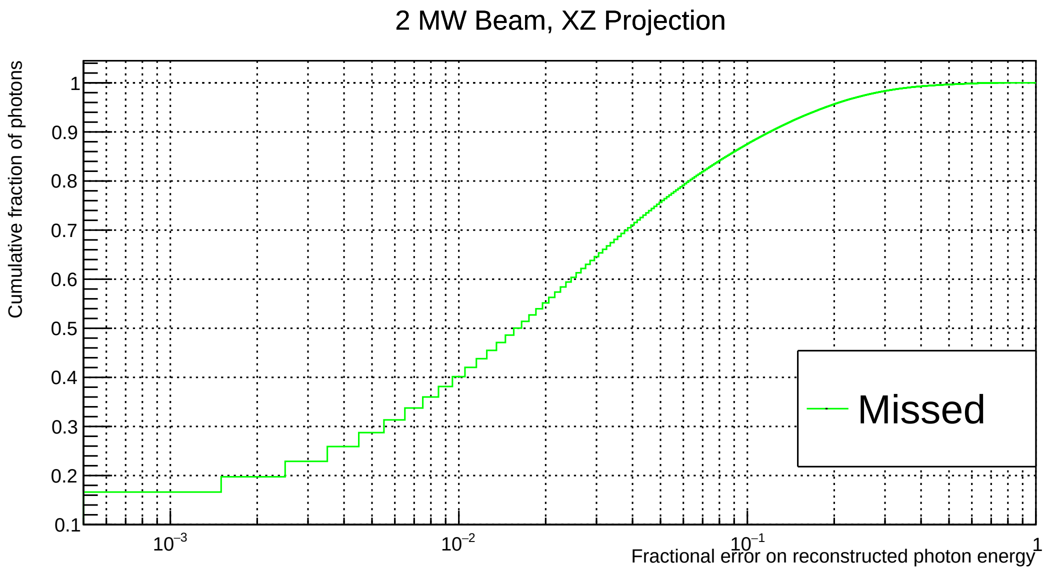

Figure A.19.: Cumulative fraction of photons versus missed energy fraction for a simple π^0-induced EM shower reconstruction algorithm based on a cone-cylinder union. All energy deposited outside of the cone-cylinder union is counted as missed. The curve depicts the fraction of photons on the y-axis with a missed energy fraction equal to or lower than the corresponding value on the x-axis. 2 MW beam of 80 GeV protons. As a primitive simulation of a 2D wire readout, only X- and Z-coordinates are used for the energy reconstruction.

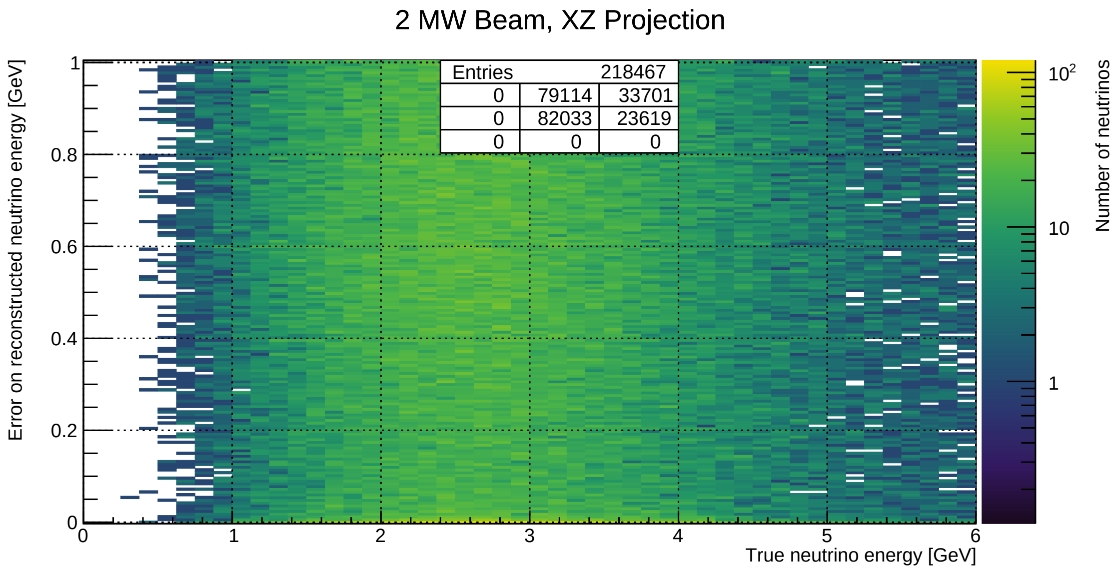

Figure A.20.: Misidentified energy versus true neutrino energy for a simple π^0-induced EM shower reconstruction algorithm based on a cone-cylinder union. All energy deposited inside the cone-cylinder union by descendants of neutrinos different from the parent of the corresponding π^0 photon is counted as misidentified. 2 MW beam of 80 GeV protons. As a primitive simulation of a 2D wire readout, only X- and Z-coordinates are used for the energy reconstruction. Entries: Central cell shows plotted entries, other cells show overflow entries in direction w.r.t. central cell.

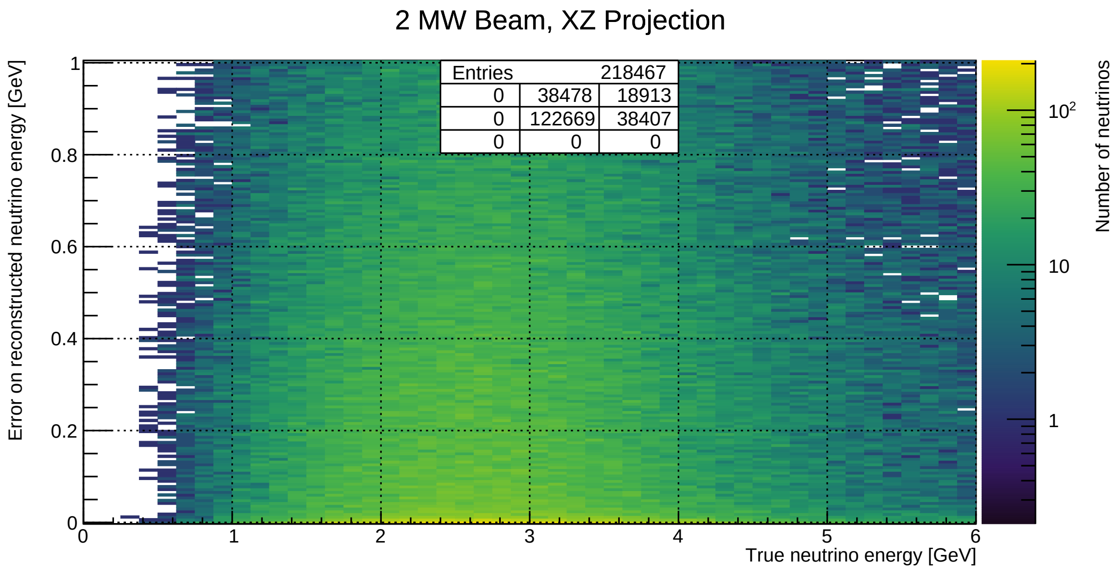

Figure A.21.: Misidentified energy versus true neutrino energy for a simple π^0-induced EM shower reconstruction algorithm based on a cone-cylinder union. Energy deposited inside the cone-cylinder union by descendants of neutrinos different from the parent of the corresponding π^0 photon is counted as misidentified. Any energy deposited by muons is excluded. 2 MW beam of 80 GeV protons. As a primitive simulation of a 2D wire readout, only X- and Z-coordinates are used for the energy reconstruction. Entries: Central cell shows plotted entries, other cells show overflow entries in direction w.r.t. central cell.

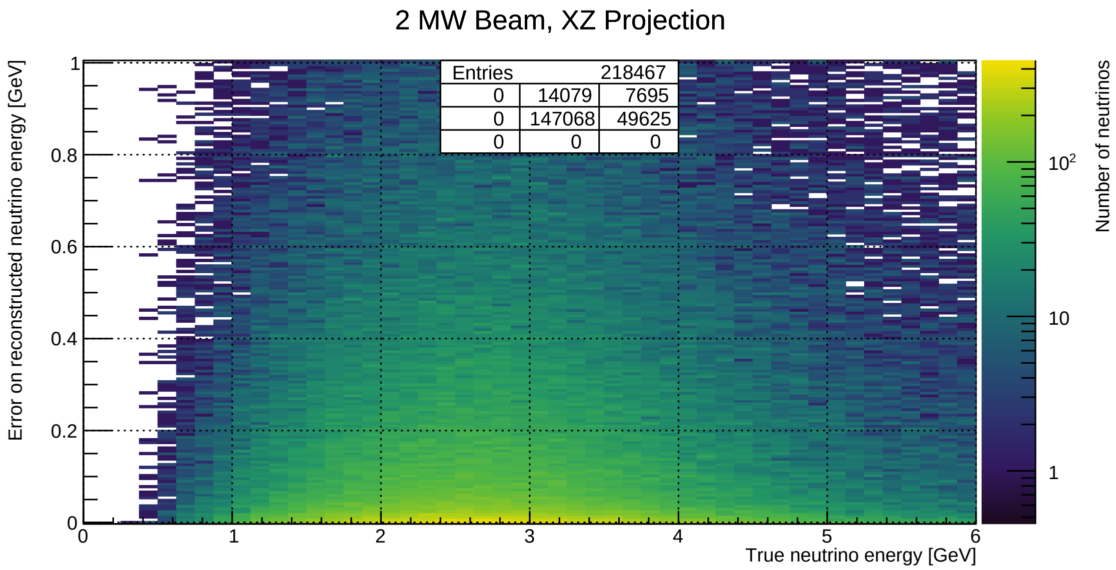

Figure A.22.: Misidentified energy versus true neutrino energy for a simple π^0-induced EM shower reconstruction algorithm based on a cone-cylinder union. Energy deposited inside the cone-cylinder union by descendants of neutrinos different from the parent of the corresponding π^0 photon is counted as misidentified. Only energy deposited by photons, neutrons, or any of their descendants is included. 2 MW beam of 80 GeV protons. As a primitive simulation of a 2D wire readout, only X- and Z-coordinates are used for the energy reconstruction. Entries: Central cell shows plotted entries, other cells show overflow entries in direction w.r.t. central cell.

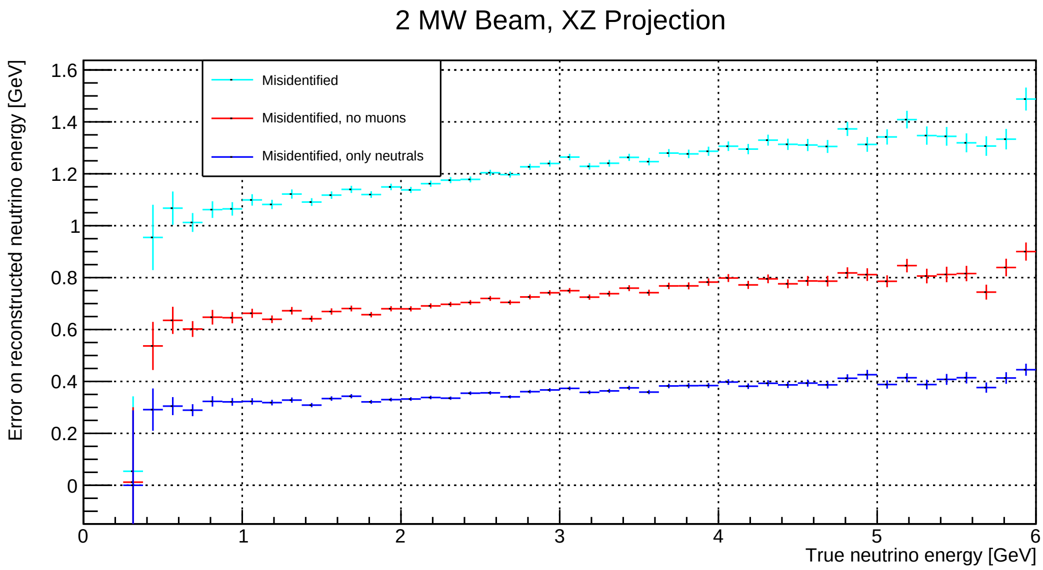

Figure A.23.: Mean misidentified energy versus true neutrino energy for a simple π^0-induced EM shower reconstruction algorithm based on a cone-cylinder union. All energy deposited inside the cone-cylinder union by descendants of neutrinos different from the parent of the corresponding π^0 photon is counted as misidentified. Colour indicates different selections of misidentified energy: total (cyan); excluding depositions from muons (red); deposition from photons, neutrons, and their descendants only (blue). 2 MW beam of 80 GeV protons. As a primitive simulation of a 2D wire readout, only X- and Z-coordinates are used for the energy reconstruction.

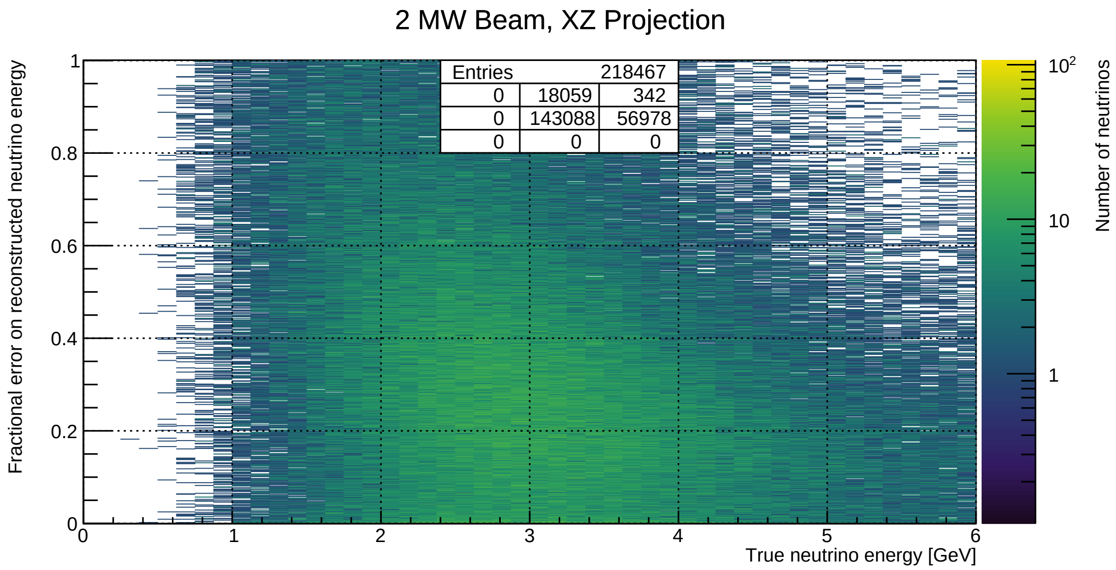

Figure A.24.: Misidentified energy fraction versus true neutrino energy for a simple π^0-induced EM shower reconstruction algorithm based on a cone-cylinder union. All energy deposited inside the cone-cylinder union by descendants of neutrinos different from the parent of the corresponding π^0 photon is counted as misidentified. 2 MW beam of 80 GeV protons. As a primitive simulation of a 2D wire readout, only X- and Z-coordinates are used for the energy reconstruction. Entries: Central cell shows plotted entries, other cells show overflow entries in direction w.r.t. central cell.

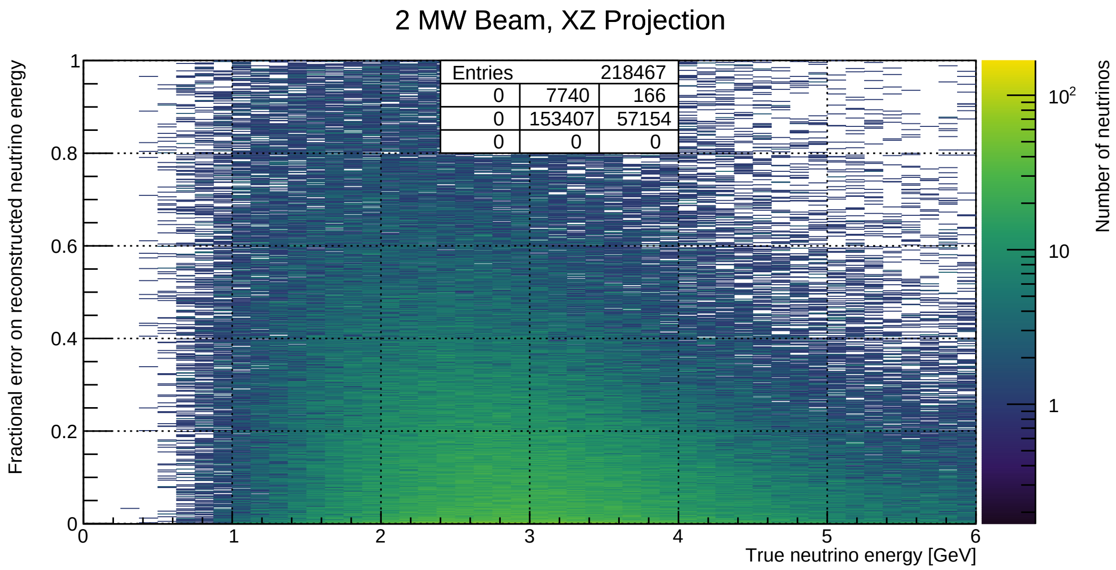

Figure A.25.: Misidentified energy fraction versus true neutrino energy for a simple π^0-induced EM shower reconstruction algorithm based on a cone-cylinder union. Energy deposited inside the cone-cylinder union by descendants of neutrinos different from the parent of the corresponding π^0 photon is counted as misidentified. Any energy deposited by muons is excluded. 2 MW beam of 80 GeV protons. As a primitive simulation of a 2D wire readout, only X- and Z-coordinates are used for the energy reconstruction. Entries: Central cell shows plotted entries, other cells show overflow entries in direction w.r.t. central cell.

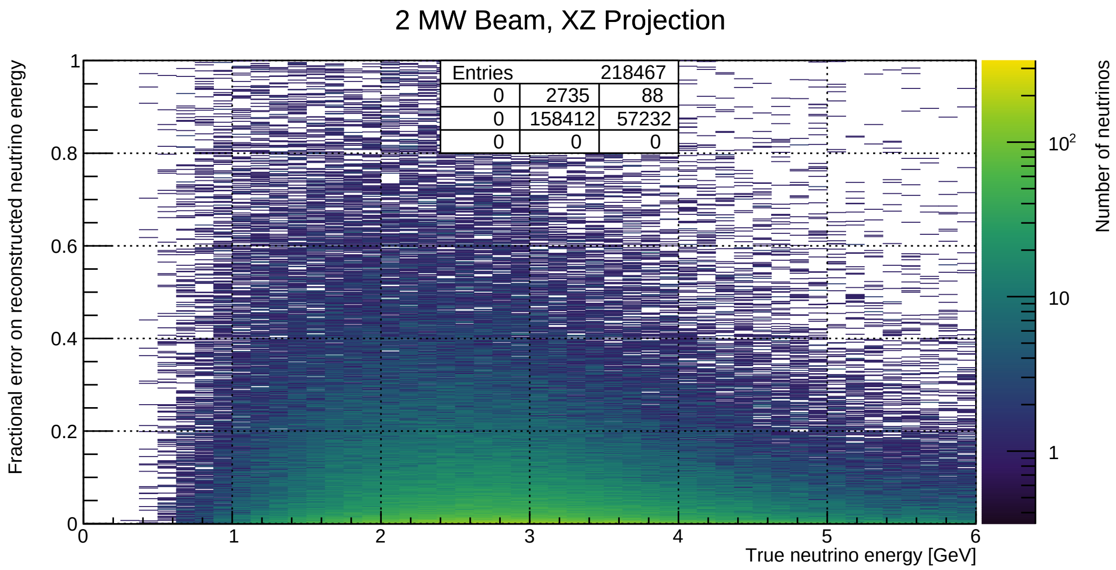

Figure A.26.: Misidentified energy fraction versus true neutrino energy for a simple π^0-induced EM shower reconstruction algorithm based on a cone-cylinder union. Energy deposited inside the cone-cylinder union by descendants of neutrinos different from the parent of the corresponding π^0 photon is counted as misidentified. Only energy deposited by photons, neutrons, or any of their descendants is included. 2 MW beam of 80 GeV protons. As a primitive simulation of a 2D wire readout, only X- and Z-coordinates are used for the energy reconstruction. Entries: Central cell shows plotted entries, other cells show overflow entries in direction w.r.t. central cell.

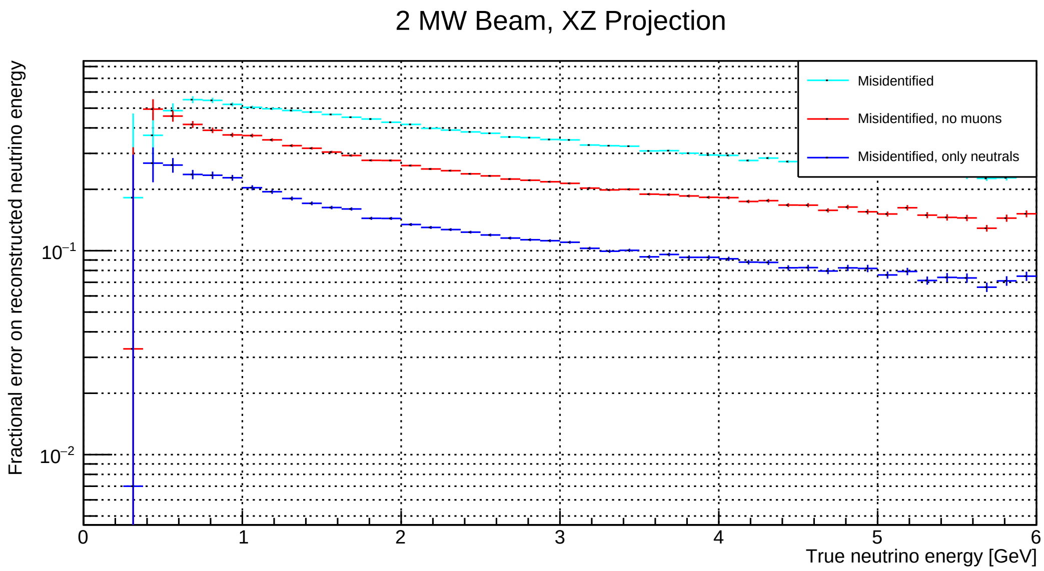

Figure A.27.: Mean misidentified energy fraction versus true neutrino energy for a simple π^0-induced EM shower reconstruction algorithm based on a cone-cylinder union. All energy deposited inside the cone-cylinder union by descendants of neutrinos different from the parent of the corresponding π^0 photon is counted as misidentified. Colour indicates different selections of misidentified energy: total (cyan); excluding depositions from muons (red); deposition from photons, neutrons, and their descendants only (blue). 2 MW beam of 80 GeV protons. As a primitive simulation of a 2D wire readout, only X- and Z-coordinates are used for the energy reconstruction.

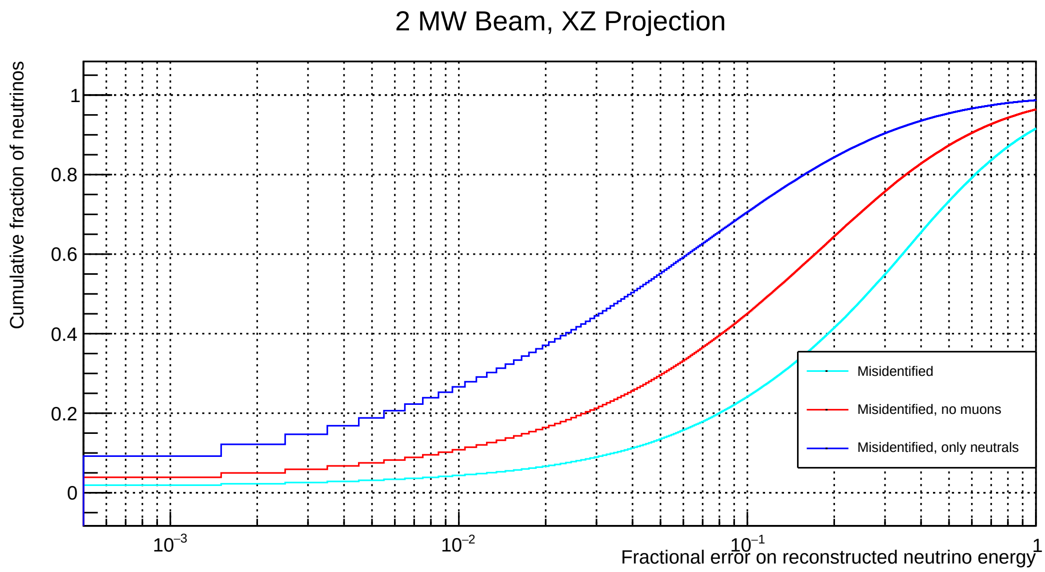

Figure A.28.: Cumulative fraction of neutrinos versus misidentified energy fraction for a simple π^0-induced EM shower reconstruction algorithm based on a cone-cylinder union. All energy deposited inside the cone-cylinder union by descendants of neutrinos different from the parent of the corresponding π^0 photon is counted as misidentified. Colour indicates different selections of misidentified energy: total (cyan); excluding depositions from muons (red); deposition from photons, neutrons, and their descendants only (blue). The curve depicts the fraction of neutrinos on the y-axis with a misidentified energy fraction equal to or lower than the corresponding value on the x-axis. 2 MW beam of 80 GeV protons. As a primitive simulation of a 2D wire readout, only X- and Z-coordinates are used for the energy reconstruction.

A.3. 10 MW Beam at 80 GeV Proton Energy

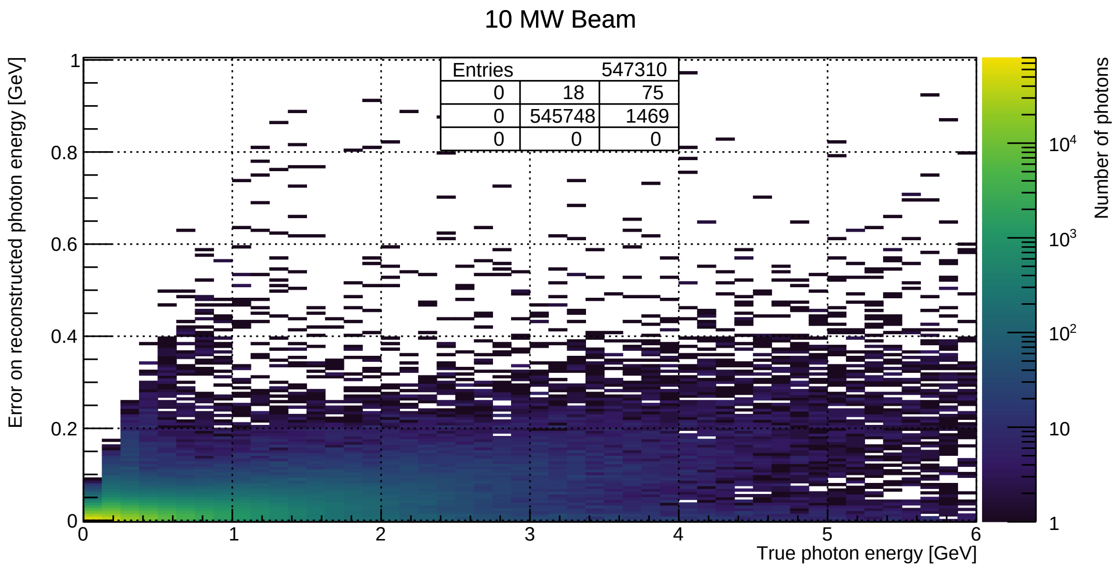

Figure A.29.: Missed energy versus true photon energy for a simple π^0-induced EM shower reconstruction algorithm based on a cone-cylinder union. All energy deposited outside of the cone-cylinder union is counted as missed. 10 MW beam of 80 GeV protons. Entries: Central cell shows plotted entries, other cells show overflow entries in direction w.r.t. central cell.

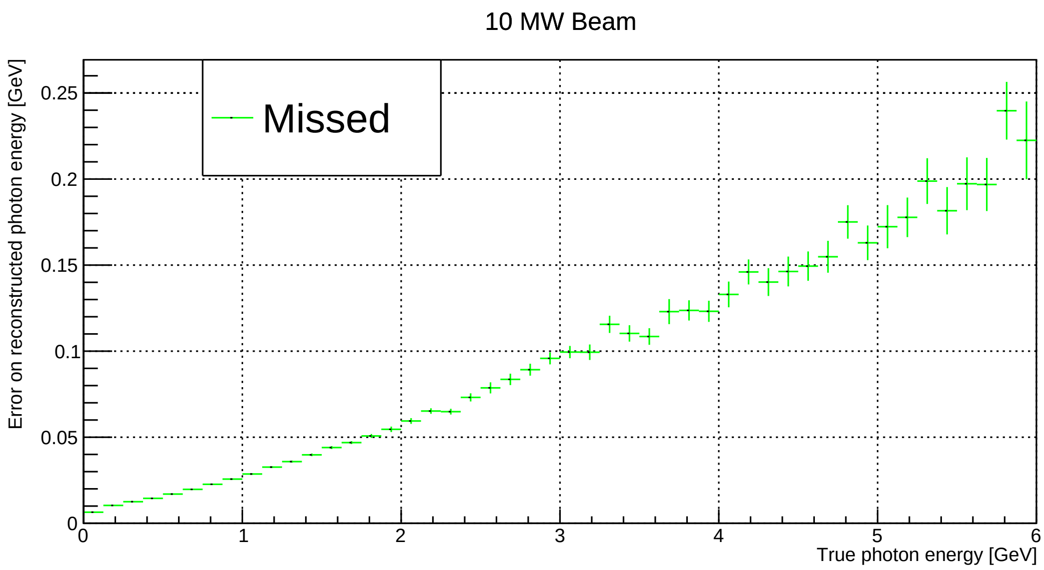

Figure A.30.: Mean missed energy versus true photon energy for a simple π^0-induced EM shower reconstruction algorithm based on a cone-cylinder union. All energy deposited outside of the cone-cylinder union is counted as missed. 10 MW beam of 80 GeV protons.

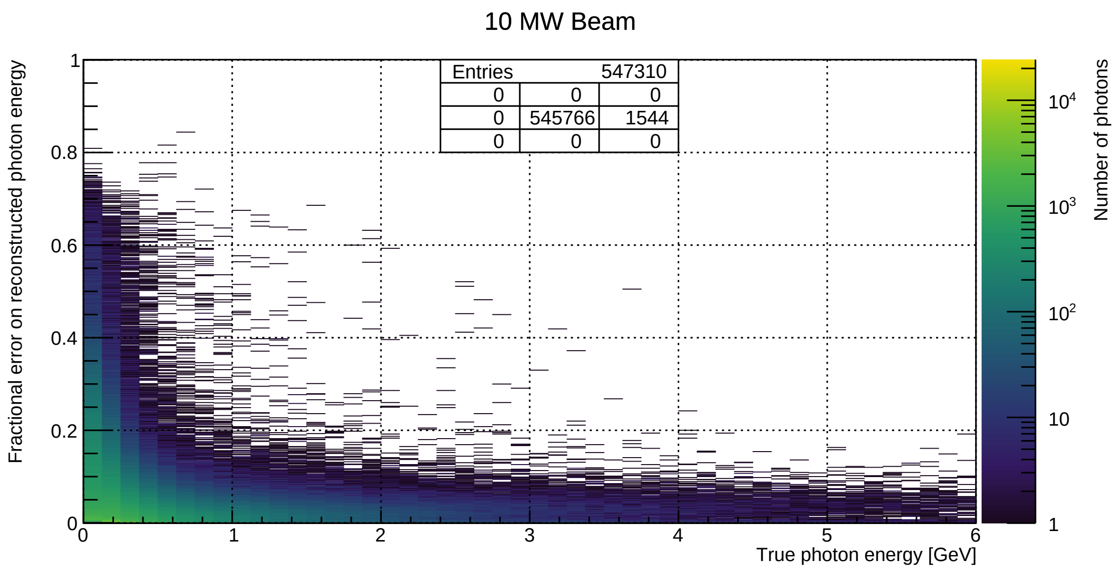

Figure A.31.: Missed energy fraction versus true photon energy for a simple π^0-induced EM shower reconstruction algorithm based on a cone-cylinder union. All energy deposited outside of the cone-cylinder union is counted as missed. 10 MW beam of 80 GeV protons. Entries: Central cell shows plotted entries, other cells show overflow entries in direction w.r.t. central cell.

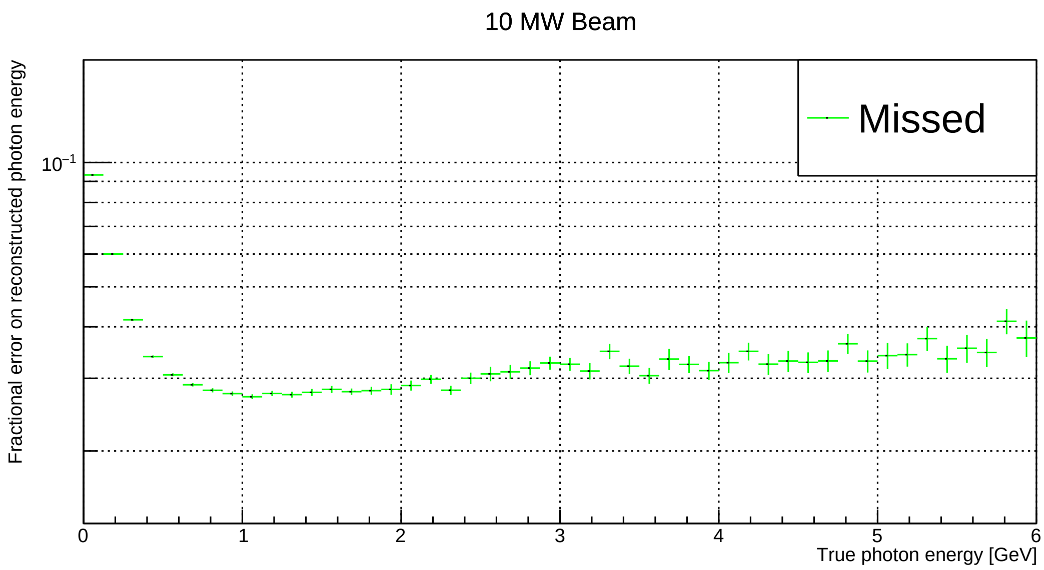

Figure A.32.: Mean missed energy fraction versus true photon energy for a simple π^0-induced EM shower reconstruction algorithm based on a cone-cylinder union. All energy deposited outside of the cone-cylinder union is counted as missed. 10 MW beam of 80 GeV protons.

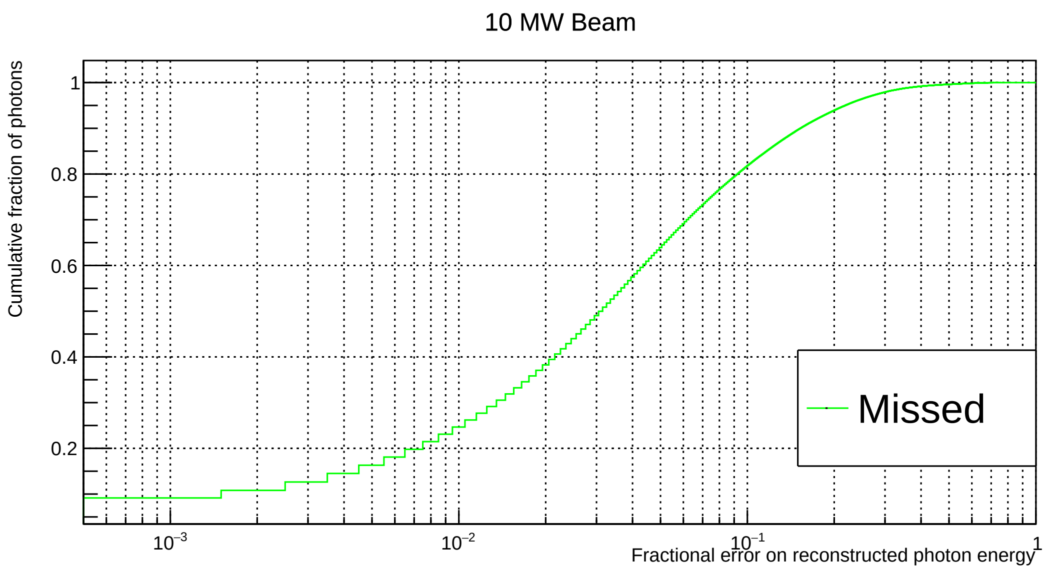

Figure A.33.: Cumulative fraction of photons versus missed energy fraction for a simple π^0-induced EM shower reconstruction algorithm based on a cone-cylinder union. All energy deposited outside of the cone-cylinder union is counted as missed. The curve depicts the fraction of photons on the y-axis with a missed energy fraction equal to or lower than the corresponding value on the x-axis. 10 MW beam of 80 GeV protons.

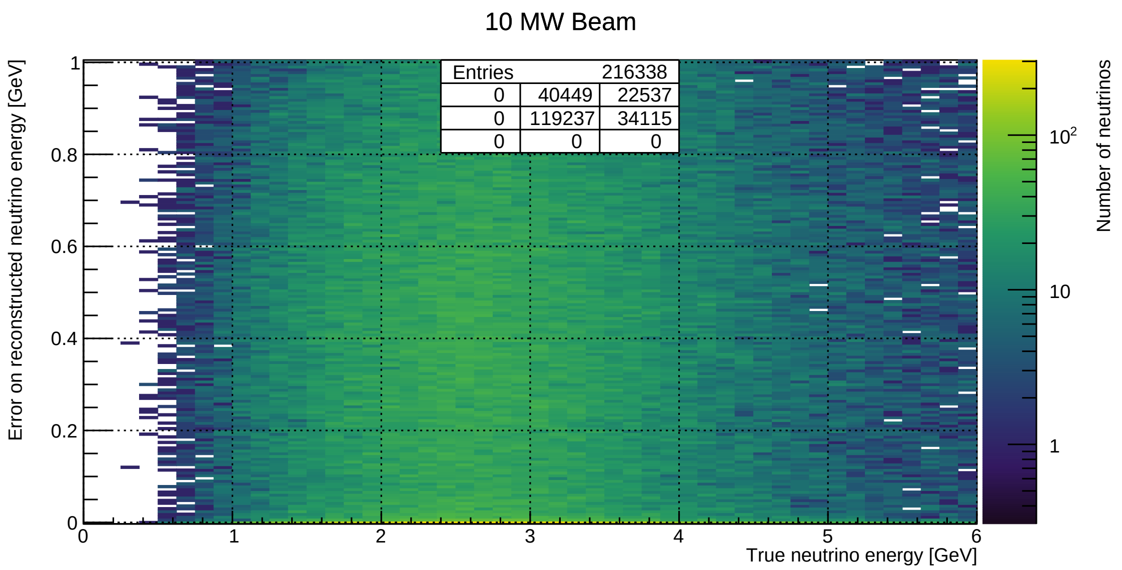

Figure A.34.: Misidentified energy versus true neutrino energy for a simple π^0-induced EM shower reconstruction algorithm based on a cone-cylinder union. All energy deposited inside the cone-cylinder union by descendants of neutrinos different from the parent of the corresponding π^0 photon is counted as misidentified. 10 MW beam of 80 GeV protons. Entries: Central cell shows plotted entries, other cells show overflow entries in direction w.r.t. central cell.

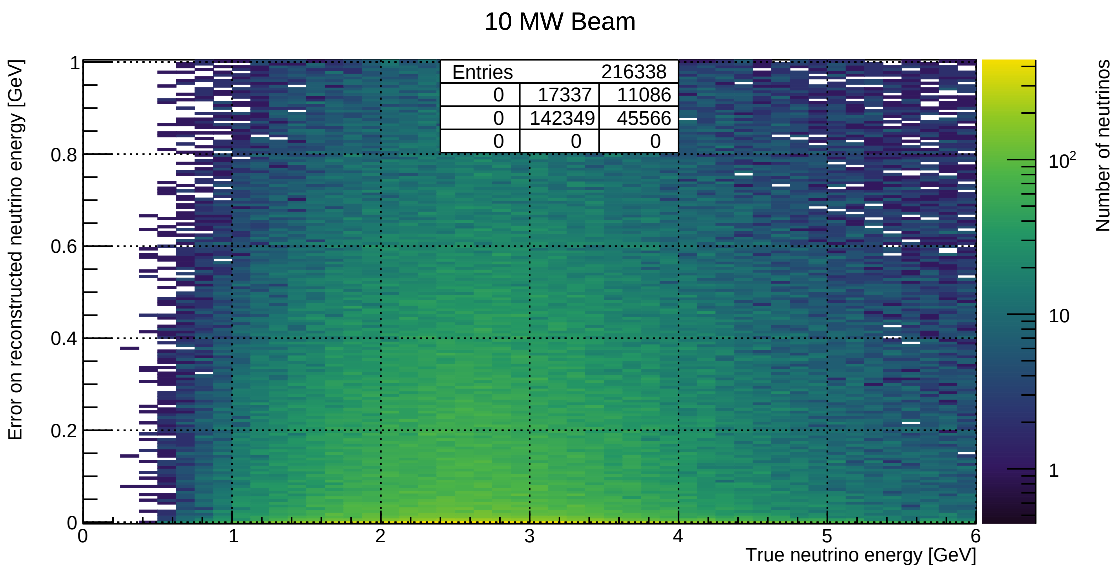

Figure A.35.: Misidentified energy versus true neutrino energy for a simple π^0-induced EM shower reconstruction algorithm based on a cone-cylinder union. Energy deposited inside the cone-cylinder union by descendants of neutrinos different from the parent of the corresponding π^0 photon is counted as misidentified. Any energy deposited by muons is excluded. 10 MW beam of 80 GeV protons. Entries: Central cell shows plotted entries, other cells show overflow entries in direction w.r.t. central cell.

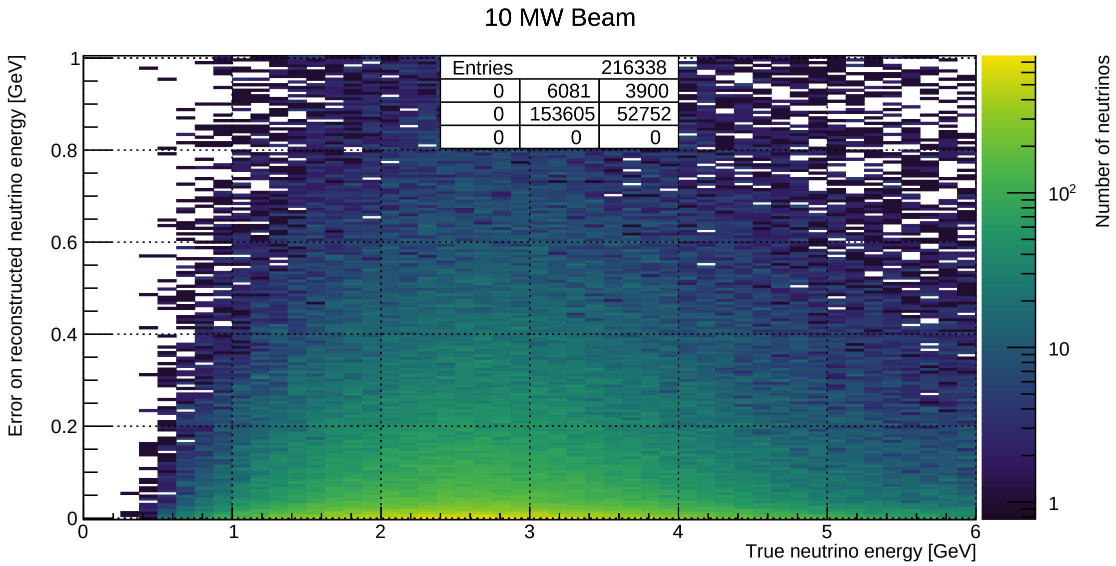

Figure A.36.: Misidentified energy versus true neutrino energy for a simple π^0-induced EM shower reconstruction algorithm based on a cone-cylinder union. Energy deposited inside the cone-cylinder union by descendants of neutrinos different from the parent of the corresponding π^0 photon is counted as misidentified. Only energy deposited by photons, neutrons, or any of their descendants is included. 10 MW beam of 80 GeV protons. Entries: Central cell shows plotted entries, other cells show overflow entries in direction w.r.t. central cell.

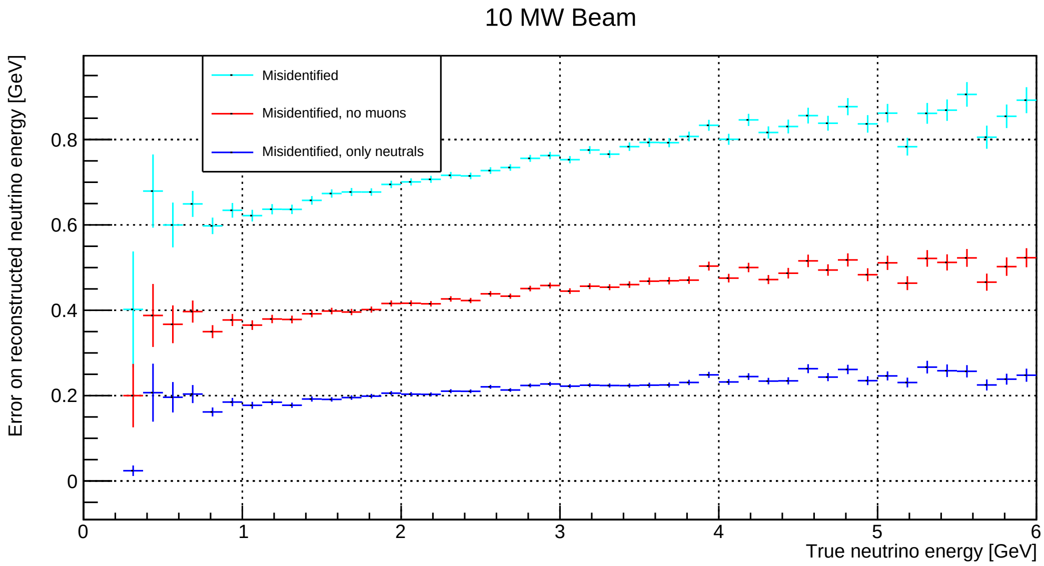

Figure A.37.: Mean misidentified energy versus true neutrino energy for a simple π^0-induced EM shower reconstruction algorithm based on a cone-cylinder union. All energy deposited inside the cone-cylinder union by descendants of neutrinos different from the parent of the corresponding π^0 photon is counted as misidentified. Colour indicates different selections of misidentified energy: total (cyan); excluding depositions from muons (red); deposition from photons, neutrons, and their descendants only (blue). 10 MW beam of 80 GeV protons.

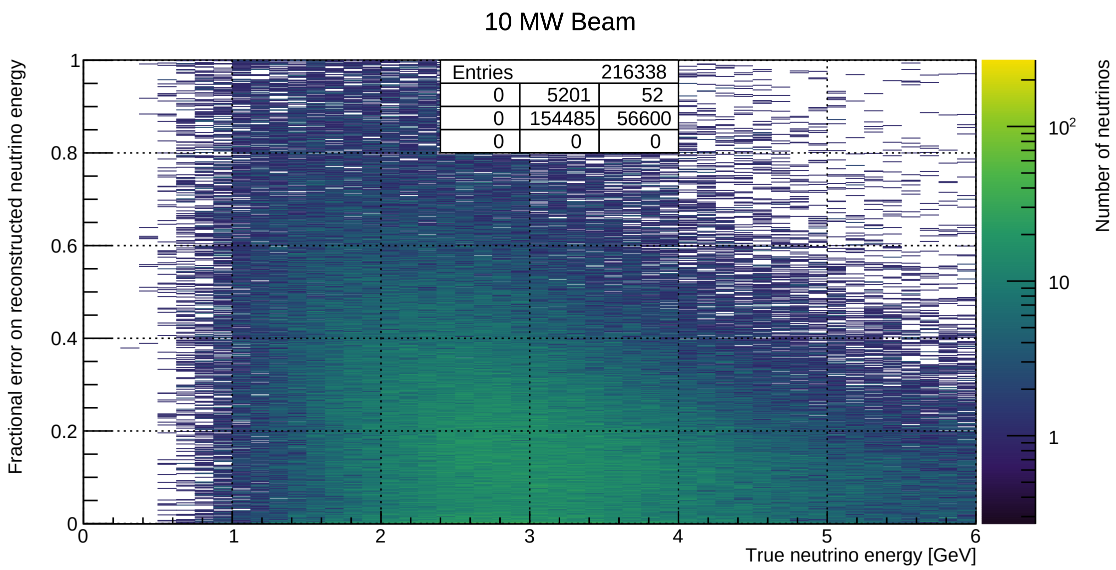

Figure A.38.: Misidentified energy fraction versus true neutrino energy for a simple π^0-induced EM shower reconstruction algorithm based on a cone-cylinder union. All energy deposited inside the cone-cylinder union by descendants of neutrinos different from the parent of the corresponding π^0 photon is counted as misidentified. 10 MW beam of 80 GeV protons. Entries: Central cell shows plotted entries, other cells show overflow entries in direction w.r.t. central cell.

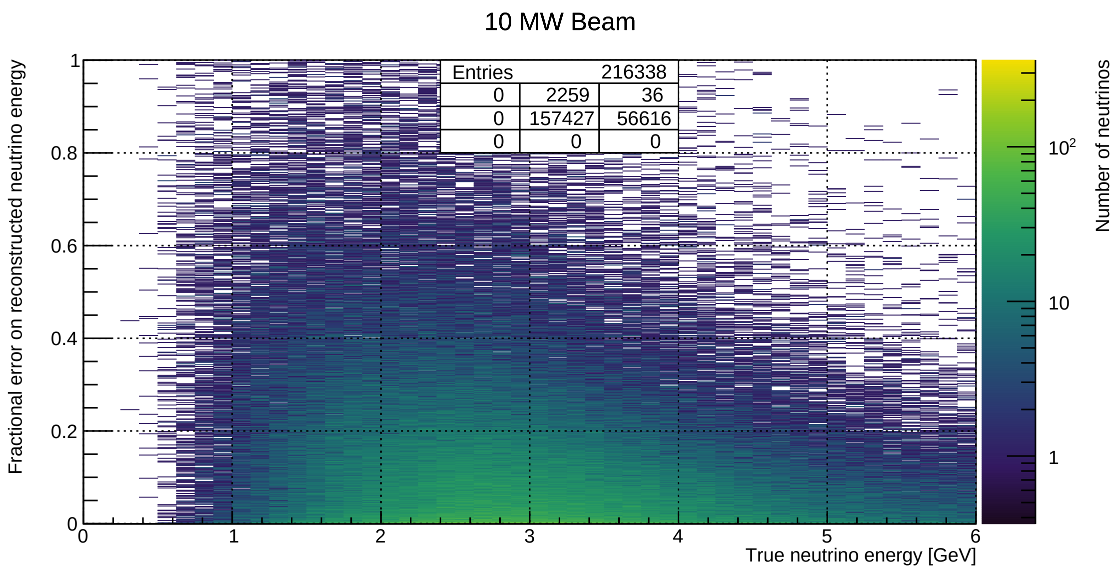

Figure A.39.: Misidentified energy fraction versus true neutrino energy for a simple π^0-induced EM shower reconstruction algorithm based on a cone-cylinder union. Energy deposited inside the cone-cylinder union by descendants of neutrinos different from the parent of the corresponding π^0 photon is counted as misidentified. Any energy deposited by muons is excluded. 10 MW beam of 80 GeV protons. Entries: Central cell shows plotted entries, other cells show overflow entries in direction w.r.t. central cell.

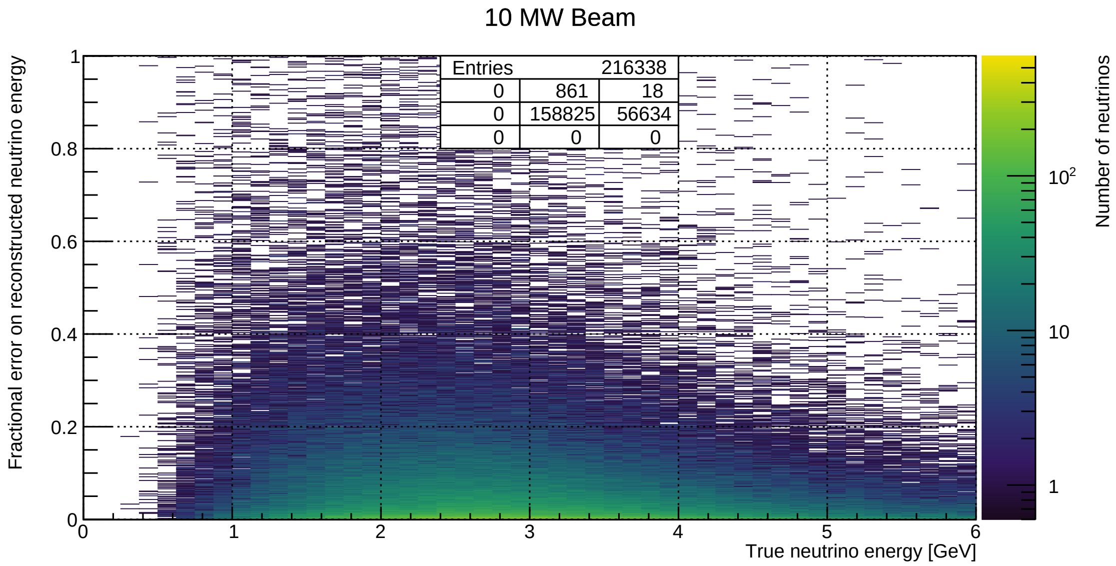

Figure A.40.: Misidentified energy fraction versus true neutrino energy for a simple π^0-induced EM shower reconstruction algorithm based on a cone-cylinder union. Energy deposited inside the cone-cylinder union by descendants of neutrinos different from the parent of the corresponding π^0 photon is counted as misidentified. Only energy deposited by photons, neutrons, or any of their descendants is included. 10 MW beam of 80 GeV protons. Entries: Central cell shows plotted entries, other cells show overflow entries in direction w.r.t. central cell.

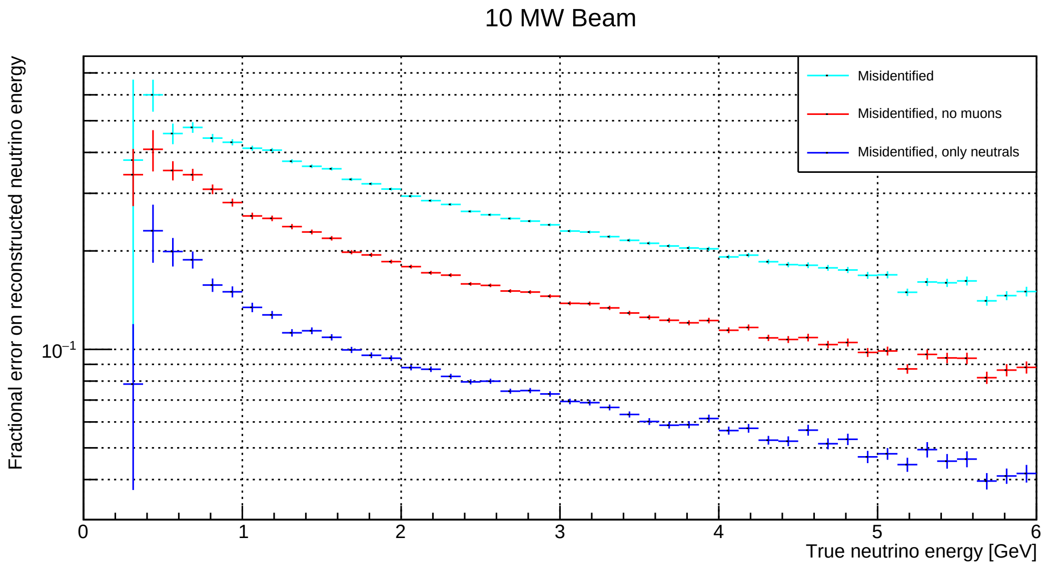

Figure A.41.: Mean misidentified energy fraction versus true neutrino energy for a simple π^0-induced EM shower reconstruction algorithm based on a cone-cylinder union. All energy deposited inside the cone-cylinder union by descendants of neutrinos different from the parent of the corresponding π^0 photon is counted as misidentified. Colour indicates different selections of misidentified energy: total (cyan); excluding depositions from muons (red); deposition from photons, neutrons, and their descendants only (blue). 10 MW beam of 80 GeV protons.

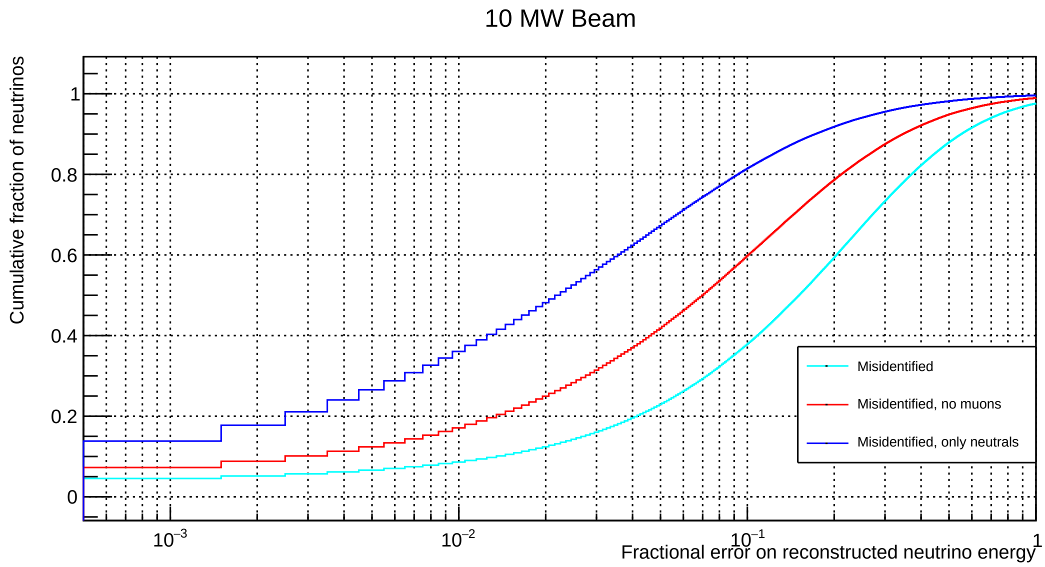

Figure A.42.: Cumulative fraction of neutrinos versus misidentified energy fraction for a simple π^0-induced EM shower reconstruction algorithm based on a cone-cylinder union. All energy deposited inside the cone-cylinder union by descendants of neutrinos different from the parent of the corresponding π^0 photon is counted as misidentified. Colour indicates different selections of misidentified energy: total (cyan); excluding depositions from muons (red); deposition from photons, neutrons, and their descendants only (blue). The curve depicts the fraction of neutrinos on the y-axis with a misidentified energy fraction equal to or lower than the corresponding value on the x-axis. 10 MW beam of 80 GeV protons.